Macro- and micronutrient dissolution from desert and volcanic aerosols in rain and seawater : impact on phytoplankton in the Southern Indian Ocean

Carla Geisen

Sorbonne Université

École doctorale des Sciences de l'Environnement d'Île-de-France (ED 129)

Laboratoire d'Océanographie et du Climat : Expérimentations et Approches Numériques (LOCEAN) - UMR 7159

Équipe de recherche CYBIOM

Macro- and micronutrient dissolution from desert and volcanic aerosols in rain and seawater: Impact on phytoplankton in the Southern Indian Ocean

Par **Carla GEISEN**

Thèse de doctorat de Biogéochimie Marine

Dirigée par Céline RIDAME et Damien CARDINAL

Présentée et soutenue publiquement le lundi 27 septembre 2021

Devant un jury composé de :

M. Stéphane Blain	Professeur	LOMIC-SU	Président du jury
Mme Brivaëla Moriceau	Chargée de recherche	LEMAR-UBO	Rapportrice
Mme Delphine Lannuzel	Associate Professor	IMAS-UTAS	Rapportrice
M. Pierre Delmelle	Professeur	ELIE-UCLouvain	Examinateur
Mme Émilie Journet	Maître de conférences	LISA-UPEC	Membre invité
Mme Céline Ridame	Maître de conférences	LOCEAN-SU	Directrice de thèse
M. Damien Cardinal	Professeur	LOCEAN-SU	Directeur de thèse

Activités scientifiques pendant la thèse

Publications

Geisen, Ridame, Journet, Delmelle, Marie, Lo Monaco, Metzl, Ammar, Kombo, Cardinal. Phytoplanktonic Response to simulated Volcanic and Desert Dust Deposition Events in the South Indian and Southern Oceans. *In rev, Limnol. Oceanogr*.

Geisen, Ridame, Journet, Delmelle, Lo Monaco, Metzl, Kombo, Cardinal. Nutrient solubility in the Southern Indian Ocean: Abiotic release of macro- and micronutrients in natural and artificial seawater after simulated volcanic ash and desert dust deposition. *In prep*

Conférences

Blowing South: Southern Hemisphere Dust Symposium, 8-10 November 2021, online

Geisen, Ridame, Journet, Delmelle, Marie, Lo Monaco, Metzl, Ammar, Kombo, Cardinal. Impact of desert and volcanic aerosol deposition on phytoplankton in the Southern Indian Ocean.*Session "Ocean Biogeochemistry 1"*

EGU General Assembly 2020, European Geoscience Union, 4-8 Mai 2020, online

Geisen, Ridame, Journet, Caron, Marie, Cardinal. Impact of desert and volcanic aerosol deposition on phytoplankton in the South Indian Ocean and Southern Ocean. D2835

Session AS2.14 Atmospheric Acidity, Air-Sea Chemical Fluxes and their Impacts

IMBeR Future Oceans2, Integrated Marine Biosphere Research project

17-21 Juin 2019 à Brest, France

Geisen, Ridame, Journet, Kombo, Ammar, Cardinal.

Dissolution of Fe and Si from desert and volcanic aerosols and impact on phytoplankton.

Session "Multiple drivers and their role in ocean global change biology"

Campagne océanographique

Mission Obs Austral, programme OISO, Jan-Fev 2019 (6 semaines)

N/O Marion Dufresne (TAAF) de La Réunion, dans l'Océan Indien et l'Océan Austral

Expériences d'incubation ; participation au quart CTD et continu de surface.

Enseignement – Sorbonne Université

ATER : Attachée temporaire d'enseignement et de recherche : septembre 2020 – août 202

Biogéochimie marine (M1) : métaux trace, isotopes ; CM et TD

Orientation et Insertion Professionnelle (L1, L3) : ateliers et TD

Professeure référente : suivi individuel d'étudiants de L1

CME : Chargée de mission d'enseignement : octobre 2017 – août 2020

Géosciences 1 (L1) : partie Terre Externe : océan, atmosphère, paléo ; TD

Développement Durable (L2 Polytech) : cycle de l'eau, climat ; TD

Atelier de Recherche Encadré ARE (L1) : nutriments dans l'eau, TD et sortie terrain

Cours de thèse

Cours ED129 : Changement climatique : sciences, sociétés, politique (21 h)

Cours ED129 : Modélisation statistique (40 h)

Club de lecture du LOCEAN

École d'été

SOLAS Surface Ocean Lower Atmospheric Study, Juillet 2018 (2 semaines)

Modélisation et télédétection, présentation des travaux de thèse (poster), réseautage

Techniques de laboratoire

Cultures de phyto- et zooplancton, incubations à bord, travail en salle blanche, ICP-MS, ICP-AES, spectrophotométrie, cytométrie en flux, marquages cellulaires, microscopie optique à épi-fluorescence et microscopie optique, compteur Coulter

Vulgarisation

HCERES : évaluation d'un programme de master international en biotechnologies, 2021

Fête de la Science, Campus Jussieu : 2018, stand du LOCEAN-IPSL

Remerciements

Mon premier remerciement va bien sûr aux deux personnes qui m'ont encadré durant les quatre dernières années : mes directeurs de thèse **Céline Ridame** et **Damien Cardinal.** Vous avez formé un sacré binôme digne du titre « papa et maman de thèse » que j'aimais tant vous donner. Vous vous complétez parfaitement, que ce soit d'un point de vue scientifique ou par votre caractère, et je pense que c'était un véritable avantage à bien des égards. Merci de m'avoir fait confiance le jour où je vous ai envoyé ma candidature complétée par une photo de bébé phoque au lieu d'un CV. **Céline**, c'était pour travailler avec toi que j'avais choisi ce sujet de thèse, et je te suis reconnaissante pour l'intensité de notre relation, que ce soit à terre ou en mer, au labo comme à l'apéro ☺. Ensuite **Damien**, ton calme et ta justesse de jugement ont vraiment été deux éléments qui m'ont énormément aidé à garder le cap du début à la fin de cette aventure. Tu étais toujours disponible et à l'écoute dans tout un tas de situations et tu m'as aidé à chercher (et à trouver) les solutions à mes problèmes. Merci aussi à tous les deux de m'avoir poussé à devenir monitrice puis ATER, l'enseignement était une très belle découverte pour moi et vous m'avez servi de modèle.

Je voudrais également remercier les membres du jury : **Stéphane Blain**, **Delphine Lannuzel**, **Brivaëla Moriceau**, **Pierre Delmelle** et **Émilie Journet** pour vos nombreux commentaires et la discussion intéressante qui a suivi ma soutenance et qui ont amélioré mon manuscrit.

Au sein du LOCEAN, je souhaite exprimer un premier grand merci aux chefs et cheffes d'équipe CYBIOM : **Nicolas Chevalier**, **Aline Tribollet** et **Claire Lo Monaco** qui ont toujours placé l'intérêt des étudiants en priorité n°1 et m'ont permis d'assister à des conférences et écoles d'été, et surtout à participer à une campagne en mer ! Merci Claire de m'avoir accueillie durant la campagne OISO-29 et de m'avoir permis de vivre cette grande aventure dans l'Océan Austral sur le *Marion Dufresne*. Aussi parmi les OISOs, je souhaite remercier **Nicolas Metzl** pour ton expertise scientifique, ton humour subtil et ta disponibilité remarquable qui ont clairement été profitables pour l'article, je suis heureuse de te compter comme coauteur !

Parmi mes collaborateurs, je remercie tout particulièrement Émilie pour m'avoir accompagné durant toute la durée de ma thèse en portant de multiples casquettes : en tant que membre de mon comité de thèse, co-auteure de mes articles, membre invité du jury de thèse, mais surtout fournisseuse officielle d'aérosols et de m'avoir initiée aux particularités de l'ICP-AES. Également au LISA, je remercie **Karine Desboeufs** pour la gentillesse, l'expertise

scientifique dans les sciences de l'atmosphère, accompagnée d'une incroyable disponibilité, et **Frank Fu** pour l'aide précieuse avec les attaques acides de mes échantillons.

Parmi mes collègues du LOCEAN au quotidien, un énorme merci va à **Fanny Kacsmar** et **Mustapha Benrahmoune** pour toute l'aide avec les repiquages, lavages et préparations de réactifs ! Merci Mustapha d'avoir assuré une bonne partie des analyses au spectro pendant que j'étais débordée à l'ICP, et merci Fanny pour les préparations d'eau de mer, la compagnie chaleureuse en salle blanche et au microscope, et d'avoir été disponible pour moi pour me guider dans les étapes de différentes préparations en début de thèse.

Ensuite sur le site de Bondy, je souhaite remercier **Irina Djouraev** et **Florence Le Cornec** pour votre expertise et les longues heures passées ensemble à l'ICP-MS. Merci aussi à **Sandrine Caquineau** et toute l'équipe pour les chaleureuses pauses café et déjeuners. Votre présence et la bonne ambiance étaient vraiment une excellente raison de venir faire quelques manips à Bondy !

Merci aussi à **Benoit Caron**, **Morgane Gallinari**, **Aymeric Chazottes** et **Olivier Aumont** pour votre soutien scientifique et moral. Merci Benoit pour toutes les heures passées au QQQ à discuter de plongée ; merci Morgane et Aymeric pour votre patience lors de vos explications concernant les protocoles d'analyse au SEAFAST et du monde obscur des statistiques. Merci Olivier pour ton regard externe sur mon parcours au labo dans le cadre du comité de thèse, mais aussi pour tes conseils de modélisation, et ce même à J-5 de la soutenance !

Un autre chaleureux merci va à deux personnes exceptionnelles du LOCEAN qui ont transformé les petites démarches administratives et logistiques dans une véritable joie : **Dany Thomas** et **pti'Claude Legarnec.** Merci à vous et profitez bien de la retraite !

Merci à tous les **copains du 46-00** grâce auxquels ce petit « couloir perdu » reste à mes yeux le meilleur spot du campus. Vous êtes tous devenus des amis plus que des collègues, j'ai vraiment passé de chouettes années parmi vous. Il y a eu les compagnons de route comme **Jonathan Fin** et **Catherine Schmechtig** au labo et **Claude Mignon** en mer**.** Merci Jo pour l'amitié, les nombreux fous rires et les délicieux gâteaux, croziflettes et autres apéros partagés (et récemment les cartons de déménagement). Merci à Catherine pour les petites merveilles de ton jardin, et tous tes récits de voyage (en RER ou en safari) durant les pauses dej ☺. Et merci encore Claude d'avoir gardé ton sang-froid quand j'ai commencé à jouer à l'apprenti chimiste pile durant une tempête au large de Crozet.

Comment rédiger une lettre de remerciements sans évoquer les *Zoulettes* ? Pour commencer une spéciale dédicace à la plus bonne-bonne-bonne de mes zoulettes : je nomme **Coraline Lesseure**. Je ne sais pas à quoi aurait ressemblé ma thèse sans toi, tu es vraiment l'âme du 46-00. Qui m'aurait rappelé tous les jours à 11h50 qu'il était temps d'acheter ma crêpe avant que les hordes d'étudiants débarquent ? Qui m'aurait fourni tous ces gâteaux et tisanes (voire dolipranes) et du gossip ? Qui m'aurait tant fait rire avec ses affirmations délirantes ? Qui aurait planifié les week-ends à Brest ou soirées apéro ? Et surtout, qui d'autre aurait organisé un pot de thèse de dix heures ? Ensuite merci au reste de la troupe, **Maële Torterotot, Marion Chapeau, Camille Merland, Mélyne Hautecœur** et de nouveau **Céline Ridame** pour la bonne ambiance à bord du *Marion Dufresne* : Les blind test, les petits mots d'amour sur les portes et surtout les soirées endiablées sur le deck sont un précieux souvenir.

Thanks also to the international army of joyful office mates: **Joana Cruz** and **Yang Feng** for the greatest start in this PhD adventure. It was a real pleasure to share the big office with you, with all the giggles and cozy cookie breaks in this colorful Brazilian-Chinese-German-French cultural mixture. *Fui feliz aqui.*

Another warm thought goes obviously to **Sarath Pullyottum-Kavil**. I am really thankful that I got to meet you. I truly cherish all these countless hours spent together in the clean lab or in front of the ICP-MS, preparing resins or spectro samples together… It felt perfect to be two in the same boat doing the same type of analysis. And our shared cookie storage in the office was the best. ☺ I really look forward to coming and visiting you in Kerala one day (soon) !!

Several warm thoughts go to **Alice Rodrigues** and **Luiza Reis,** as well as **Diego Alaguarda** and **Han Wang**, et aux stagiaires **Joelle Kombo** et **Zoé Mériguet** que j'ai eu le plaisir de co-encadrer.

Sara Sergi, quelle belle découverte de t'avoir rencontré et surtout d'avoir passé ces derniers mois de fin de rédaction et de préparation de soutenance avec toi ! Et surtout quelle joie d'organiser et de célébrer ensemble nos soutenances. Des fois, le hasard fait bien les choses. Je te souhaite de belles choses et j'espère de rapides retrouvailles.

En dehors de la recherche, je souhaite bien évidemment saluer mes copains, dont les plongeurs PMP6 : en premier lieu **Ariane Chotard** qui m'a remotivé à bien des reprises durant ces quatre années avec des pauses chocolat chaud, des balades dans le jardin des plantes avec visites de bébé félins, des bons plans bière-frites ou autres soirées cocktail maison. Merci d'avoir toujours été là pour moi, c'était top d'être ta binôme déléguée toutes ces années. En deuxième lieu, je salue le reste des « gros ~~plongeurs~~ dinosaures du dimanche » avec toutes les soirées raclettes indépendamment de la saison, les escapades à Riga, le passage du N4 et j'en passe. Merci à **Marcio, Julien, Renaud** et **Thomas** pour votre amitié. Merci aussi à toute l'équipe encadrante de PMP6 de m'avoir formée comme plongeuse puis comme monitrice durant toutes ces années, et d'avoir encouragé mes projets d'océanographe. Merci **David, Franz, Lionel, Franky, Anaïs**. Une pensée particulièrement chaleureuse s'adresse à notre cher prof émérite **Alain Couté** dont le grand sens de l'humour et d'autodérision, combinés à son expertise scientifique sans limites sur la vie sous-marine seront longtemps mémorés**.**

Ein ganz riesengroßes Dankeschön geht natürlich auch nach Berlin zum lieben Geisen-Clan. Ihr habt schon immer an mich geglaubt, das ist unglaublich viel wert. Ich hab zwar noch keine Carla-Qualle entdeckt, aber das kann ja alles noch kommen! **Birgit, Joch, Oma, Ole, Mahtab, Tiam (und auch Arian), Gottfried, gr. Ole: Danke für alles.** Danke für die telefonische Unterstützung, für die leckeren Rezept-Ideen und Oma-Tricks, für die netten Familien-Urlaube und vieles mehr. Und natürlich Danke für das weltbeste Doktor-Buffet! Einen warmen Gruß auch an **Oma Marga und Opa Ernst**. Wasser hat zwar keine Balken, aber ich schaff das trotzdem!

Je souhaite aussi chaleureusement remercier **Lars et Odile** pour tout votre soutien durant ces dernières années. Merci pour tous les dîners à la maison en prenant en considération notre appétit grandissant pour les légumes, merci pour nous avoir permis de nous installer dans le Cantal et aussi pour la coloc' folklorique à Cussac ! Merci aussi pour votre grand investissement lors de mon pot de thèse et de nous avoir trouvé l'appart génial à Boulogne.

Et finalement **mon cher Coco,** je ne sais pas comment j'aurais fait sans toi durant toutes ces années. J'ai hâte d'ajouter une nouvelle destination à notre longue liste de spots de rêve pour chasser les plus beaux couchers de soleil : (Paris)-Roscoff-Helgoland-Maurice-Cussac et maintenant la Côte d'Opale !

Jedes Kind, das weiß doch
In der Ruhe liegt die Kraft.
Und der allerbeste Treibstoff
Ist die Energie der Nacht.

Eule, Jan Delay, 2021

Table of content

I. Introduction générale

1 Nutriments dans l'océan de surface

1.1 Rôle des nutriments pour le phytoplancton

Le phytoplancton a besoin pour sa croissance d'une quantité suffisante de lumière, d'une certaine température et de différents nutriments. Les nutriments peuvent être classés en deux catégories en fonction des besoins nutritionnels du phytoplancton.

Ainsi les **macronutriments** sont généralement présents en plus grande quantité dans l'océan de surface (de l'ordre de grandeur du $\mu mol.L^{-1} = 10^{-6}$ $mol.L^{-1}$) que les micronutriments avec des gammes de concentration de 0-60 $\mu mol.L^{-1}$ $Si(OH)_4$, 0-25 $\mu mol.L^{-1}$ NO_3^- et 0-2.5 $\mu mol.L^{-1}$ PO_4^{3-} (World Ocean Atlas, 2018 ; Boyer et al., 2018), respectivement pour les silicates, nitrates et phosphates. Les macronutriments sont nécessaires au phytoplancton pour le fonctionnement de base de leurs cellules. Ainsi, l'azote (N) est par exemple indispensable à la synthèse d'acides aminés constituants des protéines, qui assurent un rôle primordial dans la structure, la régulation et la communication cellulaire. Le phosphore (P) est utilisé par les cellules entre autres pour former des acides nucléiques (ADN, ARN) et des ribosomes, et joue donc un rôle considérable dans la division cellulaire et dans le cycle énergétique (via la synthèse ATP/ADP). Enfin, le carbone (C) est un constituant important des lipides nécessaire pour les membranes cellulaires, mais il est également l'élément structurel de toutes les molécules organiques synthétisées par le phytoplancton. Finalement, le silicium (Si) est requis par les diatomées pour la production de leurs frustules en opale (SiO_2) ainsi que pour les silicoflagellés (Tréguer and Pondaven, 2000).

L'océanographe américain Alfred Redfield a établi en 1934 un ratio stœchiométrique des besoins physiologiques entre ces différents nutriments au sein des cellules phytoplanctoniques qui reste remarquablement constant entre espèces et bassins océanographiques à 106 C : 16 N : 1 P, c'est-à-dire que pour un atome de P, on trouvera en moyenne 16 atomes de N et 106 de C au sein d'une cellule phytoplanctonique. Ce rapport a plus tard été étendu pour le Si par Marc Brzezinski (1985) avec 1 N : 1 Si pour les diatomées, puis pour d'autres éléments chimiques tout aussi nécessaires au phytoplancton, mais sous forme de traces, appelés **micronutriments**. La concentration cellulaire de ces éléments est environ mille fois inférieure comparé aux macronutriments et le rapport stœchiométrique est souvent

exprimé en mmol.mol^{-1} de P (Twining and Baines, 2013) puisque P est le macronutriment le moins abondant. Ce **ratio de Redfield étendu** peut varier en fonction des espèces et bassins océaniques, mais peut s'exprimer ainsi : $(C_{124}N_{16}P_1)_{x1000}Fe_{7.5}Mn_4Zn_{0.80}Cu_{0.38}Co_{0.21}Cd_{0.21}$ (Ho et al., 2003).

Tableau I-1: Fonctions cellulaires et besoins en métaux traces pour la synthèse de nombreuses métalloprotéines par le phytoplancton. Tableau adapté de Twining and Baines (2013).

	Protéines	**Fonctions**
Fe	Cytochromes	Transport d'électrons dans la chaîne photosynthétique ; respiration
	Ferrédoxine	Transport d'électrons dans la chaîne photosynthétique ; fixation de N
	Nitrate et nitrite réductase	Conversion du nitrate en ammoniac
	Chélatase	Synthèse de la porphyrine et phycobiliprotéine
	Nitrogénase	Fixation de N
	Catalase	Conversion du peroxyde d'hydrogène en eau
	Péroxydase	Réduction d'espèces réactives de l'oxygène
	Superoxyde dismutase	Dismutation de superoxydes en peroxyde d'hydrogène et O_2
Zn	Anhydrase carbonique	Réaction d'hydratation et déshydratation du CO_2
	Phosphatase alcaline	Hydrolyse des esters de phosphate
	ARN polymérase	Réplication et transcription des acides nucléiques
	ARN_t synthétase	Synthèse des ARN_t
	Transcriptase inverse	Synthèse d'ADN simple brin à partir d'ARN
	Carboxypeptidase	Hydrolyse des liaisons peptidiques
	Superoxyde dismutase	Dismutation de superoxydes en peroxyde d'hydrogène et O_2
Mn	Complexe d'oxydation de l'eau	Oxydation de l'eau durant la photosynthèse
	Superoxyde dismutase	Dismutation de superoxydes en peroxyde d'hydrogène et O_2
	Arginase	Hydrolyse de l'arginine en ornithine et urée
	Phosphotransférases	Réactions de phosphorylation
Ni	Uréase	Hydrolyse de l'urée
	Superoxyde dismutase	Dismutation de superoxydes en peroxyde d'hydrogène et O_2
Cu	Plastocyanine	Transporteur d'électrons de la photosynthèse
	Cytochrome oxydase	Transporteur d'électrons de la mitochondrie
	Ascorbate oxydase	Oxydation et réduction de l'acide ascorbique
	Superoxyde dismutase	Dismutation de superoxydes en peroxyde d'hydrogène et O_2
	Ferroxidase multicuivre	Transporteur transmembranaire de haute affinité du Fe
Co	Vitamine B_{12}[a]	Réactions de transferts de C et H
Cd	Anhydrase carbonique	Réaction d'hydratation et déshydratation du CO_2
Mo	Nitrate réductase	Conversion du nitrate en ammoniac
	Nitrogénase	Fixation de N

Similairement au fait d'être requis en faibles quantités par le phytoplancton, les **micronutriments** se trouvent dans l'eau de mer sous forme de traces, malgré une concentration élevée dans les roches et sols. Mais leur très faible solubilité limite leur concentration de l'ordre du pmol.L^{-1}-nmol.L^{-1} (10^{-12}-10^{-9} mol.L^{-1}). Le Tableau I-1 issu des travaux de Twining and Baines (2013) regroupe les fonctions cellulaires du phytoplancton dans lesquelles interviennent différents métaux traces. Ainsi, le fer (Fe) est requis par les cellules pour le transport d'électrons au sein de l'appareil photosynthétique, ainsi que pour optimiser le rendement quantique net de la photosynthèse (Moore et al., 2007a). D'autres éléments traces comme le zinc (Zn) interviennent dans la régulation de l'expression génique (transcription, traduction) ou sont des cofacteurs dans plusieurs enzymes (Twining and Baines, 2013). Il est à noter qu'il existe de nombreuses **adaptations du phytoplancton à un environnement carencé**, comme certaines diatomées polaires habituées à des conditions pauvres en fer qui synthétisent la plastocyanone (Cu-enzyme) à la place du cytochrome c_6 (Fe-enzyme) qui joue le même rôle dans le photosystème II (Peers and Price, 2006). Ainsi ces diatomées ont des besoins nutritionnels plus faibles en Fe.

Un autre mécanisme mis en évidence chez certaines espèces de phytoplancton est la substitution d'un métal par un autre au sein d'une même protéine: le cobalt (Co) et le cadmium (Cd) peuvent ainsi remplacer le Zn dans l'anhydrase carbonique des diatomées (Price and Morel, 1990). D'un autre côté, **la limitation d'un élément et l'adaptation/acclimatation à la carence peut aussi influencer les besoins du phytoplancton pour d'autres éléments,** par exemple un contenu intracellulaire augmenté en Zn, Co et Cd en conditions de limitation en P ou des besoins accrus en Fe dans le cadre de la diazotrophie (fixation de N_2) puisque la nitrogénase est une enzyme riche en Fe (Kustka et al., 2003). Ainsi l'importance de la disponibilité de micronutriments devient évidente pour le développement des cellules phytoplanctoniques.

1.2 Distribution des nutriments dans l'océan

La distribution des nutriments dans l'océan suit plusieurs gradients marqués. En effet, la concentration de macro- et micronutriments dans l'océan de surface est marquée par **l'interface continent – océan** avec de plus fortes concentrations dans l'océan côtier comparé à l'océan hauturier (Chester and Jickells, 2012). Ce gradient est initié par un apport de nutriments plus important dans le domaine côtier, que ce soit par **voie fluviale, par resuspension de sédiments ou par un apport atmosphérique**. De plus, la consommation

des nutriments dans la couche euphotique dans laquelle évolue le phytoplancton cause un **gradient vertical** caractéristique de la distribution des nutriments, qui est appauvri en surface du fait du prélèvement par les organismes photo-autotrophes (uptake) et enrichi en profondeur du fait de la reminéralisation de la matière organique par les organismes hétérotrophes (Nozaki, 2001). Finalement, il existe d'importants **gradients horizontaux** découpant l'océan mondial en différentes régions aux conditions biogéochimiques variées et à l'origine des provinces biogéographiques avec des communautés de faune et flore spécifiques (Longhurst, 2007). Par exemple, l'Océan Austral, en surface, est riche en macronutriments (N, P, Si), mais appauvri en micronutriments et notamment en Fe, empêchant la prolifération algale (Blain et al., 2008b; Boyd and Ellwood, 2010). Cette zone est communément appelée HNLC pour High Nutrients-Low Chlorophyll, mais des régions avec d'autres carences régionales existent, comme les gyres subtropicaux tels que l'Océan Indien tropical oligotrophe, avec une faible teneur en macronutriments N et P, induisant une faible biomasse phytoplanctonique, appelée zone LNLC pour Low Nutrients-Low Chlorophyll.

1.3 Mesure des nutriments

Pour élaborer une cartographie des concentrations nutritives de l'océan de surface et en profondeur, des échantillonnages en mer ont été effectués depuis des décennies. Si les teneurs en macronutriments sont aujourd'hui bien étudiées, les données concernant les micronutriments restent encore peu exhaustives du fait des limitations techniques liées à leur faible concentration. De plus, la mesure de ces métaux se complique par l'omniprésence de contaminants métalliques sur les navires océanographiques en acier avec des engins rouillés. Afin d'éviter les contaminations en métaux de la part des navires et des systèmes de prélèvements lors des échantillonnages en mer, des conditions spécifiques d'échantillonnage et de mesure doivent donc être utilisées. Ainsi l'eau n'est pas récoltée avec des bouteilles de prélèvement Niskin standard, mais avec des engins plus adaptés, nommés « ultra-propres » ou « trace metal clean » comme les bouteilles Go-Flo® s'ouvrant seulement après immersion, ou des structures en titane au lieu du fer, montés sur des câbles Kevlar pour éviter toute contamination (e.g. Bruland et al., 1979; Cutter et al., 2017). De plus, la présence de salles blanches à air filtré et surpressurisé ou des hottes à flux laminaire embarquées sur les navires est également nécessaire pour l'échantillonnage et la filtration de l'eau.

2 Rôle des aérosols

Comme vu précédemment, les nutriments de surface peuvent avoir des origines différentes, dont les apports fluviaux, les aérosols, les sédiments marins, les remontées d'eau (upwellings, mélange hivernal), les sources hydrothermales ou encore les débris apportés par la glace (Mahowald et al., 2018; ainsi que les auteurs cités). Dans la suite de ce manuscrit, nous allons nous focaliser sur l'**apport de nutriments par voie atmosphérique**, qui représente une source significative de nutriments dits 'nouveaux' à des zones de l'océan hauturier en surface (Chester and Jickells, 2012).

2.1 Différents types d'aérosols

Un aérosol est défini comme une particule solide (comme une poussière) ou liquide (comme une goutte de pluie) en suspension dans un milieu gazeux (comme l'air). Il existe différents types d'aérosols dans l'atmosphère marine, dont les aérosols dits *'primaires'* qui arrivent dans l'atmosphère sous forme solide, mais aussi les embruns marins (de Leeuw et al., 2014); ou les aérosols *'secondaires'* formés au sein de l'atmosphère, comme les aérosols issus de précurseurs gazeux comme le diméthylsulfure (DMS) émis par le phytoplancton. Dans ce manuscrit, on s'intéressera aux aérosols primaires naturels venus des continents telles les **poussières désertiques** et les **cendres volcaniques**, mais il existe également des aérosols primaires anthropiques issus de la pollution ou de feux de forêt qui ne seront pas traités dans cette étude; le flux de masse des aérosols naturels se déposant à l'océan de surface étant beaucoup plus élevé que celui des aérosols anthropiques.

2.2 Répartition globale des régions sources

Les **aérosols désertiques** proviennent de l'érosion des zones arides et semi-arides, principalement du Sahara qui est responsable de 58 % de la masse totale émise, suivi de l'Asie centrale émettant 19 % (Figure I-1). L'Australie et l'Amérique du Sud émettent des quantités relativement faibles à l'échelle globale (respectivement 6 et 2 % de l'émission totale), mais représentent la source d'aérosols dominante dans l'Océan Austral (Mahowald et al., 2009) qui sera traitée dans les Chapitres V et VI de ce manuscrit.

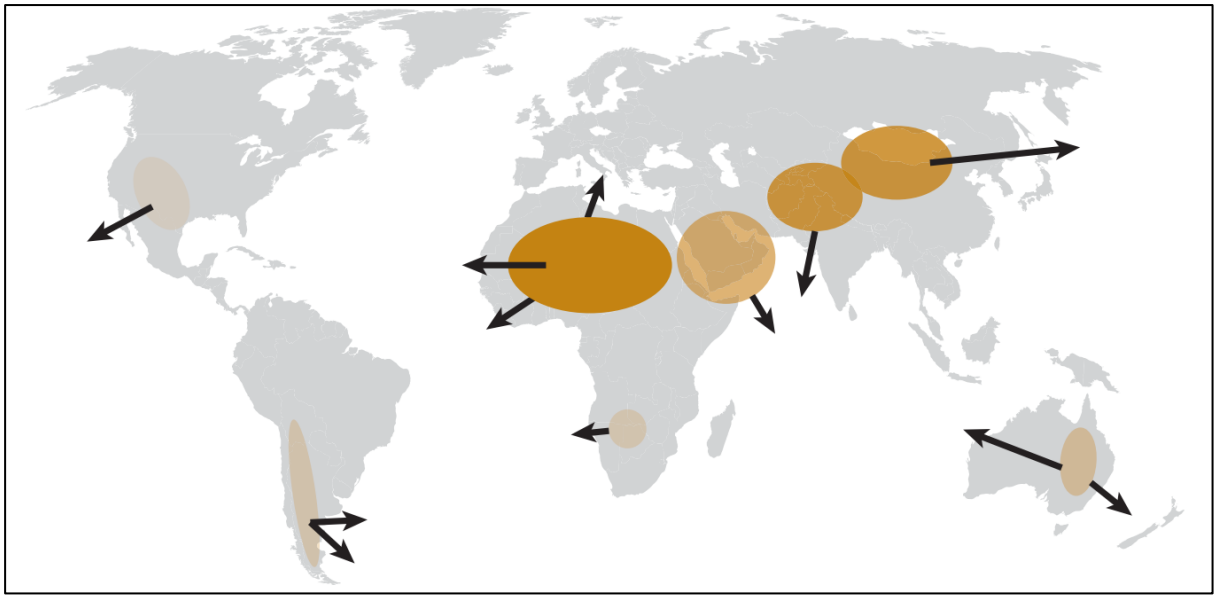

Figure I-1: Carte du monde montrant les régions sources majeures de poussières désertiques (formes orange), ainsi que les directions de transport (flèches noires). Plus une source émet de la matière, plus la coloration est intense : Sahara (58 %), Asie centrale (19 %), Péninsule arabique (12 %), Australie (6 %), Afrique du Sud (3 %), Amérique du Sud (2 %) et Amérique du Nord (0.1 %). Figure issue de Jickells and Moore (2015).

Tout comme les poussières désertiques, l'émission de **cendres volcaniques** se fait également de manière hétérogène sur notre planète. En effet, la majeure partie des volcans actifs se situe au niveau de la ceinture de feu du Pacifique (Figure I-2). Cette concentration géographique est due à la subduction de plusieurs plaques océaniques dans cette vaste région de part et d'autre de l'Océan Pacifique. Plusieurs volcans hot-spots (Figure I-2) s'ajoutent au volcanisme de subduction dans cette zone. On enregistre 50 à 60 éruptions par an et plus de 1300 éruptions durant les derniers 10 ka (ka = kilo années = mille ans) au sein de cette zone de haute activité volcanique (Olgun et al., 2011 et auteurs cités). On notera par exemple 60 éruptions détectées durant l'année 2020, selon le Global Volcanism Program (Smithsonian Institution, https://volcano.si.edu/).

Finalement, les autres types d'aérosols qui ne seront pas traités dans ce manuscrit suivent également des répartitions géographiques spécifiques, avec par exemple une plus grande proportion d'aérosols anthropiques industriels (Pacyna and Pacyna, 2001) dans l'hémisphère Nord (Baker et al., 2010; Baker and Jickells, 2017) et plus d'embruns marins dans l'hémisphère Sud.

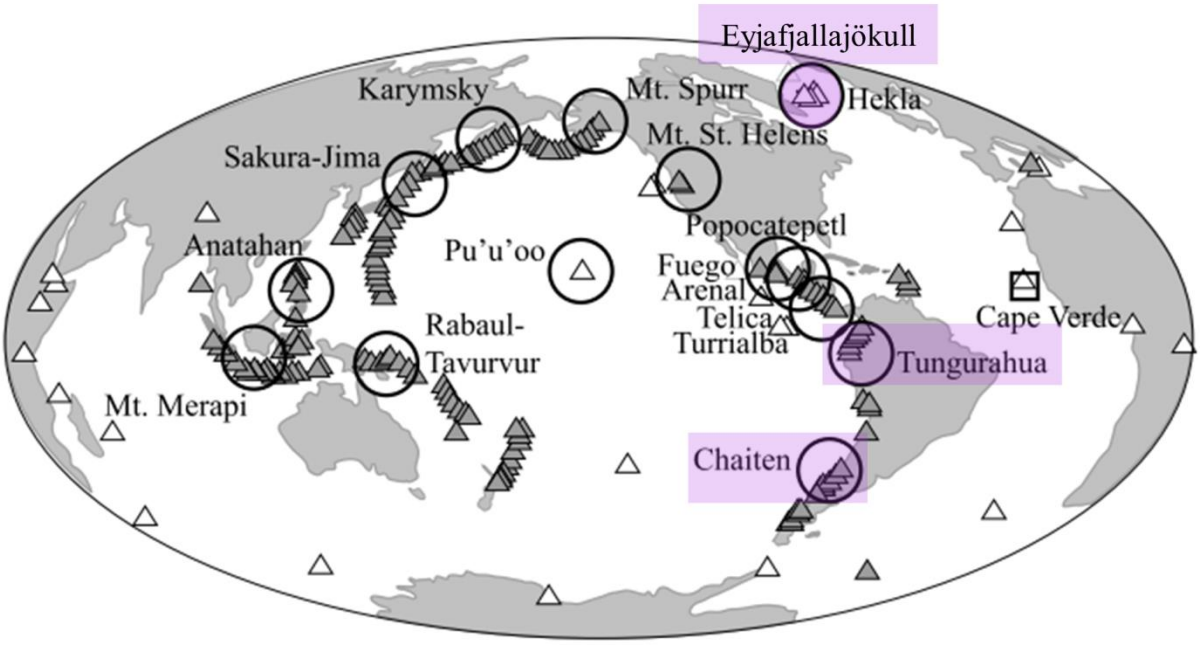

Figure I-2: Carte du monde montrant la position des volcans actifs, concentrés au niveau de la ceinture de feu du Pacifique, avec le volcanisme de subduction (triangles gris) et les hot-spots (triangles blancs). Les volcans dont la cendre est utilisée dans cette étude sont représentés en violet. Figure adaptée de Olgun et al. (2011), basée sur les travaux de Sigurdsson et al. (2000).

2.3 Flux d'émission

La masse totale de poussières désertiques émises dans l'atmosphère est estimée à 1490-1814 $Tg.an^{-1}$ (1 Tg= téragramme = 10^{12} g soit 1.5-1.8 10^{15} $g.an^{-1}$) (Mahowald et al., 2005) dont en moyenne un quart (24±3 %) est déposé à l'océan de surface.

L'émission de cendres volcaniques a été estimée à ~176-256 $Tg.an^{-1}$ pour des particules fines (< 63 µm de diamètre) (Durant et al., 2010), mais d'autres émissions volcaniques existent, comme les particules grossières (> 63 µm, estimés à ~30 $Tg.an^{-1}$), les sulfates et gaz volcaniques (~10-20 $Tg.an^{-1}$) (Hobbs et al., 2000). Olgun et al. (2011) estiment l'émission millénale de cendres aéroportées issues du volcanisme Pacifique à 239–311 $Pg.ka^{-1}$ (1 Pg = pétagramme = 10^{15} g soit 2.4-3.1 10^{14} $g.an^{-1}$). Ainsi, l'émission volcanique est un ordre de grandeur inférieur comparé aux poussières désertiques, mais la variabilité interannuelle des émissions volcaniques peut être très forte, limitant la pertinence d'un calcul d'une moyenne annuelle.

2.4 Parcours à travers l'atmosphère

Avant de se déposer sur le continent ou l'océan, les aérosols peuvent parcourir des milliers de kilomètres dans l'atmosphère (Ayris and Delmelle, 2012; Jickells et al., 2005). Durant ce voyage de quelques jours à travers la troposphère, ils sont soumis à des conditions qui vont modifier leur composition à différents niveaux décrits ci-après.

2.4.1 Altération physico-chimique

Les aérosols naturels sont constitués d'un mélange variable de minéraux qui possèdent des comportements de solubilité qui leur sont propres. Ainsi, les minéraux calcaires (limestones) qui peuvent être un composant important au sein des aérosols (jusqu'à 34 % pour les aérosols de cette thèse, voir Chapitre II, Table II-3) ont une solubilité forte et rapide alors que des (hydr)oxides avec une structure élémentaire plus stable vont être moins soumis à l'altération. C'est pour cela que la composition des aérosols sera vraisemblablement modifiée durant le trajet dans l'atmosphère, en s'allégeant de ses composants les plus labiles (Desboeufs et al., 2014) ou en modifiant la solubilité (Desboeufs et al., 2001). De plus, le contact avec des masses d'air ou des aérosols pollués peut également impliquer une modification de la composition des aérosols, notamment en ajoutant une couche de surface fortement soluble (coating issu de la pollution) (Solmon et al., 2009).

2.4.2 Tri granulométrique des aérosols en fonction de la distance à la source

La taille des aérosols peut varier de quelques nanomètres à des centaines de micromètres (10^{-9}-10^{-4} mètres) (de Leeuw et al., 2014) ce qui impacte leur temps de résidence au sein de l'atmosphère (de quelques heures à plusieurs semaines), avec les grosses particules qui sédimentent rapidement dans la colonne d'air proche de leur source et les petites particules qui voyagent plus longtemps et plus loin. Ainsi, en s'éloignant de la région source, on observe une évolution de la distribution de taille des particules en faveur des petites particules (Mahowald et al., 2014; Scanza et al., 2018). Cette diminution de la taille des particules induit une augmentation de la surface d'échange (specific surface area = SSA), ce qui aura, nous le verrons dans les chapitres II pour Si et III pour Fe, également des implications sur la solubilité des nutriments.

3 Flux d'aérosols déposés sur l'océan de surface

3.1 Modes de dépôt

En fonction de l'origine et de la taille, les aérosols se déposent via différents mécanismes. Ainsi, les poussières désertiques de petite taille avec un faible poids quittent l'atmosphère majoritairement après être entrées en contact avec de l'eau atmosphérique, c'est-à-dire sous forme de **dépôt humide** au sein d'une pluie (Bergametti and Forêt, 2014). D'un autre côté, les particules plus grandes, comme la majeure partie des cendres volcaniques, quittent l'atmosphère sous forme de **dépôt sec** sous l'effet de la gravité ou de dépôt turbulent.

Le mode de dépôt est intimement lié à la localisation géographique et ses particularités climatiques et météorologiques. Globalement, le dépôt humide est considéré majoritaire pour les poussières désertiques (Richon et al., 2018), mais des particularités locales ont été démontrées : ainsi les deux modes de dépôt des aérosols désertiques coexistent équitablement en Méditerranée orientale (Kubilay et al., 2000), alors que le dépôt humide prédomine dans la partie occidentale (Guerzoni et al., 1997). Dans l'Océan Austral, la proportion de dépôt humide a été estimée à 75-90 % (Li et al., 2008).

Enfin, Jickells and Spokes (2001) indiquent que 70 % des dépôts de cendres volcaniques se déposent par dépôt sec au niveau de l'océan Pacifique. De même, Langmann et al. (2010a) considèrent 23 % du dépôt suite à l'éruption du Kasatochi dans le Pacifique Nord sous forme de dépôt humide, et distinguent entre 70 % de sédimentation gravitationnelle proche de la source et 7 % de dépôt sec distal. Dans le cadre de cette étude, nous ne faisons pas la différence entre dépôt sec et sédimentation.

Il est important de comprendre les particularités et d'estimer les proportions du mode de dépôt, puisque ce dernier aura un impact significatif sur les paramètres chimiques de dissolution des nutriments (cette question sera abordée dans le Chapitre VI). En effet, le pH du milieu aqueux de premier contact varie, avec un pH acide pour l'eau de pluie naturelle ou anthropisée et basique pour l'eau de mer (respectivement 4.7, <4 et 8.1 en moyenne).

3.2 Flux de dépôt vers l'océan

3.2.1 Flux globaux

L'estimation des flux de dépôt est effectuée via différentes méthodologies, comme des observations satellites, des données issues de modèles (Jickells et al., 2005 ainsi que les auteurs cités), ou encore des mesures directes *in situ* dans une zone d'étude suivie d'une

extrapolation à grande échelle. Comme présenté précédemment, il est estimé qu'un quart des 1490-1814 Tg.an^{-1} de poussières émises se dépose à la surface de l'océan mondial (Mahowald et al., 2005). Ces ~450 Tg.an^{-1} sont distribués de manière hétérogène sur les différents bassins océaniques, puisque 46 % du dépôt global s'effectue en Atlantique Nord (Figure I-3a ; Tableau **I-2**) alors que l'Atlantique Sud ne reçoit que 4 % (Mahowald et al., 2005 et Tableau **I-2**). De même, le dépôt dans l'Océan Pacifique est aussi plus marqué dans l'hémisphère Nord comparé à l'hémisphère Sud, puisque les zones sources d'émission d'aérosols désertiques se situent majoritairement dans l'hémisphère Nord. Les océans Indien et Austral reçoivent respectivement 26 % et 2.3 % des dépôts globaux.

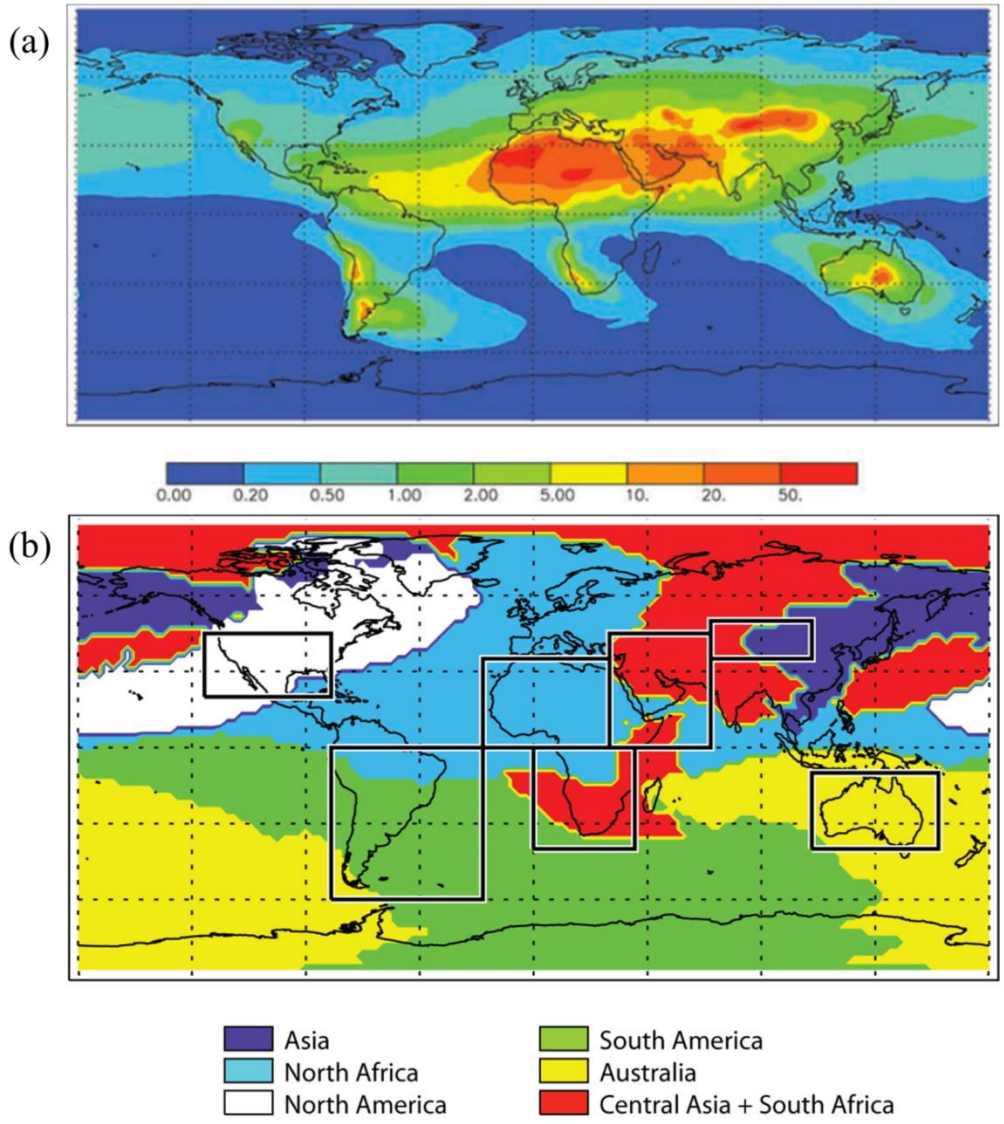

Figure I-3: Cartes montrant (a) les flux moyens de poussières désertiques déposés sur l'océan mondial (g.m^{-2}.an^{-1}), figure issue de Jickells et al. (2005) et (b) les sources dominantes de dépôt des poussières désertiques sur terre ou mer, figure issue de Mahowald et al. (2009).

L'origine majoritaire varie en fonction du bassin : ainsi l'Atlantique Nord reçoit majoritairement un dépôt saharien (Figure I-3b issue de Mahowald et al., 2009), alors que l'Atlantique Sud est plus soumis aux poussières de l'Amérique Latine et de l'Afrique du Sud. Il est à noter que ces valeurs moyennes ne correspondent pas à la réalité d'un événement de dépôt spécifique, puisque la quantité annuelle totale peut être déposée en seulement quelques évènements importants de tempêtes de poussières (Vincent et al., 2016).

Tableau I-2: Estimations à partir de la littérature des dépôts d'aérosols à l'océan

Dépôt estimé, $Tg.an^{-1}$ (10^6 $tonnes.an^{-1}$)	Pacifique		Atlantique		Indien	Austral	Global
	Nord	Sud	Nord	Sud			
Poussières désertiques	72 [(a)]	29 [(a)]	202 [(a)]	17 [(a)]	118 [(a)]	10.3 [(b)]	450 [(b)]
Cendres volcaniques	128-221[(c)]						

[(a)] Mahowald et al. (2005) ; [(b)] Jickells et al. (2005) ; [(c)] Olgun et al. (2011).

Le dépôt de cendres est beaucoup moins bien caractérisé à l'échelle globale, notamment car les flux volcaniques sont beaucoup plus irréguliers dans le temps et souvent plus localisés à proximité du volcan en question. Dans leur étude, Olgun et al. (2011) estiment le dépôt de cendres à 128-221 $Pg.ka^{-1}$ pour l'Océan Pacifique (correspondant à 128-221 $Tg.an^{-1}$ en supposant une teneur constante avec le temps (Global Volcanism Program, Smithsonian Institution, https://volcano.si.edu/). Par son dynamisme en termes de volcanisme, le bassin Pacifique reçoit la majorité des cendres volcaniques. Olgun et al. (2011) se sont basés sur des estimations géologiques de flux millénaires pour établir leur calcul et trouvent que 64±8 % des cendres issues du volcanisme à subduction sont déposées en pleine mer, prenant en compte les directions du vent ainsi que la proximité des volcans à l'océan. La Figure I-4 montre la probabilité d'un dépôt de cendres à l'échelle mondiale, et on aperçoit que la forte probabilité est concentrée au niveau de l'anneau de feu du Pacifique.

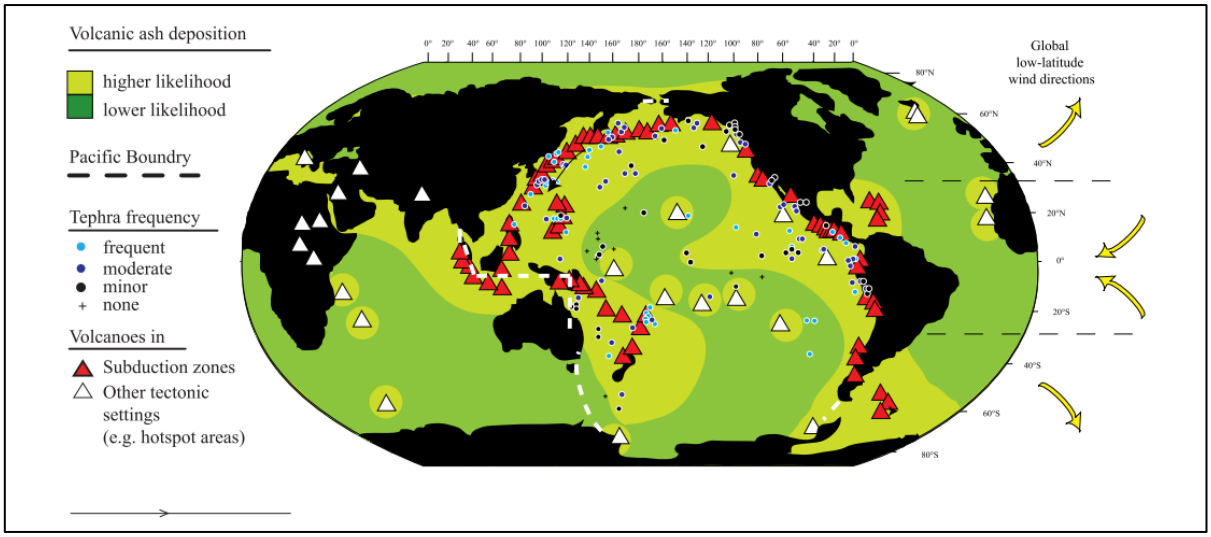

Figure I-4: Probabilité de dépôt de cendres volcaniques au-dessus de l'océan, avec distinction entre forte (vert clair) et faible (vert foncé) probabilité. Ces zones ont été estimées en fonction de la localisation de volcans historiquement actifs, de la direction du vent et de la proportion de téphra dans des sédiments marins du Quaternaire. Figure issue de Olgun et al. (2011) et basée sur les travaux de Straub and Schmincke (1998).

3.2.2 Flux d'aérosols vers l'Océan Austral

Les Chapitres V et VI de ce manuscrit s'intéressent à un dépôt représentatif d'une poussière désertique et d'une cendre volcanique sur différentes régions biogéochimiques de l'Océan Indien Sud (LNLC) et la partie Indienne de l'Océan Austral (HNLC). Dans cette section, nous comparons les rares données de la littérature existantes sur les ordres de grandeur de dépôt dans cette zone.

3.2.2.1 Flux de dépôt de poussières désertiques dans l'Océan Austral

Le dépôt de poussières Patagoniennes a été démontré sur l'Océan Austral et l'Antarctique (Erickson et al., 2003; Gassó and Torres, 2019), mais les observations d'évènements d'émission restent rares à cause de l'importante couverture nuageuse limitant leur détection par satellite (Johnson et al., 2011). De plus, la charge atmosphérique d'aérosols est en général faible dans l'hémisphère sud qui est plus maritime et en particulier au niveau de l'Océan Austral (Chester and Jickells, 2012). Le flux de dépôt atmosphérique dans notre zone d'étude a été estimé à moins de 200 $mg.m^{-2}.an^{-1}$ pour l'Océan Austral (Jickells et al., 2005) et 60-325 $mg.m^{-2}.an^{-1}$ pour la partie centrale du gyre subtropical de l'Océan Indien (Grand et al., 2015b).

De plus, un flux moyen annuel total de dépôt de poussières désertiques vers le secteur Indien de l'Océan Austral (au sud de 50° S) a été estimé à 1.11 $Tg.an^{-1}$ (Li et al., 2008), en supposant une contribution à hauteur de 60 % d'origine Amérique du Sud et 20 % d'Australie.

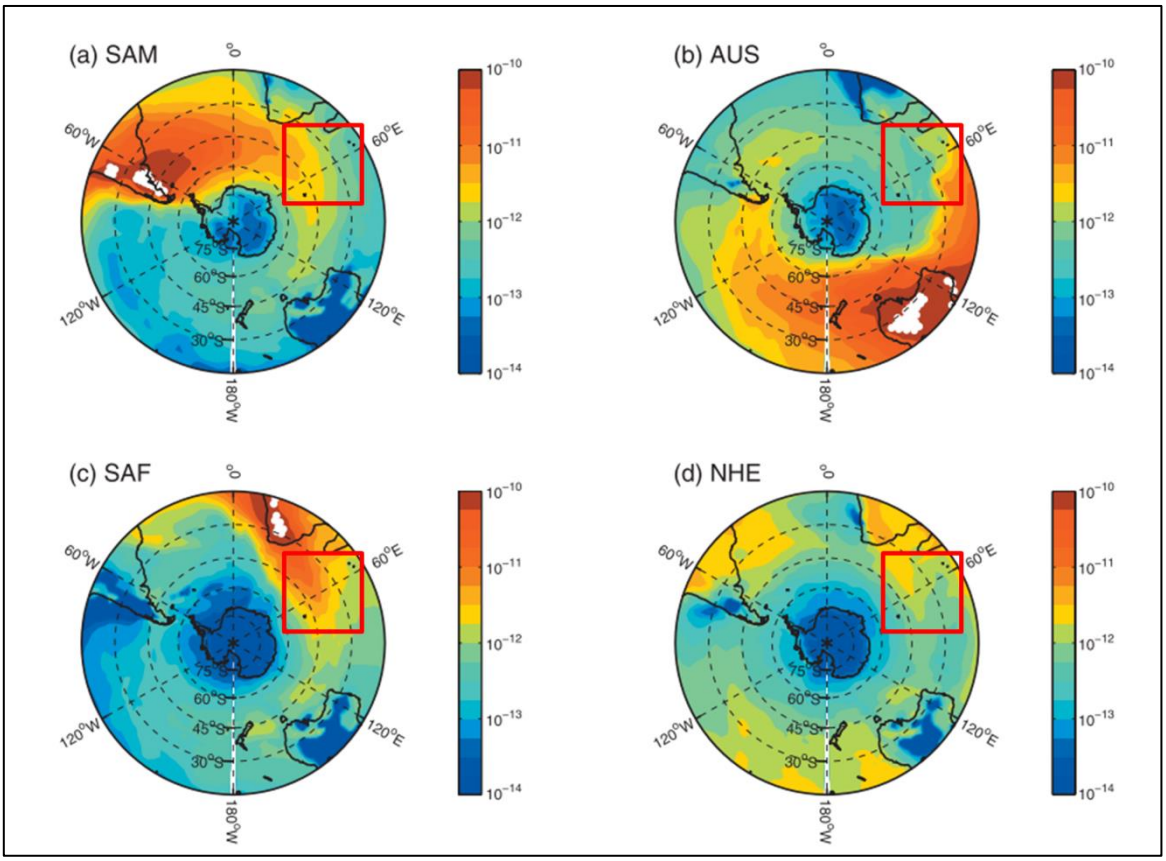

Figure I-5: Dépôt moyen annuel de poussières ($kg.m^{-2}.s^{-1}$) sur l'Océan Austral et en Antarctique venant de quatre sources individuelles : (a) Amérique du Sud (SAM) ; (b) Australie (AUS) ; (c) Afrique du Sud (SAF) et (d) l'hémisphère Nord (NHE). Les points blancs symbolisent les régions sources de l'hémisphère Sud et les carrés rouges localisent la zone d'étude de la partie B de ce manuscrit. Figure modifiée depuis Li et al. (2008).

En se basant sur la sortie du modèle atmosphérique global visualisée dans Li et al. (2008) et présentée en Figure I-5, on peut lire le dépôt moyen annuel dans la zone d'intérêt (secteur Indien, entre 30° S-60° S à une longitude de 60° E, Tableau I-3A), et à titre de comparaison dans une zone avec un plus grand flux (secteur Atlantique, avec une longitude approximative de 40° W, Tableau I-3B). Les latitudes de 30° S, 45° S et 60° S sont respectivement une bonne indication des régions LNLC, HN-LSi-LC (pour High Nitrate-Low Silicate-Low Chlorophyll), et HNLC.

Tableau I-3: Dépôt moyen annuel de poussières ($mg.m^{-2}.jour^{-1}$) et contribution relative (%, entre parenthèses) de quatre sources de poussières à différentes latitudes le long des longitudes 60° E (A) et ~40° W (B). SAM: Amérique du Sud ; AUS : Australie ; SAF : Afrique du Sud et NHE : hémisphère nord. Données sélectionnées d'après la carte issue de Li et al. (2008) montrée en Figure I-5 de ce chapitre. La source qui contribue majoritairement au mélange de dépôt à une localisation donnée est montrée en gras.

(A)	60° E	SAM	AUS	SAF	NHE	Total
	30° S	0.08 (13)	0.05 (10)	**0.32 (58)**	0.11 (19)	0.6 (100)
	45° S	0.32 (31)	0.08 (7)	**0.54 (52)**	0.11 (10)	1.0 (100)
	60° S	**0.11 (53)**	0.03 (16)	0.05 (26)	0.01 (5)	0.2 (100)

(B)	~40° W	SAM	AUS	SAF	NHE	Total
	30° S	**5.40 (91)**	0.08 (1)	0.11 (2)	0.32 (5)	5.9 (100)
	45° S	**7.56 (94)**	0.32 (4)	0.05 (1)	0.08 (1)	8.0 (100)
	60° S	**1.08 (90)**	0.05 (5)	0.01 (1)	0.05 (5)	1.2 (100)

Ainsi, nous estimons un **flux moyen compris entre 0.2 et 1.0 $mg.m^{-2}.jour^{-1}$** (Tableau I-3A) dans la zone bornée par l'Ile de la Réunion au Nord et les Iles Kerguelen au sud (autour de la longitude 60° E), avec une contribution majoritaire (53 %) des poussières d'Amérique du Sud à 60° S. Cette source contribue à hauteur de respectivement 13 % et 31 % aux latitudes 30° S et 45° S. Des flux plus importants (1.2 à 8.0 $mg.m^{-2}.jour^{-1}$) ont été déterminés dans le secteur Atlantique, davantage soumis aux poussières patagoniennes (Figure I-5a et Tableau I-3B). Il est à noter que pour les deux bassins étudiés, le dépôt maximal se situe aux alentours de 45° S. Ces moyennes annuelles empêchent cependant de visualiser des pics de dépôt plus importants, à l'échelle de l'évènement. Par exemple, Hooper et al. (2019) ont estimé un maximum de dépôt plus d'un ordre de grandeur au-dessus des moyennes saisonnières durant un événement désertique extrême dans le secteur atlantique de l'Océan Austral.

3.2.2.2 Flux de cendres volcaniques dans l'Océan Austral

Dans leur estimation visualisée en Figure I-4, Olgun et al. (2011) considèrent une probabilité faible de dépôt de cendres volcaniques dans l'Océan Indien et Austral, à part à proximité de régions de points chauds (« hot-spots »). La Figure I-6 ci-dessous montre le volcanisme actuel (rouge) et historique des 12000 dernières années (blanc), indiquant la présence de volcanisme passé et présent à Crozet et Kerguelen. A ce volcanisme local s'ajoute celui de l'Amérique Latine avec de potentiels apports de cendres dans la zone d'étude à la vue du sens majoritaire du vent (vents d'ouest). Ainsi il n'est pas irréaliste de s'intéresser aux dépôts volcaniques dans l'Océan Indien et Austral.

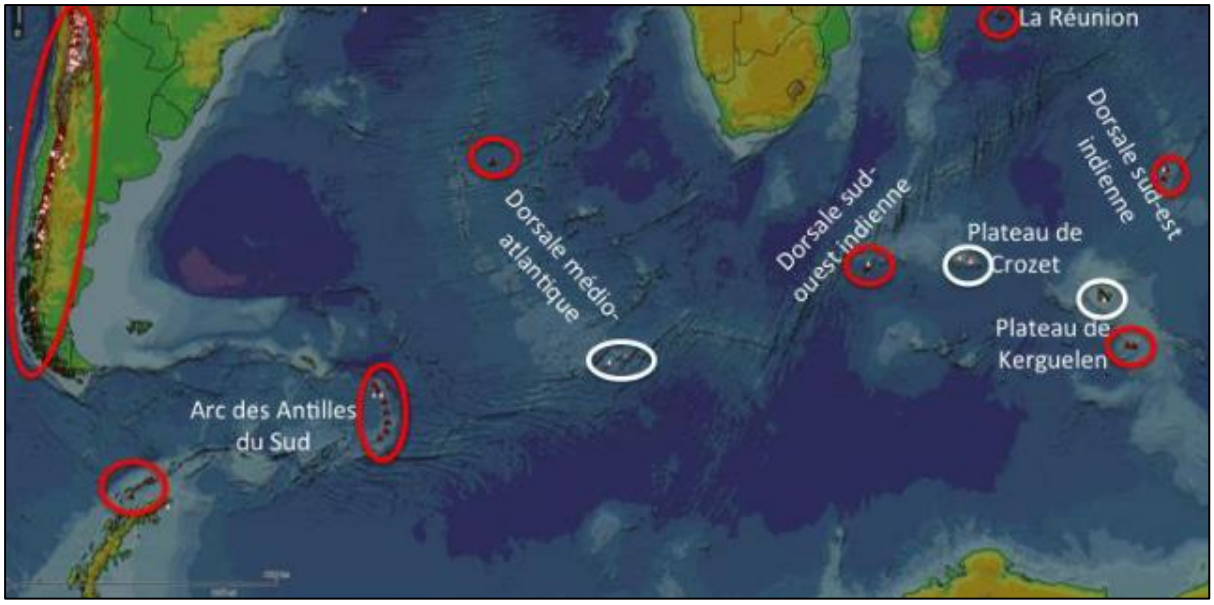

Figure I-6: Carte des volcans ayant été en activité depuis 1900 (rouge) ou au cours de l'Holocène (blanc). Adapté de http://volcano.si.edu/

De manière générale et à l'inverse des évènements désertiques, les éruptions volcaniques sont caractérisées par leur grande variabilité en termes de fréquence et de magnitude d'éruption (Durant et al., 2010). Ainsi, une éruption de grande ampleur comme celle du Mont Pinatubo dans les Philippines en 1991 (avec une émission totale de 1.3 10^4 Tg et une magnitude de 6.1 (Pyle, 2015) se produit environ 8 à 20 fois en mille ans (Durant et al., 2010), alors que des éruptions plus modestes sont plus fréquentes, comme celle du volcan alaskien Kasatoshi de 2008 qui avait expulsé 300 à 600 Tg de téphra (Pyle, 2015). On peut ainsi s'attendre à 227 éruptions de magnitude 4.5 en mille ans (Durant et al., 2010).

Après l'éruption de 1991 du Mont Hudson au Chili, des isopaques (montrant l'épaisseur des couches de cendres) de dix millimètres (mm) ont été mesurés au niveau de l'Océan Austral Atlantique côtier (Browning et al., 2014; Scasso et al., 1994), et des épaisseurs de un à dix millimètres ont été estimées au niveau du Pacifique hauturier vers 800-1200 km plus à l'Est du cratère source historique du Barva au Costa Rica il y a 350 ka (Kutterolf et al., 2008; Olgun et al., 2011).

4 Nutriments d'origine atmosphérique

4.1 Flux de nutriments à l'océan

Le flux de dépôt de poussières désertiques de 450 Tg.an^{-1} à l'océan peut également être exprimé en termes de flux de nutriments à l'échelle globale. Plusieurs études, de modélisation notamment, se sont penchées sur cette question et estiment un apport atmosphérique important d'azote par rapport aux autres nutriments, compris entre 32-67 Tg N.an^{-1} (Tableau I-4 et références citées).

Tableau I-4: Flux moyens de dépôt de nutriments (et gammes d'incertitude) à l'océan mondial à l'échelle globale, selon la littérature. La contribution du flux éolien dans l'apport total vers l'océan a été indiquée quand l'information était disponible. * Flux de l'élément dissous ou soluble et non pas flux total.

	Éolien	**Unité**	**Contribution éolienne (%)**	**Références**
N	63	Tg.an^{-1}		Okin et al. (2011)
	67 (38-96)			Duce et al. (2008)
	39			Krishnamurthy et al. (2007)
Si	14.0 ± 14.0 *	Tg.an^{-1}	3.2	Tréguer et al. (2021)
	2.2-96.9			Krishnamurthy et al. (2010) + références
	80-250			Tegen and Kohfeld (2006)
	96.8			Zender et al. (2003)
P	0.8 (0.2-1.6)	Tg.an^{-1}		Wang et al. (2015a)
	0.185			Zhang et al. (2015)
	0.32			Okin et al. (2011)
	0.33-1.05			Krishnamurthy et al. (2010) + références
	0.558			Mahowald et al. (2008)
	0.33			Zender et al. (2003)
Fe	0.7	Tg.an^{-1}	14	Mahowald et al. (2018)
	8.4			Wang et al. (2015b)
	6.1			Zhang et al. (2015)
	0.36 *			Okin et al. (2011)
	4.5-11.3			Krishnamurthy et al. (2010) + références
	11.86 (0.25-0.66 *)			Luo et al. (2008)
	16		1.3-2.3	Jickells et al. (2005)
	11.0			Zender et al. (2003)
Mn	0.300	Tg.an^{-1}	5	Mahowald et al. (2018)
	0.110			Zhang et al. (2015)
Cu	3.2 *	Gg.an^{-1}	5.4-7.7	Jeandel and Oelkers (2015) + références
Zn	4.6 *	Gg.an^{-1}	8-17	Jeandel and Oelkers (2015) + références

Il est à noter que la majorité des apports atmosphériques d'azote dissous à l'océan sont d'origine anthropique (Duce et al., 2008; Galloway et al., 2004), et que cette part anthropique a augmenté de ~29 % à ~80 % entre 1860 et 2000 (Duce et al., 2008). D'autres nutriments sont également déposés, comme le silicium dissous (14.0 Tg $dSi.an^{-1}$ avec une incertitude de 100 %, Tréguer et al., 2021) ou le phosphore sous forme de phosphates et les éléments trace, avec des flux plus réduits, se situant entre 0.2 et 1.6 $Tg.an^{-1}$ (Wang et al., 2015a ; Tableau I-4).

4.2 Solubilité des macro- et micronutriments d'origine atmosphérique

Un paramètre important pour relier le dépôt de nutriments et sa biodisponibilité est la **solubilité des nutriments contenus dans les aérosols**. Le paramètre de solubilité possède différentes définitions en fonction de la discipline considérée. Dans le cadre de cette thèse, nous considérons la solubilité d'un élément (exprimée en %) comme étant le rapport entre la concentration de l'élément dissous et la teneur totale de l'élément dans l'aérosol ajouté. Pour cela, j'ai mesuré la dissolution de l'élément, c'est-à-dire la quantité dissoute (< 0.2 µm) par unité de volume ($\mu mol.L^{-1}$). Cette quantité dissoute m'a également permis de calculer la dissolution normalisée ($\mu mol.g^{-1}$) par la charge particulaire de l'aérosol ajouté ($mg.L^{-1}$). Ainsi, les paramètres de solubilité et de dissolution normalisée utilisés dans la suite de ce manuscrit permettent de s'affranchir de la charge particulaire de l'aérosol ajouté.

Nous nous intéressons à la fraction dissoute des éléments chimiques, qui est la forme qui peut être absorbée par le phytoplancton et ainsi agir en tant que nutriment stimulant son développement. Il est à noter dans le cas du Fe notamment que cette condition n'est pas suffisante, puisque d'autres paramètres supplémentaires, comme la spéciation et la présence de ligands, s'ajoutent à cette condition initiale (Johnson and Meskhidze, 2013; Meskhidze et al., 2017).

Le Tableau I-5 présente une sélection des ordres de grandeur des solubilités et dissolutions normalisées de différents éléments issus de la littérature. La grande variabilité des solubilités et dissolutions peut être expliquée par le choix de la matrice (eau pure ou eau de mer) et du protocole expérimental (batch ou réacteur à circulation continue) incluant le rôle de la charge particulaire et du temps de contact utilisé. Le rôle du choix de l'aérosol, ainsi que de la matrice et du temps de contact pour la solubilité des macro- et micronutriments sera abordé plus en détail dans le Part A de ce manuscrit.

Tableau I-5. Solubilité (%) et dissolution normalisée (µmol.g^{-1} for N, Si, P, Fe and Mn ; nmol.g^{-1} for Co, Cd, Cu and Ni) de nutriments selon la littérature, dans l'eau de mer (**gras**) ou eau pure (*italique*).

	Poussières désertiques		Cendres volcaniques
	Solubilité	Dissolution	Dissolution
N	**n.s.** (nEC) [a] **100 000** (EC) [a]	**409-492** [b]	**35-855** [b] **; 200-1500** [c] *0-20 000* [d]
Si		**450-1110** [b]	**3-2058** [b] **; 50-200** [c] **100-17 200** / *200-13 900* [d]
P	**2-14** [e]	**43** [b]	**7-970** [b] **; 10-100** [c] **<0-370** / *10-2 180* [d]
Fe	*0.04-1.5* [f] **0.044-0.066** [g] **0.001-0.02** [h]	**20-30** [b] **0.09±0.4** [i] **<10-125** [h]	**11-130** [b] **; 10-60** [c] **10-8 920** */10-10 850* [d] **35-340** [h] **; 2.1-83.2** [k]
Mn	*2.0-3.6* [f] **28-38** [g] **; 65-87** [j]		**50-920** / *0-720* [d] **17.4-1298.6** [k]
Co	*<DL* [f] **17** [g] **; 29-38** [j]		**0-19** / *0-22* [d] **0.1-33.0** [k]
Cd	*<DL – 10.1* [f] **74-76** [g]		**0.0-4.2** [k] *0-3* [d]
Cu	*<DL – 27.5* [f] **14-22** [g]		**0-50** [c] **; 4.4-10.8** [k] **2-14** */ 1-43* [d]
Ni	*<DL – 2.1* [f] **12-25** [g] **; 40-84** [j]		**1-21** / *4-26* [d] 0.5-13.9 [g]
Zn	*11-13* [f] **57-65** [g]	**0** [b]	**0-21.2** [b] **; 2-27** [c] **0-90** / *0-100* [d] **34.0-199.7** [k]

Notes: [a] (Ridame et al., 2014a) : 0.01-20 mg.L^{-1} avec des poussières évapocondensées (EC) ou non (nEC) dans l'**eau de** mer pendant 3 et 24 h ; [b] Olgun et al. (2013) : 1 g dans 50 mL d'**eau de mer**, durant 1 et 20 h ; [c] Duggen et al. (2007) : **eau de mer** durant 20 min ; [d] Jones and Gislason (2008) : réacteur à circulation continue dans de l'**eau de mer naturelle** ou *eau pure* durant 8 h ; [e] Ridame and Guieu (2002) : 5-100 mg.L^{-1} dans l'eau de mer durant 6 heures à une semaine ; [f] Desboeufs et al. (2005) : réacteur à circulation continue dans de *l'eau pure acidifiée* durant 2 h pour un loess et une poussière d'Arizona ; [g] Jickells et al. (2016) : Dissolution dans l'**eau de mer** d'une poussière Saharienne, entre 10 min et 7 jours ; [h] (Olgun et al., 2011) : 50 mg de différentes cendres et un loess de Cape Verde dans 20 mL d'eau de mer naturelle ; [i] (Fishwick et al., 2014) et [j] (Fishwick et al., 2018) : pour un aérosol à la signature d'Afrique du Nord dans l'**eau de mer ;** [k] Hoffmann et al. (2012) : 2.67 g dans 1 L **d'eau de mer**, temps de contact 15 min. n.s. = non significatif. DL = limite de détection.

4.3 Influence des nutriments libérés par les aérosols sur le phytoplancton

Durant les deux dernières décennies, plusieurs études ont démontré le lien entre un dépôt de poussières désertiques et le phytoplancton, en s'intéressant aux cycles biogéochimiques des nutriments, à la croissance accrue du phytoplancton ou encore à l'export du carbone (*e.g.* Guieu et al., 2014a; de Leeuw et al., 2014) ; que ce soit au sein d'expériences en microcosmes (Blain et al., 2004; Marañón et al., 2010; Mélançon et al., 2016; Mills et al., 2004) ou mésocosmes (Guieu et al., 2014b; Ridame et al., 2014a) ; par le biais d'observations satellites (Cosentino et al., 2020) ou d'études de modélisation (Richon et al., 2018).

Ainsi, Mills et al. (2004) concluent qu'un **dépôt de poussières sahariennes** stimule la fixation de N_2 dans l'Océan Atlantique tropical dominé par des cyanobactéries diazotrophes et accélère ainsi dans certains cas la multiplication de biomasse algale dans cet environnement largement carencé en azote. Des effets similaires ont été observés dans d'autres bassins océaniques : Bishop et al. (2002) ont mesuré, grâce au largage en mer de flotteurs autonomes, une augmentation de la biomasse algale à la suite d'un dépôt important de poussières dans l'Océan Pacifique Nord. En Méditerranée, Ternon et al. (2010) ont mis en évidence le lien étroit entre les événements sahariens et une augmentation de l'export de carbone organique particulaire (POC) vers les eaux profondes de la mer Méditerranée Nord-Ouest en observant simultanément le dépôt atmosphérique par satellite et la sédimentation profonde de la matière organique durant une étude pluriannuelle.

Il a également été montré que différents types d'aérosols pouvaient agir sur différents types de phytoplancton de manière variable. Ainsi, un aérosol moins riche en métaux traces stimulait la communauté de *Synechococcus* hauturière, mais pas côtière, alors qu'un aérosol plus riche en métaux traces induisait des augmentations de chlorophylle a dans les deux milieux (Mackey et al., 2012). On peut donc conclure que la réponse biologique dépend de la sévérité de l'oligotrophie (Marañón et al., 2010) ; l'apport de nouveaux nutriments éoliens peut être plus profitable aux procaryotes hétérotrophes qu'aux photoautotrophes, réduisant ainsi l'effet net d'un apport atmosphérique sur la fixation de carbone (Guieu et al., 2014c; Marañón et al., 2010).

Un grand nombre de ces études se focalise ainsi sur les zones LNLC (zones tropicales et Méditerranée) qui sont soumises à de forts apports ponctuels de poussières venant notamment du Sahara, alors qu'un nombre plus restreint d'études s'intéresse aux dépôts dans l'océan Austral. Il s'agit de la zone océanique où le dépôt atmosphérique est le plus faible dans la période actuelle (Winton et al., 2015).

Même si leur effet est moins étudié que celui des poussières désertiques, les **cendres volcaniques** sont également connues pour relarguer des nutriments et induire une réponse biologique massive (bloom phytoplanctonique) (*e.g.*, Hamme et al., 2010; Langmann et al., 2010b). Pour analyser leur impact, des méthodes similaires aux études sur les poussières sont employées : la télédétection par satellite est performante pour observer à la fois l'étendue des nuages de cendres ainsi que les variations de la concentration en chlorophylle. De plus, Westberry et al. (2019) utilisent le ratio chlorophylle sur carbone (Chl:C) pour quantifier l'effet des cendres volcaniques non seulement sur la biomasse, mais également sur la physiologie du phytoplancton (changement du taux de croissance et photo-acclimatation). Ainsi, un dépôt de cendres du Kasatochi dans l'Océan Pacifique Nord a induit des modifications maximales 9 à 12 jours après l'éruption (anomalies de Chl:C de 50-100 % au-dessus des normales mensuelles). Le bloom ainsi enregistré s'est étendu sur près de 50 jours, c'est-à-dire deux à quatre fois plus long qu'un dépôt artificiel à grande échelle de fer directement disponible (ex. expériences SERIES ou SOIREE, voir revue de Yoon et al., 2018).

De plus, des expériences d'incubation de phytoplancton en cultures (Hoffmann et al., 2012). et assemblages naturels (Browning et al., 2014; Mélançon et al., 2014) en présence de cendres volcaniques ont permis de démontrer expérimentalement l'effet de cet apport naturel de nutriments sur la croissance phytoplanctonique via des paramètres comme la concentration de chlorophylle et le rendement quantique photosynthétique Fv/Fm (Achterberg et al., 2013; Duggen et al., 2007), ou de taux de croissance et de division cellulaire (Hoffmann et al., 2012).

5 Objectifs de la thèse

Afin de comprendre l'effet d'un dépôt d'aérosols comme les poussières désertiques et les cendres volcaniques sur le phytoplancton, nous allons dans un premier temps nous intéresser à la solubilité des macro- et micronutriments. Pour cela, j'ai effectué des expériences de dissolution abiotique dans des conditions ultra-propres en salle blanche sur quatre analogues de poussières désertiques, trois cendres volcaniques ainsi qu'un verre volcanique synthétique dans deux matrices artificielles représentant l'eau de mer et l'eau de pluie. Ainsi, j'ai pu comparer non seulement **l'influence du type d'aérosol (poussière ou cendre) et du mode de dépôt (sec ou humide), mais également le rôle de l'origine des différentes sources sur la variabilité de la solubilité et le relargage de nutriments.**

La dissolution de nutriments a été mesurée et la solubilité a été calculée. Le Chapitre VI **caractérise les aérosols (composition élémentaire et minéralogique, granulométrie)** et se focalise sur le relargage des macronutriments **silicium, phosphore et azote** (ainsi que l'aluminium pour interpréter le rôle des aluminosilicates dans la dissolution du Si). Puis, le Chapitre III s'intéresse aux métaux traces **fer, manganèse et cobalt** (ainsi que le potassium pour la dissolution du fer)**.** Le relargage dans l'eau de pluie artificielle de métaux trace additionnels (vanadium, zinc, cuivre, nickel, cadmium et molybdène), ainsi que de traceurs lithogéniques additionnels (magnésium, calcium, titane) utiles pour **déterminer le lien entre la minéralogie et la solubilité** seront présentés dans l'Annexe A.

Dans un second temps, nous cherchons à mettre en évidence **l'impact d'un dépôt représentatif de poussières et de cendres sur le phytoplancton de l'Océan Indien Sud et du secteur indien de l'Océan Austral**. Cet impact est déterminé grâce à des incubations à bord effectuées en conditions propres dans le cadre d'une campagne océanographique en Janvier-Février 2019 à bord du N/O *Marion Dufresne*. Dans le Chapitre V, je présenterai **la réponse biologique du phytoplancton** de différentes régions biogéochimiques face à ces dépôts, puis dans le Chapitre VI, je discuterai **le rôle de l'origine de l'eau de mer** pour la solubilité abiotique et ainsi sur **l'apport nutritif d'un dépôt représentatif en conditions naturelles**.

Ce manuscrit sera conclu par une **estimation des flux de nutriments qui arrivent à l'océan de surface via le dépôt océanique.** Pour ces calculs de flux, je prends en considération la **variabilité naturelle entre sources d'aérosols.**

PART A

Abiotic dissolution of desert dust and volcanic ash in trace metal clean laboratory conditions

- Dissolution of macronutrients (Si, P, N) from desert and volcanic aerosols in artificial rain- and seawater

- Dissolution of micronutrients (Fe, Mn, Co) from desert and volcanic aerosols in artificial rain- and seawater

- Annex of Part A
    - Enrichment factors of aerosols compared to the upper crust
    - Si dissolution rates in ARW and ASW
    - Close-up on erratic Fe solubility in ARW from desert dust
    - Dissolution of additional micronutrients in ARW: Cd, Cu, Mo, Ni, V, Zn
    - Dissolution of additional micronutrients in ASW: Cu, Ni
    - Dissolution of lithogenic tracers in ARW: Ca, Mg, Ti
    - Covariation of dissolution in ARW and mineralogy (PCA)

II. Dissolution of macronutrients (Si, P, N) from desert and volcanic aerosols in artificial rain- and seawater

1 Introduction

Aerosol deposition on the ocean surface represents a significant source of new nutrients to remote areas of the open ocean, traveling over thousands of kilometers (Ayris and Delmelle, 2012; Jickells and Moore, 2015). Aerosols have a natural origin such as desert dust, volcanic ash, or glacial loess (Jickells and Moore, 2015), or are emitted by anthropogenic activities (Pacyna and Pacyna, 2001). Satellite data demonstrated that the nutrients released into the ocean by desert dust (Erickson et al., 2003; Paparazzo et al., 2018), volcanic ash (Hamme et al., 2010; Westberry et al., 2019) or anthropogenic aerosols (Mackey et al., 2017) may trigger phytoplankton bloom events.

Aerosols may reach the sea surface through dry or wet deposition, and thus come in contact with either directly the seawater (pH ~8.1) or after prior contact with atmospheric water. Cloud water may be extremely acidic with pH reaching 2, while rain droplets are common around pH 4.9 (Pye et al., 2020). The atmospheric pathway of aerosol deposition influences thus its dissolution behavior, as many elements have varying solubilities depending on the pH (Desboeufs et al., 1999; Ingall et al., 2018). Dissolved (< 0.2 µm) nutrients are widely assumed by the scientific community to be bioavailable (Kanakidou et al., 2018) and incubation experiments were able to demonstrate that the released nutrients triggered phytoplankton growth after a wet deposition of dust (Louis et al., 2015; Ridame et al., 2014b) or a dry deposition of ash (Duggen et al., 2007; Frogner et al., 2001; Hoffmann et al., 2012).

Many studies have focused on atmospheric iron (Fe) dissolution, but macronutrients such as phosphorus (P), nitrogen (N) and silicon (Si) are also released by aerosol deposition events, and might have a significant impact on phytoplankton in ocean regions in which macronutrients are scarce. Nutrient release after dust and ash deposition might therefore be of importance in low nutrient low chlorophyll (LNLC) oligotrophic areas such as the Mediterranean Sea (Pulido-Villena et al., 2010; Ridame et al., 2014b) as well as in high

nitrate but low silicate areas (HN-LSi-LC) like the Southern Ocean north of the Polar Front (Sarmiento et al., 2004) or the subarctic North East Pacific (Whitney et al., 2005; Wong and Matear, 1999).

Mineral dust is an important source of new P to the ocean (roughly 80 % of the 558.2 Gg.year^{-1}, Mahowald et al., 2008) but only 10 % are soluble and thus considered bioavailable (Kanakidou et al., 2018; Myriokefalitakis et al., 2016; Ridame and Guieu, 2002). Moreover, Mahowald et al. (2008) estimated the volcanic P emission of 6 Gg P.year^{-1} as 50-100 % soluble, but negligible at global scale compared to desert dust, while Frogner et al. (2001) demonstrated in an experimental study that the Icelandinc Hekla ash quickly released enough dissolved inorganic P (DIP) to locally trigger significant phytoplankton growth in the North Atlantic. In their model paper on atmospheric P, Mahowald et al. (2008) estimated the amount of volcanic P by extrapolating the better known sulfur emissions. Overall, it is to be underlined that the high uncertainties concerning P solubility of different aerosol types need further research in order to fully constrain the P cycle within aquatic systems (Mahowald et al., 2008).

Natural aerosols are a less important source of N, as 80 % of atmospheric dissolved N is of anthropogenic origin (Duce et al., 2008), *i.e.* due to high-temperature combustion processes and intensive agriculture (Jickells and Moore, 2015). The physico-chemical properties of aerosols such as desert dust might be altered due to cloud processing during atmospheric transport (Desboeufs et al., 2001). Moreover, Ridame et al. (2014) were able to show that simulated cloud processes and mixing with anthropogenic HNO_3 (representative of wet deposition) increased desert dust N content and N solubility, thus triggering a phytoplankton response in the Mediterranean Sea, whereas the untreated dust (dry deposition) was a negligible source of NO_3^-.

Moreover, Si is an important nutrient for diatoms, which are the most abundant phytoplankton group in the world ocean (Kooistra, 2008). The main Si flux to the world ocean (55 to 80 %, depending on the calculation) is through riverine input (227.5 ± 56.2 Tg Si.year^{-1}) and is assumed to be completely dissolvable (Tréguer et al., 2021). The aeolian flux accounts for around 3.4 % of the global Si input to the world ocean with an estimated flux of dissolved Si (dSi) that is relatively small but bearing very high uncertainty (14.0 ± 14.0 Tg dSi.year^{-1}, Tréguer et al., 2021). Such supply may play an important role in the open ocean, as Zhang et al. (2005) estimated that up to 80 % of the dSi which is globally deposited onto the ocean surface reaches the open ocean. In these publications, no distinction was made between

mineral dust and volcanic ash deposition; moreover the high uncertainties of Si fluxes can partially be explained by the estimation instead of measurement of Si solubility (Tréguer and De La Rocha, 2013). Thus, the experimental approach used in this study aims to enable a better quantification of the Si cycle within aquatic systems.

There is to our knowledge no global estimate for volcanic ash mass deposition to the ocean (Weinbauer et al. (2017), P. Delmelle, pers. comm), increasing the difficulty to evaluate the annual nutrient volcanic deposition. Moreover, macronutrient concentration in ash is globally more variable than in dust (Weinbauer et al., 2017). Since volcanic eruptions are more sporadic than desert dust events, most estimates given by the literature are millennial averages. Olgun et al. (2011) evaluate the volcanic ash deposition on the Pacific Ocean to 128-221 $Pg.ka^{-1}$ (Petagram = 10^{15} g, *i.e.*, 1 $Pg.ka^{-1}$ = 1 $Tg.year^{-1}$). No global data is available, as most studies focus mainly on the eruption event scale (Langmann et al., 2010a; Olgun et al., 2013) and on Fe dissolution (Duggen et al., 2010).

In order to assess dissolved macronutrients reaching the sea surface, we carried out a series of abiotic leaching experiments in artificial rainwater (wet deposition) and in artificial seawater (dry deposition). The dissolution of trace metals and other lithogenic elements that will enable the identification of minerals responsible for the nutrient release (Journet et al., 2008) will be assessed in the next chapter.

The main goal of this work is (i) to characterize the dissolution kinetics of macronutrients (Si, P and N) released by several dust and ash samples in order (ii) to quantify the natural variability of nutrient solubility and (iii) to determine the factors controlling their dissolution processes. For instance, the role of mineralogy such as aluminosilicate content for Si release will be addressed by the parallel measurement of aluminum dissolution.

2 Materials and methods

2.1 Characterization of aerosols

2.1.1 Sources and collection

2.1.1.1 Desert dust

The dust samples consisted in the fine fraction (< 20 µm) of arid surface soils. Collection took place in remote areas using clean sampling techniques to avoid anthropogenic contamination. The soil samples were dry sieved on several polyethylene meshes to transform the soils into aerosols (< 20 µm, see details in Guieu et al., 2010). This technique enabled the collection of a sufficient amount of material and ensured that the dust particles did not undergo physical or chemical alteration prior to the dissolution experiments. The selected fine fraction is representative of Saharan aerosols commonly transported over long distances in the atmosphere and settling to the surface ocean (Guieu et al., 2010; Maring, 2003).

In this study, we used two Saharan dust origins: *'Douz'* from Tunisia (33°27' N, 9°20' E) and *'Hoggar'*, a composite sample from the Hoggar region in Southern Algeria (approx. 23°17' N, 5°33' E) (Figure II-1). Further, we used one Sahelian dust from Banizoumbou in Niger (13°31' N; 2°38' E, hereafter referred to as *'Bani'*) and one Patagonian sample from Sierra Grande in Argentina (hereafter referred to as *'Pata'*). Collection details can be found elsewhere (Guieu et al., 2002; Paris et al., 2011; Ridame and Guieu, 2002). These selected areas are source regions of dust emission for vast ocean basins: the north African aerosols are well-known to participate in the nutrient cycling, e.g in the Mediterranean Sea (Guieu et al., 2002; Pulido-Villena et al., 2010; Ridame and Guieu, 2002), and South American dust has been shown to reach the Atlantic Ocean (Paparazzo et al., 2018) and the Southern Ocean (Gili et al., 2016; Smith et al., 2003). Except Hoggar, the dust samples were supplied by the Laboratoire Interuniversitaire des Systèmes Atmosphériques (Emilie Journet, LISA-IPSL, Paris, France).

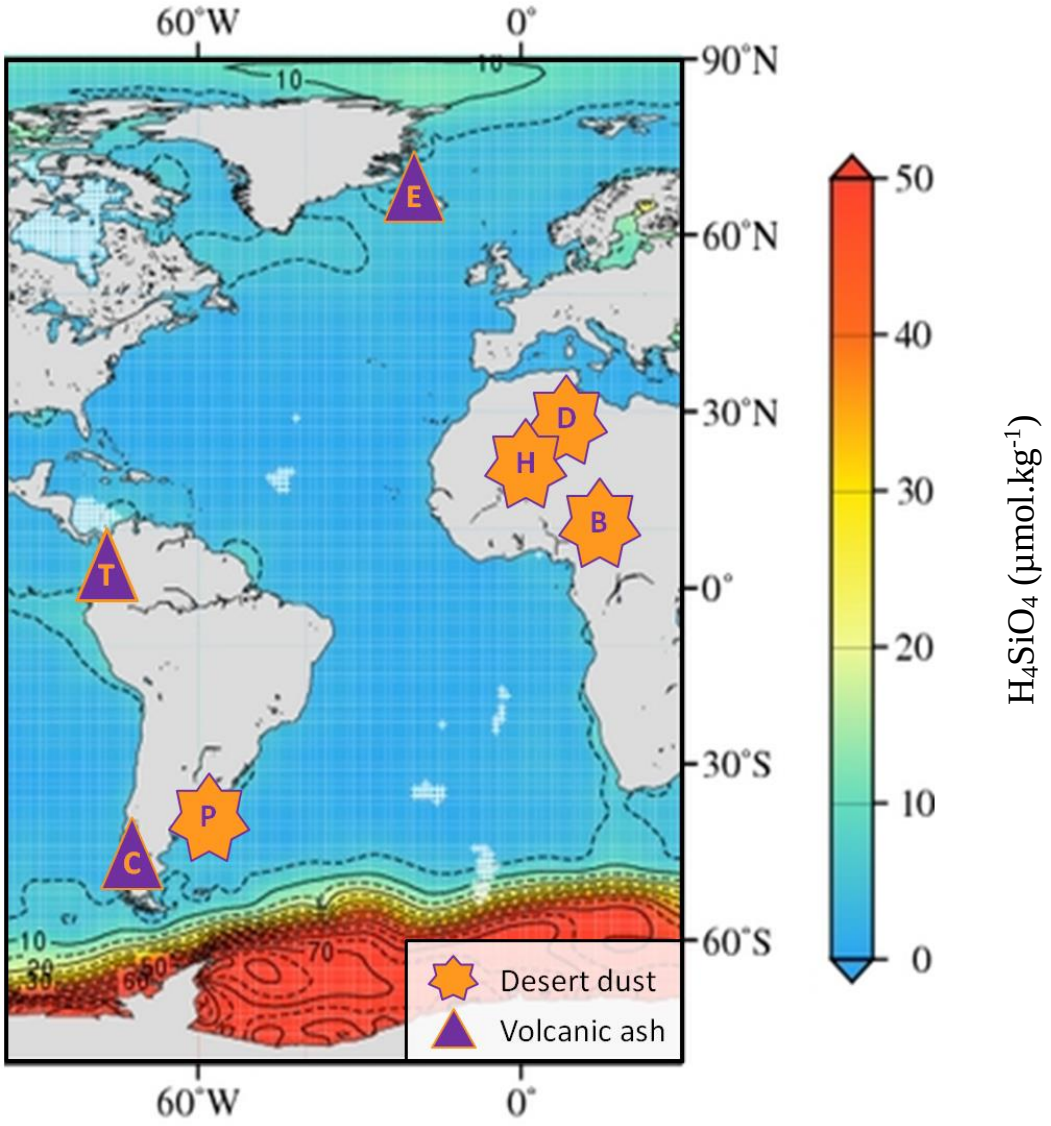

Figure II-1: Approximate location of sampling sites used in this study. Stars represent desert dust: B = Banizoumbou, Niger; D = Douz, Tunisia; H = Hoggar, Algeria; P = Patagonia, Argentina. Triangles stand for volcanic ash: C = Chaitén, Chile; E = Eyjafjallajökull, Island; T = Tungurahua, Equator. For precise GPS position, refer to text and Table II-1. The color scale of the background map shows the annual silicic acid climatology (µmol.kg^{-1}) at the sea surface. Data from World Ocean Atlas 2018, with one-degree grid and 5 µmol.kg^{-1} contour intervals.

2.1.1.2 Volcanic ash

We used the ash of two stratovolcanoes: Tungurahua hereafter referred to as *'Tun Ash'* in Ecuador and the ice capped Eyjafjallajökull hereafter referred to as *'Eyja'* in Iceland (Figure II-1). Phase 1 from the *Eyja* eruption was characterized by ice melting due to magma-ice interactions (Gudmundsson et al., 2012; Paque et al., 2016). Another ash sample was collected at the caldera Chaitén in Los Lagos, Chile. *'Chaitén'* ash is mainly rhyolitic (Durant

et al., 2012; Pierson et al., 2013), which is uncommon for a volcano from the southern Andes (Simonella et al., 2015). The South American volcanoes originate from a subduction zone whereas the Icelandic volcano is a rift zone glacier (Global Volcanism Program, Smithsonian Institution, USA). The collection of natural ash samples occurred shortly after ash deposition using clean plastic ware to avoid both trace metal contamination and the removal of natural soluble salt coatings (Witham et al., 2005). Further information on sample collection is found in Table II-1.

Table II-1: Information on eruption and ash collection conditions of used ash samples, including sample IDs found in other databases and publications

Samples	Coordinates	Eruption dates	Collection dates	Sampling locations	References
Chaitén (Cha-02)	42°50’16” S 72°39’04” W	2-4 May 2008 eruption phase 1	9 May 2008	~95 km from the volcano	Durant et al., 2012
Eyjafjallajökull (EYJ-A52)	63°37’11” N 19°36’54” W	17 April 2010, eruption phase 1	17 April 2010	Holtsa, 4-5 km from the volcano	P. Delmelle, pers. comm.
Tungurahua	1°28’03” S 78°26’58” W	23 August 2012	23 August 2012	El Santuario, ~13.6 km from the volcano	P. Delmelle, pers. comm.

In addition to the natural ash samples, we used a synthetic glass powder, synthesized by melting (> 1300 °C), homogenizing and air-quenching of an igneous rock from the Tungurahua volcano. The cooled glass was grounded to powder in acetone using a planetary ball mill. Details on glass synthesis are given in Maters et al. (2016). The composition of the synthetic sample approximates the natural *Tun Ash* and will be referred to as *‘Tun Glass’* hereafter. The particularity of the synthetic glass is to be 100 % amorphous, which enabled to identify the role of the crystalline structure of ash on dissolution processes.

Natural and synthetic ash samples were sieved through a 100 µm mesh to remove large particles. All samples were provided by the Earth and Life Institute (Pierre Delmelle, ELIE, Université Catholique de Louvain, Belgium).

2.1.2 Size distribution

Volume size distribution was measured by laser diffraction in ultrapure water (without ultra-sonication to avoid breaking up aggregates). The specific surface area (SSA) was determined by the Brunauer, Emmet and Teller (BET) gas adsorption method using nitrogen for dust (< 20 µm) and krypton for ash particles (< 100 µm). The analysis was performed at ITODYS laboratory in collaboration with L. Sicard and M. Jean Pierre. Results are shown in Table II-2.

The SSA of Hoggar was not measured in this study. For calculations in §4.2.2, we used an estimation of 20 $m^2.g^{-1}$ according to the literature (Jeandel and Oelkers, 2015), which is in good agreement with the mean value of tested African dust particles (mean = 18.6 $m^2.g^{-1}$ for Bani and Douz).

Table II-2: Particle size (µm), specific surface area (SSA, $m^2.g^{-1}$) and structural composition of dust (top) and ash (bottom) samples of this study. For analytical methods, please refer to the text. [a] data from Ridame (2001); [b] estimated from Jeandel and Oelkers (2015).

	Particle size (µm)		SSA	Structure (%)	
	mean	median	($m^2.g^{-1}$)	crystalline	amorphous
DUST					
Bani	17.3	17.2	7.7	64.6	35.4
Hoggar	10.7 [a]	9 [a]	20 [b]	42.4	57.6
Douz	11.5	8.8	29.5	67.7	32.3
Pata	8.6	6.4	62.1	51.7	48.3
ASH					
Eyja	33.6	22.1	7.3	36.3	63.7
Chaitén	38.5	26.4	0.7	18.3	81.7
Tun Ash	34.3	21.4	0.4	30.8	69.2
Tun Glass	19.9	8.5	0.9	0.0	100.0

2.2 Aerosol composition

2.2.1 Mineralogical composition

The aerosols are composed by two types of materials: crystalline and amorphous solids. Crystalline minerals are characterized by their homogeneous highly ordered arrangement of atoms, molecules or ions, and are distinguished by their physical properties such as their specific melting point (Haldar and Tišljar, 2013). Crystalline minerals are found under the form of primary minerals in limestone, acidic or basic rocks, and secondary minerals such as clay and (hydr)oxides that are products formed from primary minerals that have undergone chemical alteration. The second phase is the amorphous fraction, also called mineraloids, which is less structured (no specific melting point) and can be composed by allophanes (amorphous aluminosilicates that are also secondary minerals), volcanic glass or organic matter. Their chemical composition varies beyond the generally accepted ranges for specific minerals (Haldar and Tišljar, 2013). Metals such as Fe or Al can be combined with oxygen atoms within oxide minerals (*e.g.,* hematite Fe_2O_3), or with OH^- radicals within hydroxides (*e.g.* gibbsite $Al(OH)_3$). The metal-oxygen bond is strong and the metal is generally less soluble than if found within an aluminosilicate mineral.

Table II-3: Mineralogical composition of aerosols expressed as the weight percentage (wt.%) of the bulk aerosol, obtained by XRD. Only the crystalline part was detected with this technique, smectites and (hydr)oxides are underestimated (see text). Tun Glass is 100% amorphous and not presented in this table. Chemical formulas according to the Mineral Data Publishing database (version 1.2, ©2001).

Class	Limestones		Acidic rocks						Basic rocks	
Group						Feldspars			Pyroxenes	
Species	**Calcite**	**Dolomite**	**Quartz**	**Analcime**	**Pyrophillite**	**Microcline**	**Andesine**	**Albite**	**Enstatite**	**Augite**
Chemical formula	$CaCO_3$	$CaMg(CO_3)_2$	SiO_2	$NaAlSi_2O_6 \cdot H_2O$	$Al_2(Si_4O_{10})(OH)_2$	$KAlSi_3O_8$	$(Na,Ca)(Al,Si)_4O_8$	$NaAlSi_3O_8$	$Mg_2Si_2O_6$	$(Ca,Na)(Mg,Fe,Al,Ti)(Si,Al)_2O_6$
Possible traces	Mn, Fe, Zn, Ni, Cu, Al, Mo, Co …	Fe, Mn, Co, Zn …	Al, Fe, Mg, Ti …	K, Ca	Fe, Mg, Ca, Na, K, Ti	Fe, Ca, Na …	Fe, Mg	Fe, Ca, K, Mg	Fe, Al, Mn, Ti …	Mn
Bani			48.5			4.0		0.9		
Hoggar	1.1		21.0			4.5		6.2		
Douz	33.9	5.1	10.0							
Pata	2.9		6.2		0.6			18.6		
Eyja				1.0				23.4		
Chaitén			1.5					16.5		
Tun Ash							24.6		2.6	3.6

Class	Clay						(Hydr)oxides			
Group	Illite				Smectite			Iron oxides		
Species	**Illite**	**Kaolinite**	**Vermiculite**	**Palygorskite**	**Montmorillonite**	**Anatase**	**Magnetite**	**Hematite**		
Chemical formula	$K_xAl_2(Al_xSi_{(4-x)})O_{10}(OH)_2$	$Al_2Si_2O_5(OH)_4$	$(Mg,Fe^{3+},Al)_3(Si,Al)_4O_{10}(OH)_2 \cdot 4H_2O$	$(Mg,Al)_2Si_4O_{10}(OH)_2 \cdot 4H_2O$	$Ca_{0.25}(Al_{1.5}Mg_{0.5})Si_4O_{10}(OH)_2$	TiO_2	Fe_3O_4	Fe_2O_3		
Possible traces	Fe, Mg	Fe, Mg, Ca, K	Ca	Fe, K	Fe, P, Na, K	Fe, V …	Mg, Zn, Mn, Ni, Ti, V, Al …	Ti, Al, Mn …		
Bani	3.5	7.4				0.3				
Hoggar	2.8	3.6	2.7	0.5						
Douz	13.4	2.9		2.4						
Pata	20.6				2.8					
Eyja					10.9			0.1		
Chaitén							0.2			
Tun Ash										

The mineralogical composition of aerosols was measured by quantitative X-ray diffraction (XRD at Paris Diderot University, in collaboration with S. Nowak). Results are presented in Table II-3. It should be noted that the innovative analytical method used in this study according to Nowak et al. (2018) is based on the Rietveld refinement procedure applied to the aerosol particle samples and can be considered as *'quantitative'*: this method obtains the proportion of each detected mineral within the whole sample and not only within the detectable portion (as it is the case for standard qualitative or *'semi-quantitative'* methods). The percentage of crystalline structure (Table II-2) corresponds thereby to the sum of crystalline materials, detected by XRD (Table II-3). Unfortunately, the counterpart of this quantitative method is that clay species are less well detected: the intensity of clay XRD diffraction peaks decreased by the disoriented sample preparation (S. Caquineau, pers. comm). Moreover, smectites tend to have a heterogeneous chemical composition (*e.g.,* interfoliar cations), which further reduces their detection, hindering the characterization of 100 % of the crystalline structure. The undetected portion is considered as *'amorphous material'* (Table II-2) but might as well contain clays (Nowak et al., 2018). As the synthetic Tun Glass is totally amorphous, its mineralogical composition could not be assessed in this study, but its composition is andesitic (Maters et al., 2016).

2.2.2 Elementary composition

The elementary composition of aerosols is an important parameter for solubility calculations. In this study, we used the mean value of several published (Fu, 2018; Paris et al., 2011; Ridame, 2001; Ridame and Guieu, 2002) and unpublished data in order to obtain the best available concentration for each element and each aerosol sample. Analytical techniques differed depending on the element: C and N were quantified with an isotope ratio mass spectrometer (IR-MS Delta V^{TM} plus, Thermo Scientific^{TM}, at the Alysés platform, IRD by M. Mandeng-Yogo, LOCEAN) coupled with a C/N analyzer (Flash EA, Thermo Scientific^{TM}). Other elements were measured after acid digestion (according to the protocol from F. Fu, (2018) with inductively coupled plasma mass spectrometry (ICP-MS 7500cx, Agilent, at the Alysés platform, IRD in collaboration with I. Djouraev, LOCEAN), LISA), or or with atomic emission spectrometry (ICP-AES iCAP 6500, Themo Fisher Scientific by R. Ammar, UCLouvain) with X-ray fluorescence (XRF) spectrometry (RX platform, Université de Paris, by S. Nowak). Results are presented in Table II-4 and Figure II-2. Unpublished data was kindly provided by R. Ammar, K. Desboeufs and E. Journet (LISA).

Table II-4: Elementary composition (% in weight) of major, minor and trace elements of the aerosols from this study and average elemental concentration of the upper continental crust. Mean values (and standard deviation). [(a)] this study, [(b)] Paris et al. (2011), [(c)] Fu (2018), [(d)] Ridame and Guieu, (2002), [(e)] Desboeufs unpublished, [(f)] Ridame (2001), [(g)] Wedepohl (1995). < DL: below detection limit.

	Desert dust				**Volcanic ash**				**Continental crust** [g]
	Bani	Hoggar	Douz	Pata	Eyja	Chaitén	Tun Ash	Tun Glass	
C %	2.24 (0.12) [a]	0.98 (0.13) [a]	7.22 (0.86) [a]	1.06 (0.01) [a]	0.14 (0.01) [a]	<DL [a]	<DL [a]	<DL [a]	0.199
N %	0.20 (0.03) [a]	0.11 (0.00) [a]	0.18 (0.01) [a]	0.09 (0.01) [a]	0.03 [a]	<DL [a]	<DL [a]	<DL [a]	0.006
P %	0.04 (0.01) [a,b,c]	0.13 (0.02) [a,b,c,d]	0.07 (0.01) [a,c,e]	0.08 (0.01) [a]	0.18 (0.01) [a]	0.03 (0.00) [a]	0.11 (0.00) [a]	0.10 (0.00) [a]	0.0757
Si %	33.54 (0.76) [a,b]	26.25 (0.23) [a,b,f]	13.06 (1.30) [a,e]	25.80 [a]	26.47 [a]	34.17 [a]	27.74 [a]	27.08 [a]	28.8
Fe %	3.34 (0.22) [a,b,c]	5.42 (0.40) [a,b,c,f]	2.60 (0.12) [a,c,e]	4.55 (0.23) [a]	7.51 (0.28) [a]	1.25 (0.17) [a]	4.79 (0.25) [a]	5.33 (0.20) [a]	4.32
Al %	5.14 (0.60) [a,b,c]	7.91 (1.12) [a,b,c,f]	4.58 (0.33) [a,c,e]	7.79 (0.42) [a]	7.75 (0.34) [a]	7.44 (0.33) [a]	9.19 (0.50) [a]	9.24 (0.52) [a]	7.96
Ca %	0.27 (0.05) [a,b,c]	2.17 (0.25) [a,b,c,f]	18.47 (2.06) [a,c,e]	3.67 [a]	3.48 [a]	1.10 [a]	4.26 [a]	4.87 [a]	3.85
K %	1.21 (0.08) [a,b,c]	1.74 (0.13) [a,b,c,f]	1.23 (0.10) [a,c,e]	1.63 [a]	1.49 [a]	2.49 [a]	1.55 [a]	1.45 [a]	2.14
Mg %	0.24 (0.03) [a,b,c]	1.31 (0.24) [a,b,c,f]	1.81 (0.19) [a,c,e]	1.82 (0.10) [a]	1.40 (0.13) [a]	0.22 (0.02) [a]	2.13 (0.23) [a]	2.80 (0.28) [a]	2.20
Na %	0.27 (0.05) [a,b,c]	0.71 (0.19) [a,c,f]	0.20 (0.06) [a,c,e]	1.74 [a]	3.88 [a]	3.32 [a]	3.40 [a]	3.12 [a]	2.36
Ti %	1.13 (0.03) [a,b,c]	0.90 (0.12) [a,b,c,f]	0.33 (0.05) [a,c,e]	0.47 (0.03) [a]	1.09 (0.12) [a]	0.10 (0.01) [a]	0.56 (0.06) [a]	0.57 (0.06) [a]	0.401
Zn (ppm)	51.76 (2.89) [c]	89.77 (14.13) [a,c,f]	53.38 (4.17) [c,e]	85.93 [a]	173.75 [a]	77.04 [a]	148.77 [a]	137.83 [a]	65
Mn (ppm)	574.08 (75.08) [a,b,c]	966.34 (207.85) [a,b,c,f]	410.57 (22.56) [a,c,e]	886.65 [a]	1706.01 [a]	470.65 [a]	800.72 [a]	914.04 [a]	716
Co (ppm)	32.80 [c]	27.84 (10.88) [a,c]	11.83 (1.38) [c,e]	12.34 [a]	13.71 [a]	1.49 [a]	17.30 [a]	23.86 [a]	24
Cu (ppm)	19.96 (9.14) [c,e]	31.55 (0.54) [a,c]	18.31 (1.52) [c,e]	19.97 [a]	24.21 [a]	3.37 [a]	55.43 [a]	55.44 [a]	25
Ni (ppm)	27.22 [c]	60.31 (1.97) [a,c]	27.71 (1.00) [c,e]	16.63 [a]	19.82 [a]	1.17 [a]	38.58 [a]	50.72 [a]	56
V (ppm)	95.45 [c]	121.34 (8.90) [a,c]	64.44 (1.55) [c,e]	176.88 [a]	91.03 [a]	6.55 [a]	151.38 [a]	168.97 [a]	98
Cd (ppm)	0.48 [c]	0.38 (0.07) [a,c]	0.42 (0.00) [c]	0.35 [a]	1.12 [a]	0.09 [a]	0.49 [a]	0.59 [a]	0.1
Mo (ppm)	3.76 (2.32) [c,e]	2.01 (0.80) [a,c]	1.59 (0.01) [c,e]	1.06 [a]	3.58 [a]	1.60 [a]	1.66 [a]	2.18 [a]	1.1

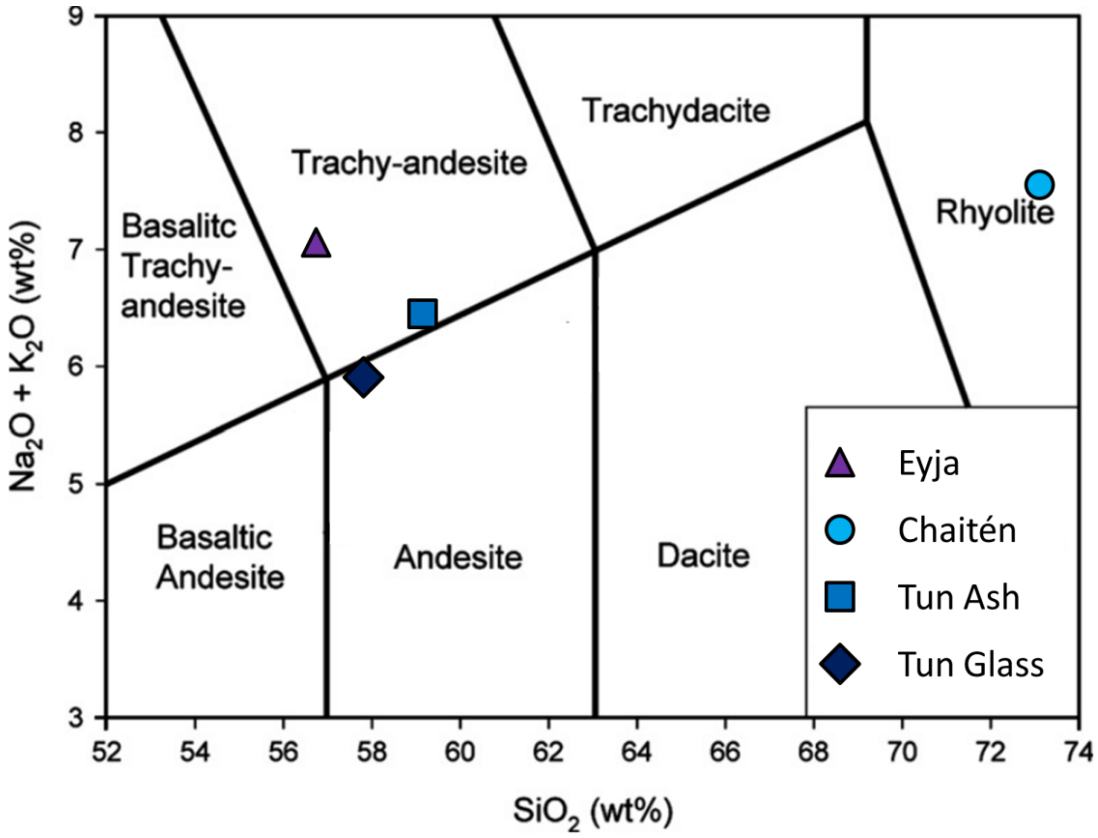

Figure II-2: Compositions of the ash and glass samples used in this study plotted in the total alkali vs. silica (TAS) classification diagram of volcanic rocks (modified from Le Maitre et al., 2002).

2.3 Abiotic dissolution experiments

2.3.1 Experimental setup

In order to simulate both wet and dry deposition modes of aerosols to the ocean surface, we set up a series of experiments in artificial rain- and seawater (hereafter referred to as ARW and ASW, respectively). Due to the small amounts of available aerosol material, dissolution experiments were performed in single runs without replicates but with an increased temporal resolution. For abiotic dissolution experiments, a particle concentration (PC) of about 250 mg.L^{-1} of aerosols was chosen. The PC of Douz was slightly higher: 308 mg.L^{-1} in ARW and 282 mg.L^{-1} in ASW, but this difference was considerated in further calculations. This PC is within the wide range of natural concentrations found in rainwater: Saharan rains collected over the Mediterranean Sea can hold dust particles in the range from 5 mg.L^{-1} to 8 g.L^{-1} (Ridame and Guieu, 2002), whereas ash loads vary even more widely depending on distance to the volcano and the amplitude of the eruption. Atmospheric PC around 2 g.L^{-1} after 1 h of contact time were found around the Mount Etna atmosphere, according to Cimino and Toscano (1998).

A PC of also 250 $mg.L^{-1}$ was chosen in the ASW experiment to compare with results in ARW and to exceed detection limits. High but realistic Saharan dust deposition events of up to 22 $g.m^{-2}$ have been measured in the Mediterranean Sea (Ternon et al., 2010), leading to a dust PC in seawater of around 0.3-1 $mg.L^{-1}$ in a surface mixed layer (SML) of 10 to 30 m depth during the stratification period (D'Ortenzio et al., 2005). Dry deposition of volcanic ash can also vary over several orders of magnitude: decimeter to meter thick ash layers to the coastal ocean surface have been recorded for the exceptional strong 1991 Mt Pinatubo eruption (Duggen et al., 2010), corresponding to a PC of 5-50 $g.L^{-1}$ diluted in a SML of 50 m depth. The 2002 Mount Etna eruption triggered a deposition of 2000 $g.m^{-2}$ to the Ionian Sea coast, but the PC decreased with increasing distance to the volcano: Olgun et al. (2013) recorded deposition rates of 0.3-94 $g.m^{-2}$ at 200 to 800 km downwind the volcano. These deposition fluxes correspond to a PC of 0.01-3.1 $mg.L^{-1}$ with an estimated SML of 30 m depth in the eastern Mediterranean Sea in fall (D'Ortenzio et al., 2005).

In pratical terms, 72.5 mg of aerosols were added to 290 mL ARW composed of ultrapure water (Millipore®, resistivity of 18.2 $M\Omega.cm^{-1}$) previously acidified with the low volatile sulfuric acid (1 ‰ H_2SO_4 SupraPur® at 2.10^{-2} M, theoretical pH of 4.9) which is found in the atmosphere (Desboeufs et al., 2005; Pye et al., 2020). For the ASW experiment, 87.5 mg of aerosols was added to 351 mL ASW, type YBCII media (unchelexed), without nutrients and metals (Chen et al., 1996). Acidity is known to be an important factor for dissolution (Desboeufs et al., 1999; Morin et al., 2015), so the experimental setup aimed to reproduce representative pH values of **4.9 in rainwater** (range 4.0-7.6 found in Desboeufs, 2005; Singh et al., 2016) and **8.1 in seawater** (range 7.8-8.4 according to Millero et al., 2009; Rhein et al., 2013) before aerosol addition (t-ini). No buffer was added to the matrix. Experiments lasted two days in ARW and nine days in ASW in order to include and exceed the representative contact time of the aerosol with each material. Experiments were performed in a trace metal clean laboratory at room temperature (22 °C) under natural light on an agitator table at 100 rpm to decrease the settling of aerosols. The ASW experiment with Douz ran only for four days. The polycarbonate experimental bottles, as well as sampling syringes and high and low density polyethylene (HDPE and LDPE) sample vials were cleaned using trace-metal clean techniques (HCl SupraPur® 5% vol).

After manual homogenization, samples for dissolved macronutrient determination were collected at chosen kinetic times (5', 10', 15', 30', 1 h, 1.5 h, 2 h, 2.5 h, 3.5 h, 4.5 h, 7 h, 24 h, 30 h and 48 h for both matrices and additional times of 72 h, 96 h, 192 h and 216 h in ASW), using 0.2 µm syringe filters (Acrodisc®). Then, samples were stored in LDPE vials at 5 °C for dissolved silicon (dSi) and at -20 °C for dissolved inorganic phosphorus (DIP) and NOx (nitrate + nitrite). Samples for dissolved aluminum (dAl) in ARW were acidified (1 % vol HNO_3 SupraPur®) and stored in HDPE vials at 5 °C. In order to subtract background levels, blank samples were collected in the polycarbonate experimental bottles for each experiment prior to aerosol addition.

2.3.2 Chemical analysis

Dissolved silicon in rain- and seawater and DIP in seawater were measured with a manual spectrophotometer (Thermo Scientific™ Evolution™ 220) according to the colorimetric methods of Grasshoff et al. (1999) for dSi and Murphy and Riley (1962) for DIP at the LOCEAN laboratory. NOx samples in both matrices were measured with the SEAL AutoAnalyzer 3HR according to Aminot et al. (2009) at LEMAR laboratory in collaboration with M. Gallinari. DIP and dAl in ARW were measured by atomic emission spectroscopy (ICP-AES, Spectro Arcos at LISA). The pH was measured prior to dSi analysis with the pH meter Orion™ 3-Star Thermo Scientific™ at room temperature. For spectrophotometric analysis, detection limit (DL) was defined as follows:

$$DL = mean(blanks) + 3 \times std(blanks) \qquad \text{Equation II-1}$$

The DL were 0.05 µM for DIP and 0.09 µM for NOx in both matrices, 0.02 µM for dSi in ARW, 0.04 µM for dSi in ASW and 62.4 nM for dAl in ARW.

2.3.3 Dissolution and solubility calculations

To be consistent with the literature on ash dissolution, the release of an element **X** normalized per gram of ash or dust (**dX_{norm}**, in µmoles.g^{-1}) was calculated following Equation II-2, where **dX** is the measured dissolved nutrient concentrations (µmol.L^{-1}), **dX_0** is the initial background value (µmol.L^{-1}) and PC stands for the particle concentration (in g.L^{-1}):

$$dX_{norm} = \frac{dX - dX_0}{PC} \qquad \text{Equation II-2}$$

In the field of mineral dust aerosol research, dissolution of X is mainly expressed as a fractional solubility percentage (**$\%X_{sol}$**), calculated according to:

$$\%X_{sol} = \frac{dX - dX_0}{X_{tot}} \times 100 \qquad \text{Equation II-3}$$

where **X_{tot}** (µmol.L^{-1}) is the total concentration of the element X in the aerosol at the added PC, assuming that 100% of the element would dissolve in the matrix. In this work, ***'dissolution'*** **(dX_{norm}, in µmol.g^{-1})** refers therefore to the concentration of a dissolved element released in ARW or ASW, normalized by the particle concentration according to Equation II-2. ***'Solubility'*** **($\%X_{sol}$, in %)** stands for the percentage of the dissolved element regarding the total pool of this element in the aerosol (Equation II-3).

2.3.4 Statistical analysis

The elementary composition of dust versus ash samples were compared using the non-parametrical Mann-Whitney test for small samples (n = 4, corresponding to the number of different dust and of ash samples). The correlations of Si and Al dissolution were assessed with linear regressions ($n \geq 10$) using the data analysis tools of Microsoft Excel. Error propagation of means was performed with a CC free calculation tool from the University of British Columbia (Richard Laffers, 2005-2008).

3 Results

3.1 Aerosol composition

3.1.1 Mineralogical composition

The main components of desert aerosols are quartz (6.2-48.5 %), clays (summing up to 9.5-23.4 %) and feldspar minerals (0-18.6 %) (Table II-3). Palygorskite, a clay species known to be specific to North Saharan dust particles (Scheuvens et al., 2013), was found in Douz and Hoggar samples (2.4 and 0.5 %, respectively). Moreover, three out of four dust samples contained calcite (1.1-33.9 % $CaCO_3$) that will be further discussed in connection with pH. Volcanic ashes were mainly amorphous (Table II-2), but their crystalline part was feldspar-rich (16.5-24.6 % of the bulk aerosol). Finally, it should be noted that Eyja ash contained 10.9 % of the clay montmorillonite which is uncommon for ash.

3.1.2 Elementary composition

Silicon is the main component of both our dust and ash particles (13.1-33.5 %, Table II-4) besides Douz containing more calcium (Ca) than Si. Moreover, desert dust contained significantly higher amounts of C and N than the continental upper crust (see enrichment factors, Annex IV §1) whereas the C and N of volcanic ash remained below the DL for three out of the four ash samples (only Eyja ash contained low but measurable C and N; Table II-4). On the other hand, ash samples contained more sodium (Na) than dust. For other elements such as P and Al, there was no significant difference between aerosol types (Table II-4).

3.2 pH

The initial pH of 5.02 ± 0.25 in ARW and 7.96 ± 0.11 in ASW (n = 8) are in good agreement with the theoretical expected values of respectively 4.9 and 8.1. The addition of aerosols triggered a rapid increase in pH_{ARW} for four aerosols (Douz, Pata, Hoggar and Eyja; Figure II-3a): the strongest increase was observed for Douz with a change of 2.63 units within 15 min of contact time, reaching a pH of 7.48. The pH increase of Pata, Hoggar and Eyja was weaker: after 30 min, the pH increased of respectively 1.87, 1.41 and 0.86 units, before stabilizing at pH 7.05, 6.89 and 6.28 after 2.5 h. The other aerosols had less influence on the pH_{ARW}: pH increased slightly for Bani and Tun Glass (ΔpH of respectively 0.20 and 0.36 units) and decreased slightly for Chaitén and Tun Ash (ΔpH of -0.37 and -0.39). In the naturally buffered ASW, the pH change was below 0.4 units for all aerosols (Figure II-3b).

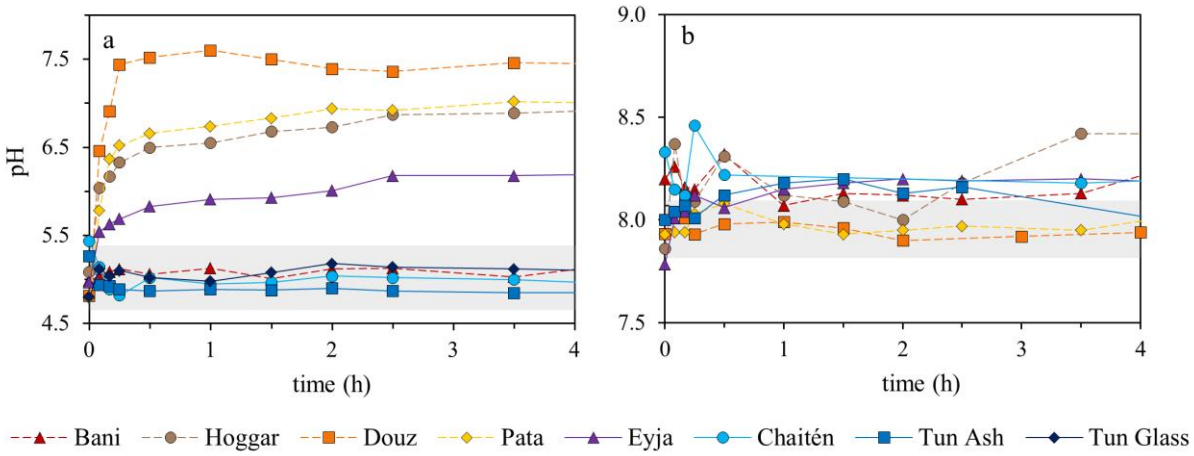

Figure II-3: Evolution of pH over time after addition of dust and ash to artificial (a) rain- or (b) seawater for a particle concentration of 250 mg.L^{-1}. Only the evolving first 4 hours of contact time are shown. Initial pH of 5.02 ± 0.25 in ARW and 7.96 ± 0.11 in ASW (n = 8) are highlighted in gray.

The observed pH variations after the addition of aerosols are consistent with literature: a pH range from 6 to 8 is common for Saharan rain, according to Ridame and Guieu (2002). In our experiments, a positive relationship was identified between the calcite content of the aerosol and the pH variation in ARW, explained by the release of CO_3^{2-}, HCO_3^- including an increase of OH^- from the limestone to the matrix (Chou et al., 1989). The high calcite content of Douz (33.9 % $CaCO_3$) triggered the highest pH increase in ARW. Pata and Hoggar contain respectively 12 and 31 times less $CaCO_3$ than Douz (Table II-3) and the evolution of the ambient ARW pH was less pronounced. Conversely, Bani is the only tested dust sample that does not contain calcite, which might explain that its pH variation (increase of 0.20 units) was closer to ash samples.

Eyja is the only ash sample that influenced the ARW pH, which may be explained by the dissolution of primary aluminosilicate minerals such as volcanic glass (Delmelle et al., 2021). This acid-base reaction consumes protons, thus increasing the pH.

3.3 Dissolution in rainwater

In this section, we will focus on the **wet deposition** mode of macronutrients to the ocean surface, *i.e.*, within a rain droplet. Indeed, an aerosol particle might encounter cloud water within its lifetime in the atmosphere before reaching the ocean surface. Hence, its dissolution starts in the rain droplet at lower pH (Baker and Croot, 2010). For the sake of comprehension of aluminosilicate dissolution (§4.2.1), we will also address the aluminum (Al) dissolution at the end of this section. The dissolution of other lithogenic tracers are found in Annex IV §4.3.

3.3.1 Silicon

The Si dissolution kinetics followed typical behavior with a high initial dissolution slowing down with time, but without reaching steady state after the 48 h of contact time (Figure II-4a). Desert dust released generally more dSi than volcanic ash except for Bani which was the dust that released the least Si: The Si dissolution reached a maximum of 59.0 µmol.g^{-1} for Pata (t48 h), but remained lower for African dust samples, varying from 6.1 to 35.6 µmol.g^{-1} (Bani and Douz, respectively) for the same contact time. Final %Si_{sol} of Douz was higher than Pata in ARW (0.82 vs. 0.64%, Figure II-4b), which will be discussed in §4.2.2.

Eyja was the ash that released the most dSi, and Eyja and Tun Glass released more Si than Bani dust. Volcanic ash released between 1.1 and 26.7 µmol dSi.g^{-1} to ARW after 48 h (Tun Ash and Eyja, respectively). Silicon from Eyja was the most soluble, followed by the synthetic Tun Glass (0.28 % and 0.11 % respectively after 48 h). Silicon from Chaitén and Tun Ash was the least soluble (0.03% and 0.01% respectively after 48 h) and comparable to Bani (%Si_{sol} of 0.05% after 48 h). For all tested aerosols, %Si_{sol} did not exceed 0.9 % for dust and 0.3 % for ash after 48 h. Noteworthy, Hoggar dust and Eyja ash had similar Si dissolution (~26 µmol.g^{-1}) and solubility (0.28 %).

3.3.2 Phosphorus

The highest and most rapid DIP dissolution in ARW was recorded for Eyja: 7.0 µmol.g^{-1} after only 10 minutes of contact time and 7.7 µmol.g^{-1} at t48 h (Figure II-4c). In contrast, other tested ash samples as well as Bani dust had low dissolution during the 48 h of contact time (< 1.0 µmol.g^{-1} of DIP). Phosphorus release by aerosols followed distinct kinetic patterns: some aerosols displayed typical dissolution curves, with a slow increase until the maximum at t48 h (Pata, Tun Ash and Chaitén). Others displayed a rapid initial release within the first hours (8.3 and 0.83 µmol.g^{-1} after 3.5 h for Eyja and Bani) followed by a slow and constant decrease in concentration. Surprisingly, the P dissolution of Douz displayed a high and rapid dissolution in the first 30 minutes (6.6 µmol.g^{-1}), followed by a rapid decrease within two hours and a plateau at 3.5 µmol.g^{-1}. This unique behavior was not observed in the seawater matrix and will be discussed in §4.3.4.

The highest %P_{sol} of 30.4 % was recorded for Douz after 30 min of contact time before stabilizing after 2.5 h at around 15.6 ± 1.0 %, similar to Pata and Eyja (Figure II-4d). By the end of the 48 h period, the %P_{sol} ranged between 3.7 and 20.1 % (Bani and Pata, respectively)

for dust particles and between 0.4 and 12.9 % (Tun Glass and Eyja, respectively) for ash particles. As for dSi, Bani was the dust with the lowest $\%P_{sol}$ and Eyja the ash with the highest $\%P_{sol}$.

3.3.3 Nitrogen

Desert dust released generally more NOx in ARW than volcanic ash, akin to the greater N bulk content in dust (§3.1.2). Pata released the highest amount of NOx in ARW and reached 13.6 µmol.g^{-1} after two hours of contact, corresponding to a peak of solubility of 20.2 % (discussed in §4.4.2). NOx from Douz and Hoggar was released within few minutes after the addition to ARW and did not vary over the 48 h experiment (Figure II-4e): respectively 5.0 and 2.2 µmol.g^{-1} were released after 15 min, corresponding to $\%NOx_{sol}$ of 3.8 and 2.9 % (Figure II-4f). Nitrogen solubility of Bani was the lowest within the dust samples and did not exceed 0.5 %, releasing less than 0.6 µmol.g^{-1} to ARW. Eyja was the only ash sample containing a detectable amount of nitrogen (0.03 %, Table II-4), and also the only ash sample that released a significant amount of NOx (1.53 µmol.g^{-1} after 30 h, corresponding to a solubility of 6.6 %).

3.3.4 Aluminum

Douz released the most dissolved aluminum (dAl_{norm} = 8.73 µmol.g^{-1} after 48 h, Figure II-4g), and presented the highest $\%Al_{sol}$ of 0.5 % compared to other tested aerosols (< 0.1 Figure II-4h). Pata dust and the synthetic Tun Glass released 1.61 and 1.86 µmol.g^{-1} at 48 h and displayed similar $\%Al_{sol}$ of 0.05 %. Aluminum from the other aerosols was weakly soluble ($\%Al_{sol}$ less than 0.03 %). Pata displayed a particular Al dissolution curve: after an initial dAl increase, the amount of dAl decreased between 1 h and 3.5 h of contact then increased to reach 2.28 µmol.g^{-1} after 24 h and decreased again to 1.61 µmol.g^{-1} after 48 h (see discussion, §4.2.1). Other aerosols such as Bani and Hoggar and Eyja displayed fluctuating dAl release within the first contact hours, but this might be due to the low dAl concentration close to detection limit.

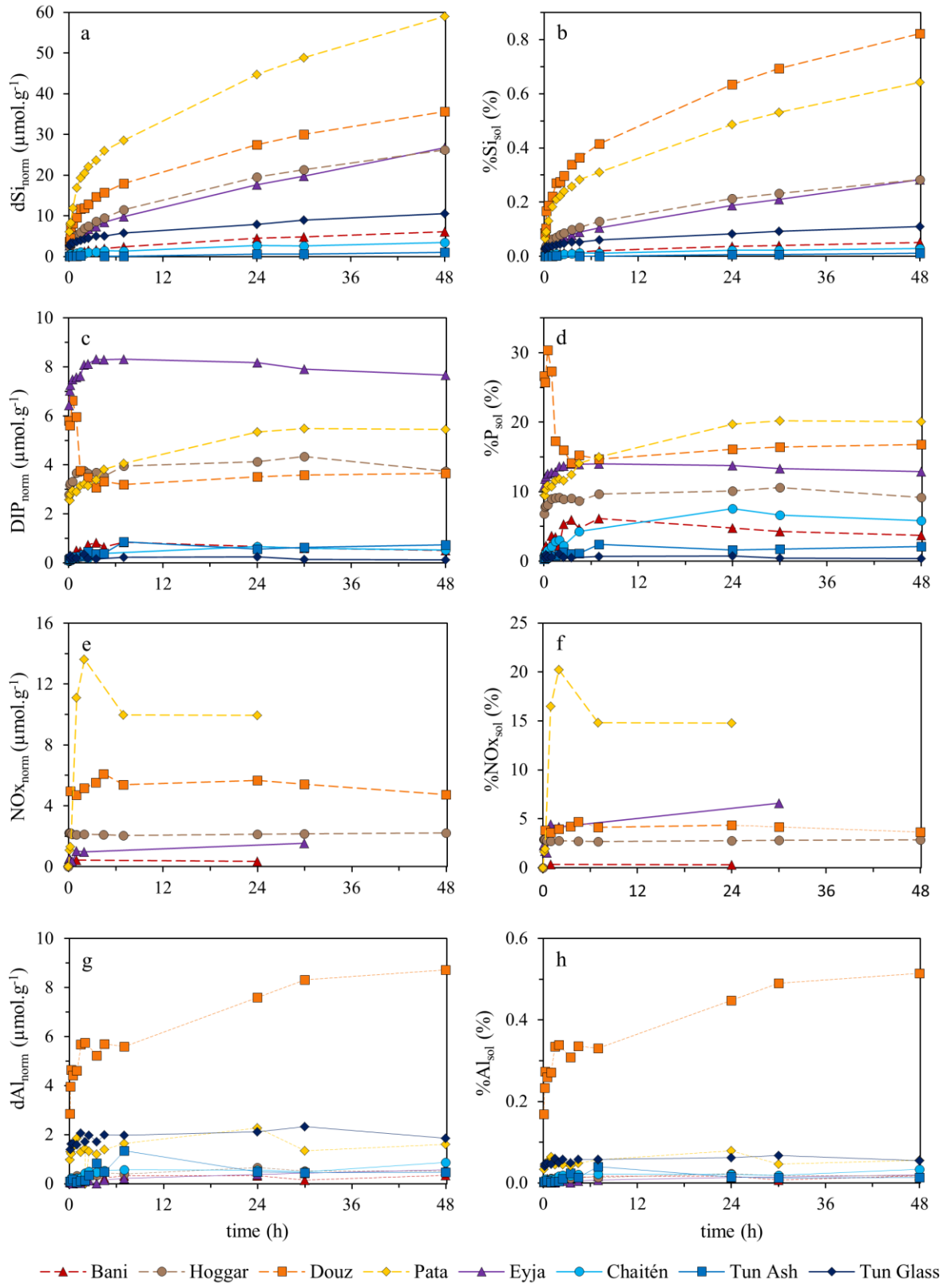

Figure II-4: Dissolution (µmol.g^{-1}, left panels a,c,e,g) and solubility (%, right panels b,d,f,h) in artificial rainwater: dSi (a,b), DIP (c,d), NOx (e,f) and dAl (g,h). Warm colors and dashed lines represent desert dust, cold colors and plain lines represent volcano ash.

3.4 Dissolution in seawater

The second pathway for aerosols to reach the surface ocean is through **dry deposition**, without prior encounter of atmospheric droplets. In this section, we will evaluate the dissolution of macronutrients through a series of leaching experiments in artificial seawater.

3.4.1 Silicon

Except for Bani, desert dust released more dSi than volcanic ash in ASW: after 48 h, dust dissolved between 8.6-64.5 µmol.g^{-1} and ash between 3.8-19.4 µmol.g^{-1} (Figure II-5a). Most dSi is released by Pata (104.7 µmol.g^{-1} after 216 h) and the highest $\%Si_{sol}$ was recorded for Pata and Douz (0.87 and 0.74 % after 96 h, respectively, Figure II-5b); the $\%Si_{sol}$ of other aerosols remained below 0.5 %. The experiment lasted nine days in ASW (except four days for Douz), but the Si dissolution of none of the aerosols reached a plateau, indicating of a non-steady state, until the end of the experiment.

3.4.2 Phosphorus

The highest DIP dissolution in ASW was observed for Douz with 1.16 µmol.g^{-1} after 72 h and for Tun Ash with 0.81 µmol.g^{-1} after 30 h (Figure II-5c). Other aerosols released less than 0.6 µmol.g^{-1}. The maximal $\%P_{sol}$ in ASW of 5.8 % and 5.3 % were recorded for Chaitén (after 216 h) and Douz (after 72 h) respectively, whereas other solubilities remained below 3 % (Figure II-5d). Several aerosols displayed rapid initial dissolution, followed by a decrease of DIP_{norm}: *i.e.,* Bani dissolved 0.45 µmol.g^{-1} after 30 h, and then concentrations became undetectable after 96 h of contact. Similar but less severe DIP_{norm} decrease was observed for Hoggar (-0.49 µmol.g^{-1}), Pata (-0.32 µmol.g^{-1}) and Chaitén (-0.24 µmol.g^{-1}).

3.4.3 Nitrogen

Globally, dust released more NOx to ASW than ash besides Eyja which released more NOx than Hoggar and Bani. NOx released from desert dust displayed a rapid release within five to ten minutes in ASW, and ranged between 0.15-6.86 µmol.g^{-1} (respectively for Bani and Pata, Figure II-5e), and between the DL and 4.48 µmol.g^{-1} for volcanic ash (respectively for Chaitén and Eyja) after t48 h. The N solubility of Eyja (20.6 % at t48 h, Figure II-5f) was higher than for desert dust (0.12-10.2 %, respectively for Bani and Pata). Nitrogen solubility could not be calculated for Chaitén, Tun Ash and Tun Glass, because their N contents were below detection limit.

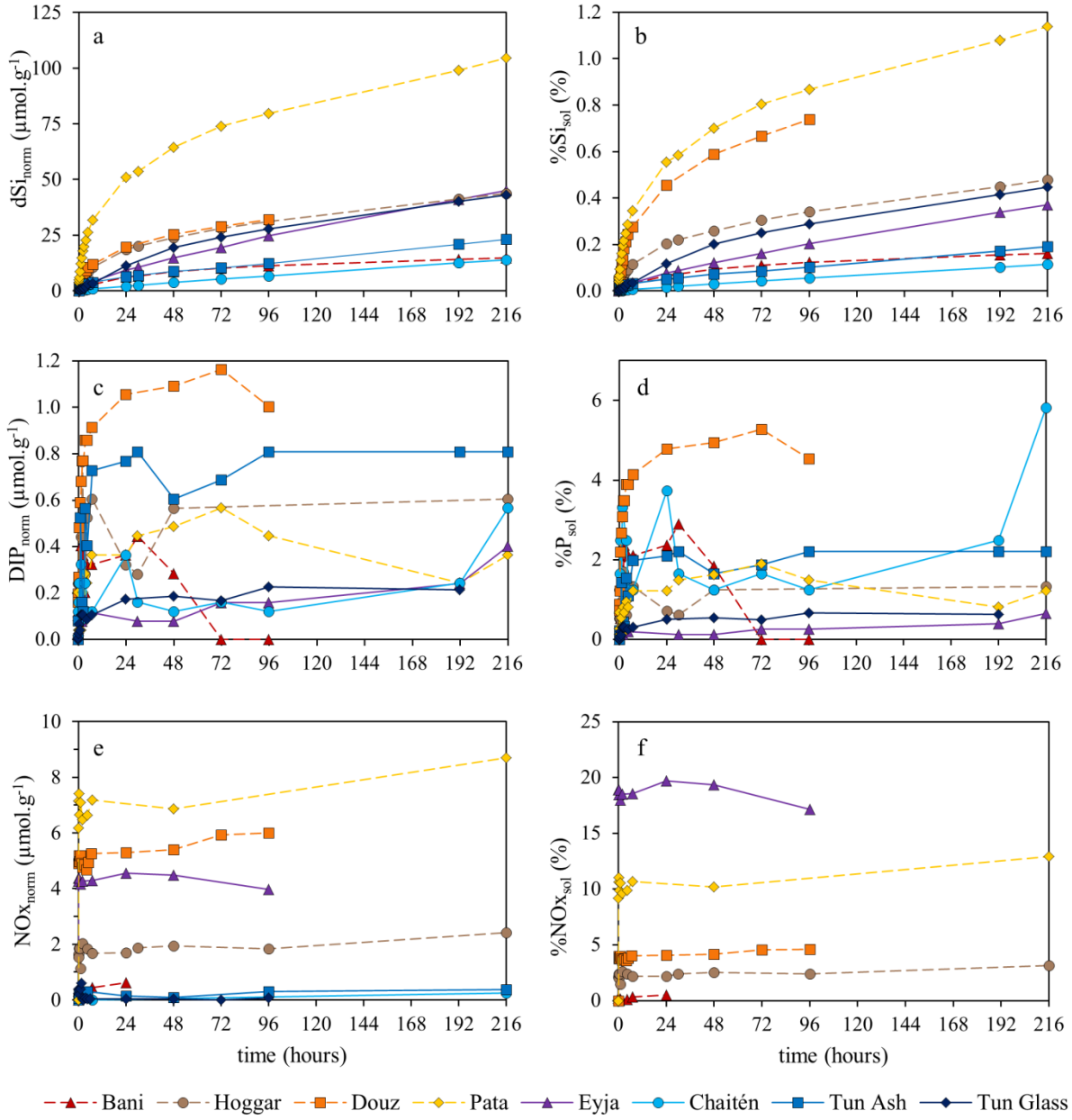

Figure II-5: Dissolution (µmol.g^{-1}, left panels a,c,e) and solubility (%, right panels b,d,f) of macronutrients in artificial seawater: dSi (a,b), DIP (c,d), NOx (e,f). Warm colors and dashed lines represent desert dust, cold colors and plain lines represent volcano ash.

4 Discussion

4.1 Aerosol composition

4.1.1 Mineralogical composition

The *'quantitative'* XRD method according to Nowak et al. (2018) detects the absolute amount of crystalline minerals within the whole sample (expressed in %). Non-detectable minerals such as badly crystallized or amorphous material cannot be assessed, which explains that the sum of identified minerals is less than 100 %. The standard semi-quantitative XRD method (*i.e.* used in Guieu et al. (2014c) for the same Douz dust) expresses the proportion of a mineral (in %) relative to the identified portion of the aerosol, which explains that their quartz and clay proportions are much higher than ours (respectively 40 % for quartz and 25 % for clay in their study vs. 10.1 and 18.8 % in our study) and that their mineral composition sums up to 100 %. In our analysis, the smectite and the badly crystallized portion of aerosols were underestimated which might explain that the clay content (9.6-23.4%, for different dust sources) is low compared to the 44 to 82 % estimated by Journet et al. (2008) with the semi-quantitative method. **Therefore, the amorphous portion in the dust aerosols (between 32.3 % for Douz and 57.6 % for Hoggar, Table II-2) is likely overestimated in our study at the expense of badly detected minerals such as the clay smectite.**

Ash samples are mainly amorphous: 63.7, 69.2 and 81.7 % for respectively Eyja, Tun Ash and Chaitén, 100 % for the synthetic Tun Glass. Simonella et al. (2015) indicated similar high volcanic glass proportions from 76 to 98 %. Feldspar and pyroxenes are major primary magmatic minerals (Delmelle et al., 2005; Paque et al., 2016) and are found in all tested ash samples: Tun Ash contains 24.6 % of the feldspar andesine and 6.2 % pyroxene, while Chaitén and Eyja contain the sodic feldspar albite (16.5 and 23.4 %, respectively). Pata also contained high albite content (18.6 %), which could be an indicator for its particular composition influenced by close-by active volcanoes (Simonella et al., 2015). The composition of Eyja is different compared to other ash samples used in this study, since the sample contains important amounts of smectite (10.9 % montmorillonite), which is uncommon for volcanic ash that mainly does not contain detectable amounts of clay (Table II-3). The presence of alteration minerals such as clay minerals in Eyja can be explained by magma-ice interactions during the first phase of the explosive eruption (Paque et al., 2016). Delmelle et al. (2005) also detected a low amorphous phase in one out of six tested volcano ashes (San Cristobal, Nicaragua) which contained a XRD signature that was typical of clay

minerals. The authors explained this singularity by hydrothermal contamination, underlining the fact that clay is greatly uncommon in ash. The presence of clay within the ash sample could explain the high SSA of 7.3 $m^2.g^{-1}$ (Paque et al., 2016), which compares better to dust samples (from 7.7 to 62.1 $m^2.g^{-1}$, Table II-2) than to the other ash samples of this study (Table II-2).

4.1.2 Elementary composition

The elementary composition varied from sample to sample but no global difference could be made to differentiate desert from volcanic samples. Nitrogen was enriched in all tested aerosols compared to the upper continental crust composition (Wedepohl, 1995), while other elements such as Si were greatly conserved, similar to the findings of Lawrence and Neff (2009), see Annex IV §1 for enrichment factors.

4.2 Dissolved silicon

Frogner et al. (2001) recorded a Si release rate of 50 $\mu mol.g^{-1}.h^{-1}$ for ash of the Icelandic volcano Hekla after roughly 20 minutes of contact time to natural and artificial seawater in their flow-through reactor experiment. This result is 13 to 30 times higher than the dissolution rate of 1.7 to 3.8 $\mu mol.g^{-1}.h^{-1}$ calculated after 15 minutes in ASW for respectively Chaitén and Tun Ash in this study (see Annex IV §2). After 1.5 h of contact to natural or artificial seawater, these authors obtained a dissolution rate of 2-8 $\mu mol.g^{-1}.h^{-1}$, whereas the rate from this study decreases to 0.2-1.5 $\mu mol.g^{-1}.h^{-1}$ for the same contact time. In their natural seawater experiment, the dissolution rate stayed constant at around 2 $\mu mol.g^{-1}.h^{-1}$, while their Si dissolution rate reached values close to zero after 4 h of contact time in artificial seawater. This result is consistent with the 0.1-0.7 $\mu mol.g^{-1}.h^{-1}$ found in this study after 4.5 h.

Olgun et al. (2013) compared the dissolution of several volcanic ash samples from Mount Etna (13 eruptions from 2001 to 2007) in Atlantic seawater. They obtained a wide Si dissolution range of 0.003 to 0.79 $\mu mol.g^{-1}$ after a contact time of 1 h, and 0.09 to 2.06 $\mu mol.g^{-1}$ after 20 h. Their results are rather low compared to our data varying from 0.4 to 1.5 $\mu mol.g^{-1}$ after 1 h and from 2.0 to 11.3 $\mu mol.g^{-1}$ after 24 h. The same authors compared Etna ash dissolution to a Cape Verde loess (simulating Saharan aerosols) using the same experimental setup, and obtained 0.45 $\mu mol.g^{-1}$ after 1 h (and 1.11 $\mu mol.g^{-1}$ after 20 h), which is lower compared to our 1.08 to 12.17 $\mu mol.g^{-1}$ after 1 h (and 6.10 to 51.05 $\mu mol.g^{-1}$ after 24 h for Bani and Pata, respectively). It is to be noted that these authors used a PC in

seawater which was 80 times higher than ours. This different PC may explain the lower dissolution relative to the amount of aerosol, as previously evidenced by Ridame and Guieu (2002) for P solubility. Moreover, Bonnet et al. (2005) did not observe Si release for Saharan desert dust to natural seawater, but their PC was 25-times lower than in our study and might have remained below detection limit.

4.2.1 Dissolution of aluminosilicates

Silicates are the most abundant minerals on Earth, and their basic structural unit is the SiO_4^{4-} tetrahedron. The silicate classification depends on the three-dimensional combination of this basic unit with other cations, either through strong covalent bonding (by sharing one O atom between two adjacent tetrahedrons), or through weaker ionic bonding with a cation (usually carrying a +2 charge such as Mg^{2+}, Fe^{2+}or Mn^{2+}) which receives two electrons from two adjacent oxygen atoms (Haldar and Tišljar, 2013). The most common rock forming minerals belong to the feldspar group (57.9 %), pyroxenes (16.4 %), and quartz (12.6 %) (Haldar and Tišljar, 2013). Clay minerals are secondary minerals and thus not majority within the rock-forming minerals, but are well represented at the earth surface. An important portion of silicates is part of the aluminosilicate group (such as feldspars or clays), where Al atoms tend to take the place of some Si atoms within the tetrahedrons by isomorphic replacement. Phyllosilicates (to which belong clay minerals) are based on interconnected six-member rings of SiO_4^{-4} tetrahedrons that are the foundation of the characteristic sheets (Haldar and Tišljar, 2013). Each clay group (*i.e.*, the illite and smectite groups) is characterized by its geometric structure based on this foundation, while each clay species is identified by its specific Si/Al_{bulk} ratio depending on the frequency of isomorphic replacement: kaolinite holds a ratio of about 1, whilst the ratio of palygorskite can reach up to 2. Other clay species have intermediate Si/Al_{bulk} ratios (0.71 and 0.79 for montmorillonite and illite, respectively). Feldspars have ratios ranging from 2 (anorthite) to 3 (albite and microcline; Haldar and Tišljar, 2013). Our eight aerosols presented Si/Al_{bulk} ratios ranging from 2.7 to 6.3 (for Douz and Bani, respectively, Table II-5). Tun Ash is characterized by a high andesine content (24.6 %, Table II-3; with $Si/Al_{andesine}$ between 2 and 3), which greatly contributes to its Si/Al_{bulk} molar ratio of 2.9 (Table II-5). **During the dissolution of aluminosilicates, both Si and Al atoms are released to the matrix depending on their frequency within the mineral.** In this study, we hypothesize that the Si and Al dissolutions occur with equal kinetics.

Table II-5: Molar Si/Al ratios (µmol/µmol) in the bulk aerosol and in the dissolved fraction at t48 h in artificial rainwater (ARW). Linear regression parameters (equation, coefficient of determination) of significant regressions (p-value < 0.05) are shown. The aluminosilicate dissolution of Pata is divided in two separate regressions (see text). n.s.: not significant.

	$(Si/Al)_{bulk}$	$dSi/dAl_{t48\text{-}ARW}$	Linear regression	R^2
Bani	6.3 ± 0.8	18.0	9.05x - 0.71	0.70
Hoggar	3.2 ± 0.5	50.3	35.55x – 1.34	0.71
Douz	2.7 ± 0.3	4.1	5.71x – 16.86	0.94
Pata	3.2 ± 0.2	36.7	12.75x – 7.33	0.95
			20.83x – 3.62	0.97
Eyja	3.3 ± 0.1	47.1	41.56x + 2.05	0.97
Chaitén	4.4 ± 0.2	3.9	3.84x – 0.24	0.68
Tun Ash	2.9 ± 0.2	2.3	n.s.	
Tun Glass	2.8 ± 0.2	5.7	5.77x – 5.75	0.70

A plateau in the dSi/dAl ratio (Figure II-6, right panels) is an indicator for a constant proportion of Si and Al dissolution, while an increasing ratio stands for a preferential Si release and/or Al sink. This latter phenomenon can be better identified by a decrease of the dAl concentration (Figure II-4g) and could have occurred for some of the timing and aerosols (e.g., after 1 and 24 h for Pata or after 7 h for Tun Ash). This is likely due to Al-hydroxide precipitation (Huertas et al., 1999) and/or Al adsorption quickly after the dissolution of the clays kaolinite (Lützenkirchen et al., 2014) and montmorillonite (Bruggenwert et al., 1987), or of the feldspar albite (Chen and Brantley, 1997). Aluminum precipitation depends on several parameters such as the pH, the aqueous Al concentration in the solution and the chemical affinity, as described by Oelkers et al. (1994). In addition, Si might also adsorb on (hydr)oxides (Swedlund and Webster, 1999), but this behavior appears not significant in our study, since we observe steady dSi increase in both ARW and ASW matrices with time.

4.2.1.1 Aluminosilicates in desert dust

In ARW, we observed several significant positive correlations (p-value < 0.05) between Si and Al dissolution for several tested aerosols (Figure II-6, left panels), indicating the dissolution of aluminosilicates: Douz released by far the most Al to ARW (Figure II-4g,h) and displayed the strongest global dSi/dAl relationship (R^2 = 0.94, p-value < 0.05, Table II-5 and Figure II-6e), accompanied with an initially increasing dSi/dAl ratio (between 5 min and 7 h in ARW, Figure II-6f) before stabilizing between 7 and 48 h at a constant ratio of about 4, indicating constant Si and Al dissolution.

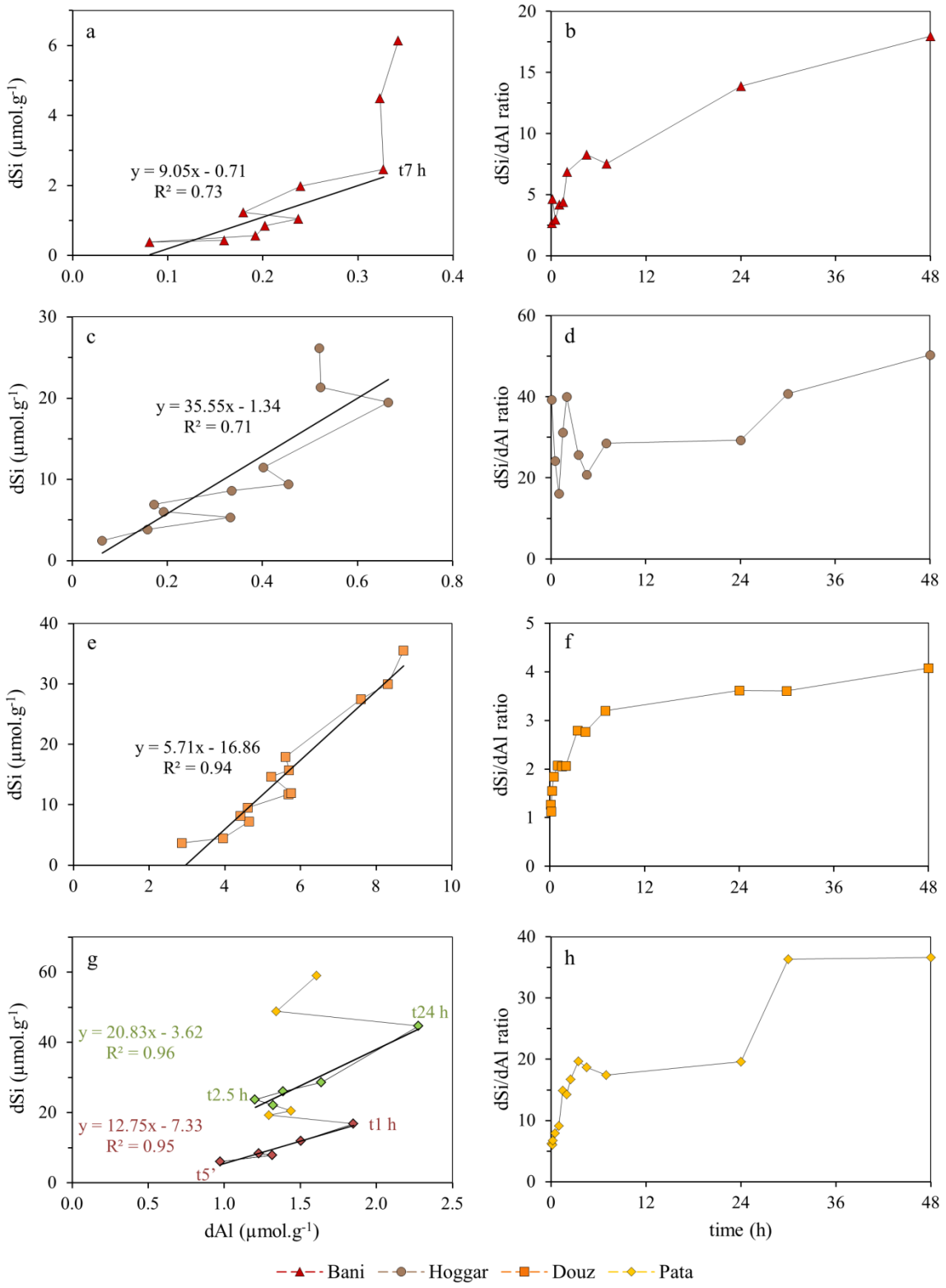

Figure II-6: Left panels: Dissolved Si (µmol.g-1) as a function of dAl (µmol.g-1) in artificial rainwater for dust (a,c,e,g) and ash (i,k,m,o). Regressions are calculated for the entire experiment (5 min - 48 h), except for Bani (a), Pata (g) and Tun Glass (o) where the edges of partial regressions are indicated on the graph. Only significant linear regressions (p-value < 0.05) are shown. Right panels: Evolution of the molar dSi/dAl ratio with contact time in artificial rainwater for dust (b,d,f,h) and ash (j,l,n,p).

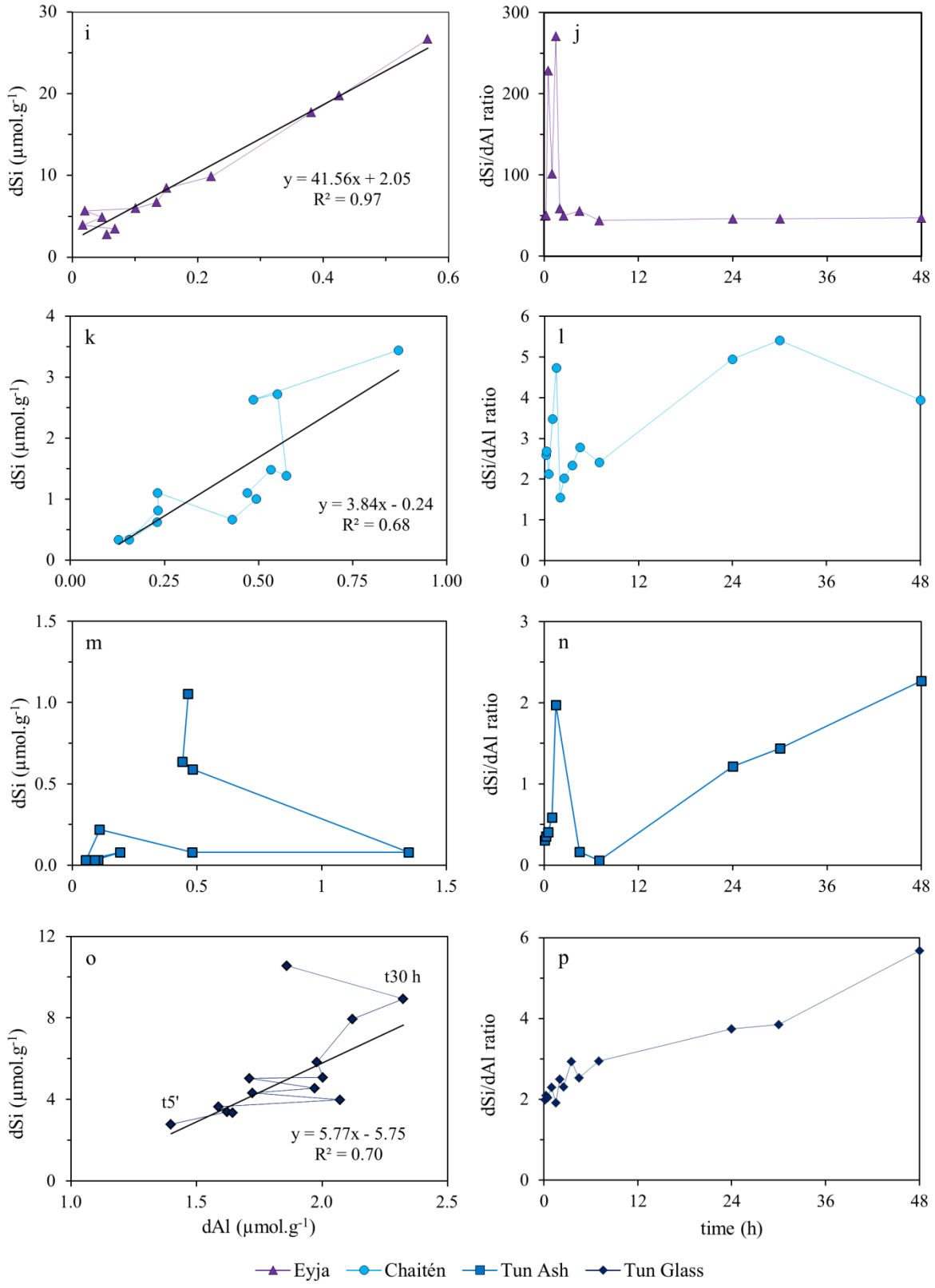

Figure II-6: Left panels: Dissolved Si (µmol.g^{-1}) as a function of dAl (µmol.g^{-1}) in artificial rainwater for dust (a,c,e,g) and ash (i,k,m,o). Regressions are calculated for the entire experiment (5 min - 48 h), except for Bani (a), Pata (g) and Tun Glass (o) where the edges of partial regressions are indicated on the graph. Only significant linear regressions (p-value < 0.05) are shown. Right panels: Evolution of the molar dSi/dAl ratio with contact time in artificial rainwater for dust (b,d,f,h) and ash (j,l,n,p).

Douz contains crystalline aluminosilicates only under the form of clay (13.4 % illite, 2.85 % kaolinite and 2.4 % palygorskite, Table II-3) but might as well contain badly crystallized smectites (Journet et al., 2008; Paris et al., 2011) undetected by the analytical XRD method. The final dSi/dAl ratio in ARW was slightly higher than the Si:Al ratio of bulk aerosols (4.1 and 2.7±0.3, respectively, Table II-5), which could be either explained by additional Si dissolution from non Al-containing minerals such as quartz (10.0 % SiO_2) or by aluminosilicates bearing the upper crustal ratio (Si/Al ratio of 3.9; Wedepohl, 1995).

Similarly, Bani and Hoggar presented significant linear regressions for aluminosilicate dissolution (p-value < 0.05, Table II-5; Figure II-6a,c) despite Al fluctuations during the first hours of contact. At the end of the experiment (t48 h), the dSi/dAl ratios reached between 18.0 and 50.3 for Bani and Hoggar respectively, but no plateau was reached (Figure II-6b,d). Noteworthy for Bani, no dAl was released after 7 h, suggesting that the 3.7 $\mu mol.g^{-1}$ of dSi released between 7 h and 48 h were not liberated from aluminosilicates, but most probably from quartz (Bani is composed by 48.5 % of SiO_2, Table II-3).

Further, Pata had a unique aluminosilicate dissolution behavior due to the decrease of dAl_{norm} after 1 h and again after 24 h of contact to ARW (separate regressions in Table II-5, Figure II-6g). This behavior was too fast to be assimilated to reverse weathering, but might be explained by Al precipitation or adsorption.

Moreover, Bani, Hoggar and Pata contain feldspar minerals in addition to the clay minerals found in Douz. Feldspar is known to have higher $(Si/Al)_{total}$ ratios, but dissolution of aluminosilicates alone cannot explain the 3 to 15-fold higher dSi/dAl obtained in this study. **Quartz or amorphous silicon, possibly present within the amorphous portion of aerosols, may be responsible for higher Si release and will be addressed in the next sections.**

4.2.1.2 Aluminosilicates in volcanic ash

The dissolution of Eyja, Chaitén and Tun Glass also displayed significant positive correlations between dSi and dAl (p-value < 0.05, Table II-5; Figure II-6i,k,o) after an erratic dAl release during the first hours, impacting the initial dSi/dAl. Eyja was the only ash that reached a dSi/dAl plateau around 50 after 7 h of contact (Figure II-6j). Other ash samples displayed increasing dSi/dAl with time, but their dSi/dAl_{t48h} ratios were in the same range as their $(Si/Al)_{bulk}$ ratios (Table II-5). The amorphous Tun Glass has likely reached a plateau with a dSi/dAl ratio close to 4 at t30 h, typical of crustal aluminosilicates (Figure II-6o), **probably resulting from the dissolution of amorphous aluminosilicates.** However, Si

continues to be released after t30 h, whereas the Al concentration decreases, which suggests the dissolution of pure Si and/or adsorption/precipitation of Al.

On the other hand, Tun Ash did not display any correlation between dSi and dAl (Figure II-6m), indicating that this sample dissolved only negligible amounts of aluminosilicates and that the dSi had most probably another origin. Nonetheless, Tun Ash contains 24.6 % of the feldspar andesine (having a $(Si/Al)_{total}$ ratio of 2.5, according to Haldar and Tišljar, 2013). This result will further be discussed in §4.2.2.

The linear relationships between dSi and dAl (Figure II-6) clearly underline the role of aluminosilicate dissolution in Si release, but other non-Al containing minerals and the amorphous part of aerosols intervene as well in Si release, since the dSi/dAl release was constantly higher than the Si/Al ratios of aluminosilicate minerals (from 1 to 3). It is commonly accepted that the first elements dissolving from minerals such as feldspars are alkali and alkaline earth metals (such as K, Mg, Ca) due to their fast removal from the mineral structure. The second dissolution step hydrolyzes Al-O-Si bonds, liberating Al in both basic and acidic conditions (Oelkers et al., 1994 and references therein). Silicon is released only after these initial steps, through the breaking of Si-O-Si bonds from Si-rich surface layers. Preferential initial Al liberation, followed by later increased Si release could explain the observed chronological dSi/dAl increase. Indeed, Köhler et al., (2003) attest an initial preferential Al release of illite at 25 °C and acidic pH, possibly explained by fast Al exchange reactions from adsorption sites. Dissolution from the feldspar albite depends on pH and preferential Al dissolution is observed for pH below 6, whereas Si release is predominant above pH 6 (Chou and Wollast, 1985). Maring and Duce (1987) identified bimodal dissolution of Al from aerosols in seawater at pH 8, displaying initial rapid Al release from weathered primary minerals prior to aluminosilicate dissolution. In our ARW experiments at pH 5-7.5, dSi/dAl ratios were exclusively above 1, indicating that the aluminosilicate dissolution alone cannot explain the entire Si release, since most clay species have a Si/Al ratio between 1-1.4. We will assess the role of other minerals to the Si release in the next sections of this manuscript.

4.2.2 Role of mineralogy in Si dissolution

Douz contains twice less Si than Pata (13.06 % vs. 25.80 %, Table II-4) and dissolves less dSi_{norm} per gram of aerosol than Pata in ARW and ASW. However, Douz presented the highest Si solubility (section 3.3.1) in ARW but not in ASW. This phenomenon can be encoded by the *solubility ratio* as follows:

$$\%\mathrm{sol}_{\mathrm{ARW/ASW}} = \frac{\%sol_{ARW}}{\%sol_{ASW}} \qquad \text{Equation II-4}$$

The $\%sol_{ARW/ASW}$(dSi) ratio for Douz was higher than 1 throughout the experiment (t1 h and t48 h shown in Table II-6), indicating an increased $\%Si_{sol}$ in ARW compared to ASW. On the other hand, Bani dissolved more dSi in ASW (solubility ratios < 1) while Hoggar and Pata displayed similar solubilities (ratios around 1), demonstrating that the dissolution behavior was aerosol-dependent. The same conclusion can be driven for ash samples, as Eyja dissolved more Si in ARW (ratio > 1), whilst Tun Ash was more soluble in ASW. Tun Glass and Chaitén initially dissolved more in ARW than in ASW. These results demonstrate that **Si solubility of most dust and ash samples depended on pH and/or the ion loading of the matrix (*i.e.*, ARW vs. ASW) but also varies with the aerosol composition**.

Table II-6: Solubility ratio of macronutrients in artificial rainwater (ARW) over artificial seawater (ASW), calculated according to Equation II-4.

	$\%sol_{ARW/ASW}$ - dSi		$\%sol_{ARW/ASW}$ - DIP		$\%sol_{ARW/ASW}$ - NOx	
	1 h	48 h	1 h	48 h	1 h	48 h
Bani	0.6	0.5	3.5	2.0	2.4	0.6 ~
Hoggar	1.5	1.1	20.2	7.3	1.0 *	1.1
Douz	2.6	1.4	10.2	3.4	0.9	0.9
Pata	1.4	0.9	19.8	12.3	1.6	1.0 ~
Eyja	5.2	2.3	98.6 *	99.8	0.2	0.3 #
Chaitén	1.7	0.9	2.5	4.7	-	-
Tun Ash	0.0	0.1	0.5	1.3	-	-
Tun Glass	4.1	0.5	4.7	0.7	-	-

Note: For missing data, solubility was used at 2 h instead of 1 h (*); 24 h instead of 48 h (~); and 30 h instead of 48 h (#). Missing ratios are due to NOx dissolution below detection limit in ARW.

Dissolved Si released from Douz was very similar to Hoggar in ASW (Figure II-5; §0), but its solubility was twice higher. The Si solubility is inversely proportional to the quartz content and proportional to illite content within the dust sample, indicating that $\%Si_{sol}$ decreases significantly with increasing quartz and decreasing illite content (Mann-Whitney test for small samples with n = 4, p-value < 0.05). However, Douz is the only aerosol (besides the amorphous synthetic Tun Glass) that does not contain any feldspar such as andesine and albite, which are known to have higher Si dissolution rates than quartz in our ARW conditions (Chou and Wollast, 1985; Stillings et al., 1996). **This result indicates that the mineralogy of dust samples alone was not sufficient to explain the increased $\%Si_{sol}$ of Douz compared to Pata.**

It is known that increasing travel distances scatter the size distribution of aerosols due to the removal of larger particles by gravitational settling. Dissolution and solubility can increase when the aerosol size decreases, inducing an increase in the specific surface area (SSA) (Ayris and Delmelle, 2012; Mahowald et al., 2014) since the exchange surface with the matrix is modified. To be comparable (between aerosols and to pure minerals), the exchange surface normalized dissolution rate ρ_{Diss} (mol dSi.m^{-2}.s^{-1}) was calculated according to:

$$\rho_{Diss} = \frac{dSi_{norm}}{t \times SSA} \qquad \text{Equation II-5}$$

where dSi_{norm} is the amount of dSi per gram of aerosol, t is the contact time in seconds and SSA is the specific surface area in m².g^{-1} (Table II-2). The Si dissolution rates of all main silicate minerals have been measured since the 1980s, initiated by the work of Chou and Wollast (1985). A summary of Si dissolution rates for aerosol-composing minerals at the equilibrium pH in ARW and ASW from the literature is presented in Table II-7. These studies carried out long duration dissolution experiments (exceeding one year) at various pH and temperature conditions, and steady state was reached after several days of contact (*e.g.* after 200 h for kaolinite at 25 °C at pH between 2 and 9, according to Huertas et al. (1999)).

Table II-7: Silicon dissolution of pure minerals (ρ_{Diss} in mol dSi.m^{-2}.s^{-1}) at ambient temperature and pressure conditions according to literature at steady state. RT: room temperature, PW: pure water and FSW: filtered seawater. *The experiment performed at 90°C extrapolated by the authors to 16 °C in the article. Values in italics are extrapolated for the cited pH values.

			pH 5	pH 6	pH 7	pH 7.5	pH 8	Temp (°C)	Matrix	References
acidic rocks		quartz	*1.610^{-12}*		5.0 10^{-12}	5.0 10^{-12}	*1.0 10^{-11}*	25		Wollast and Chou, 1988
	feldspar	microcline	1.6 10^{-12}					25		van Hess and al., 2002
		andesine	5.7 10^{-12}	*5.5 10^{-12}*	*5.1 10^{-12}*	*5.0 10^{-12}*	*3.0 10^{-12}*	25		Oxburgh and al., 1994
		albite	1.6 10^{-12}	*1.3 10^{-12}*	*1.3 10^{-12}*	1.6 10^{-12}	2.2 10^{-12}	RT	HCl solution	Chou and Wollast, 1985
basic rocks	pyroxene	enstatite	6.2 10^{-11}	3.5 10^{-11}	1.9 10^{-11}	*1.5 10^{-11}*	1.1 10^{-11}	25	PW + HCl/NaOH	Oelkers and Schott, 2001
		augite	*3.0 10^{-13}*	*4.1 10^{-13}*	*5.0 10^{-12}*	*1.9 10^{-11}*	6.3 10^{-11}	25		Sverdrup, 1990
clay		illite	3.2 10^{-15}	*1.0 10^{-15}*	*1.0 10^{-15}*	*1.0 10^{-15}*	1.6 10^{-15}	25		Köhler et al., 2003
		kaolinite	1.5 10^{-14}	9.0 10^{-15}	7.5 10^{-15}	7.0 10^{-15}	*6.0 10^{-15}*	25	PW + HCl/NaOH	Huertas et al., 1999
			1.1 10^{-13}	1.1 10^{-13}	9.7 10^{-14}	1.1 10^{-13}	*1.3 10^{-13}*	25	pH buffer	Carroll and Walther, 1990
	smectite	montmo-rillonite	2.5 10^{-13}	*5.0 10^{-14}*	*2.0 10^{-14}*			25		Zysset and Schindler, 1995
							1.0 10^{-14}	20		Huertas et al., 2001
amorphous	biogenic	phytolith	2.6 10^{-12}	5.8 10^{-12}	1.4 10^{-11}	9.5 10^{-12}	2.3 10^{-11}	25		Fraysse et al., 2006
	pedogenic	allophane	2.0 10^{-12}		2.2 10^{-12}					Ralston, 2018
	volcanic	basaltic glass	2.1 10^{-07}			7.5 10^{-07}		16*	PW and FWS	Morin et al., 2015
			2.9 10^{-11}	1.0 10^{-11}	1.4 10^{-11}	1.9 10^{-11}	2.8 10^{-11}	30		Gislason and Oelkers, 2003

In order to compare our results to the literature (Table II-7) the dissolution rate from our aerosols was estimated at steady state. We extrapolated ρ_{Diss} at 300 h of contact time in both ARW and ASW according to the power fit of the experimental data (Figure II-7). Even if 300 h may not be representative of true steady state, the choice of a longer time does not change the shape of Figure II-7. It is to be noted that the sole purpose of this steady state extrapolation was to simplify the comparison to previous experimental studies on pure minerals (Table II-7), but that the scope of this work lies within representative timespans of aerosols in rain- and seawater, where steady state is not applicable due to much shorter time scales (1-2 h in rain and 1-2 days in surface seawater).

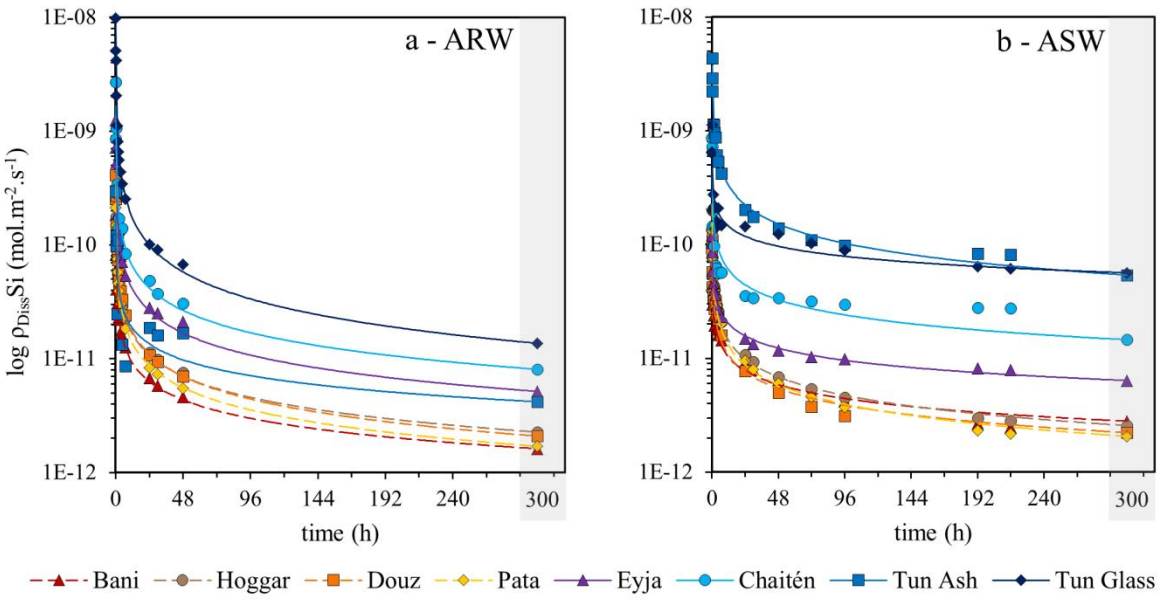

Figure II-7: Silicon dissolution rate (mol dSi.m^{-2}.s^{-1}) of aerosols in artificial (a) rain (ARW) and (b) seawater (ASW) in log scale. The data points at t300 h (shaded) are calculated from a power fit extrapolation of the steady state.

Another parameter influencing the Si solubility is the **ambient pH**. Figure II-8 shows the pH dependent Si dissolution rate of pure minerals according to literature. For instance, at 25 °C, quartz is more soluble at increasing pH above pH 3 (Crundwell, 2017; Dove and Elston, 1992; Wollast and Chou, 1988 ; Table II-7 and yellow curve in Figure II-8).

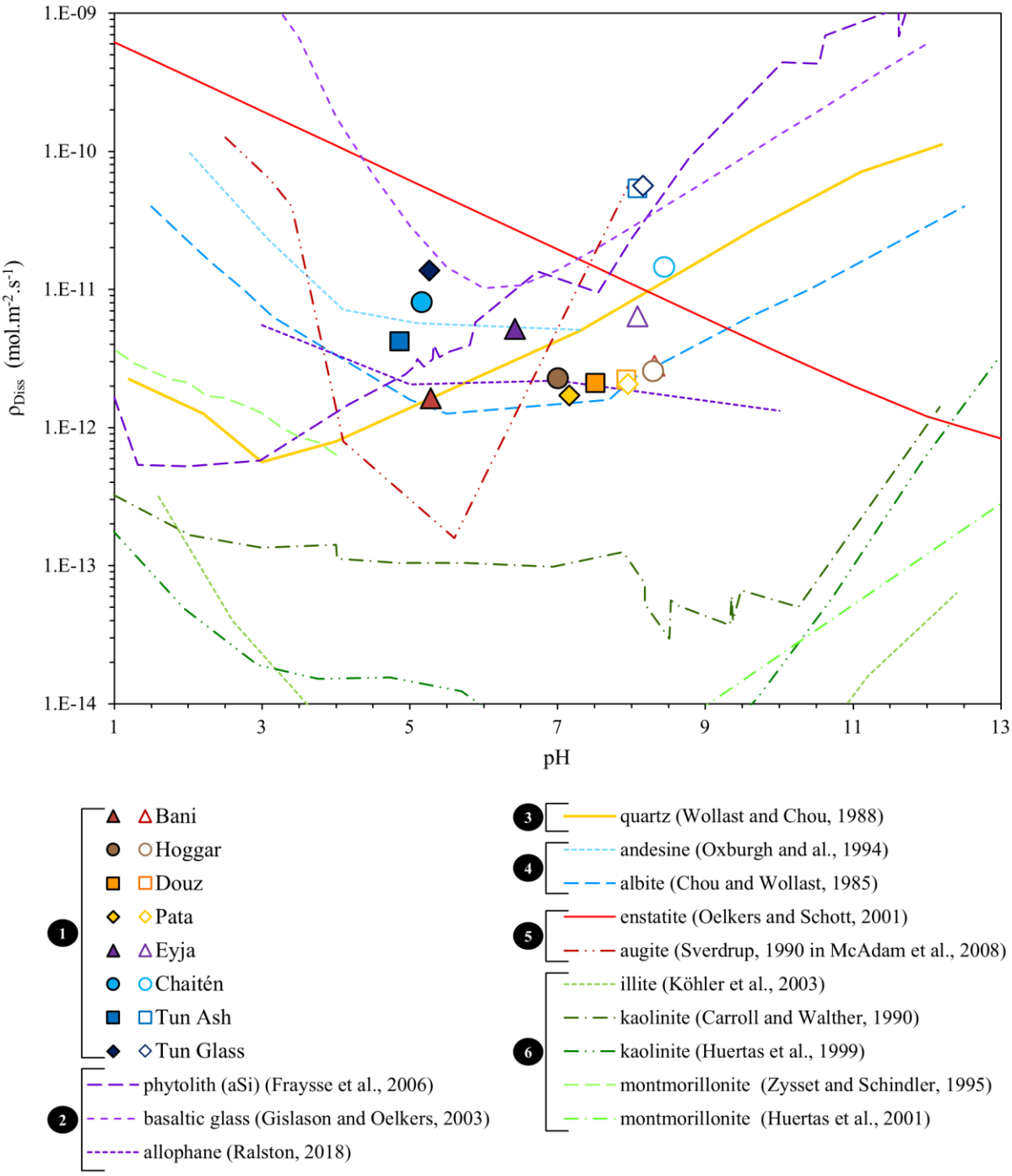

Figure II-8: Silicon dissolution rate (mol dSi.m^{-2}.s^{-1}) normalized by the specific surface area of aerosols (1) in artificial rainwater (filled symbols) and artificial seawater (open symbols with corresponding color) as a function of ambient pH at estimated steady state (300 h of contact time, Figure II-7) compared to the pH-dependent dissolution rate of pure minerals from the literature: amorphous minerals (purple lines, 2), quartz (yellow line, 3), feldspars (blue lines, 4), basic rocks (red lines, 5) and clay minerals (green lines, 6).

Other Si containing minerals such as the clays illite, kaolinite and montmorillonite dissolve more at both acid and basic pH (below pH 6 and above 8, Huertas et al., 2001, 1999; Köhler et al., 2003; Zysset and Schindler, 1996, Table II-7 and green curves in Figure II-8) but become less soluble at pH around 7, which is typical for aluminosilicate dissolution (Guy and Schott, 1989). Feldspars display a similar dissolution behavior in the case of pH but their solubility is 1 to 4 orders of magnitude higher compared to clay, depending on the species and ambient pH (Chou and Wollast, 1985; Oxburgh et al., 1994, Table II-7 and blue curves in Figure II-8). As addressed previously, Douz has the highest $CaCO_3$ content, which triggers the highest pH neutralization of the ARW. Thus, **increased $\%Si_{sol}$ of Douz might therefore partially be explained by higher dSi dissolution from quartz minerals included in the aerosol, after the basification of the ARW matrix**.

The estimated steady state Si dissolution rates of tested aerosols compare well to pure minerals from the literature (Figure II-8). The theoretical contribution of the crystalline part to the total Si dissolution rate (Table II-8) was calculated at the equilibrium pH for each aerosol and both matrices according to:

$$\rho_{Diss}(theo)_{crystalline} = \sum (\%_X \times X\rho_{Diss}) \qquad \text{Equation II-6}$$

where $\%_X$ represents the percentage of the mineral X in the aerosol and $X\rho_{Diss}$ is the theoretical steady state Si dissolution rate of the mineral X at the equilibrium pH, according to literature (Table II-7).

Table II-8: Experimental Si dissolution rates (ρ_{Diss} in mol dSi.m^{-2}.s^{-1}) in artificial rain and seawater, compared to the theoretical contribution from the crystalline part of the aerosol. **pH_{eq}**: equilibrium pH of each aerosol for a given matrix. **$\rho_{Diss}(theo)_{crystalline}$**: theoretical Si dissolution rates due to the crystalline fraction, calculated at pH_{eq} (Equation II-6, Table II-7). **$\rho_{Diss}(eSS)_{total}$**: Si dissolution rate extrapolated from the experimental data at estimated steady state (eSS, shaded part on Figure II-7). Cryst.part (%): percentage of estimated ρ_{Diss}(eSS) explained by the crystalline theoretical dissolution rate ρ_{Diss}(theo) for each matrix.

	Artificial rainwater				Artificial seawater			
	pH_{eq}	ρ_{Diss}(theo) crystalline	ρ_{Diss}(eSS) total	Cryst. Part, %	pH_{eq}	ρ_{Diss}(theo) crystalline	ρ_{Diss}(eSS) total	Cryst. Part, %
Bani	5.29	8.6 10^{-13}	1.6 10^{-12}	53	8.31	4.8 10^{-12}	2.8 10^{-12}	170
Hoggar	7.01	1.3 10^{-12}	2.3 10^{-12}	56	8.29	2.2 10^{-12}	2.6 10^{-12}	87
Douz	7.52	7.2 10^{-13}	2.1 10^{-12}	34	7.93	9.7 10^{-13}	2.2 10^{-12}	43
Pata	7.17	5.7 10^{-13}	1.7 10^{-12}	33	7.95	1.0 10^{-12}	2.1 10^{-12}	49
Eyja	6.43	3.1 10^{-13}	5.2 10^{-12}	6	8.08	5.5 10^{-13}	6.4 10^{-12}	9
Chaitén	5.17	2.9 10^{-13}	8.1 10^{-12}	4	8.44	5.2 10^{-13}	1.5 10^{-11}	4
Tun Ash	4.87	3.0 10^{-12}	4.2 10^{-12}	72	8.08	3.3 10^{-12}	5.4 10^{-11}	6
Tun Glass	5.27	0.0	1.4 10^{-11}	0	8.15	0.0	5.6 10^{-11}	0

The dissolution of the crystalline minerals explains an overall higher percentage of Si ρDiss from desert dust compared to volcanic ash in both matrices (Table II-8), except Tun Ash whose solubility is explained at over 70 % by crystalline minerals in ARW. The crystalline Si originating from dust is sufficient to explain all or most of Si released from Bani and Hoggar in ASW (170 % and 87 %, respectively) and almost half of the Si released from Douz and Pata (43 % and 49 %). The percentage over 100 % for Bani in ASW may be explained by uncertainties due to the extrapolation of steady state or by the choice of literature data, which might overestimate the contribution of quartz (Dove and Elston, 1992). **The calculated theoretical contribution of quartz dissolution to Si release from desert dust accounts for 19.4-49.2 % in ARW and 29.2-100 % in ASW (Figure II-9) but is negligible for ash (maximum contribution of 1.0 %).**

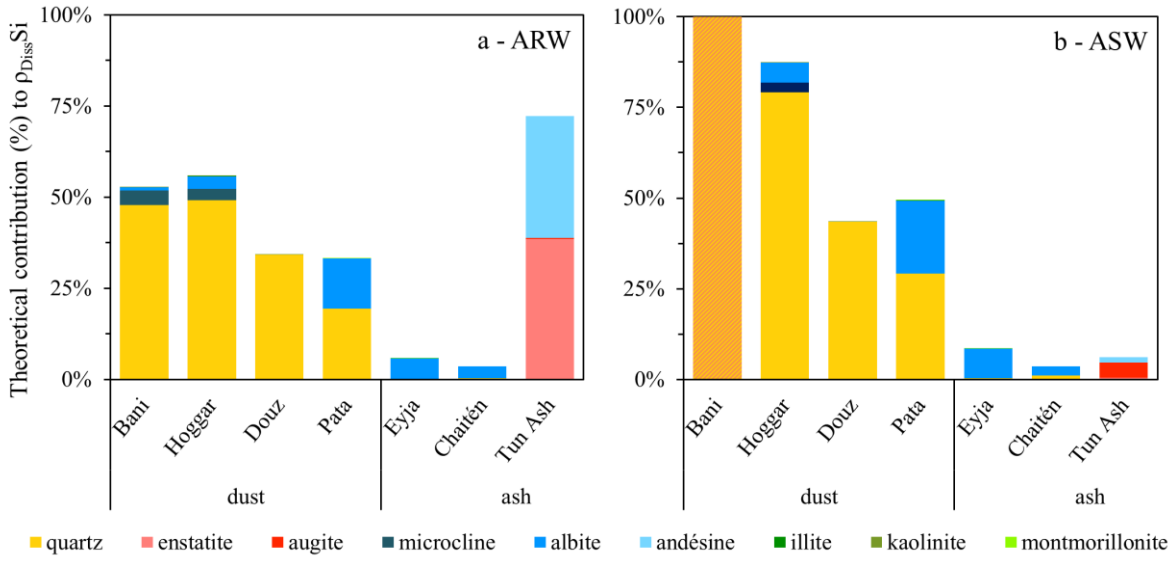

Figure II-9: Theoretical contribution of each Si containing mineral to the Si dissolution rate of aerosols estimated at equilibrium from experimental data (ρ_{Diss}(eSS), mol Si.m^{-2}.s^{-1}, according to Table II-8) in artificial rain (ARW) and seawater (ASW). Quartz is shown in yellow, basic minerals in red, feldspars in blue and clays in green. The contribution of quartz for Bani in ASW (dashed orange bar) was sufficient to explain the Si dissolution in ASW.

The crystalline contribution to the total Si dissolution decreased for dust in ARW as compared to ASW but remained high (33-56 %, Table II-8, Figure II-9a). This trend was not observed for Eyja and Chaitén (and obviously for Tun Glass which is completely amorphous), with similar low contribution in ARW and ASW (below 10 %). On the other hand, the dSi dissolution from Tun Ash is a lot better explained in ARW compared to ASW: in ARW, the dissolution of the feldspar andesine and the basic rock enstatite explain 72 % of the dSi

release (accounting each for 33.5 % and 38.5 % of the total ρ_{Diss}(eSS), Figure II-9), compared to only 1.4 % and 0.5 % in ASW, where the basic mineral augite was more soluble (4.2 % of the signal in ASW compared to 0.3 % in ARW). The contribution of clay dissolution to Si release was very low (maximal 0.2 % of the global Si release in ARW and less in ASW).

The remaining part of Si release has to be attributed to the amorphous portion, most probably basaltic glass in volcanic ash, known to be more soluble in seawater: This result is consistent with the findings from Icenhower and Dove (2000), establishing the relationship of amorphous SiO_2 dissolution and increasing NaCl concentration. Equally, Morin et al. (2015) showed increasing Si dissolution of a synthetic basaltic glass with increasing salinities observed in estuaries.

This comparison shows that the **contribution of crystalline minerals in our aerosols was insufficient to explain the total Si dissolution measured in our experiments**, except for Bani and Hoggar in ASW and Tun Ash in ARW. The study thus underlines the importance of the amorphous and/or badly crystallized and/or crystalline but undetected portion of aerosols for Si release to both ARW and ASW. **If such a result is not surprising for ash samples, this is more striking for dust samples. The amorphous contribution will be discussed in the next section.**

4.2.3 Contribution of amorphous silicon

The amorphous portion of aerosols might be an additional source of dSi with potential important Si solubility (Fraysse et al., 2006; Gunnarsson and Arnórsson, 2000). The composition of the amorphous material was unfortunately not identified in this study, but it can be biogenic (released after the degradation of organic matter from diatom frustules or phytoliths in higher plants such as grass and bamboo, Fraysse et al. 2009); pedogenic (produced during soil formation by physical and chemical weathering of parent material such as quartz, Cornelis et al., 2011; Jenny, 1941) or lithogenic (*e.g.* volcanic glass, Morin et al., 2015). Allophanes are amorphous aluminosilicates with molar SiO_2/Al_2O_3 ratios varying from 0.9 to 1.9 (Sieffermann et al., 1968). Depending on its origin and composition, the dissolution of amorphous silica (aSi) depends on pH with variable behavior: phytoliths (biogenic Si, bSi) display a dissolution rate with a relationship relative to pH similar to quartz dissolution, but more than an order of magnitude higher in the basic domain, increasing above pH 2 (Fraysse et al., 2009, 2006, Figure II-8). However, the dissolution of hydrated amorphous silica gel is stable below pH 8 but depends on the matrix, thus decreasing with increased salinity

(Marshall and Warakomski, 1980). On the other hand, continental and marine bSi, as well as volcanic basaltic glass, are known to dissolve more in seawater at higher pH, due to the catalytic effect of Na^+ and Mg^{2+} cations (Loucaides et al., 2008; Morin et al., 2015). According to Gislason and Oelkers (2003), basaltic glass dissolution decreases around pH 6 and increases in the acidic and basic regions, while the dissolution rate of pedogenic allophane varies only slightly with pH (Ralston, 2018, purple lines, Figure II-8).

Due to this wide variety of possible dissolution behaviors, it is therefore not possible to determine the contribution from the aerosol aSi pool to the $\%Si_{sol}$ without knowing their exact composition. An estimation can be made by calculating the amount of particulate aSi within the amorphous material that would be needed to explain the remaining part of ρ_{Diss}(eSS). For instance, the dissolution of crystalline material explains 56 % of Si dissolution of Hoggar in ARW (Table II-8), so theoretically, the amorphous material should resolve the remaining 44 %, *i.e.,* 1.0 10^{-12} mol dSi.m^{-2}.s^{-1} (Table II-9). The theoretical contribution of the amorphous part to the total Si dissolution rate was calculated at the equilibrium pH for each aerosol and both matrices according to:

$$\rho_{Diss}(theo)_{amorphous} = \rho_{Diss}(eSS)_{total} - \rho_{Diss}(theo)_{crystalline} \quad \text{Equation II-7}$$

$$aX\ (\%) = \frac{\rho_{Diss}(theo)_{amorphous}}{aX\rho_{Diss}} \quad \text{Equation II-8}$$

where aX represents the percentage of the amorphous mineral X in the aerosol and $aX\rho_{Diss}$ is the theoretical steady state Si dissolution rate of the amorphous mineral X at the equilibrium pH, according to literature (Table II-7); $\rho_{Diss}(eSS)_{total}$ and $\rho_{Diss}(theo)_{crystalline}$ are provided by Figure II-7 and Equation II-6, respectively.

The presence of phytoliths and freshwater diatom valves in Saharan desert dust has been reported (Folger et al., 1967; Romero et al., 1999). Using ρ_{Diss} from literature for phytoliths and allophane (Fraysse et al., 2006; Ralston, 2018) at pH 7 (pH_{eq} for Hoggar dissolution in ARW), we find that 7 % of phytoliths or 46 % of allophanes **or a combination of both** would be necessary within the 57.6 % of amorphous material in order to explain the remaining Si dissolution of Hoggar in ARW (Table II-9). In ASW, the amount of aSi needed to fulfill the ρ_{Diss}(eSS) is even less (1 % of phytoliths or 15 % of allophane, **or a combination of both**).

It is to be noted that allophanes originate from the weathering of volcanic ash and are thus not likely to be abundant within the African samples (Bani, Hoggar and Douz), whereas they

might be of importance within the South American Pata. Moreover, phytoliths enter in contact with arid dust most probably within the atmosphere and not at soil level (Romero et al., 1999). Since the dust samples used in this study are ground-collected dust analogues, the proportion of phytoliths within these samples is thus not thought to be substantial. Another hypothesis concerns undetected crystalline minerals such as smectites that also contribute to the Si dissolution. However, the dissolution rate of the smectite montmorillonite has been proven to be comparatively low (Figure II-8).

Table II-9: Hypothetical estimated amounts (%) of different amorphous minerals (phytoliths or allophane for desert dust or various volcanic glasses) within the bulk amorphous portion (%) of aerosols, needed to explain the remaining Si dissolution rate ρ_{Diss} not explained by the crystalline portion (mol Si.$m^{-2}.s^{-1}$) in order to close the Si dissolution budget.

		Artificial rainwater				**Artificial seawater**			
	Amorphous material in bulk aerosol (%)	ρ_{Diss}(theo) amorphous (mol Si. $m^{-2}.s^{-1}$)	Estimated amount of amorphous material ***aX*** **(%)**			ρ_{Diss}(theo) amorphous (mol Si. $m^{-2}.s^{-1}$)	Estimated amount of amorphous material ***aX*** **(%)**		
			Phytolith	Allophane			Phytolith	Allophane	
Bani	35.4	$7.7\ 10^{-13}$	29	38					
Hoggar	57.6	$1.0\ 10^{-12}$	7	46		$3.3\ 10^{-13}$	1	15	
Douz	32.3	$1.4\ 10^{-12}$	14	63		$1.3\ 10^{-12}$	5	57	
Pata	48.3	$1.1\ 10^{-12}$	8	52		$1.0\ 10^{-12}$	5	47	
			Basalt	Andesite*	Rhyolite*		Basalt	Andesite**	Rhyolite**
Eyja	63.7	$4.9\ 10^{-12}$	17	**10**	65	$5.8\ 10^{-12}$	21	**0.3**	4
Chaitén	81.7	$7.8\ 10^{-12}$	27	16	**104**	$1.4\ 10^{-11}$	50	0.6	**10**
Tun Ash	69.2	$1.2\ 10^{-12}$	4	**2**	16	$5.1\ 10^{-11}$	181	**2.3**	36
Tun Glass	100	$1.4\ 10^{-11}$	47	**27**	182	$5.6\ 10^{-11}$	202	**2.5**	40

Note: Each percentage of needed material attempts to explain the whole remaining ρ_{Diss} by itself, but it is most likely that a dissolution of a combination of several amorphous minerals within an aerosol occurs. The hypothetical contribution of volcanic andesitic and rhyolitic glass was calculated at * pH 4.1 for ARW and ** pH 10.6 for ASW, and might thus be overestimated.

The amorphous portion of volcanic ash is most certainly composed of volcanic glass. According to the SiO_2 and alkali metal (K_2O + Na_2O) content of the ash samples (Figure II-2), Chaitén is classified as rhyolite, whereas the other ash samples (Eyja, Tun Ash and Tun Glass) belong to (trachy)-andesites. Less data is available for pH-dependent Si dissolution rates of amorphous volcanic glass compared to crystalline minerals; we thus estimated the hypothetical amounts of andesitic and rhyolitic glass within the bulk amorphous portion (Table II-9) at pH 4.1 and 10.6 (Wolff-Boenisch et al., 2006) for ARW and ASW, respectively, instead of using the equilibrium pH of each aerosol for a given matrix (Table

II-8). Therefore, the estimations in Table II-9 for volcanic ash are possibly overestimated, supposing that the overall shape of pH-dependent dissolution rates for andesite and rhyolite approximates the shape for basaltic glass, with its lowest point around pH 5-7 increasing towards the acidic and basic pH (Figure II-10).

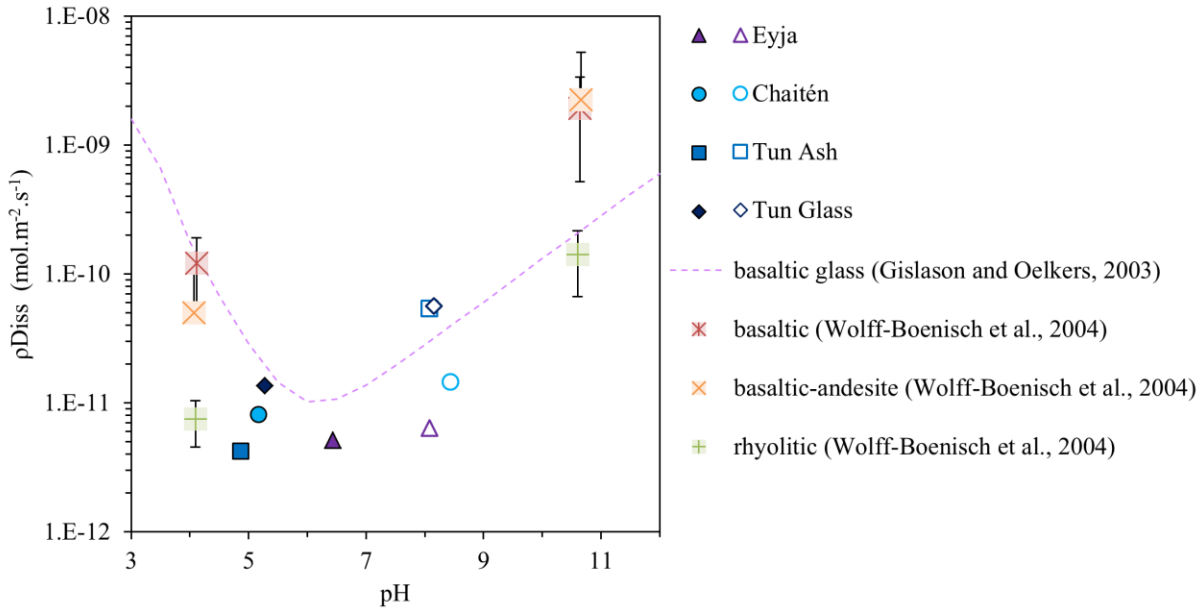

Figure II-10 : Silicon dissolution rate (mol dSi.$m^{-2}.s^{-1}$) normalized by the specific surface area of volcanic ash in artificial rainwater (filled symbols) and artificial seawater (open symbols) as a function of ambient pH at estimated steady state (300 h of contact time, Figure II-7) compared to the pH-dependent dissolution rate of various volcanic glasses from the literature.

Overall, **the addition of amorphous material to the ρ_{Diss} enabled to close the Si dissolution budget for all the aerosols,** besides Chaitén in ARW. Indeed, the remaining 7.8 10^{-12} mol Si.$m^{-2}.s^{-1}$ could not be explained by the dissolution of rhyolitic glass, as 104 % of amorphous rhyolite would be necessary within the remaining 81.7 % amorphous material. It can be noted that the amorphous material found in volcanic ash may also be under the form of silica glass coatings on secondary minerals (Jongmans et al., 1996) that may further influence the dissolution rates. However, **the estimation of the amorphous contribution bore several approximations and suppositions, thus the discussed results need to be used with care.**

In ARW, the highest ash Si dissolution was recorded by the least amorphous Eyja (63.7 %), which was the only volcanic ash sample containing high amounts of clay (montmorillonite) and increasing the pH of ARW, thus possibly increasing the aSi solubility. Eyja is also the only ash that contains clay (10.9 % montmorillonite $Ca_{0.25}(Al_{1.5}Mg_{0.5})\ Si_4O_{10}(OH)_2$), known to have greater solubility at lower pH compared to ASW (Jeandel and Oelkers, 2015; Köhler et al., 2005). But as seen above, clay minerals play only a very limited role in Si dissolution (Figure II-9). The hypothesis of pH increasing aSi dissolution is therefore more likely. In ASW, the 100 % amorphous synthetic Tun Glass took the lead of volcanic ash Si solubility, indicating again the **high solubility potential of aSi at basic pH** in a cation charged matrix such as SW (Morin et al., 2015).

4.2.4 Conclusion on silicon dissolution in artificial rain- and seawater

Silicon dissolution in both ARW and ASW displayed typical dissolution kinetic curves with initial high dissolution rates that decrease over time (Figure II-7). Steady state dissolution was not reached for any aerosol at t48 h of contact in ARW, indicating that the chemical composition of the solutions did not equilibrate with the liquid matrix (Morin et al., 2015). On the other hand, dissolution approximates steady state at t216 h in ASW (Figure II-7b).

Generally, the amount of dSi released by desert dust was remarkably similar between ARW and ASW for the first 48 h, as shown by slopes close to 1 in Figure II-11a (significant linear regression, p-value < 0.05, Table II-10).

However, **the dissolution of the crystalline part was responsible for a higher percentage of the total Si dissolution in ASW (43-100 %) compared to ARW (33-56 %) for all dust samples (Table II-8). Therefore, it seems that the amorphous part of dust particles was more soluble in ARW, explaining that the net difference between matrices remained small**, which is in agreement with preferential allophane dissolution at pH 5 compared to pH 7-10 (Ralston, 2018) but not for phytoliths (Fraysse et al., 2006 and purple curves in Figure II-8).

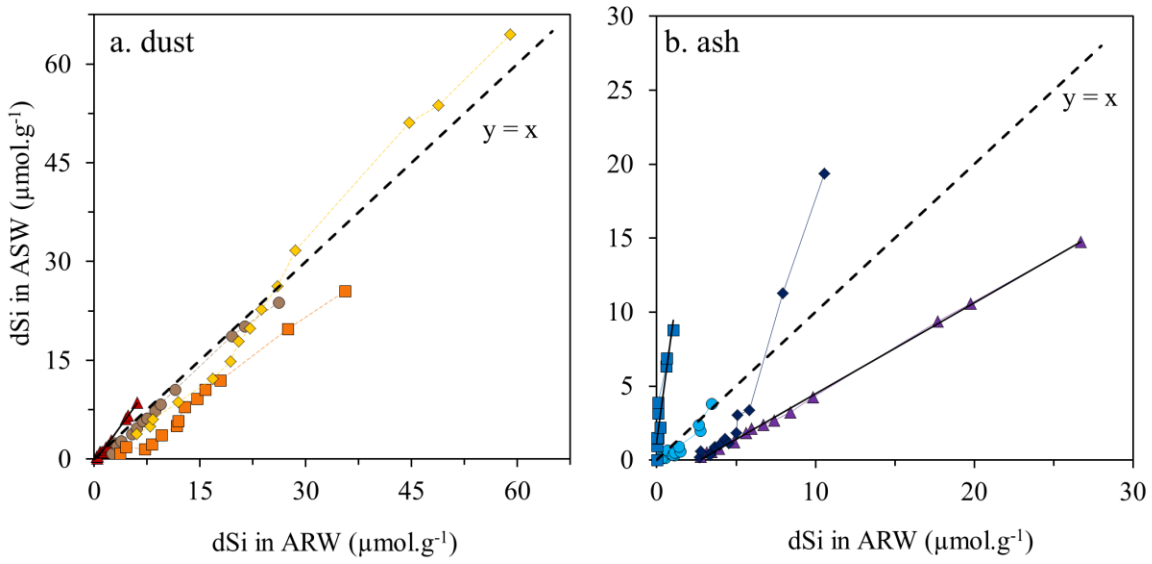

Figure II-11: Dissolved Si (µmol.g^{-1}) in artificial seawater (ASW) plotted as a function of dSi in artificial rainwater (ARW) for (a) desert dust samples and (b) volcanic ash samples for the first 48 h of contact. The dashed line (y=x) represents an equal dSi dissolution in both matrices. Slopes of linear regressions are shown in Table II-10.

In contrast, the release of dSi from volcanic ash was more variable depending on the matrix (Figure II-11b): Tun Ash dissolved much more dSi in ASW (Figure II-11b and ARW/AWW solubility ratio < 0.1 in Table II-6). As seen in §4.2.2, 72 % of the Si dissolution from Tun Ash in ARW was explained by its crystalline part, versus only 6 % in ASW (Table II-8). Therefore, the remaining dSi (28 and 94 %, respectively) should have come from the dissolution of amorphous or badly crystallized Si. The aSi of Tun Ash was therefore much more soluble in ASW. In contrast, Si dissolution from Eyja was mostly explained by the amorphous portion (the crystalline part was responsible for only 9 % in ASW and 6 % in ARW (Table II-8), but Si from Eyja was more soluble in ARW (slope in Figure II-11 of 0.61 ± 0.01 and solubility ratio >1.8 in Table II-6). For its part, Chaitén released similar amounts of dSi to both matrices, indicating that the different ash samples are composed by different types of amorphous material with variable solubilities.

Table II-10: Significant linear regressions (equation, coefficient of determination, p-value < 0.05) of dSi (µmol.g^{-1}) in artificial seawater as a function of dSi in artificial rainwater for the first 48 h of contact. The dissolution of Tun Ash is divided in two separate regressions in addition to the global regression (see text).

	Linear regressions	R^2
Bani	1.47x – 0.59	0.99
Hoggar	0.98x – 1.03	1.00
Douz	0.82x – 3.26	0.98
Pata	1.21x –5.50	0.99
Eyja	0.61x – 1.66	1.00
Chaitén	1.04x – 0. 41	0.90
Tun Ash	7.73x + 1.31	0.82
Tun Glass	2.43x – 8.33	0.93
t5‘-t3.5 h	0.62x – 1.45	0.85
t4.5 h - t48 h	3.12x – 13.70	0.99

The dissolution of Tun Glass was higher in ARW during the first 7 h of contact, but the slope shifts after the initial 3.5 h of contact; Table II-10). This suggests that the dissolution of Si-containing species from Tun Glass was pH and/or matrix dependent, causing a higher but slower $\%Si_{sol}$ in ASW for the completely amorphous sample. The initial dissolution behavior of Tun Glass was very similar to Eyja (Table II-10).

These results showed that Si released by volcanic ash (besides Tun Ash in ARW) is mostly dissolved from aSi, but also that the aSi from different volcanic ashes has highly variable dissolution and that it is difficult to draw generalities. Such variable dissolution behaviors may be explained by the complex chemical interactions within the volcano cloud that defer for each eruption (Jones and Gislason, 2008).

4.3 Dissolved phosphorus

4.3.1 Origin of phosphorus in aerosols

Phosphorus is present in aerosols under organic and inorganic form: for the Saharan soils, it is stated that the inorganic form is predominant (Ridame and Guieu, 2002). Phosphorus is a component of the mineral phase (apatite), and can also be adsorbed onto particle surfaces (Anderson et al., 2010; Kanakidou et al., 2018). In our samples, the P content ranged between 0.04-0.13 % for dust and 0.03-0.18 % for ash (Table II-4), which is consistent with the average crustal concentration, see enrichment factors in Annex IV, Table IV-1) and previous Saharan dust concentration (Guieu et al., 2010; Ridame and Guieu, 2002). The P content of magma can be several orders of magnitude higher than in ash (up to 2-3 % P_2O_5 *i.e.* 0.9-1.3 % P for magma according Mysen et al. (1999) vs. < 0.1-0.2 % P in ash, Olgun et al., (2013)). Volcanic P is assumed to be mainly found in the fine aerosol mode (*i.e.* < 2.5 µm) formed at high temperatures during an eruption (Mahowald et al., 2008), which could have an influence on the $\%DIP_{sol}$, since smaller particles have an increased P solubility (Baker et al., 2006).

4.3.2 DIP dissolution

4.3.2.1 DIP release from desert dust

Phosphorus was more soluble in the ARW compared to the ASW matrix for each of the tested dust samples (Table II-6; Figure II-12b) which is consistent with previous findings of Ridame and Guieu (2002) who used the same Hoggar dust in ultrapure water (UPW) and natural Mediterranean SW. Moreover, their P solubilities in SW are consistent with our ASW data (about 1.3 % in this study versus about 1.5 % in Ridame and Guieu., 2002), whereas we recorded a three times higher $\%DIP_{sol}$ in ARW. This difference may be explained by the acidification of the ultrapure water to pH 4.9 in this study, which was not the case in Ridame and Guieu (2002) and might increase solubility. Moreover, Jacq (2014) reported a $\%DIP_{sol}$ of 3.9 ± 0.8 % for the same Bani sample at the same PC of 250 $mg.L^{-1}$ after 1 h in ARW, which is very consistent with the 3.6 % obtained in this study. After 1 h of contact to ARW, Bani released 0.50 $\mu mol.g^{-1}$, consistent with the data of Jacq (2014) and C. Meriguet (pers. comm), with respectively 0.39 and 0.47 $\mu mol.g^{-1}$ with the same experimental setup.

As no previous DIP dissolution study with Douz is available, we cannot confirm the high early dissolution peak of Douz in ARW (~30 %, Figure II-4; see section §4.3.4.1). Bani and Douz displayed comparatively high solubilities after 48 h in ARW (> 18 %, Figure II-12b).

4.3.2.2 DIP release from volcanic ash

Volcanic ash DIP dissolution is also matrix dependent and higher in ARW at lower pH (Table II-6; Figure II-12b), as previously shown by Jones and Gislason (2008). The most flagrant difference is found in Eyja with maximal $\%DIP_{sol}$ of 12.9 % in ARW and 0.13 % in ASW after 48 h, corresponding to a difference of two orders of magnitude (Table II-6), whereas Tun Ash and Tun Glass (with comparatively low solubility below 2.5 %, Figure II-12b) have similar behavior in both matrices. Consequently, the $\%DIP_{sol}$ from ash was not systematically higher in ARW compared to ASW, as it was the case for desert dust. In comparison, Jones and Gislason (2008) have shown $\%sol_{ARW/ASW}$ ratios of 4-6 for one part of their ash samples, comparable to our Chaitén sample with a ratio of 4.7 after 48 h.

Mahowald et al. (2008) assumed in their model study a 50-100 % solubility from volcanic P in SW, which is largely overestimated according to our experimental data where **DIP solubility did not exceed 15 % in ARW and 6 % in ASW,** which is more comparable to the cited P solubility of 10 % for mineral dust (Mahowald et al., 2008). Besides this model study, several abiotic dissolution experiments showed, however, dissolution values similar to ours: We obtained dissolutions ranging between the detection limit and 0.77 $\mu mol.g^{-1}$ in ASW after 24 h (for Eyja and Tun Ash, respectively), which was consistent with the values for several natural Etna ash samples from Olgun et al. (2013) in Atlantic seawater (0.01-0.97 $\mu mol.g^{-1}$ after 20 h). Moreover, P dissolution of ash in ARW for three out of the four ash samples (0.23 to 0.40 $\mu mol.g^{-1}$ after 4.5-7 h for Tun Glass, Chaitén and Tun Ash) were in the range of those found by Jones and Gislason (2008) in de-ionized water for eight ash samples (0.01-2.18 $\mu mol.g^{-1}$ within 8 h). On the other hand, the 8.31 $\mu mol.g^{-1}$ found after 7 h in ARW for Eyja was about four times greater than the highest dissolution found by these authors for Hekla ash. Jones and Gislason (2008) underlined in their study that their Icelandic Hekla sample differed from other sources by its low Si and high P and Fe content, which was also observed for our Icelandic Eyja sample (Table II-4). Moreover, Eyja is characterized by a SSA which is up to 18 times higher than other ash samples (Table II-2), which might explain its higher solubility. The SSA and $\%DIP_{sol}$ of Eyja compares more to the mineral dust than to other ash samples, indicating again the variability between natural samples and influence on physical parameters on dissolution.

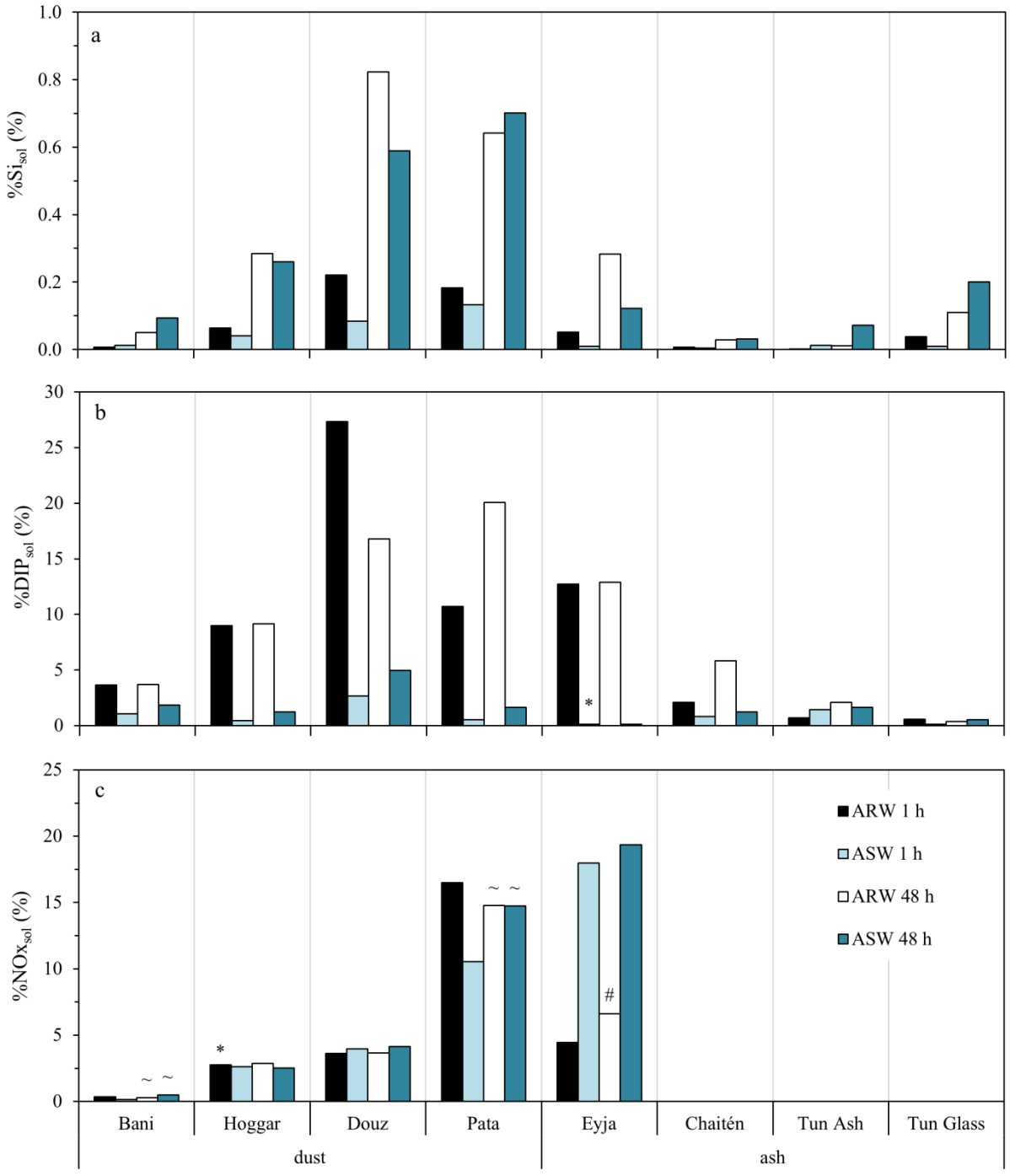

Figure II-12: Solubility (%) of macronutrients in artificial rainwater (ARW, black and white) and seawater (ASW, blue shades) after 1 h and 48 h of contact, for (a) dSi, (b) DIP, (c) NOx. In the case of missing data, solubility was used at 2 h instead of 1 h (*); 24 h instead of 48 h (~); and 30 h instead of 48 h (#). $\%NOx_{sol}$ could not be calculated for the ash samples Chaitén, Tun Ash and Tun Glass, since their %N content was undetectable.

4.3.3 DIP release rates

The initial dissolution rate of 1.6-2.5 µmol.g^{-1}.h^{-1} found by Frogner et al. (2001) for the volcanic ash of Hekla in Iceland after 30 min in natural and artificial seawater was more than five times higher than the 0.1-0.49 µmol.g^{-1}.h^{-1} in ASW found in this study for Tun Glass and Chaitén. Eyja remained under the detection limit at this early stage of contact to ASW and could not be compared.

In ARW, the release of DIP was rapid, as 30-85 % of DIP for dust and 13-85 % for ash was released within the first ten minutes (Table II-11). The P dissolution was slower in ASW: 9-40 % for dust and < DL-14 % for ash was released in the first 10 min. The rapid DIP release in ARW is consistent with the findings of Ridame and Guieu (2002), who found that roughly 75 % of DIP was released within ten minutes.

Thus, in our study, %DIP$_{sol}$ was highly dependent on the matrix, which can be caused by the different pH or cation loading. Higher and faster P solubility was recorded in ARW compared to ASW, which is consistent with literature for desert dust (Anderson et al., 2010; Chen et al., 2006; Ridame and Guieu, 2002).

Table II-11: Percentage of the total released macronutrients that dissolved within 10 minutes, compared to the maximum dissolved nutrient concentration. <DL: undetectable DIP release in ASW or NOx in ARW. When data at t10 min was missing, t5 min (*) or t15 min (**) was used instead for the calculation.

	$\frac{dSi_{10min}}{dSi_{max}} \times 100$		$\frac{DIP_{10min}}{DIP_{max}} \times 100$		$\frac{NOx_{10min}}{NOx_{max}} \times 100$	
	ARW	ASW	ARW	ASW	ARW	ASW
Bani	6.2	2.5	29.7	9.1	<DL	51.7 *
Hoggar	11.1	5.5	73.3	39.9	99.8	63.9
Douz	12.6	5.8	84.6	13.8	81.4 **	81.7
Pata	13.4	4.7	46.6	35.7	8.1	82.2
Eyja	11.8	1.2	84.6	<DL	36.7	93.7
Chaitén	9.7	1.8	13.2	14.2	<DL	54.0 *
Tun Ash	3.1 *	4.1	20.9	9.9	<DL	22.0 *
Tun Glass	26.4	1.4	49.7	2.9	<DL	66.7

4.3.4 DIP adsorption rates

Our dissolution experiments were performed in abiotic conditions, thus the DIP could not have been taken up by primary consumers or heterotrophic bacteria. However, we recorded a decrease in the ambient DIP concentration during some of the experiments, which must therefore be due to **DIP precipitation or adsorption** to particles and/or the walls of

experimental bottles. In order to estimate the magnitude and speed of this process, we calculated mean adsorption rates according to:

$$mean\ adsorption\ rate = \frac{-\Delta DIP_{norm}}{\Delta time} = \frac{-(DIP_{norm}(t_2) - DIP_{norm}(t_1))}{t_2 - t_1} \qquad \text{Equation II-9}$$

where we assume a linear DIP_{norm} decrease between the time t_1 of maximal and t_2 of minimal concentrations. This mean adsorption rate takes into account the PC and the timespan during which the concentration decreases, which will facilitate comparison with literature and spot outliers.

4.3.4.1 DIP adsorption in desert dust

Bani displayed typical DIP adsorption in both ARW and ASW, initiated after respectively 7 and 30 h of contact and lasting until the end of the 48 h and 216 h experiments (Table II-12). The adsorption rate was quite similar in ARW and ASW, and DIP even reached its initial value in ASW (no net release after 96 h). Moreover, Ridame et al. (2003) found in pure water a DIP adsorption rate of 20 $nmol.g^{-1}.h^{-1}$ onto the same Hoggar dust for PC between 5-96 $mg.L^{-1}$ after 1.3 h. This rate could not be confirmed in our study where Hoggar did not adsorb detectable amounts of DIP in any of the two matrices. Further, the South American Pata dust undergoes DIP adsorption only in the ASW matrix (2.7 $nmol.g^{-1}.h^{-1}$ between 72 and 192 h).

Table II-12: DIP adsorption in ARW and ASW for concerned aerosols, expressed as the amount of adsorbed DIP normalized per gram of aerosol, and adsorption rates calculated according to Equation II-9 taking into account the adsorption period (timespan during which the net DIP_{norm} concentration decreased).

	Artificial rainwater			**Artificial seawater**		
	$adsorption_{norm}$ ($\mu mol\ P.g^{-1}$)	period (h)	DIP ads rate ($nmol\ P.g^{-1}.h^{-1}$)	$adsorption_{norm}$ ($\mu mol\ P.g^{-1}$)	period (h)	DIP ads rate ($nmol\ P.g^{-1}.h^{-1}$)
Bani	0.33	41	8.1	0.45	42	10.6
Douz	3.14	2	1570 *	0.16 **	24	6.7
Pata				0.32	120	2.7
Eyja	0.65	44.5	14.6			
Chaitén	0.16	24	6.5			
Tun Glass	0.12	24	4.9			

Note: Only cases where several successive data points display the same trend are presented in this table in order to exclude possible outliers. *Douz adsorption in ARW is probably overestimated despite several high values confirming the value. **Douz adsorption in ASW is shown despite a single value, as the trend is confirmed by literature (Louis et al., 2015).

Further, the highest dissolution and possible re-adsorption in our experiments were observed for Douz in ARW. After 30 minutes, the aerosol released 6.6 µmol.g^{-1}, before stabilizing at 3.5 µmol.g^{-1} after 2.5 h (Figure II-4c). This observed rapid decrease corresponds to an adsorption rate of 1.57 µmol.g^{-1}.h^{-1} (Table II-12), which seems too high to be accurate, according to magnitudes around the nmol.g^{-1}.h^{-1} found in literature (Louis et al., 2015; Ridame et al., 2003). In ASW however, the DIP adsorption onto Douz was lower: 0.16 µmol.g^{-1} within the last 24 h of contact in ASW (Figure II-5c), *i.e.*, an adsorption rate of 6.7 nmol.g^{-1}.h^{-1} between t = 72 and 96 h (Table II-12). Unfortunately, this adsorption rate was calculated between only two data points (because the Douz experiment in ASW run for a shorter period of time) and must thus be considered with caution. However, a similar behavior of rapid DIP release (0.8-3.4 µmol.g^{-1}) within three hours followed by **a P scavenging back onto the particles within few days** has been recorded in a minicosm study (Louis et al., 2015), corresponding to adsorption fluxes of 10-220 nmol.g^{-1}.h^{-1}.

This behavior can be explained by the mineralogical and elementary dust composition: for instance, Douz contains over 30 % of both **calcite and of amorphous material**, and Millero et al. (2001) have shown that DIP adsorbs on either of these structures in natural seawater in presence of Mg^{2+} and Ca^{2+} ions. Moreover, the tested dust samples contain high amounts of '*free iron'* (see Chapter III), indicating **that their amorphous portion contains large amounts of iron (hydr)oxides that might as well be involved in DIP adsorption** (Paris et al., 2011). Louis et al. (2015) also observe a strong correlation between dFe and DIP dissolution and removal behavior, indicating a common adsorption back onto ferric oxide-rich particles. This process will further be discussed in Chapter III for iron dissolution and adsorption.

4.3.4.2 DIP adsorption in volcanic ash

After a DIP release in ARW, Eyja displayed a steady P adsorption (Figure II-4c) with an adsorption rate of 14.6 nmol.g^{-1}.h^{-1} (Table II-12). Jones and Gislason (2008) used an ash sample from the Icelandic Hekla volcano that contains approximately 5 % of interstitial snow which might have an impact on the adsorption of ash leachates to the ash particles (Jones and Gislason, 2008). This sample might therefore be comparable to our Eyja ash sample with known magma-ice interactions during the explosive eruption (Paque et al., 2016), thus explaining why Eyja displays a 2-3 times faster adsorption compared to Chaitén and Tun Glass. In opposition to our results, Jones and Gislason (2008) recorded P adsorption only in their Atlantic Ocean but not Southern Ocean seawater and de-ionized water experiments. The

authors link this increased DIP adsorption to a higher baseline DIP concentration in Atlantic Ocean waters and point out that their high CP (4.2 $g.L^{-1}$ *i.e.*, almost 20 times higher than in our experiment) might encourage DIP adsorption. **Thus, DIP adsorption might be less severe in natural SW**.

Further, Jones and Gislason (2008) explained that andesitic ash particles (containing median SiO_2 between 57-63 %) might scavenge DIP. The feldspar andesine is found under crystalline form in Tun Ash (24.6 %, Table II-3) and under amorphous form in Tun Glass (Maters et al., 2016). Eyja and Chaitén contain the feldspar albite that may be responsible for the adsorption.

The **DIP adsorption could be controlled by the saturation state of amorphous iron (hydr)oxides**, leading to a possible Fe precipitation and P scavenging in the ASW matrix (Jones and Gislason, 2008). In our ash samples, Eyja contains 41.7 % of its Fe under free form, *i.e.*, within (hydr)oxides (Table II-2). Only 0.1 % of the ash sample is under the form of hematite (crystalline iron oxide, Table II-3), indicating that a significant portion of the amorphous 63.7 % of the aerosol might contain amorphous iron (hydr)oxides, probably playing a role in DIP. However, no significant correlation was found between the severity of P adsorption and the free Fe content.

4.4 Dissolved nitrogen

4.4.1 Origin of nitrogen in aerosols

Nitrogen found within desert dust can be organic or inorganic, and dust and ash can liberate oxidized (NO_2^-, NO_3^-) and reduced (NH_4^+) forms of N to pure water and seawater (Jones and Gislason, 2008). Tested desert dust samples contained much more nitrogen (0.09-0.20 % for respectively Pata and Bani) compared to the mostly undetectable N in ash samples (only Eyja with 0.03 % was detectable). Chemical processes occurring during the atmospheric transport can increase the N content and reactivity of aerosols by adding a nitrate coating around carbonate-rich particles (Desboeufs et al., 2001; Krueger et al., 2004). It is possible to mimic these processes by artificially enhancing the nitrate and sulfate content of soil-transformed dust particles by evapocondensation (as described in Desboeufs et al. (2001)), but the samples from our study did not undergo any treatment, which explains their low $\%N_{sol}$ compared to $\%N_{sol}$ of evapocondended dust (Ridame et al., 2014b).

4.4.2 NOx dissolution

4.4.2.1 NOx release from desert dust

Dissolution of NOx from Saharan dust occurred mainly instantaneously in both matrices (99.8 and 81.4 % was released to ARW within the first minutes for Hoggar and Douz; 63.9 and 81.7 % in ASW, Table II-11). No effect of pH or matrix was observed on the NOx dissolution from Douz and Hoggar (Figure II-12): an instantaneous release in ARW and ASW of 4.1 ± 0.3 % and 4.0 ± 0.3 % for Douz and 2.8 ± 0.1 % and 2.3 ± 0.4 % for Hoggar (mean values over the entire experimental contact time). Solely Bani and Pata had higher NOx solubilities in ARW compared to ASW during the first hour of contact ($\%sol_{ARW/ASW}$ of 2.4 and 1.6, respectively, Table II-6), but there was no difference after 24 h of contact.

Dissolution of Bani was low, with a maximum of 0.5 % after 24 h in ASW and below or close to DL in ARW. Using the same Bani sample with a PC of 100 $mg.L^{-1}$, Jacq (2014) also found a NO_3^- dissolution in ARW below detection limit after a contact time of one hour. Chen et al. (2006) record similar N dissolution of natural aerosols from the Gulf of Aqaba in pure water and SW, with major dissolution of NO_3^-, followed by NH_4^+ and traces of NO_2^- in both matrices.

Despite similar N content (~0.18 %), Douz and Bani display very different $\%NOx_{sol,}$ with the N from Douz being over an order of magnitude more soluble than Bani in both matrices (<0.5 and up to 4.7 %, respectively, Figure II-12c). Moreover, the South American Pata dust displayed very high $\%NOx_{sol}$ of up to 20.2 % after 2 h in ARW and 12.9 % after nine days in ASW, well above African dust samples (below 6 % in both matrices). This high dissolution of Pata was confirmed by the study of Paparazzo et al. (2018), who measured a NO_3^- dissolution of airborne Patagonian dust in natural filtered seawater. Using a PC of 50 and 500 $mg.L^{-1}$, the authors obtained a dissolution of 23 $\mu mol.g^{-1}$, which even exceeds the 6.8 $\mu mol.g^{-1}$ of our study. This difference may be explained by the natural instead of artificial matrix.

4.4.2.2 NOx release from volcanic ash

NOx dissolution for all of our tested volcanic ash samples was higher in ASW compared to ARW: Eyja had a higher NOx release in ASW (Table II-6) with a maximum of 4.8 $\mu mol.g^{-1}$ in ASW after 30 min. Other ash samples dissolved detectable (but 7-19 times lower) amounts only in the ASW matrix. These results were constant with abiotic experiments performed in both pure water and seawater in the literature.

Jones and Gislason (2008) measured oxidized and reduced N (NOx and NH_4^+) dissolution in pure water: out of eight tested volcanic ash samples from various geographic regions and eruption styles, only three volcanoes (the Icelandic Hekla, the Colombian Galeras and the Caribbean Montserrat) released significant amounts of NOx (0.3-13.3 µmol.g^{-1} of NO_3^- and 0.4-6.4 µmol.g^{-1} NO_2^- within 8 h for respectively Galeras and Montserrat), comparable to the NOx release of 0.47 µmol.g^{-1} from Eyja after 7 h in ARW. Other ash samples of this study were not a significant source of NOx, comparable to Chaitén, Tun Ash and Tun Glass.

In the SW matrix, Olgun et al. (2013) measured NO_3^-, NO_2^- and NH_4^+ release of 17 Etna ash samples after 20h to Atlantic SW and obtained a higher NO_3^- than NH_4^+ release for most samples (0.082-0.277 µmol NO_3^-.g^{-1}), comparable to the 0.04-0.15 µmol NOx.g^{-1} after 24 h in our ASW matrix for Tun Glass and Tun Ash, respectively. As opposed to the findings of Olgun et al. (2013), Duggen et al. (2007) recorded DIN release to SW mostly under the reduced NH_4^+ form (0.20-1.10 µmol.g^{-1}), and the oxidized forms account for less N release (0.01-0.45 µmol.g^{-1} NO_3^- and < 0.05 µmol.g^{-1} NO_2^-). In our study, we measured NOx without distinction of the oxidized forms and without accounting for the reduced form, but overall the published dissolution of ash in SW compares well to 0.40-0.58 µmol NOx.g^{-1} after 1h and 0.04-0.15 µmol.g^{-1} after 24 h for respectively Tun Glass and Tun Ash but were fivefold lower than Eyja (4.16 and 4.48 µmol.g^{-1} after 1h and 24h), indicating again the unique individual pattern of the Icelandic sample with NOx solubility comparable to desert dust in both ARW and ASW matrices. This finding is consistent with the higher N content of Eyja compared to other ash samples and to the upper crust (N enrichment factor of 5.55, see Annex IV, Table IV-1) and its uncommon mineralogical composition including the clay smectite (increasing its SSA, *e.g.*, Paque et al. (2016)).

5 Conclusion

In this study, we used natural ash and dust analogues of varying source regions: dust from African and South American desert regions and ash from South American and European volcanoes. While the elementary composition of the tested ash samples did not significantly differ from the dust samples for most elements, **the individual mineral and elementary composition of each aerosol sample affected its dissolution behavior**. Tested ash samples were mainly **amorphous** (volcanic glass but also some crystalline feldspar), while desert dust samples were composed by a greater amount of **crystalline minerals such as quartz, clay and feldspar**. The Patagonian dust sample seemed to be influenced by proximate volcanism, as shown by its high albite content (Simonella et al., 2015), whereas the presence of alteration minerals in the Icelandic Eyja ash sample indicates magma-ice interactions (Paque et al., 2016). Therefore, the analysis of a large panel of aerosols from various origins enabled us to **take into consideration the natural variability within and between aerosol types (desert dust and volcanic ash) and their individual nutrient release**.

We performed abiotic dissolution experiments at a constant particle concentration of 250 $mg.L^{-1}$, which is representative in rainwater for dust (Ridame and Guieu, 2002) but possibly underestimated for ash (Cimino and Toscano, 1998) and overestimated for dry deposition of aerosols to seawater supposing a homogenous distribution within the surface mixed layer. The choice of a constant PC independent of aerosol type and deposition mode **enabled direct comparison of macronutrient dissolution from ash vs. dust particles in artificial rain- vs. seawater**. The initial rainwater pH of 4.9 was increased within the first minutes and hours after the contact with calcite-bearing aerosols, while no major variation was observed in the natural buffered seawater. After representative contact times of five minutes to two days in rainwater and nine days in seawater, we were able to calculate normalized dissolution ($\mu mol.g^{-1}$) and fractional solubility percentages (%) of the macronutrients Si, N and P.

The release of dSi depended on the aerosol and their individual caracteristics: some ash samples dissolved more in one or the other matrix, while other samples were not impacted by the pH and ion loading. On the other hand, DIP and NOx release were highly dependent on the matrix: DIP release was higher and faster in ARW, while NOx release was faster in ASW.

The dissolution of **quartz** was one of the main contributors to the Si release for desert dust and represented about 20-50 % of dSi dissolution in rainwater and even 30-100 % in seawater. Moreover, **aluminosilicate** dissolution also played a central role in Si release, as demonstrated by significant positive correlations of Si and Al dissolution in ARW for most tested aerosols. However, the contribution of crystalline aluminosilicates was limited and mainly due to feldspar dissolution, while different clay species released surprisingly low quantities of Si at both representative rain- and seawater pH. Therefore, the amorphous portion of aerosols, which had not been characterized in this study, contained most probably significant amounts **of amorphous aluminosilicates such as allophanes or basaltic glass**.

These non-crystalline minerals are mainly formed by the weathering of volcanic tephra (Ito and Wagai, 2017) and may be responsible for the most important part of Si dissolution in desert dust samples. Indeed, we were able to demonstrate that a lower dissolution of crystalline Si in ASW was balanced out by a higher dissolution of amorphous Si, leading to an overall equivalent Si dissolution of desert dust in both matrices. On the other hand, the Si dissolution from volcanic ash was more heterogeneous. We were not able to explain these differences within the present study which underlines the urgent need to characterize the amorphous composition of ash aerosols to fully constrain their nutrient release, as solubilities are variable from one mineral to another. The mineralogical composition of the tested aerosols being highly variable, it is surprising to obtain solubilities of the same order of magnitude.

Furthermore, DIP was more soluble at rainwater pH and globally more soluble in dust compared to ash. Volcanic P was less soluble than estimates from the literature and lies below 15 % in ARW and 6 % in ASW. We also identified important DIP adsorption for nearly all aerosols in both rain and seawater. This adsorption could be explained by the calcite content of the aerosol (Millero et al., 2001), as calcite-containing aerosols displayed high DIP adsorption rates of 0.015-1.57 µmol $P.g^{-1}.h^{-1}$ in ARW. Phosphorus adsorption may also be correlated to amorphous iron (hydr)oxides (Jones and Gislason, 2008; Millero et al., 2001), underlining once again the importance of the characterization of the amorphous phase to fully understand nutrient release processes.

Dust contains higher amounts of N compared to the mainly undetectable N content in ash. **NOx release from desert dust was pH-independent and mainly instantaneous (within the first ten minutes of contact) while most tested ash samples released significant amounts of NOx only in seawater**. NOx release did not depend only on the N content, as dust samples with similar elementary composition had very variable solubilities. The Patagonian dust sample was highly soluble (20 % after 2 h in ARW and 15 % after 24 h in ASW) compared to African dust from this study and the literature (below 6 % in both matrices). Moreover, the Icelandic ash sample contained clay comparable to desert dust, which might explain its higher N content and solubility.

Overall, we can conclude by underlining that the elementary composition alone was not sufficient to fully explain the variability of macronutrient solubility from aerosols, as specific origin and mineralogy, combined with travel distance and specific surface area are important parameters. For instance, the calcite content influenced rainwater equilibrium pH, possibly increasing Si dissolution from quartz minerals, DIP adsorption (Millero et al., 2001), as well as nitrate coating of aerosols (Desboeufs et al., 2001) during the atmospheric journey.

Other important parameters to fully constrain the impact of natural aerosols such as desert dust and volcanic ash for the phytoplankton community include the release of micronutrients such as iron, manganese and cobalt. Chapter III of this manuscript focuses on the dissolution of trace metals, while the Part B of this manuscript seeks to link representative dust and ash depositions to the Southern Indian Ocean with the ambient phytoplankton response (Chapter V) and the natural variability in nutrient dissolution, respectively (Chapter VI).

III. Dissolution of micronutrients (Fe, Mn, Co) from desert and volcanic aerosols in artificial rain- and seawater

1 Introduction

The trace metal (TM) composition of natural aerosols varies depending on their mineralogy and geographical origin as well as encountered atmospheric aging processes. Globally, it is assumed that mineral dust contains on average 3.5 % of Fe (*e.g.,* Luo et al., 2008), but this content may vary between 2 and 8 % (Lafon et al., 2004; Mahowald et al., 2005). On the other hand, Fe in volcanic ash ranges from 1-11 wt.% according to Olgun et al. (2011), and ash from hot spot volcanoes present a higher Fe content than subduction zone volcanoes (12 and 5 %, respectively). Less focus has been made on other TM that are found in much smaller amounts within aerosols (roughly a few ppm = parts per million = 10^{-4} %).

Trace metals like iron (Fe), manganese (Mn) and copper (Cu) act as micronutrients for phytoplankton, since they play important cellular roles such as operating as co-enzymes in many metabolic processes (Sunda, 2012; Twining and Baines, 2013). Hence, their distribution in the oceanic water column follows nutrient-specific depletion in the euphotic surface layer (Nozaki, 2001) and their concentration may become limiting for phytoplankton growth in the open sea. This has been notably proven for Fe limitations within HNLC areas such as the Southern Ocean (*e.g.*, Blain et al., 2002; Boyd et al., 2000).

Several studies have been focused on Fe release from desert dust and volcanic ash to different matrices such as ultrapure water, artificial rain- and seawater (*e.g.,* Boyd et al., 2010; Mahowald et al., 2009; Olgun et al., 2011), but fewer studies extended the topic on the dissolution of other TM (Gislason and Oelkers, 2003; Hoffmann et al., 2012; Mackey et al., 2015; Mahowald et al., 2018). Thus, this chapter attempts to fill the knowledge gap for the dissolution of a wider range of simultaneously dissolving TM.

During atmospheric transport, aerosols are likely to enter in contact with atmospheric water such as rain droplets that may alter their composition and chemical properties. In this study, we will hence address the dissolution and solubility behavior of TM from four different desert dusts, three volcanic ashes and one synthetic volcanic glass in both rain and seawater, representing the wet and dry deposition modes of aerosols to the ocean surface.

2 Materials and methods

The majority of the parameters that characterize the four desert dust analogues, three natural volcanic ashes and one synthetic volcanic glass have been described in Chapter II, § 2.1 and §2.2. Table III-1 recapitulates the elementary concentration of the elements of interest for this study, and the Fe containing minerals are shown in Table III-2.

Table III-1: Elementary composition (in weight; mean and standard deviation) of the dust and ash samples from this study. [(a)] this study, [(b)] Paris et al. (2011), [(c)] Fu (2018), [(d)] Desboeufs unpublished and [(e)] Ridame (2001). For an extensive composition of the aerosols, see Table II-4.

	Fe (%)	K (%)	Mn (ppm)	Co (ppm)
Bani	3.34 (0.22) [a,b,c]	1.21 (0.08) [a,b,c]	574.08 (75.08) [a,b,c]	32.80 [c]
Hoggar	5.42 (0.40) [a,b,c,e]	1.74 (0.13) [a,b,c,e]	966.34 (207.85) [a,b,c,e]	27.84 (10.88) [a,c]
Douz	2.60 (0.12) [a,c,d]	1.23 (0.10) [a,c,d]	410.57 (22.56) [a,c,d]	11.83 (1.38) [c,d]
Pata	4.55 (0.23) [a]	1.63 [a]	886.65 [a]	12.34 [a]
Eyja	7.51 (0.28) [a]	1.49 [a]	1706.01 [a]	13.71 [a]
Chaitén	1.25 (0.17) [a]	2.49 [a]	470.65 [a]	1.49 [a]
Tun Ash	4.79 (0.25) [a]	1.55 [a]	800.72 [a]	17.30 [a]
Tun Glass	5.33 (0.20) [a]	1.45 [a]	914.04 [a]	23.86 [a]

Table III-2: Aerosol structure (%), Fe containing minerals (%) and Fe pools (%) of dust and ash samples of this study. *data from Paris et al. (2011).

	Structure (%)		Fe containing minerals (%)			Fe pools (%)		
	Cryst.	Amorp.	Clays	Feldspars	(Hydr)oxides	free	struct	± SD
Bani	64.6	35.4	3.5 ill; 7.4 kaol	4.0 mic; 0.9 alb		76.2	23.8	0.4
Hoggar	42.4	57.6	2.8 ill; 3.6 kaol; 2.7 verm; 0.5 paly	4.5 mic; 6.2 alb		51 *	49 *	
Douz	67.7	32.3	13.4 ill; 2.9 kaol; 2.4 paly			61.6	38.4	3.5
Pata	51.7	48.3	20.6 ill; 2.8 mont	18.6 alb		58.7	41.3	3.45
Eyja	36.3	63.7	10.9 mont	23.4 alb	0.1 hema	41.7	58.3	5.92
Chaitén	18.3	81.7		16.5 alb	0.2 magn	4.1	95.9	13.0
Tun Ash	30.8	69.2		24.6 and		11.0	89.0	7.1
Tun Glass	0	100				8.5	91.5	5.9

Note: Cryst = crystalline, amorp = amorphous ; ill = illite, kaol = kaolinite, verm = vermiculite, paly = palygorskite, mont = montmorillonite, mic = microcline, alb = albite, and = andesine, magn = magnetite and hema = hematite ; struct = structural Fe, SD = standard deviation of triplicates.

Mineralogical Fe pools (Table III-2) were obtained by quantifying the Fe oxides with the citrate, bicarbonate, dithionite extraction method (CBD, according to Lafon et al., 2004). The CBD analysis was performed at the LISA laboratory by R. Amar and enabled to calculate the proportion of '*structural Fe'* that is trapped in the crystal lattice of aluminosilicate minerals, in opposition to the '*free Fe'* present in (hydr)oxides (Lafon et al., 2004).

2.1 Chemical analysis

A precise description of the experimental setup of the abiotic dissolution experiments in ARW and ASW can be found in Chapter II, §2.3.1. Briefly, 250 $mg.L^{-1}$ of aerosols were added to ARW and ASW and subsampled over a period of 48 h and 216 h, respectively, using 0.2 µm syringe filters (Acrodisc®) after manual homogenization. Samples for several elements of interest were taken simultaneously for each selected contact time out of the same experimental bottle for each individual aerosol: the release of TM was assessed with spectrometry depending on the matrix (see below). To avoid metal adsorption on the vial walls, samples were acidified (HNO_3 SupraPur® 1 % vol in ARW and 2 % in ASW) and stored in HDPE vials at 5 °C prior to analysis. Prior to aerosol addition, one blank sample was collected in each polycarbonate experimental bottle for each experiment.

The chemical analyses enabled the calculation of **TM dissolution** (dX_{norm}, in $nmol.g^{-1}$; *i.e.,* the concentration of a dissolved element released in ARW or ASW, normalized by the particle concentration and the **TM solubility** ($\%X_{sol}$, in %; *i.e.,* the percentage of the dissolved element regarding the total pool of this element in the aerosol; see Chapter II §2.3.3).

2.1.1 Trace metal analysis in artificial rainwater

The TM concentrations in ARW were measured by atomic emission spectroscopy (ICP-AES, Spectro Arcos at LISA, Paris for Fe, Mn and K) and by inductively coupled plasma mass spectrometry (ICP-MS, 7500cx Agilent, at the Alysés platform, IRD, Bondy for Fe and Co). We considered "experimental detection limits" (DLe) for ICP analysis, defined by the smallest reproducible standard of the day of analysis. This procedure is more restrictive than classical detection limit (DL), and the DLe often lies above the DL (Table III-3).

Table III-3: Experimental detection limits (DLe, nmol.L^{-1}) for ICP-AES and ICP-MS measurements in ARW, and detection limits (DL, pmol.L^{-1}) for SeaFast measurements in ASW. n.a: not analyzed

	Fe	K	Mn	Co
ICP-AES, nM	30.2	43.1	30.7	n.a
ICP-MS, nM	9.0	n.a	n.a	0.8
SeaFast, pM	4.63	n.a	9.16	0.13

2.1.2 Trace metal analysis in artificial seawater

In ASW, the TM analysis was performed with a seaFAST-pico™ coupled to an Element XR sector field inductively coupled plasma mass spectrometer (SF-ICP-MS) at LEMAR, Brest for Fe, Mn, Co, Cu and Ni (Lagerström et al., 2013; Tonnard et al., 2020). SeaFAST detection limits have been calculated according to $mean_{blank}$ + 3x SD_{blank} and 4 mL samples were diluted with TM-poor TONGA reference seawater (0.5 nM Fe) to obtain the needed sample volume of 7.5 mL.

2.2 Data validation

We compared the TM release to the variability amongst the initial ARW and ASW concentrations. Thus, we measured the mean ± standard deviation (SD) of the eight individual experiments at initial time, and took into account only the released concentrations of an element X ($dX - dX_0$) that were greater than this initial variability (SD of dX_0).

Linear regressions were performed using the data analysis tools of Microsoft Excel. Error propagation of means was performed with a CC free calculation tool from the University of British Columbia (Richard Laffers, 2005-2008).

3 Results

3.1 Aerosol composition

There was a notable TM depletion of Chaitén compared to other ash samples, *e.g.,* a factor of 16 for Co compared to Tun Glass and a factor of 6 for Fe compared to Eyja (Table III-1). On the other hand, the elementary composition of dust samples was more similar (with enrichment factors of dust were around 1; *e.g.,* no global difference of the aerosol Fe/Al ratio compared to the continental crust, Annex IV, Table IV-1).

A clear distinction can be made concerning the Fe mineralogy of the two aerosol types (Table III-2), as desert dust samples contained a majority of free Fe (51-76.2 %) *i.e.*, present in (hydr)oxides, whereas the Fe found in volcanic ash was mostly found in aluminosilicates (58.3-95.9 % structural Fe). This difference could not be explained by the aerosol Fe content that remained overall similar despite the different variability described above (2.6-5.4 % and 1.3-7.5 % for dust and ash, respectively).

3.2 Dissolution of micronutrients in artificial rainwater

This section addresses the micronutrients: Fe, Mn and Co that have been analyzed in both ARW and ASW. Further, we will present the dissolution of potassium (K) at the end of this section, as we identified a covariation of Fe and K dissolution in ARW (§4.2.5). Several additional micronutrients (Cd, Cu, Mo, Ni, V and Zn), as well as the lithogenic tracers Mg, Ca and Ti have also been measured (ARW as well as ASW for Cu and Ni) and will be presented in the Annex IV, §4.1.

3.2.1 Iron

An overall much higher Fe dissolution was recorded from volcanic ash compared to desert dust (Figure III-1a). Indeed, the synthetic Tun Glass and the natural Chaitén ash released respectively 1.32 and 0.99 µmol.g^{-1} of Fe after 48 h of contact time, whereas the maximum release of Fe from desert dust after 48 h remained below 0.13 µmol.g^{-1}.

Moreover, the Fe solubility percentages (%Fe_{sol}) for all the tested aerosols in ARW did not exceed 0.5 % (Figure III-1b) and Chaitén and Tun Glass were more than one to two orders of magnitude more soluble compared to desert dust: Chaitén ash reached the maximum %Fe_{sol} of 0.445 % at the end of the experiment, compared to 0.002 to 0.025% (for Hoggar and Douz, respectively, Figure III-1b).

Iron dissolution from the ash samples Chaitén, Tun Ash and Tun Glass followed typical dissolution curves (monotonically increasing); with only Tun Ash reaching a plateau that could indicate dissolution close to steady state (stable around 0.17 µmol.g^{-1} after 7 h corresponding to 0.02 % of $\%Fe_{sol}$). The other three ash samples continued to liberate dFe after 48 h of contact time in ARW. On the contrary, Eyja rapidly released 0.40 µmol.g^{-1} in the first 5 minutes, and then the Fe dissolution decreased steadily until reaching 0.07 µmol.g^{-1} after 3.5 h. After this minimum, dFe increased again until 0.39 µmol.g^{-1} after 48 h without reaching a plateau. This result will be discussed in §4.2.5.

The Fe dissolution behavior of the four tested dust samples was more variable: despite the similar dissolution and solubility for Bani and Douz at t48 h (dFe_{norm} of ~0.13 µmol.g^{-1} and $\%Fe_{sol}$ of ~0.024 %), the dissolution of Douz presented the particularity of a high and rapid dFe release (reaching 0.26 µmol.g^{-1} after 15 minutes), followed by a decrease and successive peaks, before decreasing (0.10 µmol.g^{-1} after 7 h). A similar erratic Fe dissolution was recorded for the other dust samples, but with concentrations close to detection limit that may explain the variability. The lowest Fe dissolution and solubility were recorded for Hoggar (dFe_{norm} = 0.02 µmol.g^{-1} and $\%Fe_{sol}$ = 0.002 % at t48 h). Thus, the hypothesis of analytical issues is preferred over an over-interpretation of these data (a close up of the solubility data is presented in Annex IV, Figure IV-2).

3.2.2 Manganese

Manganese (Mn) dissolution follows clear monotonically increasing dissolution curves in ARW for all eight tested aerosols, with only Douz and Tun Glass reaching steady state after 48 h of contact (Figure III-1c). There was a high variability amongst aerosols: the highest dissolution is observed for Bani and Eyja (over 2.0 µmol.g^{-1} after t48 h) whereas dissolution remained at or below 0.6 µmol.g^{-1} for the other aerosols. A maximal Mn solubility of 23 % was observed for Bani which was more than three times higher than for Eyja (7.3 % after 48 h) and more than six times higher than for other dust samples (Figure III-1d). The lowest solubilities of 0.8 and 0.5 % (t48 h) were associated with Pata and Tun Glass respectively and Tun Ash was close to the detection limit and did not exceed 0.04 %.

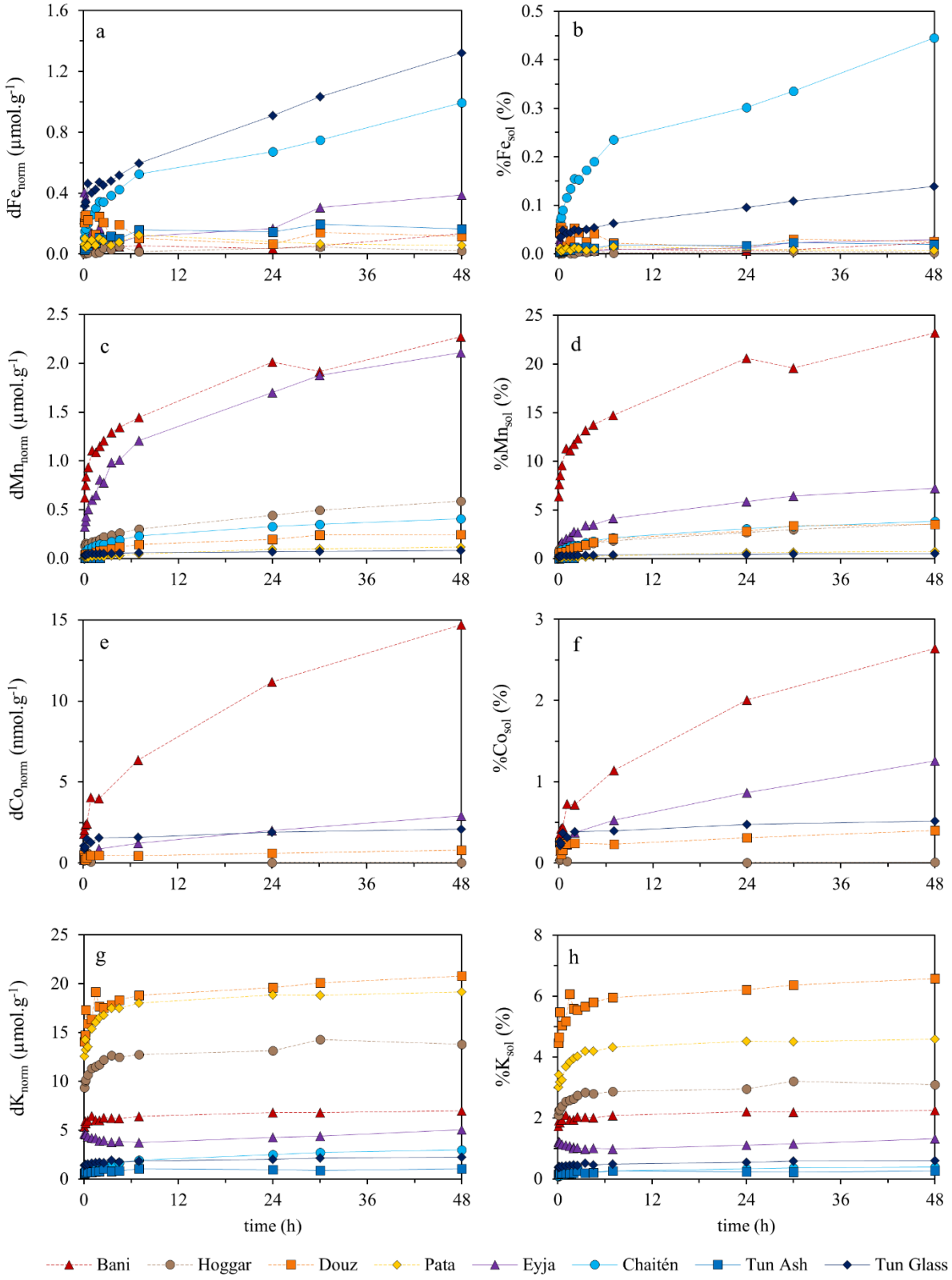

Figure III-1: Dissolution (left panels, in µmol.g-1 for a,c,g and in nmol.g-1 for e) and solubility (%, right panels) of micronutrients in artificial rainwater: dFe (a,b), dMn (c,d), dCo (e,f) and the lithogenic tracer dK (k,l). Warm colors and dashed lines represent desert dust, cold colors and plain lines represent volcano ash.

3.2.3 Cobalt

Bani has by far the highest cobalt (Co) dissolution (up to ~15 nmol.g^{-1} at t48 h, Figure III-1e) and solubility (2.6 % at t48 h, Figure III-1f). Eyja and Tun Glass dissolved less than 3 nmol.g^{-1} and Douz and Hoggar less than 1 nmol.g^{-1} over the duration of the experiment (Figure III-1e) corresponding to a solubility lower than ~1 %. Finally, Chaitén, Pata and Tun Ash did not release measurable amounts of Co.

3.2.4 Potassium

Potassium (K) release occurred mainly in the first ten minutes of contact. Desert dust released more K than volcanic ash: the dissolution range varied between 7.0-20.8 µmol.g^{-1} for dust (Bani and Douz) and 1.1-5.0 µmol.g^{-1} for ash (Tun Ash and Eyja) after t48 h (Figure III-1g). This difference can be explained by the higher $\%K_{sol}$ of the dust samples, ranging from 2.3-6.6 % (Bani and Douz) compared to the 0.3-1.3 % from ash samples (Figure III-1h). Potassium dissolution was monotonously increasing for all aerosols except for Eyja ash, where the solubility kinetic followed an inversed bell shape with an initial $\%K_{sol}$ of 1.2 %, followed by a rapid decrease (minimal with 1.0 % after 2 h) and a slow increase of $\%K_{sol}$, reaching 1.3 % after 48 h. This result will be discussed in §4.2.5.

3.3 Dissolution of micronutrients in artificial seawater

3.3.1 Iron

The Fe release to ASW remained mainly below 120 nmol.g^{-1}, besides an early dissolution peak of 190 nmol.g^{-1} for Hoggar after 30 min (Figure III-2a). This peak is sudden but seems to be confirmed by the following data point of 120 nmol.g^{-1} after one hour. Moreover, this release corresponds to a solubility of 0.02 % which remains coherent compared to the other samples ($\leq$ 0.02 and $<$ 0.04 % for dust and ash, during the 216 h contact time). Due to dFe fluctuations within dissolution kinetics (*e.g.*, ΔdFe of 0.7-1.4 nmol.L^{-1}-h^{-1} around t48 h for Bani and Chaitén), there was no distinct trend for Fe release between dust and ash. We recorded a wide dissolution range from dust of 37-114 nmol.g^{-1} (for Douz and Bani, respectively after t48 h), with no Fe release from Pata before t96 h, compared to the slightly narrower dissolution range from ash of 9.3-84.0 nmol.g^{-1} (for Tun Ash and Chaitén).

The highest solubility in ASW was observed for Chaitén (peak value of 0.038 % at t48 h, Figure III-2b). Bani and Hoggar both reached 0.019 %, after 48 and 216 h (Bani) and 30 min (Hoggar). The Fe from other aerosols displayed solubilities below 0.01 % to ASW during the entire experiment.

3.3.2 Manganese

Manganese release in ASW was rather high compared to other micronutrients and its dissolution mostly followed typical curves increasing with time and tending towards a plateau of steady state (Figure III-2c). Desert dust released more Mn (0.81-1.57 µmol.g^{-1} after 48 h for Pata and Bani, respectively) compared to volcanic ash (below ~0.12 µmol.g^{-1}). Only Eyja was comparable to dust samples (0.75 µmol.g^{-1} at t48 h). Manganese from dust was also 2-34 times more soluble compared to Mn within ash: after 48 h of contact, the %Mn_{sol} was 5.4-16.9 % for dust and 0.5-2.6 % for ash (Figure III-2d). The Mn release from Pata occurred only after an initial lag time of one hour and Tun Ash did not release detectable Mn to ASW during the 216 h.

Noteworthy, the Mn release from Bani was initially high then decreased (until 1.2 µmol.g^{-1} at t7 h) before reaching a second peak at t48 h. The same trend can be observed for the dissolution of other TM in the ASW after the addition of Bani dust.

3.3.3 Cobalt

The Co release was overall regular (steadily increasing with time) for most of the aerosols. The highest dissolution was recorded for Douz (9.4 nmol.g^{-1} at t48 h, Figure III-2e). A general trend indicated a greater Co release from dust compared to ash, besides Pata releasing relatively low amounts of Co (maximum of 2.1 nmol.g^{-1} at t216 h comparable to Tun Glass and Bani). Moreover, the Co release occurred only after an initial lag time of 4.5 h and 24 h for Pata and Chaitén, respectively, whereas Tun Ash released no Co to ASW during the 216 h experiment. Cobalt from Douz was the most soluble, reaching 4.7 % of solubility after 48 h, whereas other aerosols remained below 2 % (Figure III-2f). Noteworthy, Chaitén displayed a high Co solubility variation (including a peak solubility of 1.3 % at t30 h).

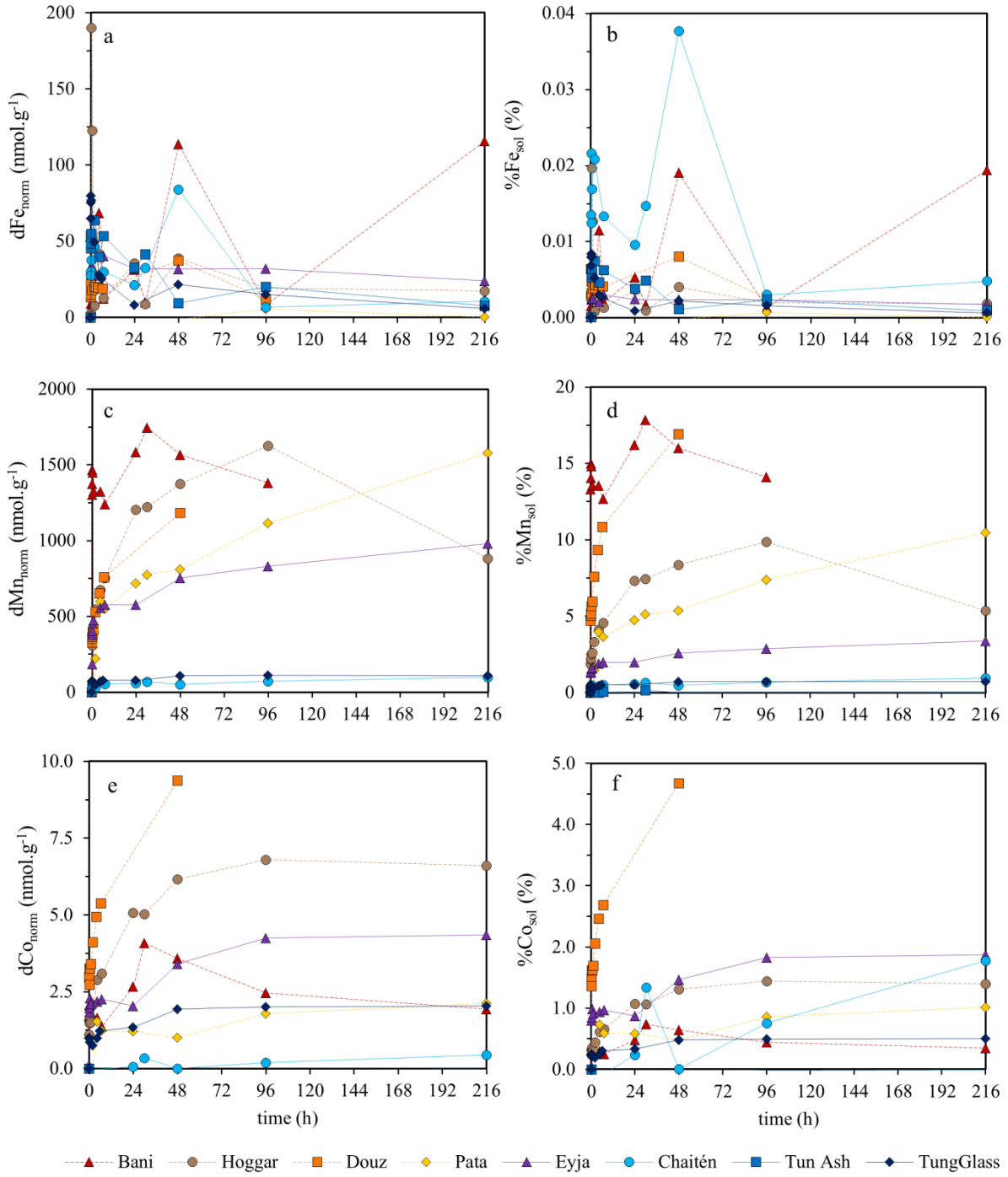

Figure III-2: Dissolution (left panels, in nmol.g^{-1}) and solubility (%, right panels) of micronutrients in artificial seawater: dFe (a,b), dMn (c,d) and dCo (e,f). Warm colors and dashed lines represent desert dust, cold colors and plain lines represent volcano ash.

4 Discussion

4.1 Aerosol composition

4.1.1 Elementary composition

Aluminum (Al) is often used as a crustal marker element in aerosols, which enabled us to compare element-to-Al ratios of our aerosols to published data, as reviewed by Scheuvens et al. (2013) for North African sediment and dust samples. Overall, Hoggar contains the highest Al content (7.91 %, Table II-4), representative of southern Algerian samples (Scheuvens et al., 2013). Elementary ratios from our Hoggar and Bani samples are comparable to other published data from respectively South Algerian and Western Nigerien dust: some ratios such as K/Al and Fe/Al are well conserved for a given source region whilst other ratios seem to vary between our samples and the published data: Hoggar's Fe/Al ratio of 0.69 is 30 % higher compared to the published data of 0.50-0.54 (Castillo et al., 2008; Moreno et al., 2006). Despite these cited differences, the samples used in this study remain characteristic for their respective source regions (Sahara and Sahel).

The composition of volcanic ash depends on the eruption type. Fe in ash ranges from 1-11 wt.% according to Olgun et al. (2011) with ash from hot spot volcanoes presenting higher Fe content than subduction zone volcanoes. This observation is consistent with our data, where the South American subduction zone samples contain 1.25 to 5.33 % Fe (Table III-1), which is lower than the Icelandic ash containing 7.51 % Fe.

4.1.2 Iron content related to mineralogical composition

As seen in the detailed description of the mineralogical and elementary aerosol composition in Chapter II, the aerosols contain no or only very limited amounts of crystalline iron oxides such as hematite and magnetite (0.1 % Fe_2O_3 within Eyja and 0.2 % Fe_3O_4 within Chaitén, Table III-2). Thus, the 2.60-5.42 % and 1.25-7.51 % of Fe found in dust and ash, respectively (Table III-1) have another origin. The pyroxene augite and the clay vermiculite display Fe as part of their crystalline structure and chemical formula (Mineral Data Publishing database, version 1.2, ©2001), but these minerals contribute only to 3.6 % of Tun Ash and 2.7 % of Hoggar, respectively and can thus not explain the Fe content.

Several other primary and secondary minerals may contain Fe under the form of possible traces (Table III-2), and the analysis of Fe pools enabled to identify the type of minerals that contain Fe, which can be grouped in two categories: ***'structural iron'***, namely contained in

the crystal lattice of aluminosilicate minerals (Lafon et al., 2004; Paris et al., 2011); and ***'free iron'*** within hydroxides (goethite, gibbsite) or oxides (such as hematite, magnetite), as well as the amorphous ferrihydrite.

The desert dust from this study contained mainly free Fe (51-76.2 %, Table III-2). **As no crystalline (hydr)oxides have been detected, the amorphous portion (35.4-57.6 % of the total mass of the dust samples, Table III-2) must contain badly crystallized (hydr)oxides that remain undetected by XRD.** For instance, Paris et al. (2011) detected goethite and hematite in Bani and Hoggar with the diffuse reflectance method, but this analysis is only qualitative and did not enable quantification of the minerals. Moreover, **amorphous free iron (hydr)oxide impurities** have been observed on crystalline species such as clay (Mermut and Cano, 2001) and feldspar (Journet et al., 2008). Despite the fact that they remained undetected by XRD, the presence of (hydr)oxides could be assumed through a visual comparison of the sample colors: the orange and red shades of Bani and Douz are a good indicator for the presence of respectively goethite and hematite in the samples.Thus, the (hydr)oxide content in our study is most definitely underestimated, when compared to Paris et al. (2011).

On the other hand, the Fe from volcanic ash from this study is mainly structural (58.3-95.9 %, Table III-2), *e.g.*, contained in aluminosilicate minerals. As seen in Chapter II, aluminosilicates may be crystalline (clay and feldspar) and/or amorphous (allophanes). Further, it has been demonstrated that volcanic ash is mainly composed by amorphous volcanic glass particles (Simonella et al., 2015) on which are adsorbed soluble acid salts (Frogner et al., 2001). An important surface Fe-enrichment has been observed for Chaitén ash (Durant et al., 2012) and will be addressed in §4.2.4, while other ash samples from the literature are better known to have Fe-depleted aerosol surfaces (Ayris and Delmelle, 2012).

4.1.3 Iron content of pure minerals

Obviously, Fe-(hydr)oxides contain a higher amount of Fe than aluminosilicates (57.5-77.4 % compared to 0.25-7.68 % for different clay species and 0.13-0.54 % for feldspars, see literature review in Table III-4), even if some clay species contain more Fe (*e.g.* 23.0 % for the smectite nontronite, according to Journet et al. (2008)) but that have not been detected in our aerosols. Mean Fe in pure minerals displays great variability (variation coefficients up to 56 %, cf. Table III-4) due to the analysis of multiple kaolinite and montmorillonite samples within one study (Mermut and Cano, 2001), and of two different feldspars (Journet et al., 2008).

Table III-4: Iron content (%Fe) of pure minerals according to literature.

Fe pool	**Structural Fe**						**Free Fe**			
Group	Clay					Feldspar	(Hydr)oxide			
Species	Illite	Kaol	Verm	Paly	Mont		Magn	Hema	Goet	Ref
Fe %	3.38-4.65		7.68		2.55	0.13-0.54	77.44	57.5	62.87	1,2
		0.25-0.80		2.62	0.84-3.06					3
	3.05	0.46					72.3	69.9	62.8	4
Mean Fe%	**3.69 ±0.84**	**0.50 ±0.28**	**7.68**	**2.62 ±0.05**	**1.78 ±0.99**	**0.34 ±0.29**	**74.85 ±3.61**	**64.13 ±6.24**	**62.85 ±0.02**	

Note: Kaol = kaolinite, verm = vermiculite, paly = palygorskite, mont = montmorillonite, magn = magnetite, hema = hematite, goet = goethite. (1) Journet et al. (2008a), (2) Journet (2008b), (3) Mermut and Cano (2001), (4) Marcotte et al. (2020). Values in bold were used for estimations of the contribution of pure minerals to the Fe bulk content of our aerosols in Figure III-3.

Strong Fe-O lattice bonds maintain Fe within the Fe-(hydr)oxide minerals, whereas Fe replaces structural elements of the crystalline network (Al, Si) of aluminosilicates (Malden and Meads, 1967) in which the Fe bound is weaker than the Fe-O bonds (Deer et al., 1992). The presence of the Fe-containing smectite within the Hoggar sample was confirmed by Ridame and Guieu (2002), and it can be assumed that this clay is present even if not detected in our Hoggar sample, due to analytical issues of the quantitative XRD method used in this study (see Chapter II, discussion §4.1.1 for details).

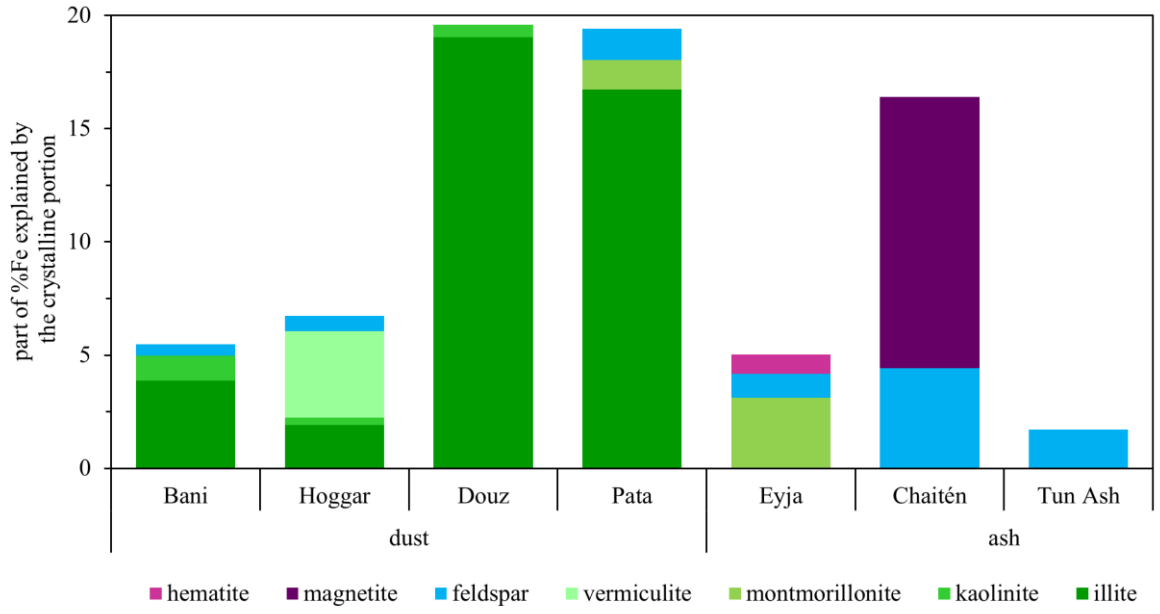

Figure III-3: Contribution of the detected crystalline portion to the iron content of aerosols (Fe%). Tun Glass is 100% amorphous and not included in this figure. Clay minerals are shown in green. Badly crystallized (hydr)oxides and smectite (clay) might be underestimated by XRD.

Based on the quantitative mineralogical composition of our seven aerosols (Table II-3; Tun Glass is 100 % amorphous) and on the mean Fe content in pure minerals (Table III-4), we estimated the contribution of each pure mineral to the Fe bulk content in aerosols. As the contribution of the crystalline structure was relatively low in our ash samples (19-37 % for natural samples and 0 % for the synthetic amorphous Tun Glass; Table III-2), this explains the low contribution of crystalline Fe to the total Fe content (Figure III-3): from ≤ 5.0 % in Eyja and Tun Ash to ~16 % in Chaitén, due to the presence of magnetite. In the desert dust, crystalline minerals explain an overall greater proportion (from 5 to 20 %) of the total Fe content in aerosols.

Clay minerals (different shades of green in Figure III-3) represent the major contribution to the crystalline Fe present in desert dust (~90-100 % of the crystalline %Fe; the rest of the crystalline Fe is provided by feldspar), whereas their contribution to total %Fe within ash was negligible (besides montmorillonite contributing to ~60 % of the crystalline %Fe for Eyja).

However, only a minor portion of the total Fe can be explained by the detected crystalline portion (5 to 20 % for dust and 2 to 16 % for ash, Figure III-3). **The remaining Fe (80-95 % for dust and 84-100 % for ash) is thus associated with undetected minerals that may be either (i) amorphous ferrihydrite (Bostick, 2018) and/or (ii) badly crystallized (hydr)oxides (Hettiarachchi et al., 2019) and/or (iii) structural Fe from smectites (Journet et al., 2008) which have all not been detected in our study.**

4.2 Dissolved iron from aerosols

4.2.1 Iron dissolution and solubility

4.2.1.1 Dissolution in artificial rainwater

Volcanic ash dissolved on average more Fe in ARW than desert dust. Leaching experiments with volcanic ash from the literature display dissolution ranging from below 1 to more than 400 nmol $Fe.g^{-1}$ in deionized water (review from Duggen et al., (2010) and references therein) which is in good agreement with our results (71-403 $nmol.g^{-1}$ after one hour in ARW). Moreover, Eyja had a unique release behavior that will be assessed in §4.2.5.

Iron dissolution from desert dust in the literature is mostly expressed as solubility (*i.e.* as the dissolved portion of the bulk Fe content of the aerosol). Paris et al., (2011) displayed $\%Fe_{sol}$ for four dust samples ranging from 0.0025±0.0005 % to 0.04±0.01 % after 1 h of contact time at initial pH 4.7. The authors used the same Hoggar and Bani samples as in our study and

found an equal solubility for Hoggar but four times higher for Bani (0.01±0.00 % and 0.04±0.01 %). This difference might be explained by their lower PC of 15 $mg.L^{-1}$ compared to our 250 $mg.L^{-1}$. Indeed, an increased aerosol loading has been shown to decrease Fe solubility (Guieu and Thomas, 1996). Several authors displayed higher $\%Fe_{sol}$ for dust ranging between 0.03-1.6 % (Desboeufs et al., 2001, 1999; Bonnet et Guieu, 2004; Jacq, 2014; Mahowald et al., 2009 and references therein), but lower solubilities are also found (0.001-0.02 % for PC of 5-400 $mg.L^{-1}$, Guieu and Thomas, 1996).

Moreover, **atmospheric chemical processing may increase aerosol Fe solubility**, as $\%Fe_{sol}$ from 1.4 to 54 % were observed during several oceanic cruise observations, with a median Saharan $\%Fe_{sol}$ of 1.7 % (Baker et al., 2006). **Organic complexation** (*e.g.* the presence of oxalate in rainwater) also enhanced $\%Fe_{sol}$ of dust (Paris et al., 2011). Since our dust samples have not been exposed to such atmospheric processes, the absence of Fe6binding ligands could explain the lower solubility. Except for Chaitén and the synthetic Tun Glass, the Fe solubility remained below 0.06 % during the 48 h of contact time in ARW.

4.2.1.2 Dissolution in artificial seawater

Due to the rather high variability in Fe release amongst aerosols, no clear differentiation could be made between dust and ash in ASW. With a similar experimental setup but using natural SW amended with ligands and a ten times higher PC than us, Olgun et al. (2011) found a lower Fe dissolution from a Cape Verde loess sample compared to different ash samples. The authors found a dissolution of 240 nmol $dFe.g^{-1}$ after one hour contact time in natural SW for Chaitén ash originating from the same eruption as our sample, which was six times higher than in our ASW experiment (40 nmol $dFe.g^{-1}$). **This difference can be explained by the presence of organic ligands in natural SW that were absent in our ASW; this aspect will be one of the main features discussed in <u>Chapter VI</u>.**

4.2.1.3 Iron release in artificial rain- versus seawater

Besides Tun Glass and Chaitén, releasing high amounts of Fe to ARW, the Fe solubility of aerosols remained low in both matrices, below 0.06 % in ARW and below 0.04 % in ASW. Thus, we confirm the **global trend of a higher Fe solubility in ARW compared to ASW** previously demonstrated in the literature (Sholkovitz et al., 2012, and references therein).

4.2.2 Contribution of crystalline minerals to iron release

Like for the Si dissolution addressed in Chapter II, we sought to determine the mineralogical origin explaining the Fe release. Less data on pure mineral dissolution rates is available for iron in the literature compared to Si release. We will base our calculations on the findings of Journet et al. (2008), who published Fe content and solubility for various **clay** species (amongst which illite, kaolinite and montmorillonite), **feldspar** (oligoclase and orthoclase) and **iron (hydr)oxides** (goethite, hematite and magnetite). In this section, we will compare the solubilities of various minerals of interest composing the aerosols.

4.2.2.1 Mineral iron solubility in rainwater

In order to assess the role of individual minerals in aerosol Fe release, we needed to determine their solubility at the representative pH. The large uncertainties amongst literature studies (Table III-5) and the unavailability of $\%Fe_{sol}$ at pH 4.7 for some minerals complicate further calculations for the relative contribution of the crystalline portion of aerosols to Fe release in rainwater. Moreover, the literature on pure mineral solubility at pH_{SW} (~8.1) is even more limited, thus we limit the following calculations to rainwater pH only. When data was available, $\%Fe_{sol}$ was chosen at the representative pH_{ARW} (4.3-4.7).

For the clay montmorillonite and the feldspar group, no representative $\%Fe_{sol}$(ARW) was available. We thus used the $\%Fe_{sol}$(pH 2.0) from literature (Journet et al., 2008, see Table III-5). This approach most certainly overestimates the solubility of the concerned minerals, as it is proven that Fe solubility decreases with increasing pH (*e.g.* Desboeufs et al. (1999) and Table III-5).

The general trends presented in Table III-5 can be summarized as (i) a general decrease of the Fe solubility from a pure mineral with increasing pH, (ii) a higher Fe solubility of structural Fe compared to free Fe, and (iii) a high variability between literature studies (partially due to the different experimental setup of flow-through compared to batch). In the following calculations, we used the calculated mean value of best available Fe solubilities and underline that more research on the Fe solubility of pure minerals at representative pH is needed.

Table III-5: Iron solubility ($\%Fe_{sol}$) of pure minerals according to literature at different pH values. The best available solubility data (underlined values) were used to calculate the **estimated $\%Fe_{sol}$(ARW)** for each mineral **(mean ± SD, lowest row, in bold)**. If available, mean $\%Fe_{sol}$ at pH ~4.7 was used; otherwise, mean $\%Fe_{sol}$ at pH 1.7-2.0 was used. kaol = kaolinite, verm = vermiculite, mont = montmorillonite, magn = magnetite, hema = hematite, goet = goethite.

Fe pool	**Structural iron**					**Free iron**			
Group	Clays				Feldspars	(Hydr)oxides			
Species	Illite	Kaol.	Verm.	Mont.		Magn.	Hema.	Goet.	Ref
Mean Fe% (pure minerals)	3.69 ±0.84	0.50 ±0.28	7.68	1.78 ±0.99	0.34 ±0.29	74.85 ±3.61	64.13 ±6.24	62.85 ±0.02	a
$\%Fe_{sol}$	0.95-1.39	4.26±0.4	3.0±0.4	2.6±0.4	0.76-5.25	0.003	0.010	0.005	b,c
pH			4.0				0.021	0.030	d
1.7-2.0	7.1	9.5				0.67	0.79	0.80	e
$\%Fe_{sol}$			0.17				0.006	0.003	d
pH	1.0	1.6				0.11	0.04	0.13	e
4.3-4.7	0.17						0.0006	0.0006	f
Estimated **$\%Fe_{sol}$ (ARW)**	**0.59 ±0.59**	**1.6**	**0.17**	**2.6±0.4**	**3.0±3.2**	**0.11**	**0.016 ±0.021**	**0.04 ±0.07**	

Note: Experimental conditions (batch vs. flow-through reactor) differ between the studies: [(a)] Table III-4; [(b)] Journet et al. (2008a) and [(c)] Journet (2008b): at an initial pH of 2.0 after 1 h of contact time at a PC of 40 $mg.L^{-1}$; [(d)] Sofikitis (2004): at pH 2.0 and 4.7 after 1 h at a flow rate of 20 $mL.min^{-1}$; [(e)] Marcotte et al. (2020) for the size fraction 10-25 µm at pH 1.7 and 4.3 after 2 h at a flow rate of 9 $L.min^{-1}$; [(f)] Paris et al. (2011): at pH 4.7 after 1 h at a PC of 15 $mg.L^{-1}$.

4.2.2.2 Contribution of crystalline minerals to aerosol Fe dissolution

The theoretical contribution of crystalline minerals to the global iron solubility of aerosols was calculated as follows according to the calculations detailed above (Table III-5). Similar to the calculations of the contribution of different crystalline minerals to the dissolution of Si (Chapter II, §4.2.2, Equation II-6), we based our calculations on the formula from Paris et al. (2011):

$$\%Fe_{sol}(\text{theoretical crystalline}) = \sum(\%Fe_X \times \%Fe_{sol}.X) \qquad \text{Equation III-1}$$

where $\%Fe_X$ represents the percentage of Fe within the Fe-bearing mineral X and $\%Fe_{sol}.X$ is the theoretical Fe solubility of the mineral X. The calculations of Table III-5 include several approximations and thus need to be used with caution. They are, however, our best estimation to establish the theoretical contribution of pure minerals to the Fe solubility, as expressed in Figure III-4 and Table III-6.

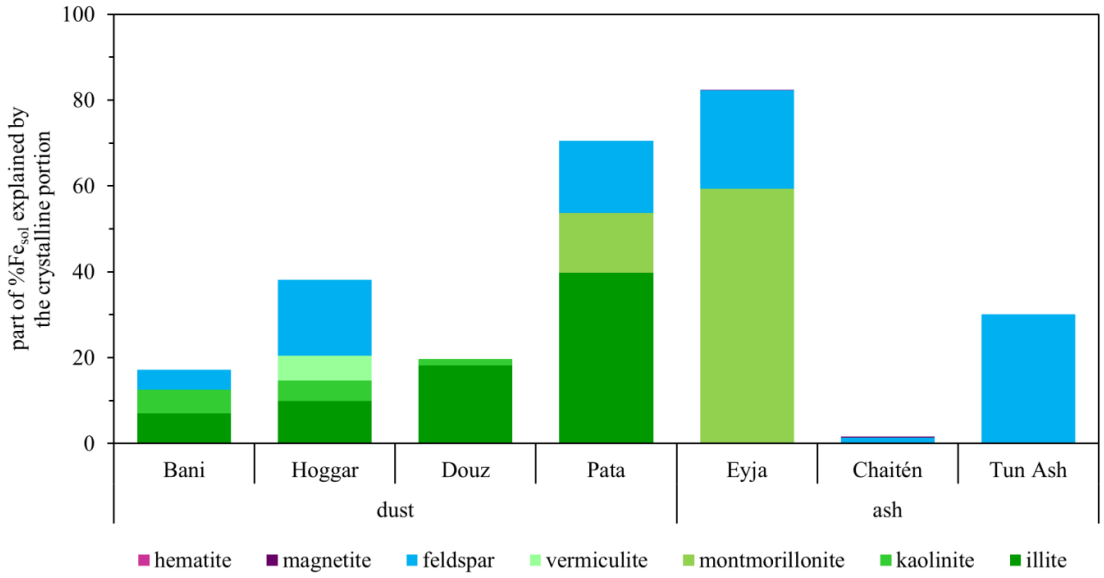

Figure III-4: Contribution of the crystalline portion of aerosols to the total iron solubility (%Fe_{sol}) of aerosols after 1 h in ARW according to Equation III-1. Clay minerals are shown in green. Tun Glass is 100% amorphous and not included in this figure.

According to these calculations, crystalline minerals contribute to at least 17-70 % of %Fe_{sol} from dust (Figure III-4, Table III-6). Like for the bulk Fe% content within the aerosol (Figure III-3), clay minerals are also the main contributor to the %Fe_{sol} in desert dust explained by the crystalline portion (54-100 % of the crystalline %Fe_{sol}; the rest of the crystalline %Fe_{sol} is provided by feldspar). Thus, the crystalline portion identified in this study explained 16-72 % of the total %Fe_{sol} of dust in ARW (Table III-6). This contribution is 1.3-6 times less compared to the 95-96 % estimated by the literature for clay alone (Journet et al., 2008; Paris et al., 2011) at pH 2.0 and 4.7, respectively. **This difference can be caused by the analytical issues to detect and properly quantify clay species from the smectite group** (*i.e.*, montmorillonite, nontronite, beidellite) with the used XRD method. Thus, we cannot exclude their presence within the aerosols, and their Fe solubility was therefore not included in these measurements but it could contribute to the global %Fe_{sol}.

On the other hand, the contribution of the crystalline portion from volcanic ash to the %Fe_{sol} was more heterogenous and varied from 1.6 to 85 % (excluding the amorphous Tun Glass). Finally, it should be underlined that these percentages are most probably overestimated, since the Fe solubility is expected to be higher at pH 2 compared to pH 4.7. The amorphous portion of the aerosols plays therefore an important role in the Fe release, above all for volcanic ash.

Table III-6: Theoretical contribution (%) of pure crystalline minerals to (A) the bulk aerosol iron content and (B) iron solubility compared to the total %Fe and $\%Fe_{sol}$(ARW-1h) measured in this study (gray highlighted). The theoretical crystalline $\%Fe_{sol}$ was calculated at pH 4.7 when literature data was available, or else at pH ~2. Shown are the mean values ± propagated standard errors.

	(A) Fe content			(B) Fe solubility	
	%Fe from this study Table III 1	Theoretical crystalline %Fe	Part of %Fe explained by crystalline	%Fesol 1h-ARW (experimental) 100 %	$\%Fe_{sol}$ explained by crystalline (pH 4.7 or 2)
Bani	3.34±0.22	0.18±0.04	5.5±1.2	0.011±0.004	16.4±6.0
Hoggar	5.42±0.40	0.36±0.04	6.7±0.9	0.006±0.002	38.3±12.8
Douz	2.60±0.12	0.51±0.11	19.6±4.4	0.016±0.000	19.4
Pata	4.55±0.23	0.89±0.18	19.4±4.1	0.011±0.004	71.8±26.1
Eyja	7.51±0.28	0.38±0.13	5.0±1.7	0.010±0.000	85.0
Chaitén	1.25±0.17	0.20±0.05	16.4±4.5	0.116±0.016	1.6±0.2
Tun Ash	4.79±0.25	0.08±0.07	1.7±1.5	0.008±0.001	31.3±3.9
Tun Glass	5.33±0.20	0.0	0.0	0.042±0.002	0.0

Despite a comparatively high proportion of crystalline Fe within Chaitén ash (16.40 % of the total Fe is found in the crystalline portion, of which 12.0 % magnetite and 4.4 % feldspar, Figure III-3), only 1.6±0.2 % of the measured Chaitén $\%Fe_{sol}$ could be explained by the dissolution of crystalline minerals (Table III-6). A possible explanation could be the Fe-rich amorphous coating of the Chaitén sample, which will be further assessed in §4.2.4.

Only Eyja had an important part (85%) of its $\%Fe_{sol}$ explained by aluminosilicate dissolution. It should be noted that these calculations did not consider **the ASW pH or the pH variation of the ARW matrix after the aerosol addition**, due to the scarce literature or data for iron solubility at pH ranging from 4.7 to 8.2 (important for our experiments in unbuffered ARW and ASW). Indeed, as addressed in Chapter II, §3.2, the release of $CaCO_3$ by some aerosols influenced the pH of the unbuffered ARW matrix, increasing the pH during the dissolution experiments of up to 2.63 units, reaching equilibrium pH values of 4.87 to 7.48. In the following calculations of Fe solubility, we were unfortunately not able to refine our calculations to the same precision as we did for Si dissolution (Chapter II, §4.2.2). More fundamental research is thus needed on the pH-dependent Fe-dissolution of pure minerals (*e.g.*, feldspar) to fully identify the responsible minerals in aerosol Fe release.

4.2.3 Amorphous iron

Iron can be found under amorphous form in the aerosols, such as ferrihydrite nanoparticles ($Fe(OH)_3$) which can be a product of chemical weathering of the crystalline goethite (FeOOH) during cloud processing (Shi et al., 2009). Amorphous Fe in dust particles is known to be highly labile (Chen and Siefert, 2003; Paris et al., 2011; Shi et al., 2009), and the highest Fe release of 402.7 $nmol.g^{-1}$ after 1 h in ARW was observed by the completely amorphous Tun Glass (Figure **III-1**). **Due to its amorphous composition, Tun Glass can be used as a proxy for volcanic ash after a long journey in the atmosphere (Delmelle, pers. comm.), which indicates that the Fe solubility of ash might increase within the atmosphere**. This sample enables to highlight the importance of amorphous Fe for Fe dissolution and we can hence make the assumption that the Fe solubility of Tun Glass (0.042 % after 1 h and 0.14 % after 48 h in ARW) corresponds to the dissolution of amorphous volcanic aluminosilicates. Thus, volcanic structural Fe would have intermediate Fe solubilities compared to the rather soluble clay and rather insoluble (hydr)oxides (Table III-5) at ARW pH.

The composition of the amorphous portion from the aerosols of this study is unknown, and as the one in soils may be biogenic, lithogenic or pedogenic *i.e.*, produced by the degradation of organic matter, or during rock or soil formation. These different origins of amorphous material may influence the Fe content and solubility, and no correlation was recorded between the measured Fe solubility and neither the bulk amorphous portion nor the Fe pool, as previously demonstrated by Paris et al. (2011).

Thus, ash is mainly composed by amorphous aluminosilicates with lower SSA and lower crystalline contribution to $\%Fe_{sol}$. Ayris and Delmelle (2012) emphasized the importance of the SSA in iron dissolution and solubility from ash particles. In general, a higher SSA stands for a bigger contact zone between aerosol and matrix and therefore for an increased solubility (Baker et al., 2006), but also possible scavenging (Delmelle et al., 2005). In our study, a variation in the SSA was not responsible for different net solubilities between aerosol types, since ash samples with lower SSA displayed higher Fe solubilities in ARW than dust samples, without systematically displaying Fe adsorption. The SSA of our ash samples (0.36-7.29 $m^2.g^{-1}$) ranged in the average for volcanic ash (<1 to a few $m^2.g^{-1}$; Delmelle et al., 2005) and was about two orders of magnitude lower than dust particles (7.69-62.05 $m^2.g^{-1}$) besides the particular case of Eyja, where smectite incorporation in the ash surface composition might explain its high SSA (Paque et al., 2016).

4.2.4 Iron coating on Chaitén ash

The highest Fe solubility in ARW was displayed by Chaitén ash (0.12 % and 0.45 % after 1 and 48 h, respectively), which is 3-23 times higher than other ash samples after 48 h and even 20-73 times higher compared to dust samples. This high solubility can be explained by the surface Fe-enrichment that Ayris and Delmelle (2012) recorded for the Chaitén sample:

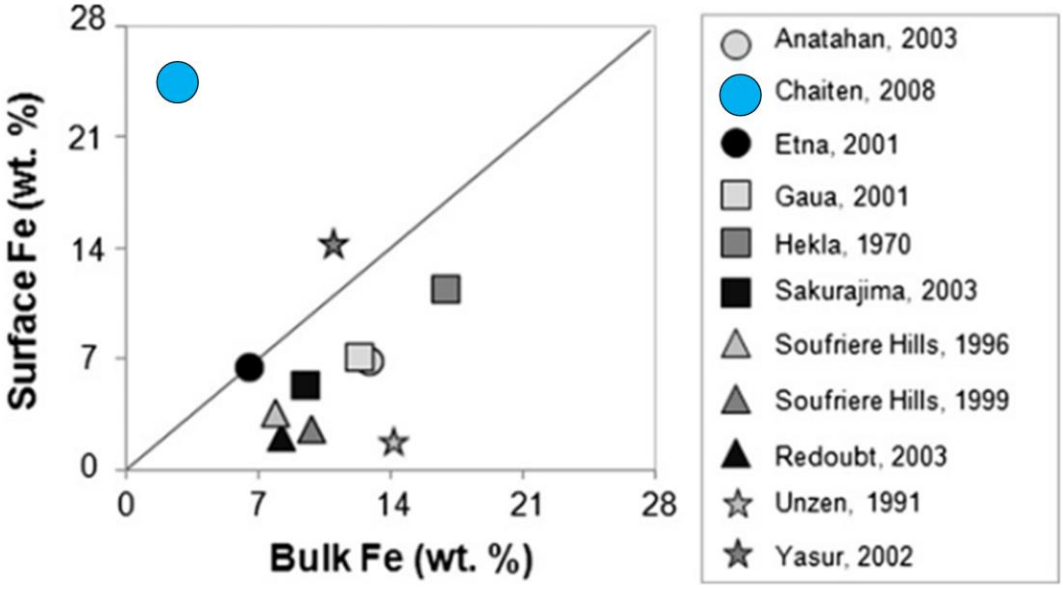

Figure III-5: Correlation between surface Fe (%) and bulk Fe (%) of several natural ash samples including Chaitén ash from the same eruption. Figure adapted from Ayris and Delmelle (2012).

This surface enrichment is uncommon compared to other ash samples measured by the authors, displaying surface Fe-depletion or no difference between surface and core. In our study, after a rapid initial Fe release (0.24 % within 7 h, Figure III-1a), Chaitén displays a second dFe release step with a gentler slope (additional 0.21 % in 41 h). This second step is most probably caused by Fe release from silicates (Ayris and Delmelle, 2012), such as aluminosilicates whose dissolution has been discussed in Chapter II §4.2.1.2 (Figure II-6). The authors cite also oxide minerals as potential Fe sources (Ayris and Delmelle, 2012), but we find this hypothesis less likely, considering the results of Table III-5 displaying the low $\%Fe_{sol}$ of (hydr)oxides compared to clay species.

4.2.5 Iron adsorption

4.2.5.1 Volcanic ash Fe adsorption

Eyja contains the most Fe of all tested aerosols (7.51 %) which is comparable to the 8.9 % found in the ash from the 2000 eruption of Hekla, another Icelandic basaltic-andesite volcano (Jones and Gislason, 2008). Hekla and Eyja both contain rather high Fe and P levels and low Si compared to other various ash samples. Eyja is the only aerosol from our study that displays a clear dissolution-readsorption type behavior in ARW, with initial high dissolution of 0.4 µmol.g^{-1}, followed by a steady decrease in dFe, reaching a minimum of 0.1 µmol.g^{-1} after 1.5 h, and increasing again (Figure III-6a). This same unique behavior was observed for the K dissolution of Eyja (significant linear regression, Figure III-6b), whereas all other aerosols displayed regular K dissolution increasing until they reached steady state (Figure III-1k). This covariation in the Fe and K concentrations may be caused by a Fe and K adsorption on lithogenic ash particles, as described by Rogan et al. (2016) for Fe from the 2008 Eyja eruption. Journet et al. (2008) did not observe iron readsorption but stated identical Fe and K-Mg dissolution patterns for the dissolution of minerals such as the clays illite and montmorillonite and the feldspar orthoclase. It should be noted that Eyja is the only ash sample containing montmorillonite (10.9 % along with the dust Pata that contains 2.8 %). Fe might thus act as a K substitute within the aluminosilicate lattice of the clay (Journet et al., 2008), where Fe is held by weak ionic bonds with a %Fe$_{sol}$ of around 0.9 % at pH 2.

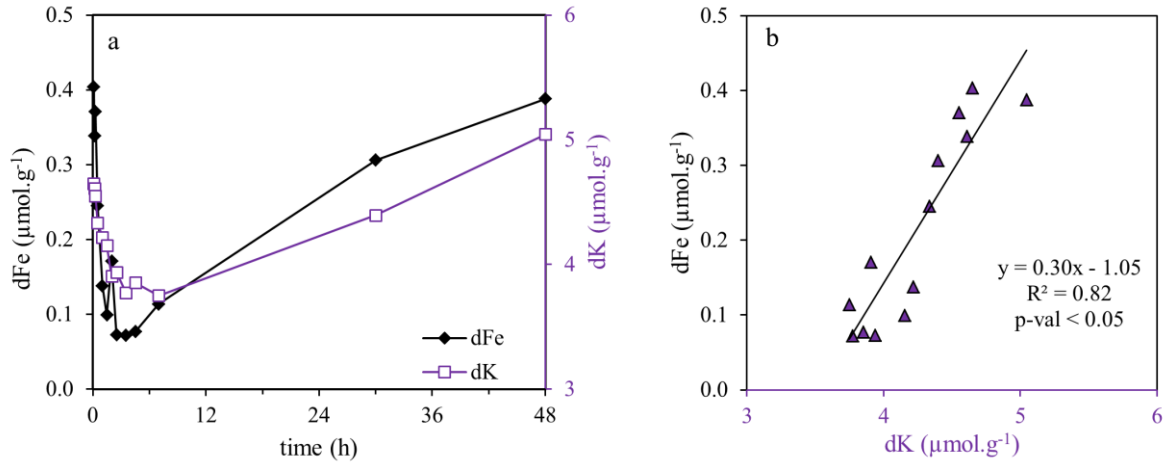

Figure III-6: Iron and potassium dissolution from Eyja ash in artificial rainwater. (a) Dissolution and (b) significant correlation of 0.30 ± 0.04 (p-value< 0.05)

Noteworthy, the mineralogy of Eyja ash was comparatively close to the tested desert dust samples: it is the only ash that contains clay, which may explain its high dust-like SSA of 7.3 $m^2.g^{-1}$ (Paque et al., 2016). Iron scavenging is a process known to be particle size and pH dependent: smaller particles are more likely to adsorb trace metals than large particles (Delmelle et al., 2005), which might explain that large aerosols with a small surface area (SSA < 1 $m^2.g^{-1}$ for Chaitén, Tun Ash and Tun Glass) did not display net readsorption during the 48 h experiment in ARW.

4.2.5.2 Desert dust Fe adsorption

Iron scavenging on aerosols in SW has previously been reported for desert dust (Zhuang and Duce, 1993), and for instance for Douz dissolution in a minicosm experiment (300 L) with filtered surface seawater (Louis et al., 2015). In our study, the four tested desert dust particles displayed fast and repetitive Fe increase-decrease processes within the first 7 h of contact in ARW (multiple peaks, see close up in Annex IV, Figure IV-2a) that seem too erratic and fast to be a physico-chemical phenomenon compared to the slow and more regular two steps adsorption-desorption process of Eyja mentioned above.

4.3 Role of the matrix on TM dissolution

In their volcanic ash dissolution study, Jones and Gislason (2008) state that several ash samples released TM such as Mn and Co within a short contact time, and independently of the matrix (pure water or SW). These TM are not a structural component of the minerals identified within our study, but might be found under the form of traces, for instance within basic rocks, clays or (hydr)oxides (see Table II-3). Few studies have focused on the dissolution of these TM from pure minerals (Menut et al., 2020), limiting the extent of the discussion to a comparison of the two matrices. Noteworthy, a principal component analysis (PCA, see Annex IV §5) enabled us to highlight the link between the TM dissolution (Co, Mn, Ni and Cd) and the aerosol content of quartz, the clay kaolinite and (to a lesser extent) the feldspar microcline.

4.3.1 Manganese

Bani released the highest amount of Mn in both matrices, with initial faster dissolution in the ASW matrix (near immediate) whereas the release was gradual in ARW, with a slightly higher dissolution starting from 7 h. Moreover, desert dust released more Mn than volcanic ash to ASW but this result was not observed in ARW (Figure III-7b). Indeed, dust released overall more Mn to ASW whereas ash released either more Mn to ARW (Eyja and Chaitén) or equally low amounts in both matrices (Tun Ash and Tun Glass).

The overall range of ash Mn dissolution from this study is confirmed by the literature: ash samples from various origins released 17-1300 $nmol.g^{-1}$ after 15 min in SW (Hoffmann et al., 2012), comparable to the 10-400 $nmol.g^{-1}$ for ash here after the same contact time in ASW. Desert dust has shown to have solubilities at ARW pH of 4-16 % for Cap Verde loess and the same Bani sample (Desboeufs et al., 1999; Jacq, 2014) thus comparable to the 0.1-11 % found after one hour in this study. On the other hand, the cruise based solubility measurements of natural Saharan aerosols (50-64 % at pH 4.7; Baker et al., 2006) were higher than the maximal 23 % found in ARW in our study, indicating that the air-collected natural aerosols (Baker et al., 2006) may have been enriched in soluble Mn within the atmospheric pathway. Finally, Menut et al. (2020) indicated a mean Mn solubility of 25 % for the clays illite and smectite, which may thus contribute to the release of Mn by desert dust.

4.3.2 Cobalt

No generality can be extracted from the influence of the matrix on Co dissolution, as Bani and Chaitén released more Co to ARW, whereas Douz, Hoggar and Eyja were more soluble in ASW (Figure III-7c), and Tun Ash and Tun Glass remained equally insoluble in both matrices.

Hoffmann et al. (2012) recorded 0.1-33 nmol $Co.g^{-1}$ ash after 15 min in SW (but with three out of their four samples releasing maximal 1.0 $nmol.g^{-1}$). These findings are consistent with both ash and dust dissolution in ASW from this study (0-2 and 0-3.3 $nmol.g^{-1}$, respectively). Further, Gulf of Aqaba aerosols had a solubility of 17±7 % after seven days of contact in filtered SW (Mackey et al., 2015), which is one to two orders of magnitude higher than the solubility of 0.3-1.9 % found after nine days in our study. However, these aerosols have been sampled in the atmosphere and have thus undergone physico-chemical alteration, explaining their greater solubility.

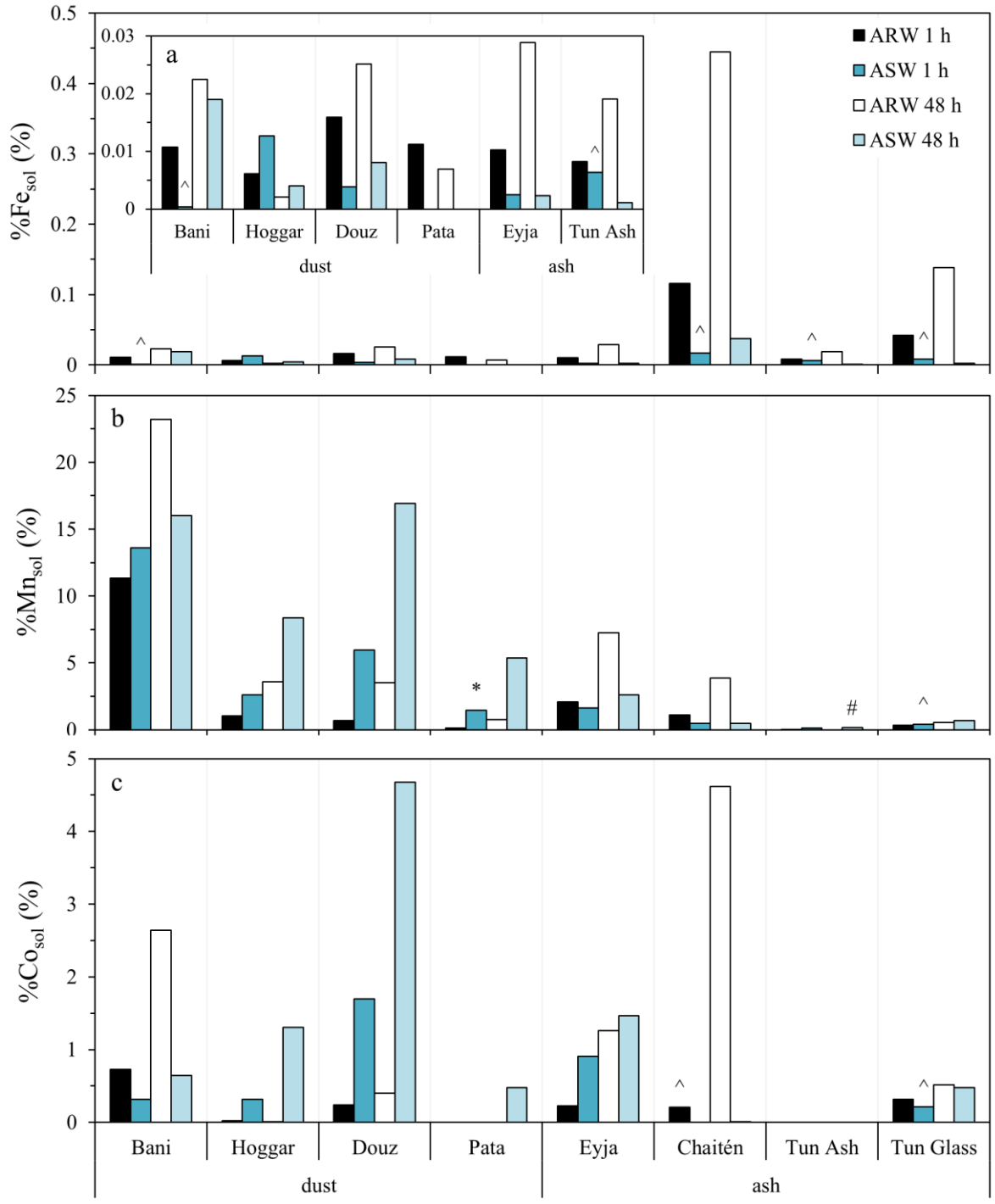

Figure III-7: Solubility (%) of micronutrients in artificial rain- (black and white) and seawater (blue shades) after representative contact times (1 h = black or dark blue and 48 h = white or light blue): (a) Fe, (b) Mn and (c) Co. In the case of missing data, solubility was used at 0.5 h (^) or 2 h (*) instead of 1 h and 30 h (#) instead of 48 h. The Fe solubility (a) contains a supplementary close up excluding Chaitén and Tun Glass.

5 Conclusion

Iron in desert dust was mainly free, *i.e.*, found within badly crystallized or amorphous Fe (hydr)oxides. In opposition, volcanic ash contained Fe mostly under structural form within the lattice of crystalline or amorphous aluminosilicates, such as feldspars or volcanic glass, respectively. We were able to explain 17-70 % of the Fe solubility from dust, and 1.65-85 % of the Fe solubility from ash in the rainwater matrix. Aluminosilicates (mainly clay) accounted for the greatest contribution within the identified crystalline minerals, especially within desert dust. The remaining unexplained portion consists in the badly crystallized and amorphous material that has not been identified in this study but would greatly improve the understanding of the responsible dFe source.

The variability in the dissolution behaviors between individual aerosols hindered the establishment of clear trends distinguishing dust from ash which is somehow surprising given their difference in mineralogy and SSA. However, it can be stated that dust released overall more Mn and Co to ASW, but surprisingly less Fe to ARW compared to ash. Moreover, the TM solubility is known to greatly depend on the pH (*e.g.*, Desboeufs et al., 1999). In that respect, the overall solubility for a given aerosol was increased in the rather acidic artificial rainwater compared to the slightly basic seawater for Fe and Cu. But this conclusion cannot be made for Mn, as desert dust released overall more Mn to ASW, whereas ash was more soluble in ARW.

In this chapter, we identified and quantified the high variability in micronutrient release from desert dust and volcanic ash samples. Therefore, we underline the importance to include these ranges of naturally occurring solubilities in order to provide upper and lower limits when calculating global nutrient fluxes. In the following section of this manuscript (Part B), we focus solely on two aerosols, namely the South American Pata dust and the Icelandic Eyja ash for further ship based experiments. This case study localized the Southern Indian Ocean focused on the phytoplankton response (Chapter V) and the influence of different natural seawater matrices on nutrient release (Chapter VI)

IV. Annex Part A

1 Enrichment factors

Table IV-1: Elementary enrichment factors for desert dust and volcanic ash relative to crustal abundances. Enrichment factors were calculated according to Fishwick et al. (2017) by dividing the mean element/aluminum mass ratios of each aerosol sample by mean element/aluminum mass ratios for the upper continental crust (Wedepohl, 1986). A factor above 1 indicates that the aerosol contains a higher amount of a certain element than the average upper crust (*e.g.,* C and N in dust samples).

	Desert dust				Volcanic ash			
	Pata	Douz	Hoggar	Bani	Eyja	Chaitén	Tun Ash	Tun Glass
C	5.46	63.07	4.98	17.44	0.71	< DL	< DL	< DL
N	16.05	52.86	18.11	45.80	5.55	< DL	< DL	< DL
P	1.13	1.55	1.68	0.88	2.50	0.42	1.26	1.19
Si	0.92	0.79	0.92	1.80	0.94	1.25	0.83	0.81
Fe	1.08	1.05	1.26	1.20	1.79	0.33	0.96	1.06
Al	0.98	0.58	0.99	0.65	0.97	0.88	1.15	1.16
Ca	0.97	8.34	0.57	0.11	0.93	0.30	0.96	1.09
K	0.78	1.00	0.82	0.87	0.72	1.57	0.63	0.58
Mg	0.85	1.43	0.60	0.17	0.66	0.11	0.84	1.10
Na	0.75	0.15	0.30	0.18	1.69	2.08	1.25	1.14
Ti	1.20	1.43	2.26	4.35	2.79	0.24	1.22	1.23
Zn	1.35	1.43	1.39	1.23	2.75	1.35	1.98	1.83
Mn	1.26	1.00	1.36	1.24	2.45	0.99	0.97	1.10
Co	0.53	0.86	1.17	2.12	0.59	0.07	0.62	0.86
Cu	0.82	1.27	1.27	1.24	0.99	0.15	1.92	1.91
Ni	0.30	0.86	1.08	0.75	0.36	0.02	0.60	0.78
V	1.84	1.14	1.25	1.51	0.95	0.08	1.34	1.49
Cd	3.60	7.30	3.81	7.44	11.46	0.98	4.22	5.09
Mo	0.98	2.51	1.84	5.29	3.35	1.66	1.31	1.71

2 Si dissolution rates

Dissolution rates were measured by dividing the normalized dSi release by the contact time in ARW and ASW. The rates (Figure IV-1) display a classical shape, with a maximal release during the first minutes slowly decreasing, described for desert dust (Desboeufs et al., 1999) and volcanic ash (Frogner et al., 2001).

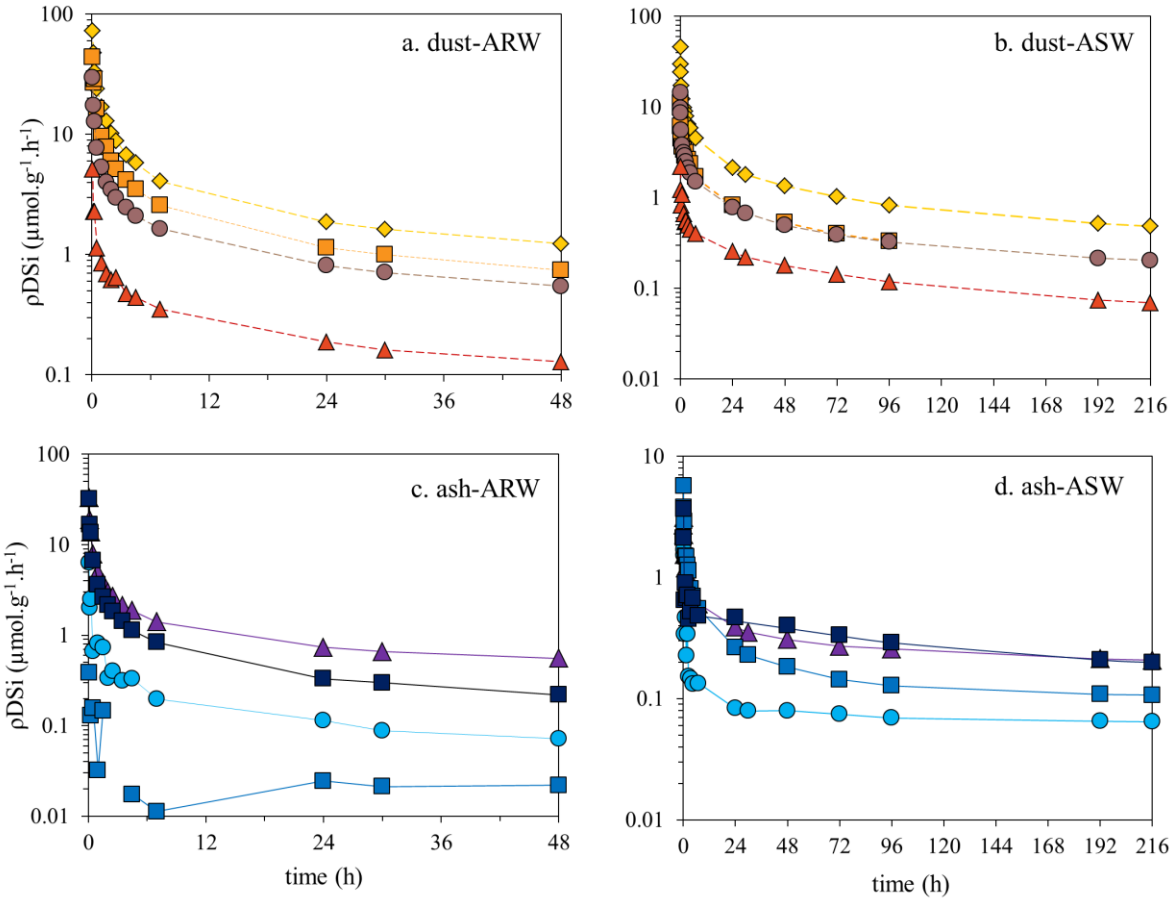

Figure IV-1: Silicon dissolution rates (µmol.g^{-1}.h^{-1}; in log scale) from desert dust (a,b) and volcanic ash (c,d) in artificial rainwater (a,c) and artificial seawater (b,d). Note the lower dissolution rate of ash in ASW (d).

3 Close-up on erratic Fe solubility in ARW from desert dust

The role of iron oxide particles on DIP scavenging has been highlighted (Louis et al., 2015). As addressed in Chapter II, §4.3.4, we observed DIP readsorption in both ARW and ASW matrices, namely for Bani, Douz, Eyja, Chaitén and Tun Glass in ARW. However, the re-adsorptions occurred mainly during the last hours of contact (*i.e.*, after 24 h in ARW), and cannot be compared to the initial erratic Fe solubilities of desert dust (Figure IV-2a). Douz dust presented an early and rapid DIP release and removal process with a peak after 30 minutes of contact followed by a rapid decrease within 2 h (Figure IV-2b) that was evaluated as too high and fast to be accurate. It seems thus exaggerated to conclude on a common scavenging process of Fe and P for Douz in ARW.

The iron from the four tested dust is more than 50 % under 'free' (hydr)oxide form (Table III-2), and their Fe release to ARW was lower compared to volcanic ash. The initial concentrations were close to the experimental detection limit; thus, the hypothesis of analytical issues is preferred over an over-interpretation of these data.

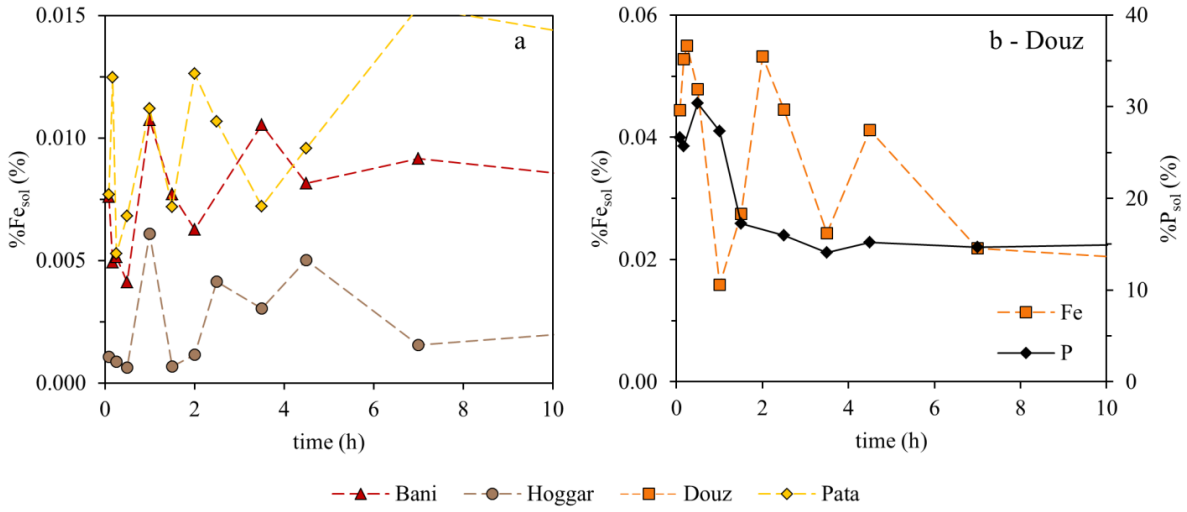

Figure IV-2: Fluctuations in (a) iron solubility after dust addition to artificial rainwater during the first ten hours of contact, and (b) simultaneous iron and phosphorus fluctuations for Douz dust.

4 Dissolution of additional elements in ARW

The TM concentrations in ARW were measured by inductively coupled plasma mass spectrometry (ICP-MS, 7500cx (Agilent), at the Alysés platform, IRD, Bondy for Cd, Cu, Mg, Mo, Ni, Ti, and V) and by atomic emission spectroscopy (ICP-AES, Spectro Arcos at LISA, Paris for Ca, Mg and Zn). Copper and Ni in ASW were analyzed with a seaFAST-pico™ coupled to an Element XR sector field inductively coupled plasma mass spectrometer (SF-ICP-MS) at LEMAR, Brest (Lagerström et al., 2013; Tonnard et al., 2020). We considered "experimental detection limits" (DLe) for analysis in ARW (defined by the smallest reproducible standard of the day of analysis) and standard detection limits (DL) in ASW ($mean_{blank}$ + 3x SD_{blank}). Detection limits are given in Table IV-2. The following elements are presented in alphabetical order within each section.

Table IV-2: Experimental detection limits (DLe, $nmol.L^{-1}$) for ICP-AES and ICP-MS measurements in ARW, and detection limits (DL, $pmol.L^{-1}$) for SeaFast measurements in ASW. n.a: not analyzed

	Ca	Cd	Cu	Mg	Mo	Ni	Ti	V	Zn
ICP-MS, nM	n.a	0.4	26.5	205.7	0.5	28.2	1.0	1.0	n.a
ICP-AES, nM	41.9	n.a	n.a	69.3	n.a	n.a	n.a	n.a	25.8
SeaFast, pM	n.a	n.a	6.94	n.a	n.a	16.8	n.a	n.a	n.a

4.1 Dissolution of additional micronutrients in ARW

4.1.1 Cadmium

Cadmium dissolution was low and close to the detection limit (below 4 $nmol.g^{-1}$ for all tested samples, Figure IV-3a), which compares well to other published and unpublished results (Hoffmann et al., 2012). It appears that the $\%Cd_{sol}$ exceeds 50 % for 5 of the tested samples but the low concentrations close to DL might artificially enhance these solubilities. Only Eyja had a low fractional solubility below 10 % throughout the 48 h kinetics (Figure IV-3b).

4.1.2 Copper

Besides Tun Glass that released 375 $nmol.g^{-1}$ after 48 h (Figure IV-3c), the dissolution of copper (Cu) to ARW remained below 75 $nmol.g^{-1}$ or was close to the detection limit, which is in good agreement with other experimental results performed on the same aerosols (R. Ammar & E. Journet, unpublished data). Final $\%Cu_{sol}$ after 48 h varied between

4.6-18.1 % for desert dust (Hoggar and Douz, respectively, Figure IV-3d) and 3.9-43.0 % for volcanic ash (Tun Ash and Tun Glass).

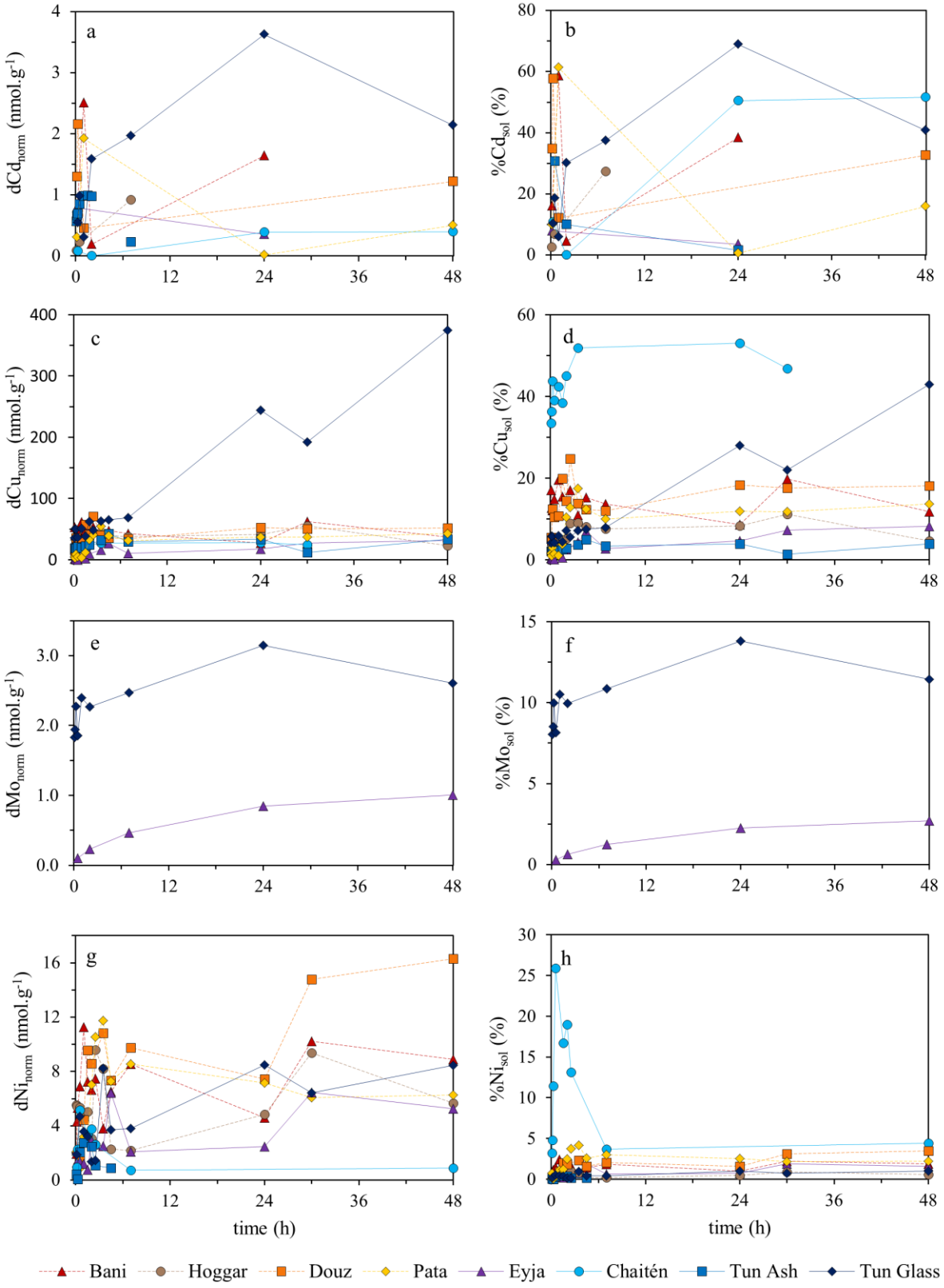

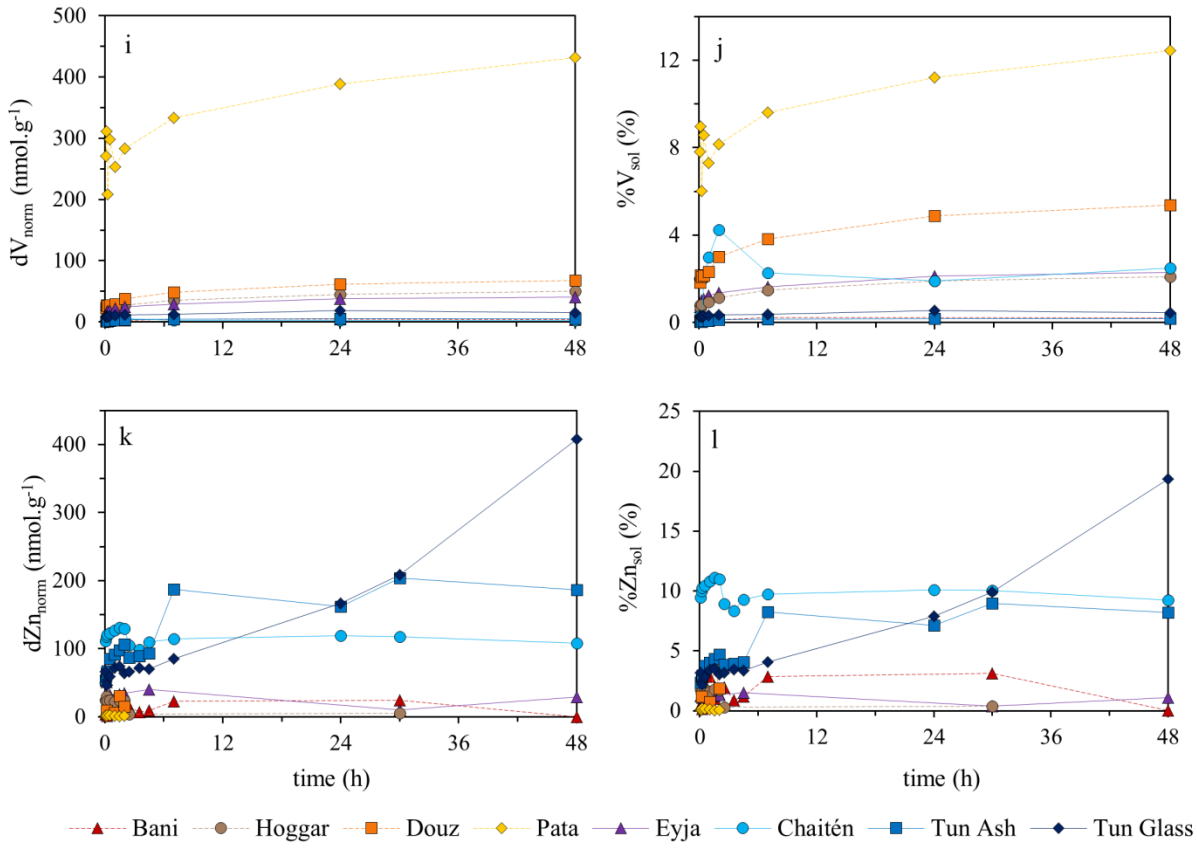

Figure IV-3: Dissolution (in nmol.g^{-1}, left panels) and solubility (%, right panels) of additional micronutrients in artificial rainwater: dCd (a,b), dCu (c,d), dMo (e,f), dNi (g,h), dV (i,j) and dZn (k,l). Warm colors and dashed lines represent desert dust, cold colors and plain lines represent volcano ash.

4.1.3 Molybdenum

Only two of the 8 tested samples dissolved significant amounts of Mo in ARW over the duration of the experiment: the natural ash Eyja and the synthetic Tun Glass. Molybdenum from the synthetic sample was more soluble (11.5 % at t48 h, Figure IV-3e) liberating 2.6 nmol.g^{-1} (Figure IV-3f) compared to the natural sample with a solubility of 2.7 % after the same contact time, liberating 1.0 nmol.g^{-1}. None of the tested dust samples releases detectable amounts of Mo.

4.1.4 Nickel

The same observation as for Cu can be made for the dissolution of nickel (Ni) in ARW. Despite approaching the DLe, the measured concentrations were very similar to other dissolution experiments with the same aerosol samples (R. Ammar & E. Journet, unpublished

data). Final dissolution ranged between 5.7-16.3 nmol.g^{-1} for dust samples (Hoggar and Douz, Figure IV-3g) and 0.9-8.5 nmol.g^{-1} for ash (Chaitén and Tun Glass) after t48 h.

Besides Chaitén (displaying a solubility peak of over 25 % after 30 min of contact time in ARW), ash samples displayed %Ni_{sol} less than 2 % over the duration of the experiment, comparable to %Ni_{sol} for desert dust between 0.6-3.5 % after 48 h (for Hoggar and Douz; Figure IV-3h).

4.1.5 Vanadium

Vanadium was mostly dissolved from Pata dust (up to 432 nmol.g^{-1} after 48 h of contact with ARW, Figure IV-3h) with the highest V solubility (12.4 %). Saharan dust from Douz and Hoggar and ash from Eyja had similar dissolution curves and reached 67.9, 50.0 and 40.9 nmol.g^{-1} respectively, but Douz had more than twice greater %V_{sol} than Chaitén, Eyja and Hoggar (5.4% versus respectively 2.5, 2.3 and 2.1% after 48 h, Figure IV-3j). Tun Ash and Tun Glass had solubilities below 0.5 %.

4.1.6 Zinc

Volcano ash liberated more Zn than desert dust to ARW: the natural ash samples rapidly dissolved and stabilized between 30 and 200 nmol.g^{-1} whereas the artificial Tun Glass sample continued to release dZn even at t48 h, reaching a dZn_{norm} of over 400 nmol.g^{-1} (Figure IV-3k). %Zn_{sol} from ash samples was found between 1.1 % (Eyja) and 20 % (Tun Glass, Figure IV-3l), whereas the Zn dissolution from dust samples was low or below detection limit.

4.2 Dissolution of additional micronutrients in ASW

4.2.1 Copper

The most Cu was released by the synthetic Tun Glass to ASW, with a typical dissolution curve increasing until t48 h (52 nmol.g^{-1}, Figure IV-4a), and then slightly decreasing until the end of the experiment. Other aerosols released less than 15 nmol.g^{-1} (*i.e.*, 4 to 15 times less than Tun Ash) to ASW. Douz was the greatest source of dCu amongst dust, and the release of ~9.0 nmol.g^{-1} occurred rather instantly to ASW. Further, the highest Cu solubility after 48 h was reached by Tun Glass and Douz with 6.0 and 4.9 %, respectively (Figure IV-4b). The Cu solubility from Chaitén was quite variable.

Moreover, the Cu solubility in our study was strictly greater in ARW compared to ASW for all tested aerosols (Figure IV-5a). Tun Glass dissolved by far the most Cu in both matrices (372.8 and 52.2 nmol.g^{-1} at t48 h in ARW and ASW, respectively). Also in both matrices, Chaitén, Tun Glass and Douz were the most soluble (~20-50 % in ARW and ~4-6 % in ASW).

The ARW solubility is thus consistent with the 40 % used by Paytan et al. (2009) in their toxicity study of aerosol dissolution for marine phytoplankton. Moreover, Sholkovitz et al. (2010) found a Cu solubility from Saharan dust of 1-7 % in Sargasso SW, which compares perfectly to our solubility data in ASW. Moreover, the authors find 10-100 % Cu solubility from anthropogenic aerosols in SW (Sholkovitz et al., 2010b), underlining again the possible TM contamination within the atmosphere, originating for instance from fossil fuel or biomass burning (Paytan et al., 2009). Equally, Chen et al. (2009) confirm that the 49 % Cu solubility found in their study with the same Gulf of Aqaba aerosols in Sargasso SW may largely be explained by anthropogenic sources.

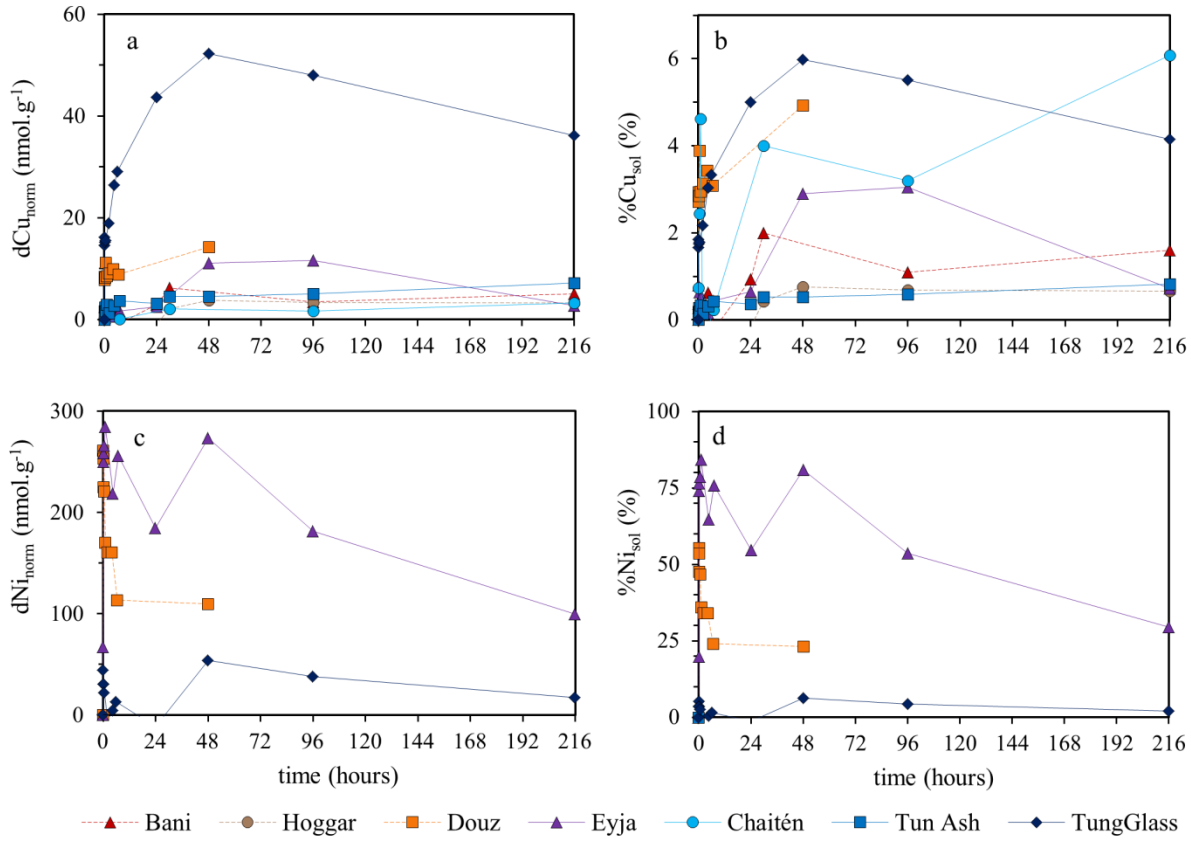

Figure IV-4: Dissolution (in nmol.g^{-1}, left panels) and solubility (%, right panels) of additional micronutrients in artificial seawater: dCu (a,b) and dNi (c,d). Warm colors and dashed lines represent desert dust, cold colors and plain lines represent volcano ash.

4.2.2 Nickel

Only three aerosols released measurable amounts of dNi to ASW. The highest dissolution and solubility were observed for Eyja (274 nmol.g^{-1} and ~80 % of %Ni$_{sol}$ at t48 h, Figure IV-4c). Tun Glass had the lowest measurable dissolution and solubility (54 nmol.g^{-1} and <10 % of %Ni$_{sol}$ at t48 h). Douz displayed an initial high release of 261 nmol.g^{-1} at t5 min, decreasing until 109 nmol.g^{-1} after t48 h (with Ni solubility between 55 and 23 %).

The highest Ni dissolution was observed in ASW, and Eyja and Douz released almost 300 nmol.g^{-1} to ASW whereas the dissolution to ARW remained below 20 nmol.g^{-1}. The resulting solubility of 80 % for Eyja in ASW is high and could not be confirmed by the literature. As described for Co and Cu, these aerosols are most likely influenced by anthropogenic emissions within the atmosphere known to enhance TM solubility.

Thus, we can assume that the 25-48 % found for Douz in this study are the upper limit of Ni solubility from natural aerosols, and that the 80 % found for Eyja were most definitely contaminated. Equally, Hoffmann et al. (2012) recorded a dissolution of 0.5-13.9 nmol Ni.g^{-1} ash after 15 min in SW, which is around 20 and 10 times less than our findings for Eyja and Douz, reinforcing the hypothesis of contamination.

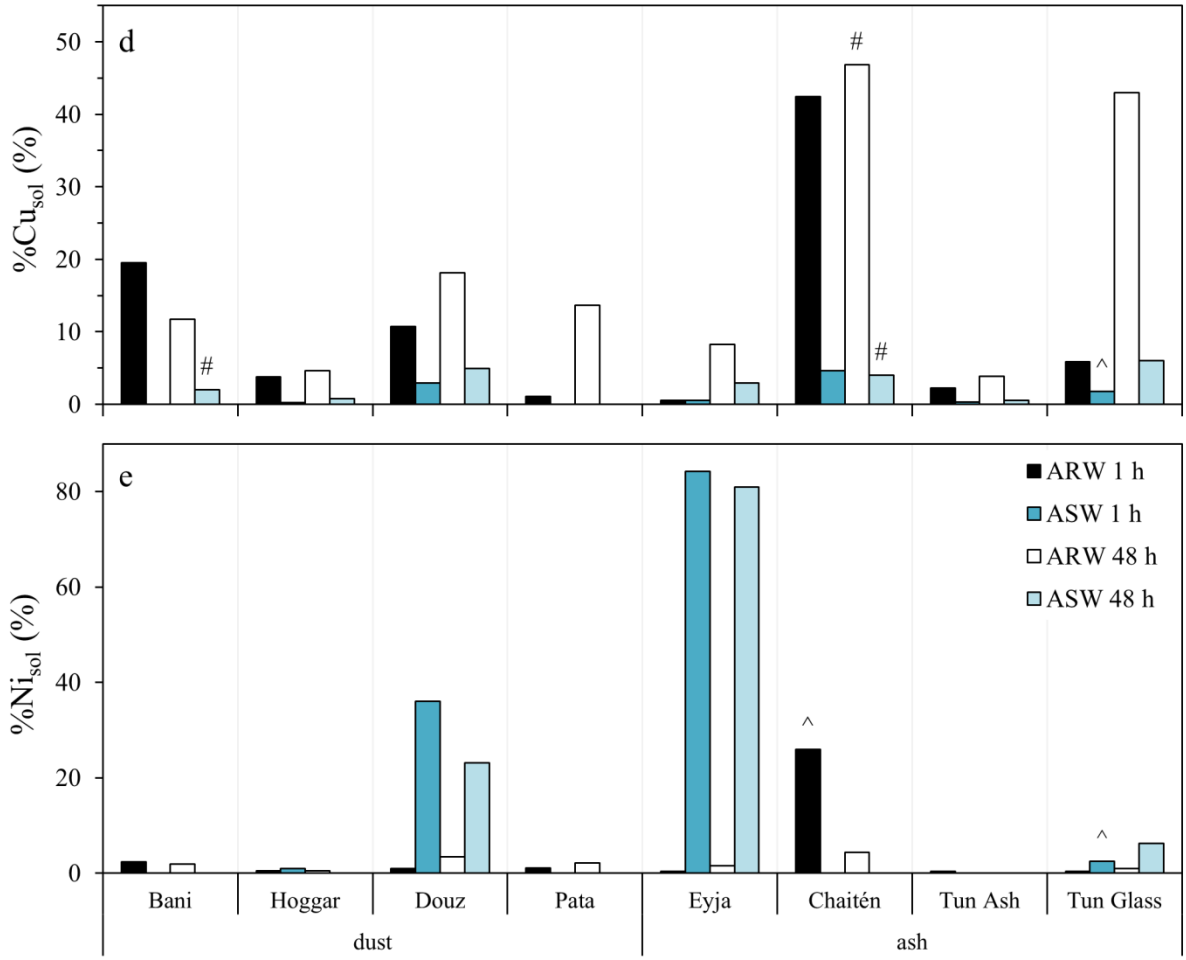

Figure IV-5: Solubility (%) of micronutrients in artificial rain- (black and white) and seawater (blue shades) after representative contact times (1 h = black or dark blue; and 48 h = white or light blue): (a) Cu and (b) Ni. In the case of missing data, solubility was used at 0.5 h (^)instead of 1 h and 30 h (#) instead of 48 h.

4.3 Dissolution of lithogenic tracers in ARW

When aerosols enter in contact with rain droplets, they dissolve not only macro- and micronutrients that will be consumed by phytoplankton after their deposition to the sea surface and that constitute the main topic of this manuscript. The aerosols also release other elements that are not biologically controlled and may remain conservative in the water column (*e.g.* Mg, K, and ~Ca) or are scavenged with depth (*e.g.* Al and Ti) (Nozaki, 2001). In this section, we address the dissolution and solubility in ARW of these elements, as an attempt to further explain the nutrient release. Indeed, the dissolution behavior of these lithogenic tracers might help to identify the minerals within the aerosols that liberate the

nutrients (*e.g.* the role of Al for Si dissolution addressed in Chapter II §4.2.1 or the correlation of K and Fe in Fe adsorption, Chapter III §4.2.5).

4.3.1 Calcium

As for Al, Douz presented the maximum Ca release of 1.2 µmol.g^{-1} after 48 h (Figure IV-6a), corresponding to a $\%Ca_{sol}$ of 26.8 %. Pata and Hoggar released three and five times less Ca than Douz (dCa_{norm} of 0.40 and 0.25 µmol.g^{-1}, respectively) but their $\%Ca_{sol}$ of 43.5 and 45.6 % was about 1.7 times higher. Besides the $CaCO_3$ containing Eyja, other ash samples as well as Bani dust released less than 0.02 µmol.g^{-1} to ARW. Solubility $\%Ca_{sol}$ was strictly higher for dust samples (18.1-45.6 % after 48 h for Bani and Hoggar, respectively) compared to ash samples (between DL for Tun Ash and 13.3 % for Eyja, Figure IV-6b). For discussion on $CaCO_3$ dissolution, please refer to Chapter II, §3.2.

4.3.2 Magnesium

The release of Mg followed regular steadily increasing dissolution curves, and desert dust released globally more Mg than volcano ash (Figure IV-6c). Highest dissolution was reached by Hoggar dust (59.1 µmol.g^{-1} at t48 h of contact time with ARW) but dust from Douz and Pata released similar high amounts of Mg (29.6 and 39.3 µmol.g^{-1}, respectively at t48 h). However, Bani dust (maximum of 6.8 µmol.g^{-1}) remained comparable to ash releasing 0.2-10.9 µmol.g^{-1} in the same experimental conditions (for respectively Tun Ash and Eyja). $\%Mg_{sol}$ was also higher for desert dust (4.0-11.0 % after 48 h in ARW for respectively Douz and Hoggar) compared to volcanic ash (0.03-2.9 % for Tun Ash and Chaitén, Figure IV-6d).

4.3.3 Titanium

Despite low concentrations close to the detection limit, Ti dissolution compares well to other experimental results (R. Ammar & E. Journet, unpublished data) with the same aerosols. Overall, ash dissolved more Ti than dust: 8.1-58.5 nmol.g^{-1} (for Chaitén and Eyja), compared to 2.5-19.9 nmol.g^{-1} (for Douz and Bani, Figure IV-6e). $\%Ti_{sol}$ was very low and remained below 0.05 % for all aerosols; comparable to most $\%Fe_{sol}$; and ash samples were 2-11 times more soluble compared to desert dust after 48 h (0.019-0.046 % for Tun Ash and Chaitén vs 0.004-0.008 % for Douz and Bani, Figure IV-6f). Initial high dust solubilities may be artificially caused by concentrations close to DL inducing analytical issues.

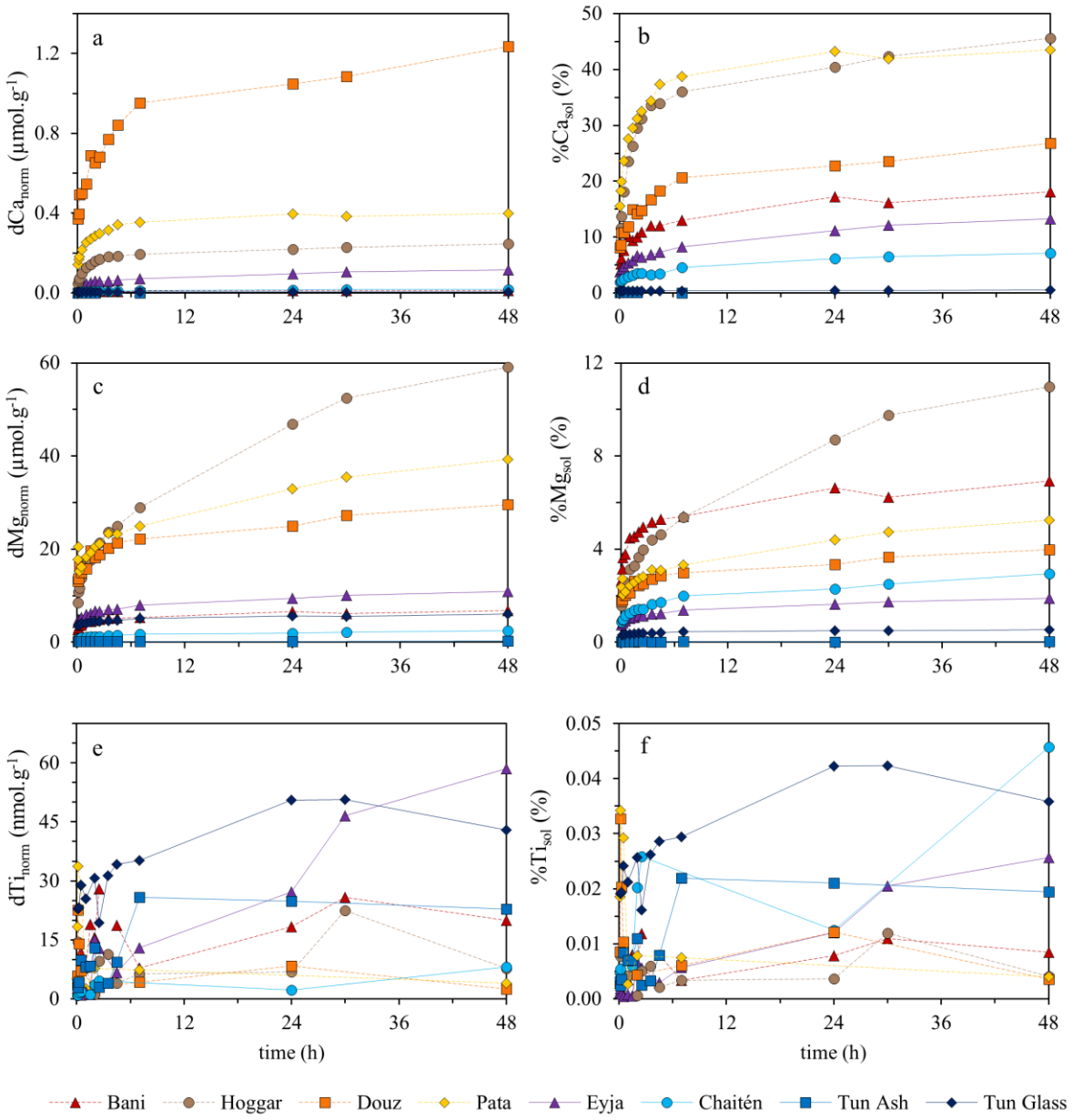

Figure IV-6: Dissolution (left panels, in µmol.g^{-1} for a,c or in nmol.g^{-1} for e) and solubility (%, right panels b,d,f) of lithogenic tracers in artificial rainwater: dCa (a,b), dMg (c,d) and dTi (e,f). Warm colors and dashed lines represent desert dust, cold colors and plain lines represent volcano ash.

5 Covariation of dissolution in ARW and mineralogy

The aim of this section is to link the dissolution from three macronutrients (Si, P and N), nine micronutrients (Fe, Mn, Co, Cu, Ni, V, Zn, Cd and Mo) and five lithogenic tracers (Al, K, Mg, Ca and Ti), in order to constrain the minerals that are responsible for the nutrient release.

A principal component analysis (PCA) was performed on the dissolution and solubility datasets, in order to determine dissolution patterns among the 8 aerosols and to identify links between the dissolution of 17 individual elements to mineralogy. We used a reduced dataset of the dissolution and solubility after a representative contact time of one hour in ARW. Missing data is not allowed in the PCA analysis; therefore, we set 8 undetectable values to 0.0 $\mu mol.g^{-1}$ and replaced 7 aberrant values out of the total 136 values using interpolation.

The PCA enabled us to identify covariation patterns within elements, and tent to explain these patterns with descriptive variables including **aerosol structural parameters** (the amorphous vs. crystalline portions, as well as free vs. structural Fe), mineralogy (content of different clays, feldspars and basic rocks), particle size parameters (SSA, mean and median particle diameter) and pH variations (after 1 h in ARW).

The **dissolution data** shows a clear link between the release of the macronutrients Si, N and (to a lesser extent) P and the dissolution of alkali and alkaline earth metals K, Mg and Ca. A strong correlation is visible (axis 1 explains 44 % of the information, Figure IV-7a) between the macronutrient release and (i) the aerosol content of the clay illite, (ii) the SSA of aerosols and (iii) the evolution of pH_{ARW}. The calcite content is only badly represented within this axis (30.4 % of the calcite signal is explained by axis 1), which is surprising knowing the impact of calcite dissolution on pH (see Chapter II, §3.2) and on Ca release. The dissolution of alkaline earth metals is a good proxy for the dissolution of aluminosilicates (Oelkers et al., 1994). In our analysis, Al is also linked to axis 1 (but the quality of the representation is only 42 %), which seems to confirm the correlation of illite content to the dissolution of illite-composing elements.

A second cluster regroups the dissolution of Fe, Zn and Mo with (i) the amount of structural iron within the aerosols (ii) the amount of amorphous material and (iii) the mean particle diameter. This correlation has already partially been described in §4.2.3. Structural iron is found within aluminosilicate minerals (Paris et al., 2011), but these minerals can be under amorphous or badly crystallized form such as the clay smectite. Smectites are known to contain highly soluble Fe (Journet et al., 2008) which may explain the correlation to the

dissolution of iron. Molybdenum is known to adsorb on smectite surfaces (Tuchowska et al., 2019) which may explain its correlation to the cluster.

The second axis enables us to group the dissolution of Co, Mn, Ni and Cd to the aerosol content of the minerals quartz, the clay kaolinite and (to a lesser extent) the feldspar microcline (Figure IV-7b). These minerals do not contain the cited elements within their crystalline structure, but they are likely to hold soluble traces of TM under the form of coating. Surprisingly, the size parameters did not correlate with dissolution data.

(a) Dissolution– principal plane (axes 1-2)

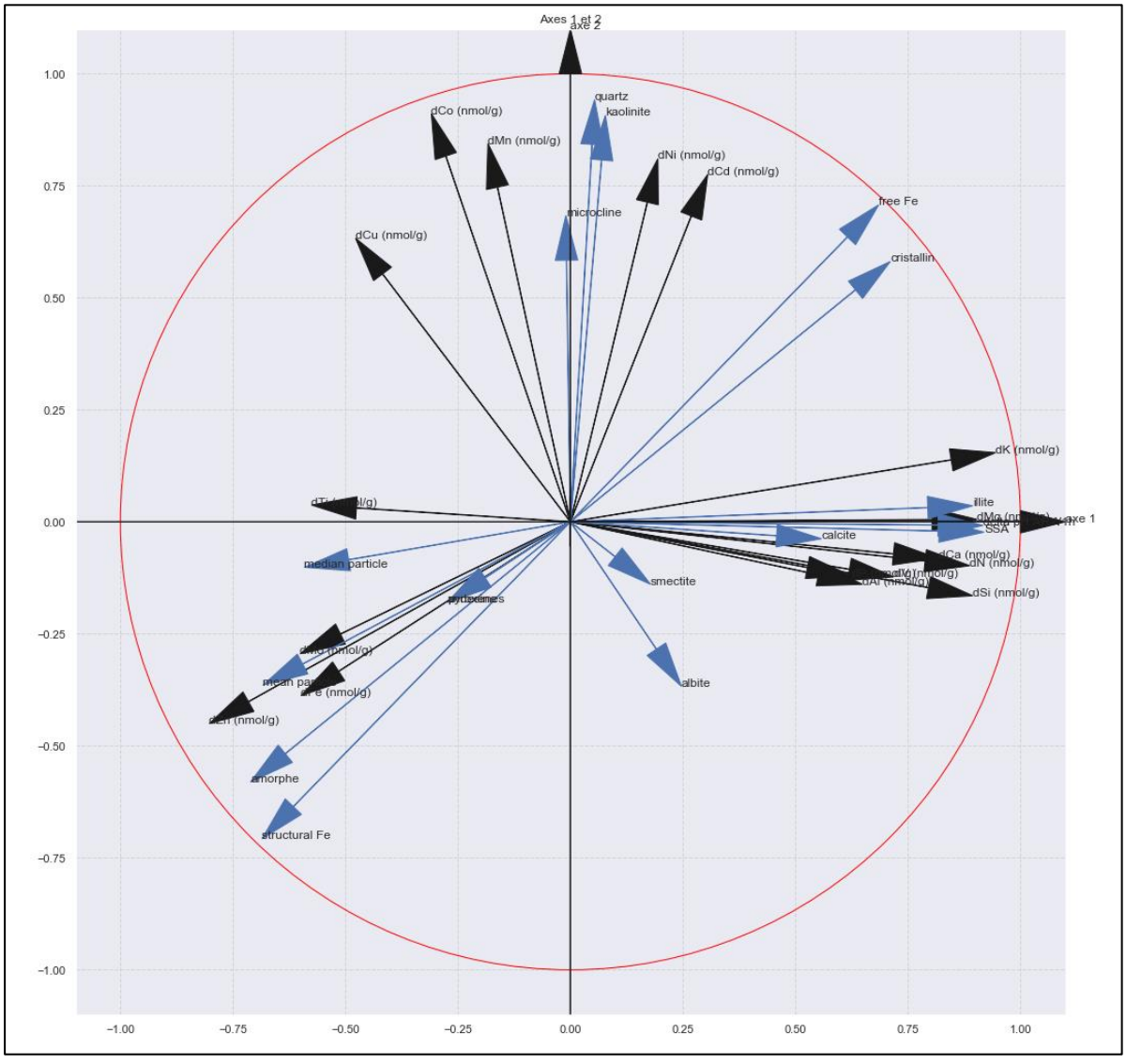

Figure IV-7: Output of the Principal Component Analysis (PCA) of **dissolution** of 17 elements after one hour in artificial rain water (black arrows), combined with descriptive variables (blue arrows). (a) The first axis explains 44.0 % and the second axis 22.1 % of the inertia, (b) the first axis explains 44.0 % and the second axis 14.7 % of the inertia.

(b) Dissolution–axes 1-3

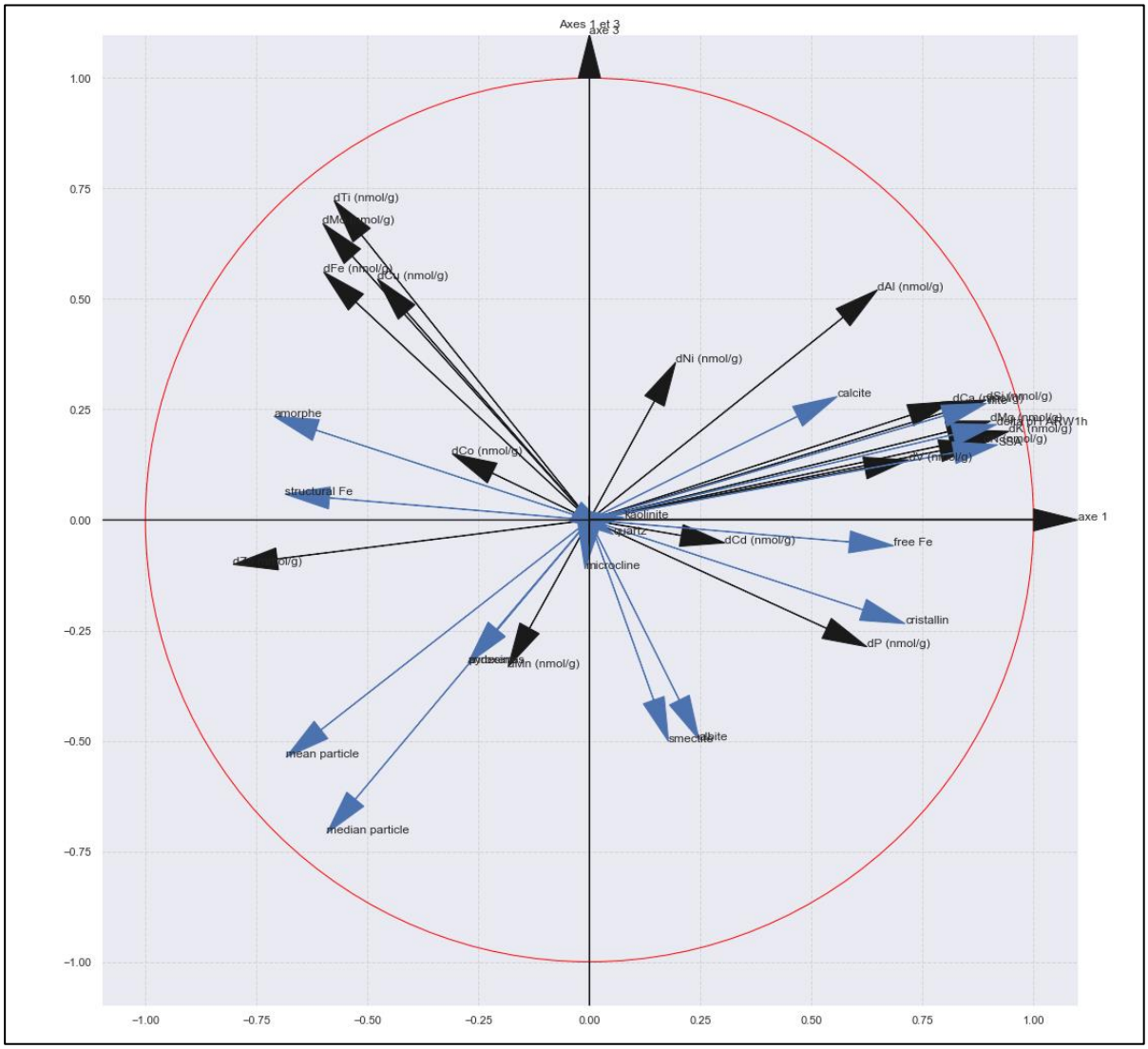

(a) Solubility – principal plane (axes 1-2)

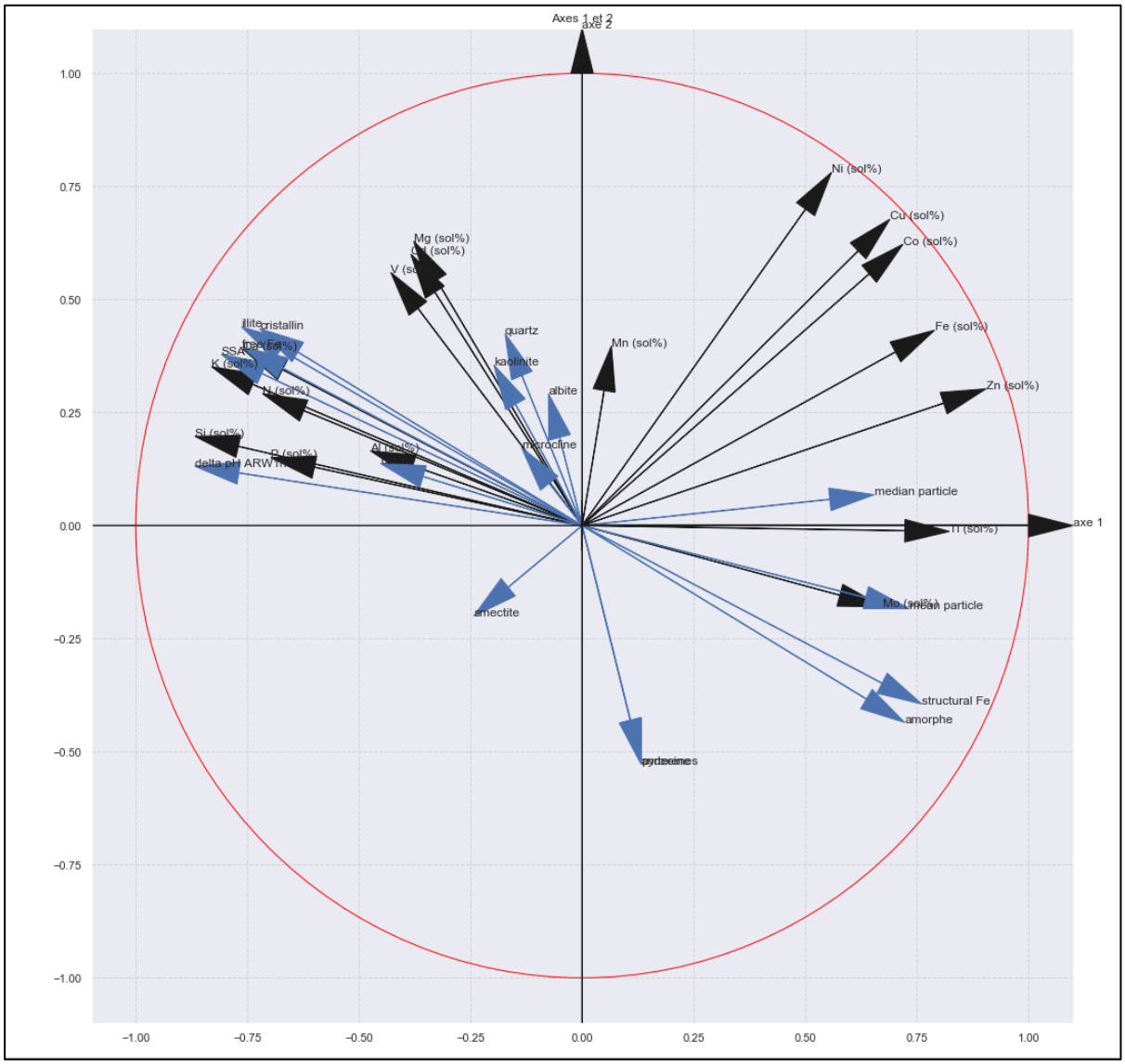

Figure IV-8: Output of the Principal Component Analysis (PCA) of **solubility** of 17 elements after one hour in artificial rain water (black arrows), combined with descriptive variables (blue arrows). (a) The first axis explains 44.7 % and the second axis 20.3 % of the inertia, (b) the first axis explains 44.7 % and the second axis 16.0 % of the inertia.

The **solubility data** groups the same elements and explanatory parameters in a slightly different manner: the macronutrient solubility (%Si_{sol}, %N_{sol}, %P_{sol}) is correlated as before for the dissolution dataset to the alkaline element solubility (%Ca_{sol}, %K_{sol}), the illite content and SSA. According to the principal plane (axis 1 – 2, explaining 65 % of the information, Figure IV-8a) this cluster is also correlated to the amount of crystalline minerals and the proportion of free iron, which might be an indication linking macronutrient solubility to (hydr)oxide content.

(b) Solubility – axes 1-3

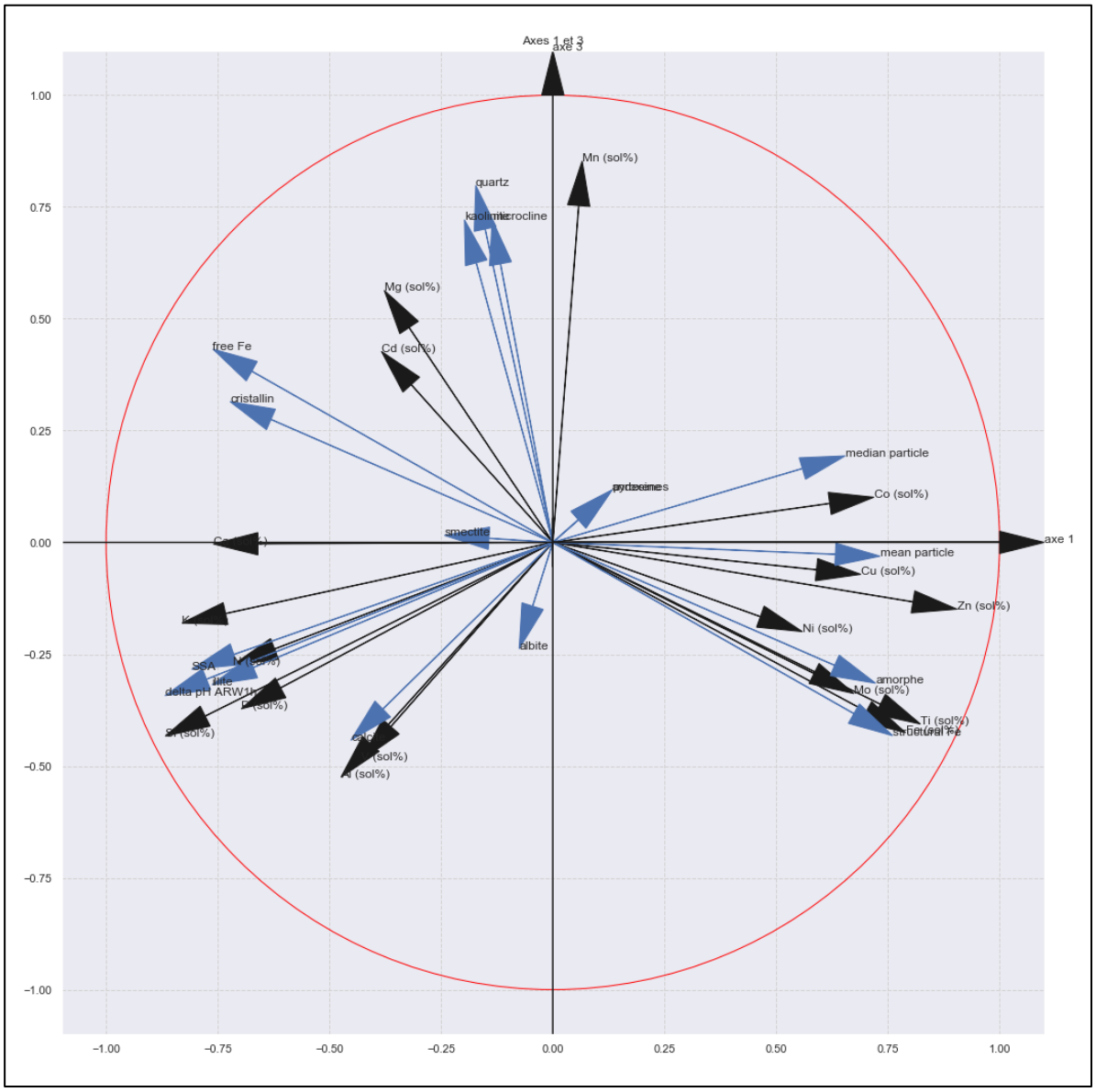

This result is not observed in the following sections, and axis 3 (holding 16 % of the information) separates the two groups. Similarly, axis 2 (20.3 % of information) separates iron solubility $\%Fe_{sol}$ from the amount of amorphous material and structural Fe, but the secondary plane (axis 1 – 3, 50.7% of the information, Figure IV-8b) merges these parameters with $\%Ti_{sol}$ and $\%Mo_{sol}$, knowing that titanium is an element frequently found in Fe containing minerals through isomorphic replacement.

Part B

Case Study in the South Indian and Southern Oceans

Phytoplanktonic response and natural variability in nutrient release after a representative aerosol deposition event

- Phytoplanktonic Response to simulated Volcanic and Desert Dust Deposition Events in the Southern Indian Ocean
- Nutrient solubility in the Southern Indian Ocean: Abiotic release of macro- and micronutrients in natural and artificial seawater after simulated volcanic ash and desert dust deposition
- Annex of Part B
    - Statement on possible Fe contamination
    - Calculation of sinking velocities after aerosol deposition
    - Contribution of phytoplankton size classes to the total biomass
    - Response of heterotrophic bacteria and haptophytes
    - Linear regressions of nutrient solubility and temperature
    - Ambient seawater characteristics of the Southern Indian Ocean

V. Phytoplanktonic response to simulated volcanic and desert dust deposition events in the Southern Indian Ocean

Carla Geisen[1*], Céline Ridame[1], Emilie Journet[2], Pierre Delmelle[3], Dominique Marie[4], Claire Lo Monaco[1], Nicolas Metzl[1], Rawaa Ammar[2,3], Joelle Kombo[1], Damien Cardinal[1]

[1]Sorbonne Université, LOCEAN – IPSL Laboratoire d'Océanographie et du Climat : Expérimentations et Approches Numériques, UMR 7159, (SU CNRS MNHN IRD), 75252 Paris Cedex 05, France. [2]LISA (Laboratoire Interuniversitaire des Systèmes Atmosphériques), UMR 7583, CNRS, Université Paris-Est Créteil et Université de Paris, Institut Pierre Simon Laplace (IPSL), Créteil, France. [3]Earth and Life Institute, Environmental Sciences, UCLouvain, B-1348 Louvain-la-Neuve, Belgium. [4]CNRS, Sorbonne Université, UMR 7144 Adaptation et Diversité en Milieu Marin, Station Biologique de Roscoff, 29680 Roscoff, France.

Corresponding author : Carla Geisen now at [*]Laboratoire d'Océanographie et de Géosciences, UMR 8187 (LOG – ULCO) (carla.geisen@univ-littoral.fr)

In review at L&O

Key Points

- Representative desert dust and volcanic ash depositions released significant amounts of Fe and Si but not NOx to seawater.
- The triggered phytoplankton response was mainly caused by diatom development.
- The Kerguelen plateau presented the highest response in primary production, despite being naturally fertilized.

Running head

Phytoplankton response to dust and ash addition

Abstract

We conducted microcosm incubation experiments in contrasted biogeochemical areas of the South Indian Ocean and Indian sector of the Southern Ocean. The goal was to assess the phytoplankton response to nutrient release by desert dust and volcanic ash aerosols. A dry or wet deposition of either dust from Patagonia or ash from the Icelandic Eyjafjallajökull volcano or dissolved nutrients (Si, Fe, N and/or P) were added to trace metal clean incubations of surface seawater collected from five stations. These deposition experiments enabled the measurement of the biological response along with solubility calculations of nutrients. Both types of aerosols alleviated the iron deficiency occurring in the Southern Ocean during austral summer and resulted in a 24-110 % enhancement of the primary production, depending on the station. The release of dissolved silicon may also have contributed to this response, although to a lesser extent, whereas neither the dust nor the ash relieved nitrogen limitation in the Low Nutrient and Low Chlorophyll area. Diatom growth was responsible for 40 to 100 % of the algal biomass increase within the responding stations, depending on the region and aerosol type. The high particle concentrations which are characteristic of ash deposition following volcanic eruptions may be of equal or higher importance to phytoplankton compared to desert dust, despite ashes' lower nutrient solubility to the ocean.

Plain Language Summary

The South Indian and Southern Oceans are known for contrasting nutrient concentrations and different microalgal communities, which are limited by the low content of several nutrients. In most parts of this area, nutrients are supplied by oceanic interfaces (aerosols, sediments, ice…) and only limited amounts of atmospheric dust reach currently the remote open ocean. Aerosol deposition nevertheless constitutes one of the major sources of new nutrients within this vast ocean area in the present-day and was greatly enhanced during glacial times and/or volcanic eruption events. After deposition on the sea surface, the particles release nutrients such as iron and silicon to the seawater, which may temporally stimulate algal development.

In this study, we show that a representative deposition of desert dust or volcanic ash triggers a phytoplanktonic response in different regions of the Southern Indian Ocean. Some algae groups such as diatoms benefit more from the new nutrients, thereby modifying the structure of the planktonic community. On the other hand, the same deposition had no effect in the

eastern part of the South Indian Ocean, as the ambient nitrogen limitation was not relieved by the aerosols.

1 Introduction

The Southern Ocean (SO) is the largest High Nutrients Low Chlorophyll (HNLC) area of the ocean, where phytoplankton growth is mostly limited by low surface iron (Fe) concentrations (Martin, 1990; Moore et al., 2002). Due to latitudinal gradients of dissolved macronutrients decreasing northwards, the SO can be further divided in distinct biogeochemical regions (Figure V-1), characterized by different nutrient limitations. In the Subantarctic Zone (SAZ), dissolved inorganic phosphorus (DIP) and NOx (NO_3^- + NO_2^-) remain high but dissolved silicon (dSi) is scarce (Nelson et al., 2001), The Fe limitation of the Antarctic Zone (AZ) is thus shifted to a Fe-Si co-limitation (Hoffmann et al., 2008; Hutchins et al., 2001), referred to as High Nitrate-Low Silicon-Low Chlorophyll (HN-LSi-LC) (Dugdale et al., 1995). Further north, the Subtropical Front (STF) marks the boundary with the Low Nutrient Low Chlorophyll (LNLC) region of the Subtropical Zone (STZ) of the South Indian Ocean (SIO). This region within the oligotrophic subtropical gyre is characterized by low NOx and surface concentrations (McClain et al., 2004; Morel et al., 2010).

One of the factors which are responsible for the Fe-depletion in the SO is the shortage of so-called new Fe supply, i.e., Fe reaching the euphotic zone from external sources. The fluvial Fe supply to the remote SO can be neglected, making atmospheric aerosol deposition the main Fe source, except in upwelling areas associated to hydrothermal vents, or in areas subjected to Fe-rich sea ice melting, or within naturally fertilized coastal regions such as the Kerguelen and Crozet plateaus (Ardyna et al., 2019). The monthly-averaged dust deposition flux to the SO is very low (10-45 $mg.m^{-2}.month^{-1}$ during austral summer, Meskhidze et al. 2007), but intense sporadic events may affect phytoplankton growth. These events occur especially during the austral summer months, when the water column is stratified and the emissions from the Patagonian source are more frequent (Gassó and Torres, 2019). Several studies suggest that dust deposition to the SO was up to 20 times higher during the Last Glacial Maximum (e.g. Mahowald et al. 1999). At this time, dust-mitigated input of Fe to the ocean surface layer may have fertilized ocean phytoplankton production, thereby contributing to millennial-scale CO_2 fluctuations associated with glacial-interglacial cycles (Conway et al., 2015; Martin, 1990; Watson et al., 2000).

Several studies have also shown that volcanic ash is a significant source of dissolved Fe (dFe) that can stimulate phytoplankton growth in HNLC regions (Mélançon et al., 2014; Olgun et al., 2011). A clear evidence has been provided by direct observation after the 2008 eruption of the Kasatochi volcano in the Gulf of Alaska (Langmann et al., 2010a). The range of ash deposition to the ocean is highly variable (Durant et al., 2010) and is influenced by various factors, such as the volume of ejected ash, the ash grain distribution and in-plume processes (Ayris and Delmelle, 2012; Duggen et al., 2010).

Several mesoscale artificial Fe enrichment experiments (Boyd et al., 2007 and references therein) have demonstrated the relief of the Fe limitation for phytoplankton growth in the SO, and microcosm studies have highlighted a biological response after dust or ash additions to the Atlantic sector of the SO (Browning et al., 2014; Trimborn et al., 2017). Nevertheless, the SIO and Indian SO represent a large ocean basin in which the biological and biogeochemical responses to atmospheric deposition events are poorly documented.

To better assess the impact of desert dust and volcanic ash deposition events to the under-sampled SIO and Indian SO, we performed short term (two days) microcosm experiments with representative aerosol particle concentrations. Phytoplankton primary production (PP) and community composition were measured after simulated dry or wet aerosol deposition or dissolved nutrients additions. The novelties of this study are the comparison of the nutrient release and phytoplanktonic responses between (i) dust and ash deposition events, (ii) HNLC and LNLC areas, and (iii) dry and wet deposition modes.

2 Materials and Methods

2.1 Cruise transect, hydrological and biogeochemical context

Our study was part of the VT163/OISO-29 (MD217) cruise (Lo Monaco and Metzl, 2019), on board the R/V *Marion Dufresne* during the austral summer, from January 5th to February 15th 2019. Experiments were performed at five stations, located in the contrasted LNLC, HN-LSi-LC and HNLC areas defined by major fronts (Figure V-1), as well as a reference station of the bloom area of the naturally Fe-fertilized Kerguelen plateau (St. A3) (Blain et al., 2007; Fripiat et al., 2011).

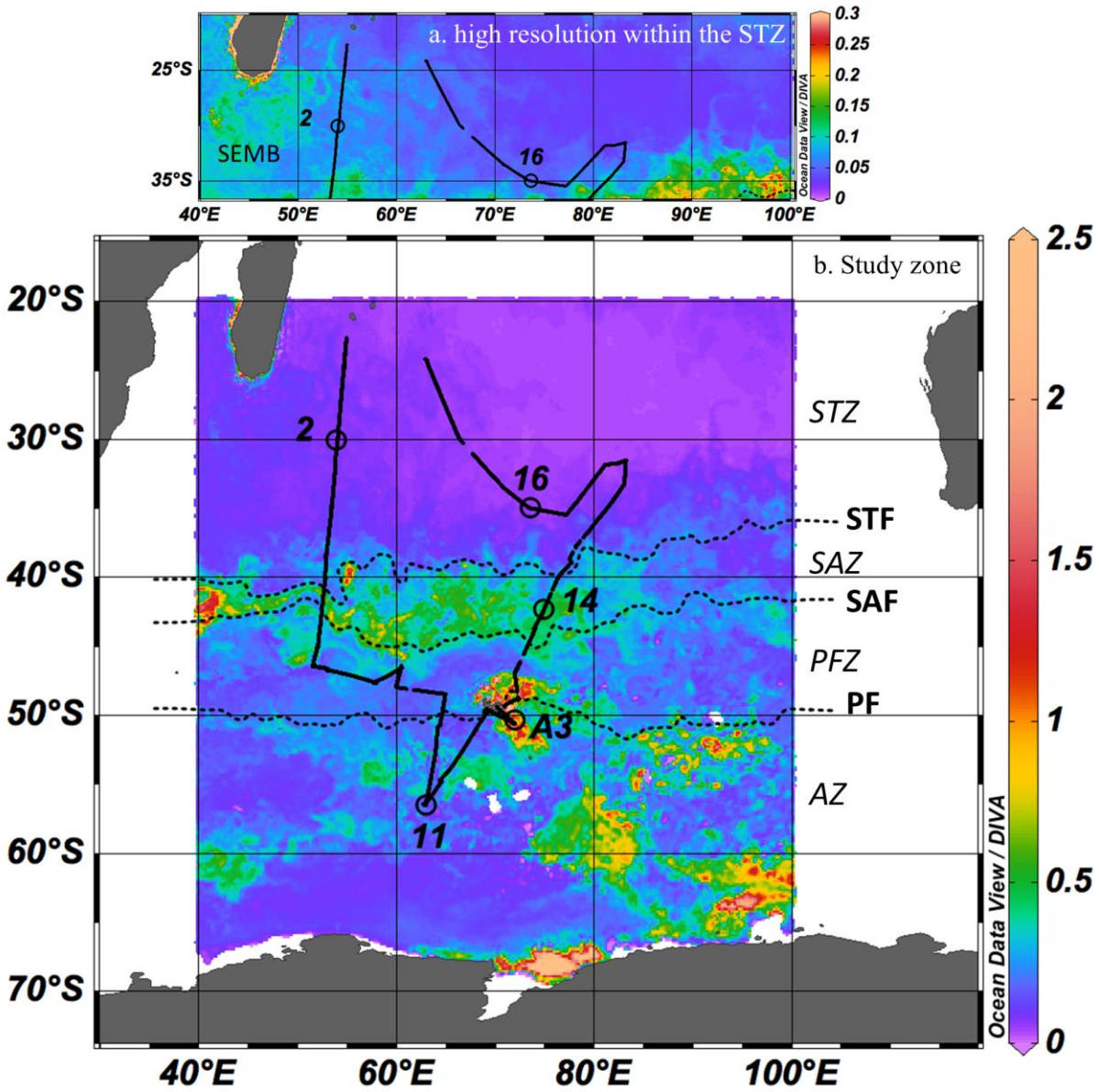

Figure V-1. OISO-29 cruise transect with the locations of the five stations (LNLC-2, HNLC-11, Kerguelen-A3, HN-LSi-LC-14 and LNLC-16) where bioassay experiments were performed, and satellite-derived chlorophyll-a concentration (µg.L^{-1}) averaged over January 2019 (MODIS). The position of major fronts was determined from satellite-derived temperature data (January 2019, MODIS): STF: subtropical front (18 °C), SAF: Subantarctic front (13 °C) and PF: polar front (5 °C). Fronts delimit the STZ: subtropical zone, SAZ: Subantarctic zone, PFZ: polar front zone and AZ: Antarctic zone. The map (a) shows the STZ with a higher resolution than the general map (b), thus enabling the detection of the South East Madagascar bloom (SEMB). Figures were produced using Ocean Data View (Schlitzer, 2021).

2.2 Bioassay experiments

We carried out trace metal clean nutrient/aerosol additions during bioassay experiments at five stations (Figure V-1, Table V-1). All materials were acid-washed (HCL Suprapur) and manipulations took place under laminar flow hoods. Unfiltered surface seawater (SW, ~10 m depth) was collected within the surface mixed layer using Go-Flo bottles and Kevlar wire to avoid trace metal contamination. Dry deposition events of desert dust or volcanic ash were simulated by adding aerosols at a final particle concentration (PC) of 2 $mg.L^{-1}$ and 25 $mg.L^{-1}$ for the dust and ash treatments, respectively (see below for details about the aerosols). All treatments were performed in triplicate in 2.3 L polycarbonate bottles. Possible trace metal contamination of the surface SW from the added nutrient solutions was tested (see Annex VII §1).

Table V-1: Experimental nutrient and aerosol additions performed in triplicate at each station, with mono- and multiple nutrient additions: +Fe (2 $nmol.L^{-1}$ $FeCl_3$); +Si (2 $\mu mol.L^{-1}$ Na_2SiO_3); +FeSi (2 $nmol.L^{-1}$ $FeCl_3$ + 2 $\mu mol.L^{-1}$ Na_2SiO_3); +N (2 $\mu mol.L^{-1}$ $NaNO_3$); +NP (2 $nmol.L^{-1}$ $NaNO_3$ + 0.2 $\mu mol.L^{-1}$ KH_2PO_4) and single aerosol additions of +Dust (2 $mg.L^{-1}$) and +Ash (25 $mg.L^{-1}$). At station 11, simulated dry and wet deposition events were performed. The Control corresponds to unamended seawater.

Region	Station	Zone	Control	+Dust	+Ash	+Fe	+Si	+FeSi	+N	+NP
LNLC	2	STZ	x	dry	dry	x	x	x	x	x
LNLC	16	STZ	x	dry	dry	x	x	x	x	x
HN-LSi-LC	14	SAZ	x	dry	dry	x	x	x		
Plateau	A3	AZ	x	dry	dry	x	x	x		
HNLC	11	AZ	x	dry/wet	dry/wet	x				

Additional wet deposition events of dust and ash were simulated at HNLC-11 (Table V-1). Artificial rainwater (ARW) was prepared following the protocol described by Paris et al. (2011). Briefly, aerosols were added to ultrapure water (Millipore®, resistivity of 18.2 $M\Omega.cm^{-1}$) previously acidified with sulfuric acid (1‰ H_2SO_4 SupraPur® at 2.10^{-2} M, theoretical pH of 4.7). After a contact time of 60 min (PC of 100 $mg.L^{-1}$ dust and 1250 $mg.L^{-1}$ ash with n = 1), 2 % of the unfiltered ARW was added to the incubation bottles filled with unfiltered surface SW, thus obtaining the same PC as in the dry deposition mode. Subsamples were filtered through a 0.2 µm polycarbonate membrane for the detection of macronutrients and dFe concentrations in ARW.

Before aerosol/nutrient additions, one SW sample was taken for the determination of the initial PP, pigments and cellular abundances, and replicate samples (n = 3) were collected for macronutrient and dFe concentrations. After aerosol/nutrient additions, the microcosms were incubated for 48 h in on-deck incubators with circulating surface SW equipped with blue filters (Lee Filters) to simulate the appropriate irradiance encountered at 10 m depth. The PP was determined between 24 h and 48 h for all treatments, whereas the samples used for other analyses were collected at the end of the experiment (48 h).

2.3 Abiotic dissolution experiments

To monitor the abiotic release of nutrients in SW at all stations, 250 mL of 0.2 µm filtered surface SW were introduced into triplicate polycarbonate bottles and amended with the same aerosol PC and under the same deposition mode as in the bioassay experiments. An additional abiotic wet deposition performed at HNLC-11 consisted in adding 2 % of unfiltered ARW into 0.2 µm filtered SW. Bottles were then placed in the same experimental conditions than microcosms. Subsamples were collected after 48 h for the macronutrients and dFe concentrations. For back-calculations of Fe release in ash ARW, we used supplementary subsamples filtered after 12 h (refer to Equation V-1).

2.4 Characterization of dust and ash

2.4.1 Aerosol collection and deposition

Collection took place in remote areas using clean sampling techniques and samples were stored in double zip bags to avoid anthropogenic contamination.

2.4.1.1 Desert dust

The fine fraction (< 20 µm) of a Patagonian arid surface soil (south of Sierra Grande, Argentina, hereafter referred to as Pata) was used in all experiments. Dust from this region has been shown to reach the SO (Gili et al., 2016; Li et al., 2008). This material corresponds to the first top centimeters of the surface soil exposed to wind erosion. The soil was dry sieved in order to produce a dust analogue (Guieu et al., 2010), hereafter referred to as aerosol for simplification, according to the protocol described by Guieu et al. (2014). The dust PC used in this study (2 $mg.L^{-1}$) corresponds to an estimated deposition event of 9 $g.m^{-2}$ diluted in the upper first meters (see details in Annex VII§2). Local dust deposition rates in the SO are low (annual mean deposition of 8.0 $mg.m^{-2}.day^{-1}$ (Li et al., 2008)). Thus, this deposition rate

is probably overestimated for present-day conditions in the SOI and SO, but is assumed to be realistic for the Last Glacial Maximum (Conway et al., 2015; Mahowald et al., 1999) and for other offshore oceanic areas such as the modern open Mediterranean Sea (Ternon et al., 2010). The chosen PC is also in agreement with those used in several microcosm studies performed in LNLC and HNLC areas (e.g. Mills et al. 2004; Marañón et al. 2010; Mélançon et al. 2016).

2.4.1.2 Volcanic ash

The ash originated from the 2010 explosive eruption of the Eyjafjallajökull volcano (63°37'11" N, 19°36'54" W) in Iceland (hereafter referred to as Eyja), and was collected on the ground immediately after an ash fall event that occurred in Holtsa (~4–5 km from the volcano) on April 17th 2010. The ash sample was sieved at 100 µm to remove large particles that are not representative of the material transported over long distances in the atmosphere (Witham et al., 2005).

The present-day global deposition flux of volcanic ash is not known and annual estimates for the SO and SIO are not available. In this study, we used an ash PC of 25 mg.L^{-1}, corresponding to an estimated deposition event of 300 g.m^{-2}, *i.e.,* equivalent to a 0.2 mm-thick ash deposit (see details in Annex VII§2). This PC is on the same order of magnitude than the estimates reported for historical eruptions (e.g. Olgun et al. 2011) and comparable to previous bioassay experiments in the Atlantic sector of the SO (Browning et al., 2014).

2.4.2 Aerosol composition

Total P, Si and Fe of Pata and Eyja were measured after acid digestion (Fu, 2018) with Inductively Coupled Plasma Mass Spectrometry (ICP-MS 7500cx, Agilent) after alkaline fusion. The total N content was quantified with an isotope ratio mass spectrometer (IR-MS Delta V plus, Thermo Fischer Scientific) coupled with a C/N analyzer (Flash EA, Thermo Fisher Scientific).

The median particle diameter was calculated from volume size distribution measured by laser diffraction in ultrapure water (without ultra-sonication to avoid breaking up aggregates). Specific surface area (SSA) was determined by the Brunauer, Emmet and Teller (BET) gas adsorption method using nitrogen for dust (< 20 µm) and krypton for ash particles (< 100 µm). The mineralogical composition of the crystalline portion of aerosols was measured by quantitative X-ray diffraction (XRD) according to Nowak et al. (2018) and the proportion of the amorphous phase was determined by adding an internal standard.

2.5 Biological and chemical parameters

2.5.1 Primary Production

Net CO_2 fixation rates were determined using the ^{13}C-tracer addition method. One milliliter of $NaH^{13}CO_3$ (99 %, Eurisotop) was added 24 h after the beginning of incubation to 2.3 L polycarbonate bottles to obtain a ~10 % final enrichment. The bottles were vigorously shaken, and put back into on-deck incubators for additional 24 h. After incubation, 1 to 2.3 L were gently filtered using pre-combusted 25 mm Whatman™ GF/F filters and stored at -80 °C. The sample filters were dried at 40 °C for 48 h before analysis. Carbon in particulate matter and ^{13}C isotopic ratios were quantified using an online continuous flow elemental analyzer (Flash 2000 HT), coupled with an Isotopic Ratio Mass Spectrometer (Delta V Advantage via a conflow IV interface from Thermo Fischer Scientific). The atom% excess of the dissolved inorganic carbon (DIC) was calculated by using measured DIC concentrations at the LOCEAN laboratory (SNAPO-CO_2).

2.5.2 Cellular abundance

The cellular abundances of pico- and nanoeukaryotes (< 30 µm), cyanobacteria and heterotrophic bacteria were determined using a FACS Canto II flow cytometer, equipped with a 488 nm laser and the standard filter setup, according to the protocol detailed in Marie et al. (1999). Briefly, 1.5 mL SW were immediately fixed with glutaraldehyde and placed in the dark before being frozen and stored at -80 °C prior to analysis. Samples were thawed at room temperature and beads were added as an internal reference. Phytoplankton cells were analyzed (3 min at 100 µL.min^{-1}) and populations were discriminated on the basis of their forward (FSC) and side (SSC) scatters as well as their phycoerythrin and chlorophyll auto-fluorescence. For heterotrophic cells, samples were stained using SYBR Green-I, incubated in the dark and analyzed (2 min at 50 µL.min^{-1}).

2.5.3 Pigments

One to two liters of SW were filtered onto GF/F filters at initial time and after 48 h incubation, then immediately placed at -80 ºC prior to analysis at the SAPIGH analytical platform, Institut de la Mer (IMEV, Villefranche-sur-Mer, France). Filters were extracted at -20 ºC in 2 mL methanol (100 %) containing an internal standard (vitamin E acetate, Sigma©), disrupted by sonication and clarified one hour later by vacuum filtration through GF/F filters. The extracts were analyzed within 24 h on a complete Agilent© Technologies 1200 series

High Performance Liquid Chromatography (HPLC) system. The general procedure for HPLC pigment analysis, identification and quantification are described in Ras et al. (2008). The sampling at final time at the LNLC stations (2 and 16) could not be carried out due to the insufficient volume of SW remaining after the sampling of other parameters. Taxonomic pigments were used as size class markers of phototroph groups (pico-, nano- and microphytoplankton). The chemotaxonomic correspondence of HPLC-determined pigments and the associated size-class came from Uitz et al. (2006), as further presented in Annex VII§3.

2.5.4 Macronutrients

At initial time, SW for dSi, DIP and NOx determination was filtered on-line from the Go-Flo bottles through acid-cleaned 0.2 µm capsule filters (Sartorius Sartobran-P-capsule 0.45/0.2 µm). At final time (48 h in the abiotic experiments and 1 h in ARW), samples were filtered on acid-cleaned PALL Supor 0.2 µm polyethersulfone (PES) filters. Samples were stored at +5 °C (dSi) or -20 °C (DIP and NOx) prior to analysis. Dissolved Si and DIP were measured with a spectrophotometer (Thermo Fisher Evolution 220) according to the manual colorimetric methods of Grasshoff et al. (1999) and Murphy and Riley (1962), respectively. The concentration of NOx was measured with the SEAL AutoAnalyzer 3HR, according to Aminot and Kérouel (2007). Ammonium was not measured in this study. The detection limits were 0.03 µM dSi, 0.03 µM DIP and 0.08 µM NOx.

2.5.5 Dissolved iron

The same filtration protocol as for macronutrients was used for dFe samples. After filtration, the samples were acidified (0.2 % HCl Ultrapur) and stored at +5 °C before analysis. Dissolved Fe in SW was measured by ICP-MS coupled with an automated sample preconcentration system (SeaFAST) according to Wuttig et al. (2019), and dFe in ARW was measured by ICP-AES (Spectro Arcos). The detection limits were 0.005 nM in SW and 8.0 nM in ARW. Due to Fe contamination issues of the ash ARW samples during analysis, we estimated the Fe release and resulting solubility in ash ARW according to a back-calculation of dFe release after the addition of 2 % ash-containing ARW to the abiotic filtered SW:

$$\mathrm{dFe_{ARW}} = \Delta \mathrm{dFe_{SW.12h}} / 0.02 \qquad \text{Equation V-1}$$

where $dFe_{SW.12h}$ corresponds to the first available data point 12 h after addition of ARW in filtered SW. This calculated concentration might be biased by secondary Fe release and/or scavenging processes during the first 12 h in the SW matrix.

2.5.6 Data processing

The nutrient solubility of aerosols ($\%X_{sol}$, in %) was calculated as follows:

$$\%X_{sol} = \frac{dX - dX_0}{X_{tot}} \times 100 \qquad \text{Equation V-2}$$

where dX and dX_0 are the concentrations of a dissolved nutrient X at final and initial time, and X_{tot} is the amount of X in the added aerosol sample.

The contribution of each phytoplankton size class (x = *micro, nano or pico*) to the Tchla increase ($\Delta Tchla_x$, in %) in the nutrient/aerosol treatment *(trtm)* after 48 h relative to the mean control *(ctr)* after 48 h was assessed from:

$$\Delta Tchla_x = \frac{Tchla_x(trtm.48h) - Tchla_x(mean\ ctr.48h)}{Tchla(trtm.48h) - Tchla(mean\ ctr.48h)} \times 100 \qquad \text{Equation V-3}$$

The relative change (RC, in %) in each parameter was calculated as follows:

$$RC\ (in\ \%) = (C_{trmt.48h} - C_{ctr.48h}) \times 100 / C_{ctr.48h} \qquad \text{Equation V-4}$$

with C_{trtm}, the concentration of the parameter at 48 h and C_{ctr}, the mean of the triplicate controls at 48 h.

2.6 Statistical analysis

Means (n = 3) at final time in the biotic experiments were compared using a one-way ANOVA followed by a Fisher LSD means comparison test. When assumptions for ANOVA were not respected, the tests were performed on the log-transformed data or means were compared using a Kruskal–Wallis test and a post hoc Dunn test. Means of nutrient release for dust and ash in the abiotic experiments were compared the Student's t-test. Statistical tests were done using the XLSTAT software. The significance threshold was set to p-value < 0.05.

3 Results

3.1 Characterization of aerosols and nutrient release

3.1.1 Composition of aerosols

The mineralogy and nutrient content of dust and ash materials differ (Table V-2): Pata contains more N but less P and Fe than Eyja, and the Si content is similar for both aerosols. The SSA of Pata (< 20 µm) is nine times higher than Eyja (< 100 µm). Pata contains twice more clay than Eyja, which has a lower crystallinity. Compared to Saharan dust, which usually contains less than 10 % of feldspars (Journet et al., 2008), Pata dust is enriched in magmatic silicate minerals, including albite (18.6 wt.%, Table V-2), likely originating from the eruptive products emitted by nearby volcanoes (Simonella et al., 2015).

Table V-2: Mineralogical composition and total nutrient content (weight %) of the fine fraction of Pata (< 20 µm) and Eyja (< 100 µm) used in the bioassay and abiotic experiments. n.d. stands for 'not detectable'.

		Desert Dust (Pata)	Volcanic Ash (Eyja)
		Patagonia Argentina	Eyjafjallajökull Iceland
Mineralogy (%)	Lime stones	calcite 2.9	n.d.
	Acidic rocks	albite 18.6; quartz 6.2	albite 23.4; analcime 1.0
	Clays	illite 20.6; smectite 2.8	smectite 10.9
	(Hydr)oxides	n.d.	hematite 0.1
	amorphous	48.3	63.7
Specific surface area ($m^2.g^{-1}$)		62.1	7.3
	N (%)	0.09 ± 0.01	0.03
	P (%)	0.08 ± 0.01	0.18 ± 0.01
	Si (%)	25.8	26.47
	Fe (%)	4.55 ± 0.23	7.51 ± 0.28

3.1.2 Abiotic nutrient release

3.1.2.1 Dry deposition mode

Eyja released more dFe and DIP than Pata (Table V-3A) and similar amounts of dSi, whereas the NOx release by both aerosols remained undetectable. Compared to ash, dust solubility was more than ten times and four times higher for Si and Fe, respectively, whereas the released nutrient concentration was equal (dSi) or lower (dFe) (Table V-3A).

Table V-3. Means of N, P, Si and Fe release (concentration after the experiment minus initial SW or ARW concentrations) and solubility (%) of Pata and Eyja after 48 h of contact in 0.2 µm filtered surface seawater for particle concentrations of 2 mg.L^{-1} Pata and 25 mg.L^{-1} Eyja in **(A)** dry deposition mode (means at the five stations) in filtered SW and **(B)** in wet deposition mode (HNLC station 11 only). **(C)** Nutrient release and solubility after 1 h of contact with ARW at station 11 for particle concentrations of 100 mg.L^{-1} Pata dust and 1250 mg.L^{-1} Eyja ash. n.d. stands for 'not detectable'.

(A)	Released concentration	NOx, µM	DIP, µM	dSi, µM	dFe, nM
	Pata	n.d.	n.d.	0.2 ± 0.2 ^{a}	0.7 ± 0.6 ^{a}
	Eyja	n.d.	0.10 ± 0.05	0.3 ± 0.1 ^{a}	3.8 ± 1.6 ^{b}
	Solubility	N, %	P, %	Si, %	Fe, %
	Pata	n.d.	n.d.	1.25 ± 0.52 ^{a}	0.041 ± 0.035 ^{a}
	Eyja	n.d.	6.8 ± 3.4	0.11 ± 0.05 ^{b}	0.011 ± 0.005 ^{b}
(B)	Released concentration	NOx, µM	DIP, µM	dSi, µM	dFe, nM
	Pata	-0.5 ± 0.0	n.d.	-2.2 ± 0.6 ^{a}	0.7 ± 0.3 ^{a}
	Eyja	-0.4 (n=1)	0.4 ± 0.0	-1.2 ± 0.3 ^{b}	9.0 ± 0.1 ^{b}
	Solubility	N, %	P, %	Si, %	Fe, %
	Pata	< 0	n.d.	< 0	0.041 ± 0.017 ^{a}
	Eyja	< 0	29.7 ± 2.2	< 0	0.027 ± 0.000 ^{a}
(C)	Released concentration	NOx, µM	DIP, µM	dSi, µM	dFe, nM
	Pata	0.15 ± 0.03 ^{a}	1.65 ± 0.05 ^{a}	1.92 ± 0.10 ^{a}	47.2 ± 0.9 ^{a}
	Eyja	0.11 ± 0.01 ^{a}	15.41 ± 0.60 ^{b}	15.41 ± 0.24 ^{b}	856.7 ± 35.4 ^{b} *
	Solubility	N, %	P, %	Si, %	Fe, %
	Pata	2.18 ± 0.50 ^{a}	60.6 ± 1.8 ^{a}	0.21 ± 0.01 ^{a}	0.058 ± 0.001 ^{a}
	Eyja	0.38 ± 0.02 ^{b}	20.8 ± 0.8 ^{b}	0.13 ± 0.00 ^{b}	0.051 ± 0.002 ^{b} *

Note: Only detectable nutrient releases (mean concentrations after 48 h in the dust/ash treatments significantly different from means in the control at t-ini, p-value < 0.05) are shown. Means that are not significantly different between dust and ash treatment for each element are labeled with the same superscript letter *a* or *b* (p > 0.05). Negative dissolution values express a decrease of NOx or dSi in SW after ARW addition. * Fe release and solubility of Eyja ash in ARW are estimated according to Equation V-1.

3.1.2.2 Wet deposition mode

The nutrient release by ash in SW after the addition of 2 % ARW was higher for dFe and DIP compared to dust (Table V-3B). Dissolved Fe and DIP concentrations in SW that were released after a wet compared to a dry deposition event were similar for Pata and higher for Eyja (Table V-3A and B). Surprisingly, the wet deposition induced a decrease in dSi and NOx concentrations (Table V-3B) whereas both aerosols were a source of dSi only in dry deposition mode.

With a 12.5-fold higher PC in ARW, Eyja released about eight times more dSi and DIP and 18 times more dFe in ARW than Pata, whereas the release of NOx was similar for both aerosols (Table V-3C). The solubility of all tested nutrients from Pata was higher relative to Eyja in ARW.

3.2 Initial features of the incubated seawater

The surface SW at the studied stations had contrasted physico–chemical and biological features (Table V-4), displaying a southward decrease in SST and SSS and an increase in macronutrients. At the LNLC stations (2 and 16), the molar NOx/DIP ratio was notably lower than the Redfield ratio (16/1, Redfield 1934). The low dSi concentrations at HN-LSi-LC-14 and Kerguelen-A3 led to molar dSi/NOx ratios lower than the optimal ratio for diatoms (Si/N = 1.12 ± 0.33, Brzezinski, 1985), whereas the nutrient ratio at HNLC-11 was closer to the optimal value (Table V-4). The NOx and DIP concentrations were the highest at the AZ stations (A3 and 11), whereas the highest dFe concentration (0.54 nM) was recorded at LNLC-2 and the lowest at HNLC-11 (Table V-4).

The LNLC stations were characterized by the lowest phytoplanktonic biomass, dominated by picophytoplankton. The PP at HN-LSi-LC-14 was over seven times higher than at the LNLC stations and the algal biomass was dominated by nanophytoplankton (mainly nanoflagellates and chromophytes, data not shown). The highest PP and Tchla were recorded at Kerguelen-A3 where the phytoplankton community was largely dominated microphytoplankton (Table V-4) and mainly diatoms. The PP at HNLC-11 was eight times lower relative to Kerguelen-A3, and the phytoplankton community was co-dominated by nano- and microplankton.

Table V-4. Initial physico-chemical and biological properties of the surface seawater used for the microcosm experiments. Mean nutrient concentration ± standard deviation of replicates (*n* = 3). DL = detection limit. PP = primary production; Tchla = total Chlorophyll a. Phytoplankton size fractions according to Uitz et al. (2009): pico: 0.4-2 µm, nano: 2-10 µm, micro: > 10 µm.

Station	2	16	14	A3	11
Zone	STZ	STZ	SAZ	AZ	AZ
Region	LNLC	LNLC	HN-LSi-LC	Plateau	HNLC
Latitude, degrees S	29.97	35.00	42.49	50.64	56.50
Longitude, degrees E	54.11	73.47	74.90	72.05	62.99
Sampling date	12 Jan 2019	05 Feb 2019	30 Jan 2019	27 Jan 2019	23 Jan 2019
Temperature, °C	24.6	22.0	12.8	4.4	2.1
Salinity	35.47	35.48	34.49	33.83	33.83
NOx, µM	< DL	< DL	8.11±0.41	20.60±0.77	25.25±0.01
DIP, µM	0.03±0.00	0.09±0.01	0.65±0.02	1.04±0.05	1.58±0.16
dSi, µM	1.79±0.05	1.61±0.05	0.99±0.00	1.59±0.06	16.67±0.15
NOx/DIP	< 2.7	< 0.9	12.5	19.8	16.0
dSi/NOx	> 22.4	> 20.1	0.12	0.08	0.67
dFe, nM	0.54±0.12	0.37	0.39	0.35±0.13	0.27±0.02
Synechococcus, cells.mL^{-1}	1 703	< DL	13 620	349	< DL
picoeukaryotes, cells.mL^{-1}	452	882	5 786	401	571
nanoeukaryotes, cells.mL^{-1}	339	209	2 798	644	1 176
heterotrophic bacteria, cells.mL^{-1}	655 782	547 742	1 310 728	615 636	441 028
PP, mg C.m^{-3}.d^{-1}	2.78	3.67	26.7	54.42	7.24
Tchla, µg.L^{-1}	0.085	0.049	0.603	1.40	0.157
% micro	13	10	28	92	45
% nano	24	28	54	7	54
% pico	63	62	18	1	2

3.3 Biological responses

3.3.1 Primary production

Except at LNLC-16, the PP significantly increased after dust or ash additions (Figure V-2), as well as after a Fe or Si addition. The highest increase was observed at Kerguelen-A3 (+105 % for aerosol additions). No significant difference was observed after Fe addition alone or in combination with Si. At the LNLC stations, N and NP additions led to the highest PP increase.

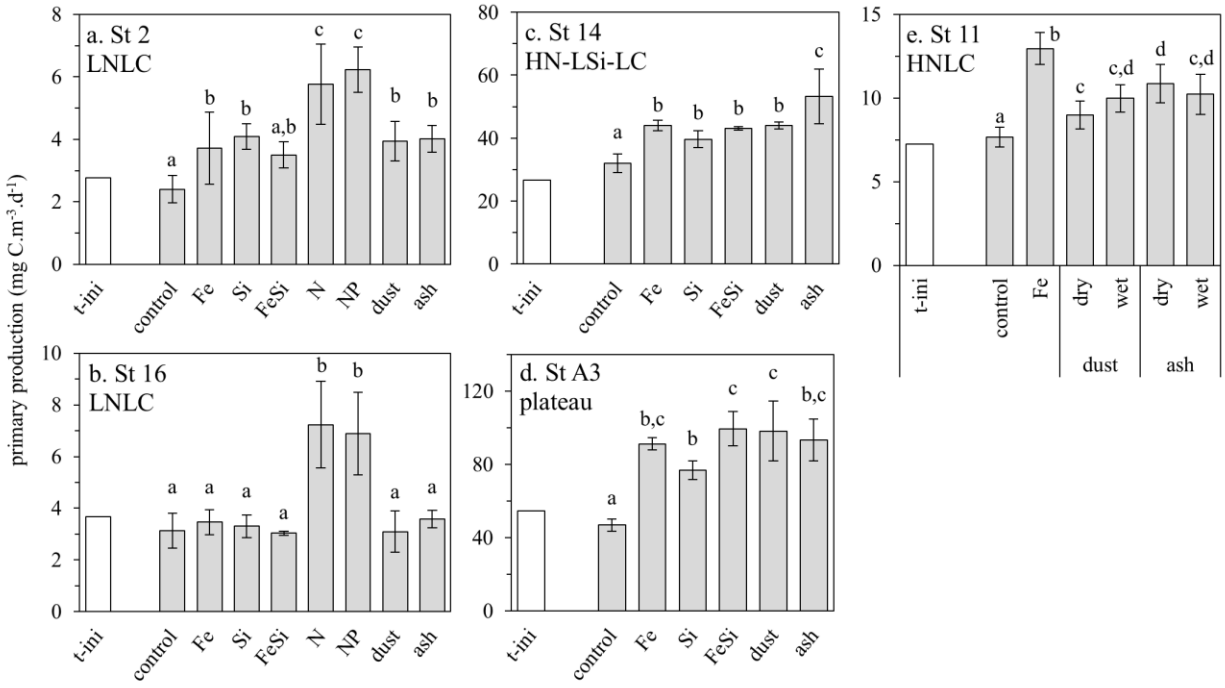

Figure V-2. Primary production (PP, mg $C.m^{-3}.d^{-1}$) at the beginning of the experiment (t-ini, white bars) and after 48 h of incubation for each treatment at the stations LNLC St 2 (a) and 16 (b), HN-LSi-LC St 14 (c), plateau St A3 (d) and HNLC St 11 (e). Error bars indicate standard deviation of triplicates. Means that are not significantly different ($p > 0.05$) are labeled with the same letter within a station.

3.3.2 Cellular abundances

Aerosol additions had a contrasted impact on cellular abundances (< 30 µm) according to the phytoplankton class, the aerosol type and the station (Figure V-3). In the LNLC area, picoeukaryotes were more stimulated by dust than by ash addition at LNLC-2 (+96 % and +50 %, respectively), whereas only ash stimulated their growth at LNLC-16 (+38 %, Figure V-3a,d). Additions of both aerosol types had a similar effect on *Synechococcus* (~+70 % at St. 2, Figure V-3c), and no impact on nanoeukaryotes at these stations.

At HN-LSi-LC-14, ash addition enhanced picoeukaryote abundance (+32 %, Figure V-3f), whereas dust stimulated nanoeukaryotes and heterotrophic bacteria (+44 %, Figure V-3j and +36 %, see Supplementary Material in Annex VII, Figure VII-2). On the contrary, at Kerguelen-A3, dust and ash triggered similar responses in phytoplanktonic abundances, which increased by 140, 75 and 40 % for *Synechococcus*, pico- and nanoeukaryotes, respectively (Figure V-3i-k). Moreover, ash also stimulated heterotrophic bacteria (+30 %, Figure VII-2). At HNLC-11, a wet and dry addition of dust or ash induced only a stimulation of the nanoeukaryote abundance (~+40 %), similar to that after nutrient addition (Figure V-3m).

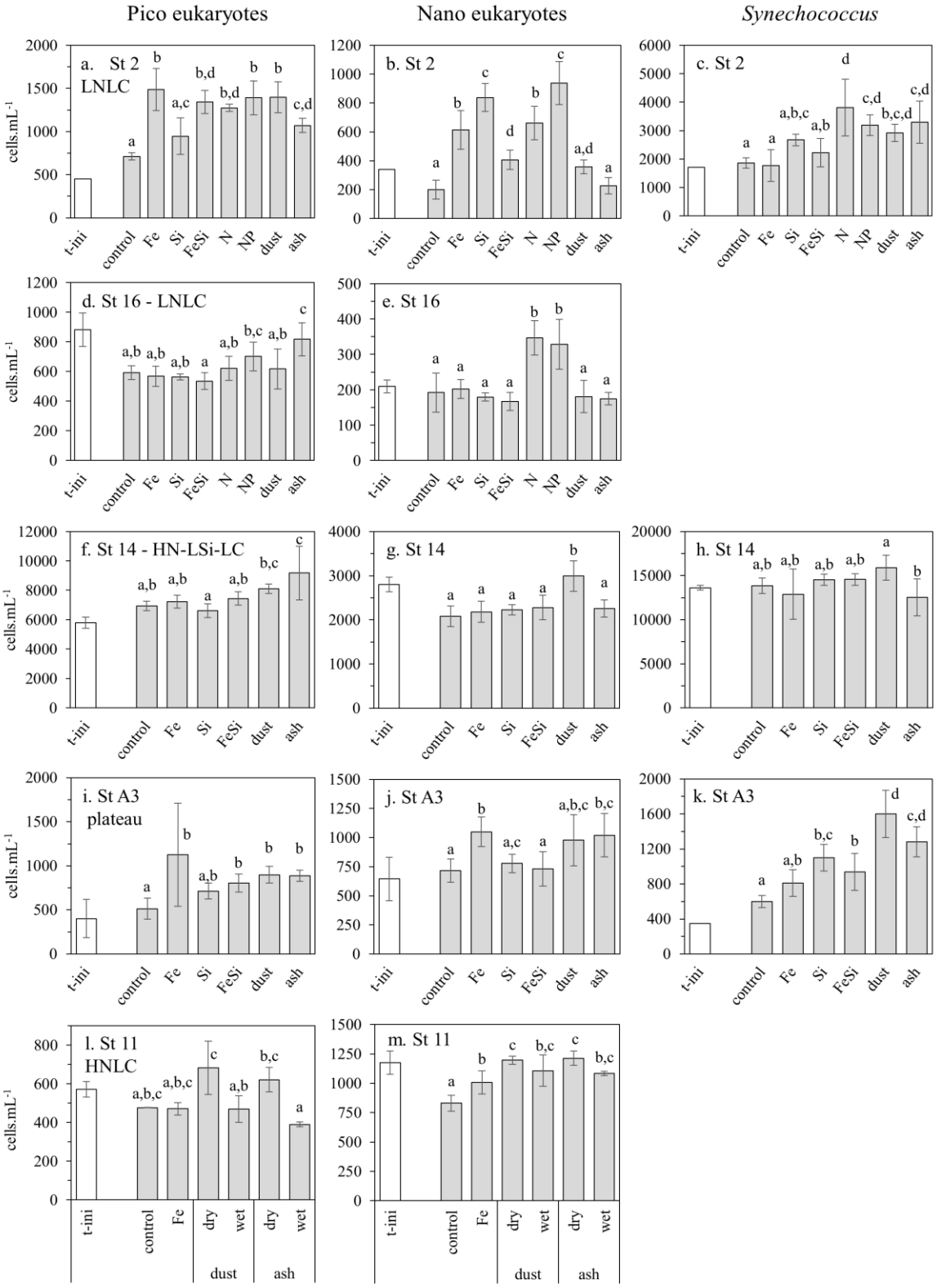

Figure V-3. Cell abundance (cells.mL^{-1}) of pico eukaryotes (a,d,f,i,l), nano eukaryotes (b,e,g,j,m) and Synechococcus (c,h,k) at the beginning of the experiment (t-ini, white bars) and after 48 h of incubation for each treatment at the LNLC St 2 (a-c) and 16 (d-e), HN-LSi-LC St 14 (f-h), plateau St A3 (i-k) and HNLC St 11 (l-m). Error bars indicate standard deviation of triplicates. Means that are not significantly different ($p > 0.05$) are labeled with the same letter within a station.

3.3.3 Pigments

The addition of aerosols or nutrients induced an increase in both Tchla and fucoxanthin concentrations relative to the controls at t48 h at stations 14, A3 and 11 (Figure V-4). At Kerguelen-A3, these increases were higher after ash compared to dust addition (Figure V-4b,e), whereas they were similar at HN-LSi-LC-14 and HNLC-11.

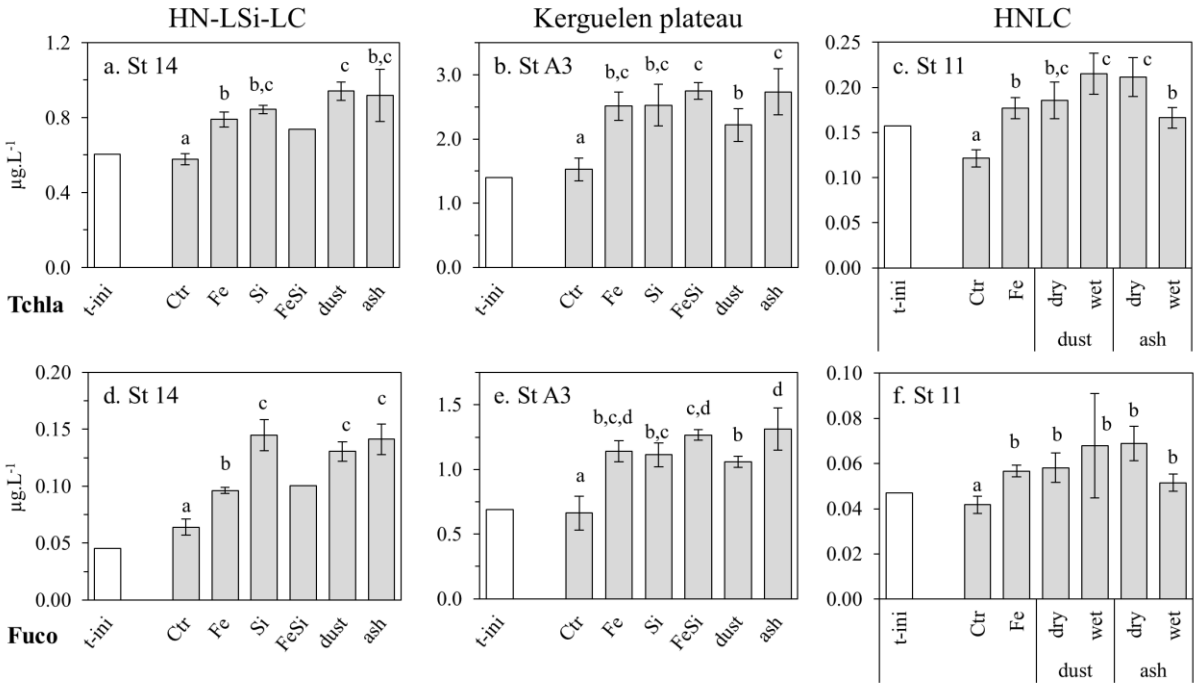

Figure V-4: Pigment concentration (µg.L^{-1}) of total Chlorophyll-a (a-c) and fucoxanthin (d-f) at the beginning of the experiment (t-ini, white bars) and after 48 h of incubation for each treatment at HN-LSi-LC St 14 (a,d), plateau St A3 (b,e) and HNLC St 11 (c,f). Error bars indicate standard deviation of triplicates. FeSi treatment at St 14 is not included in statistics, due to n = 1. Means that are not significantly different ($p > 0.05$) are labeled with the same letter within a station.

At these three stations, the addition of aerosols or nutrients benefited mostly microphytoplankton, and in particular diatoms, which sustained from 52 up to 100 % of the Tchla increase (Figure V-5). The community structure was thus modified at these stations (Annex VII, Figure VII-1). Interestingly at HN-LSi-LC-14, while the respective contribution of diatoms and dinoflagellates to Tchla were quite similar in the control at t48 h (~15%, Figure VII-1a), the diatom contribution doubled after ash and Si additions, whereas that of dinoflagellates did not change.

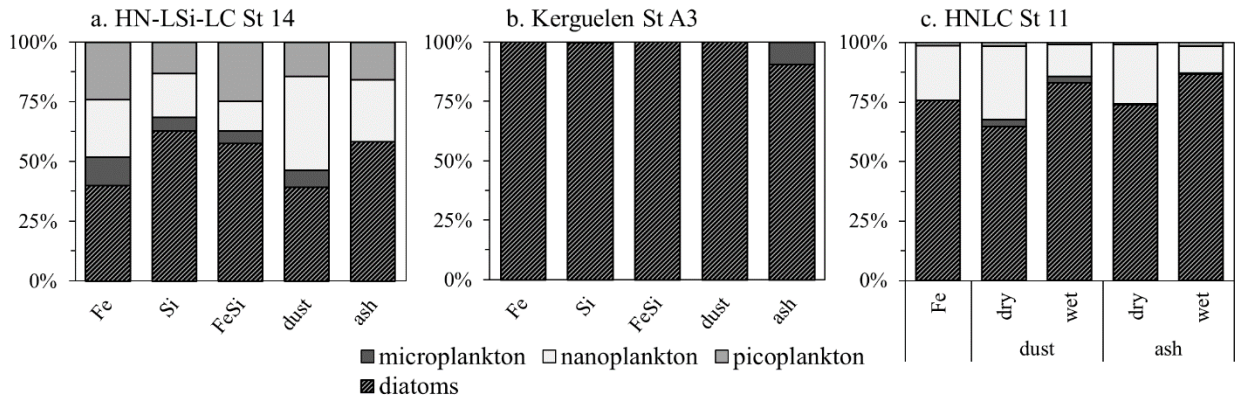

Figure V-5: Size depending relative contribution to Tchla increase (%) after 48 h of incubation for each treatment relative to control at HN-LSi-LC St14 (a), Kerguelen St A3 (b) and HNLC St 11 (c), with micro- (dark), nano- (light) and picophytoplankton (median grey). Diatom contribution within the microplankton size fraction is dashed.

4 Discussion

The abiotic experiments (Table V-3) demonstrated that the dust and ash samples released significant amounts of Fe and Si to SW. However, none of these materials acted as a source of NOx in SW (Table V-3). These findings are consistent with previous abiotic studies performed with Saharan dust (Mills et al., 2004; Ridame et al., 2014b) and ash specimens (Browning et al., 2014; Jones and Gislason, 2008). Arguably, Pata and Eyja relieved or reduced the ambient Fe and/or Si limitations of PP in the SO but were not able to alleviate the N limitation in the SIO (Figure V-2).

Moreover, we cannot exclude a bias caused by grazing, as we did not remove zooplankton predators from the natural plankton community prior to the incubation experiments.

4.1 Phytoplankton response to aerosol additions

4.1.1 LNLC stations

Interestingly, the phytoplankton response to aerosol additions were contrasted between the LNLC stations: aerosols led to a significant PP increase at the western LNLC-2, whereas no change was observed at the eastern LNLC-16. This difference can be related to the initial nutrient limitation: the eastern station was N-limited, as previously shown by Twining et al. (2019), whereas the PP in the western station was N, Fe and Si-limited (Figure V-2a), and dust and ash stimulated significantly the picoeukaryotes and *Synechococcus* abundances at LNLC-2. The detection of *Prochlorococcus*-specific pigments at initial time at these stations

(16–30 ng.L^{-1} of divinyl-chlorophyll a) without flow cytometric detection might indicate that the cell fluorescence was too low to be detected by cytometry. As pigment content could not be analyzed at final time at these stations, we cannot conclude on the response of microphytoplankton to the nutrient/aerosol additions.

Despite a generally low seasonality within the STZ, the three-week difference in the sampling time between the western and eastern stations (Table V-4) may contribute to the differences in the initial nutrient dynamics and the phytoplankton community structure, leading to different biological responses. Moreover, the community at the western station may be influenced by the South East Madagascar Bloom (Figure V-1a), explaining an initial algal biomass twice as high at the western compared to the eastern station which lies in more typical oligotrophic waters.

Moreover, heterotrophic bacteria (stimulated after FeSi and NP additions at the eastern LNLC-16, Annex VII, Figure VII-2) may compete for nutrient uptake and thus explain the limited autotroph response, as already observed in the oligotrophic tropical Atlantic (Marañón et al., 2010).

4.1.2 HN-LSi-LC station

The about ten times lower dSi/NOx ratio compared to the optimal ratio for diatoms (Si/N=1.12, Brzezinski, 1985) suggests a potential Si limitation of the diatom activity at HN-LSi-LC-14, as demonstrated by PP increase (Figure V-2c) and previous studies in the Indian (Sedwick et al., 2002) and Australian (Hutchins et al., 2001) sectors of the SAZ. Diatoms responded equally to dust, ash and Si additions (Figure V-4d), indicating that the diatom Si-limitation could be alleviated by aerosol input. In the abiotic experiment, a dry deposition of dust or ash released around 0.3 µM dSi (Table V-3A), which indicates that the initial Si-limitation could be eased with a relatively low absolute release, representing +20 to +33 % of the initial stock. Despite the low contribution of diatoms to the initial biomass, their strong development after aerosol addition explained roughly half of the increase in Tchla (+39 and +60 % for dust and ash, respectively, Figure V-6) as already reported within the Australian SAZ after Fe and/or Si additions (Hutchins et al., 2001). Thus, pico- and nanoeukaryotes may be less competitive than diatoms for new nutrient uptake.

The *Synechococcus* abundance, which was the highest at this station, did not change after new nutrient supply. This suggests that this species was either not nutrient-limited, and/or could not benefit from this addition and/or was subjected to important grazing, as previously described by Hutchins et al. (2001) in the SAZ of the Australian sector of the SO.

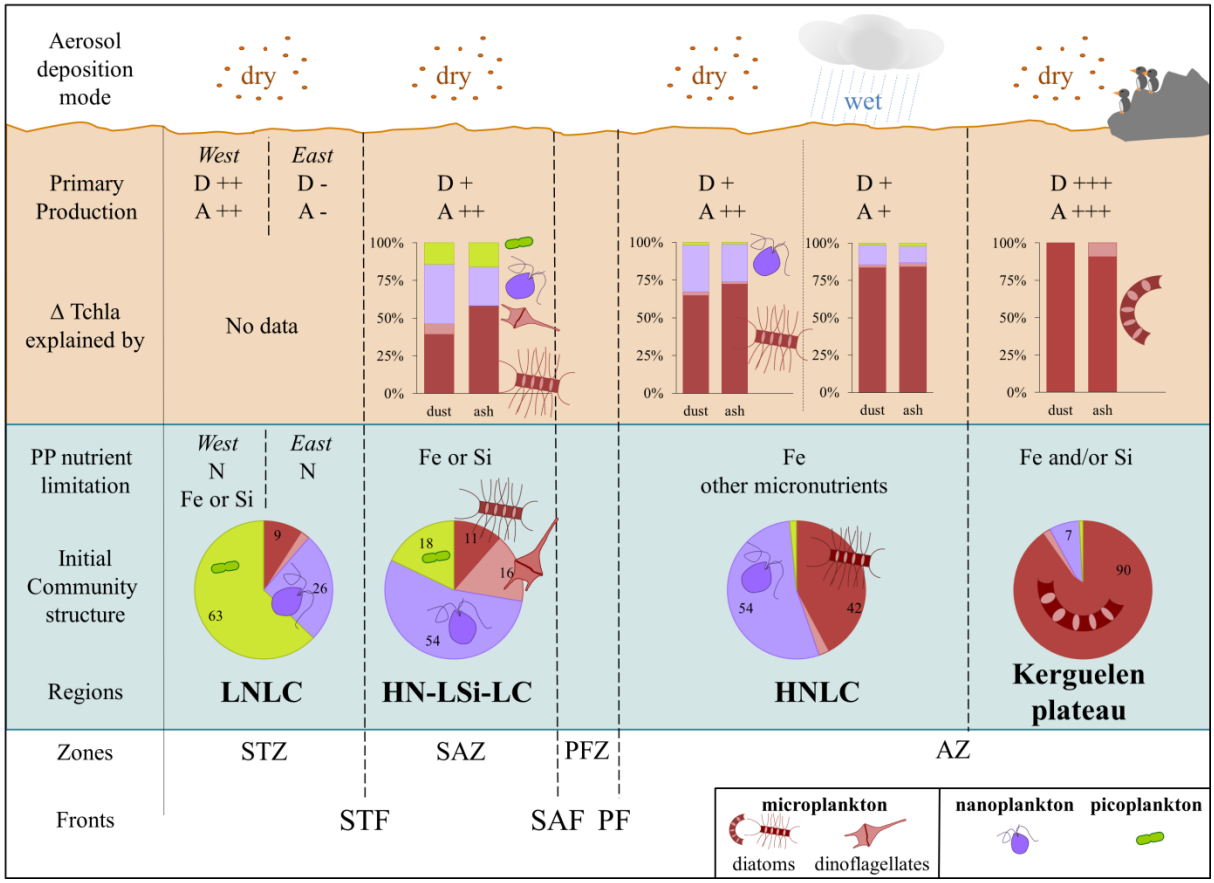

Figure V-6. Schematic representation of the biological response of phytoplankton communities after dry or wet dust (D) and ash (A) deposition to the sea surface within different biogeochemical regions of the South Indian Ocean and Southern Ocean. The top part of the figure (orange box) shows the phytoplankton response to aerosol deposition (PP and ΔTchla), while the bottom part (blue box) represents the initial conditions prior to deposition (nutrient limitation and phytoplankton structure).

Primary production is expressed in relative change (%), as follows: +++ above 100%; ++ above 50%; + below 50%; − no significant change compared to control. ΔTchla shows the contribution (%) of different phytoplankton classes explaining the global increase in Tchla. The community composition (initial and final) is based on the pigment signature, with red: microplankton (dark: diatoms and light: dinoflagellates), purple: nanoplankton and green: picoplankton. The schema concerns solely the surface layer and response after 48 h, regardless of depth and particle sinking.

The represented taxa are representative for the SO: microplankton: *Eucampia* and *Chaetoceros* (coastal and open ocean diatoms, respectively), *Ceratium* (dinoflagellate); nanoplankton: *Phaeocystis* (haptophyte); pico-plankton: *Synechococcus* (cyanobacteria). Zones and fronts (from North to South): Subtropical Zone and Front (STZ and STF); Subantarctic Zone and Front (SAZ and SAF); Polar Front Zone and Polar Front (PFZ and PF); and Antarctic Zone (AZ).

4.1.3 HNLC station

The PP of HNLC-11 was mainly Fe limited, despite a higher surface dFe concentrations in this study compared to published data from the same ocean area and season (KEOPS-1, January–February 2005) (Blain et al., 2008a). The measured dFe concentration was however comparable to the same stations during austral spring (KEOPS-2, October–November 2011) (Bowie et al., 2015), as well as to the central Indian and Atlantic sectors of the SO (Chever et al., 2010; Grand et al., 2015a).

At this station, we compared the phytoplankton response to both dry and wet deposition modes, well-known to influence nutrient solubility (Chester and Jickells, 2012; Duggen et al., 2010). Dust and ash, as well as Fe addition led to a stimulation of PP and Tchla, confirming that dry and wet depositions of dust and ash were a significant source of bioavailable Fe for phytoplankton and more specifically for diatoms. This confirms also the results from the abiotic experiment (Table V-3) and the previous studies in HNLC areas (Browning et al., 2014; Langmann et al., 2010a; Mélançon et al., 2014). Interestingly, in the Atlantic sector of the SO, Trimborn et al. (2017) found no biological response after four to eight times lower Fe and dust additions than in our study, suggesting that there is a required dFe threshold to observe phytoplankton response in the severely Fe-limited SO (Boyd et al., 2010).

4.1.4 Kerguelen plateau station

Aerosol additions triggered a PP increase similar to that observed after Fe and/or Si additions, indicating a Fe and Si growth limitation that can be explained by the low dSi concentration at Kerguelen-A3 (10.5 times lower than at HNLC-11) and the season in late summer (end of January) at the end of the diatom bloom (Closset et al., 2014; Timmermans et al., 2008).

The plateau station was initially dominated by diatoms which also explain the major increase in Tchla (Figure V-6) after an aerosol/nutrient deposition. Surprisingly, *Synechococcus* abundance increased after Si addition. Silicon is not recognized as a nutrient for cyanobacteria, but Si bioaccumulation within pico-cyanobacteria such as *Synechococcus* has already been observed in the West Pacific and Sargasso Sea as well as in cultured strains (Baines et al., 2012; Krause et al., 2017; Wei et al., 2021). However, to our knowledge, such silicifying *Synechococcus* have not yet been detected near Kerguelen Islands.

Kerguelen-A3 was the most productive station (Table V-4) and also the station where the highest biological increase was observed after aerosol/nutrient additions, with a mean relative change in PP of 100 % (Figure V-2d), compared to ~46 % at HNLC-11. The variability in the intensity of the biological response between the plateau and surrounding open ocean

populations could be explained by a precondition of the Kerguelen phytoplankton community to frequent nutrient supply from the sediment through winter mixing, accelerating the response to aerosol addition. The HNLC population is acclimated to Fe limiting concentrations, and it may require a longer period of time to reach maximal biological response. Thus, the short time scale of our experiments (48 h) may not have been sufficient to overcome the lag phase. A similar phenomenon has been described by Moore et al. (2007) during the CROZEX in situ Fe addition experiment in the same sector of the SO, where the biological response occurred mostly after three days of incubation. Similarly, Timmermans et al. (2008) observed a twice longer lag phase (12 versus 6 days) in their HNLC phytoplankton experiment compared to the Kerguelen plateau phytoplankton community during translocation experiments.

4.2 Influence of physico–chemical parameters on nutrient release

4.2.1 Aerosol type: importance of origin and mineralogy

Surprisingly, the biological response induced by a dry deposition of the two aerosol types was similar, independently of the studied biogeochemical area or the phytoplankton size class. In our experiment, we observed identical Si release despite different PC, a result reflecting a significantly higher Si solubility in dust than ash (Table V-3A), that could be (partly) due to higher SSA, combined to the differences in mineralogy (Table V-2) with variable solubilities and dissolution kinetics (Geisen, 2021).

At LNLC-2 and Kerguelen-A3, the PP increase occurred regardless of the nature of the added aerosol. At these stations, no significant difference in PP was observed between dust, ash and Fe additions, suggesting that the Fe released by aerosols may be bioavailable and sufficient to relieve the ambient Fe-limitation. It is likely that the Fe-limitation was not very severe at these stations and that the mean 0.7 nM dFe provided by dust deposition was sufficient to reach the maximal response rate of cell division and PP. The LNLC community remained nonetheless N limited.

In contrast, at HNLC-11 and HN-LSi-LC-14, a dry deposition of ash triggered around twice more PP than a dry deposition of dust ($p < 0.05$). At station 11, Fe addition induced more PP increase than aerosols, which suggests that unknown synergistic effects between the released elements weakened the positive effect of Fe release (Hoffmann et al., 2012; Paytan et al., 2009) or that the local communities were differently influenced by the direct nutrient supply of the Fe solution compared to the potentially more gradual nutrient dissolution from the

aerosols. The greater PP response after the addition of ash compared to dust or nutrients may indicate that other micronutrients (such as manganese, e.g. Frogner et al. 2001) released by Eyja ash could relieve additional PP limitations at HN-LSi-LC-14 and HNLC-11 in dry deposition mode.

4.2.2 Deposition mode

The addition of dust and ash in both dry and wet deposition modes performed at the HNLC station 11 enabled to compare the influence of the initial contact medium on nutrient release, with varying pH (8.1 and 4.7 for sea- and rainwater, respectively) and ionic charge, as well as the presence of dissolved organic matter in natural SW. Fe dissolution of dust particles is known to decrease with increasing pH (Desboeufs et al., 1999; Journet et al., 2008; Paris et al., 2011), whereas organic matter, and in particular the presence of Fe-binding ligands, increases Fe solubility and bioavailability in SW (Hassler et al., 2011; Paris and Desboeufs, 2013; Wagener et al., 2008). Thus, nutrient release may be impacted by a complex array of antagonistic parameters.

In our abiotic experience, the highest Fe solubility for dust and ash occurred in ARW (Table V-3C). Moreover, although the deposition mode did not significantly influence the dFe release from dust to SW (0.7 nM after 48 h of contact, Table V-3A,B), ash released 2.4 times more Fe to SW in wet compared to dry deposition mode (9.0 and 3.8 nM, respectively). The addition of 2 % ARW to SW should theoretically release 0.94 and 17.1 nM dFe to SW after wet dust or ash deposition. The difference between the measured wet deposition and theoretical release (significant only for ash deposition) may indicate that Fe adsorption and/or precipitation processes dominate over secondary Fe dissolution in the SW. Moreover, the quality and quantity of organic matter in the SW may explain the high variability in Fe solubility, as previously reported (Bressac and Guieu, 2013; Wagener et al., 2008).

A wet deposition of either aerosol induced a moderate increase in PP (~+40 %, Figure V-2e), intermediate between the higher impact of dry ash deposition (+50 %) and a lower reaction after a dry dust deposition (+24 %). Equally, Tchla and fucoxanthin increases were independent of the dust deposition mode, consistent with the equal abiotic Fe dissolution, indicating that the Fe released by both mechanisms was equally bioavailable.

5 Conclusions

Our results from incubation experiments demonstrate that the desert dust and volcanic ash materials, despite contrasted mineralogical and chemical composition released significant amounts of Fe and Si to seawater in the Indian and Southern Oceans. A representative deposition of both dust and ash was sufficient to trigger a phytoplankton response, mainly driven by a stimulation of the diatom community (Figure V-6). Ash addition elicited an equivalent or greater biological response than dust, depending on the severity of the initial Fe-limitation. However, neither the tested dust nor the ash was a significant source of NOx.

After dust or ash additions, the maximum relative and absolute increase in PP was observed at the most productive station over the Kerguelen Plateau, whereas the lowest relative response was found at the HNLC station despite similar nutrient limitations. We hypothesize that acclimation of the ambient phytoplankton community to either frequent nutrient supply through winter mixing, causing a rapid doubling of the PP or, on the contrary, scarce nutrient supply induced an initial lag phase and thus a longer time laps before reaching a maximum response. Moreover, the HNLC phytoplankton community was only slightly affected by a wet rather than a dry deposition of aerosols, as the dominant diatom community responded equally to both deposition modes.

Future work should focus on the dissolution and possible bioavailability of other trace elements such as manganese and cobalt dissolved from dust and ash particles (Fishwick et al., 2018) as these may also limit phytoplankton growth in the open ocean (Mackey et al., 2012; Perron et al., 2020). Since the seasonal and spatial variability of organic matter concentration in surface seawater may impact nutrient dissolution and scavenging processes (de Leeuw et al., 2014), its influence on the response of phytoplankton to aerosol additions should also be investigated (Bressac and Guieu, 2013; Hernández-Ruiz et al., 2020).

Moreover, nutrient bioavailability in the SO may be disturbed in the future, according to climate change predictions (Deppeler and Davidson, 2017). Predicted changes in the SO for 2100 include increased sea surface temperature, and around twice higher CO2 concentrations leading to ocean acidification. While dust deposition to the SO has doubled during the 20th century (McConnell et al., 2007) and is thought to further increase, the pycnocline and mixed layer depth will become shallower (Deppeler and Davidson, 2017). Thus, more aerosols should dissolve in a lower volume of warmer, fresher and more acidic surface ocean, increasing PC and nutrient release (Deppeler and Davidson, 2017). Thus, further research is

needed to better constrain the evolution of aerosol load and associated nutrient bioavailability in a changing ocean.

Acknowledgments

The study has been financed by the French Research Program LEFE (Les Enveloppes Fluides et l'Environnement) through BISOU and ITALIANO projects and by the DADDY project supported by IPSL. We thank INSU and the French oceanographic fleet ('Flotte océanographique française") for financial and logistic support to the OISO program and the VT163/OISO-29 oceanographic campaign (https://doi.org/10.17600/18000972). We thank the PACHIDERM analytical platform (LEMAR) for NOx and trace metal analysis; I. Djouraev (LOCEAN) for ICP-MS analysis at the Alysés platform, IRD; M. Benrahmoune and F. Kaczmar (LOCEAN) for managing clean labs and help in sample processing; F. Fu (LISA) for acid attack of aerosols; M. Mandeng-Yogo (LOCEAN) for IR-MS and CN analysis at the Alysés platform, IRD; S. Nowak (LISA) for XRS analysis at Paris Diderot University; I. Obernosterer and P. Catala (LOMIC) for inter-comparison of flow cytometric data; L. Sicard (ITODYS) and M. Jean Pierre (LISA) for nitrogen BET analysis and C. Vaulot (IS2M) for SSA for krypton BET analysis. D. Lannuzel, B. Moriceau and two anonymous reviewers are thanked for providing relevant comments on the manuscript.

Conflict of Interest

The authors declare no competing interests.

Data Availability Statement

The dataset is available at the address: **https://www.seanoe.org/data/00696/80825/**

VI. Dissolution of macro (Si, P, N) – and micronutrients (Fe, Mn, Co) in natural and artificial seawater after simulated volcanic ash and desert dust deposition in the Southern Indian Ocean

Carla Geisen[1], Céline Ridame[1], Emilie Journet[2], Pierre Delmelle[3], Claire Lo Monaco[1], Nicolas Metzl[1], Joelle Kombo[1], Morgane Gallinari[4], Damien Cardinal[1]

[1]Sorbonne Université, LOCEAN – IPSL Laboratoire d'Océanographie et du Climat : Expérimentations et Approches Numériques, UMR 7159, (SU CNRS MNHN IRD), 75252 Paris Cedex 05, France. [2]LISA (Laboratoire Interuniversitaire des Systèmes Atmosphériques), UMR 7583, CNRS, Université Paris-Est Créteil et Université de Paris, Institut Pierre Simon Laplace (IPSL), Créteil, France. [3]Earth and Life Institute, Environmental Sciences, UCLouvain, B-1348 Louvain-la-Neuve, Belgium. [4]LEMAR (Laboratoire des Sciences de l'Environnement Marin, UMR 6539, Institut Universitaire Européen de la Mer, Brest, France.

Corresponding author: Carla Geisen (carla.geisen@locean.ipsl.fr)

In prep.

1 Introduction

The Southern Ocean (SO) is delimited by several ocean fronts that divide this vast ocean region from North to South into individual water masses with different biogeochemical features such as shifts in the surface temperature (Chapman et al., 2020; Orsi et al., 1995). The fronts act as physical boundaries, and the specific nutrient limitations within individual water masses initiate contrasting ecological habitats with phytoplankton groups acclimated to local variable nutrient conditions (Hörstmann et al., 2021).

North of the subtropical front, picoplankton dominated the Low Nutrient Low Chlorophyll (LNLC) waters (Estrada et al., 2016) where all macronutrients and mainly nitrogen (N) and to a lower extent phosphorous (P) are limiting the phytoplankton growth (Geisen et al., submitted). Further south, the High Nitrogen Low Silicon Low Chlorophyll (HN-LSi-LC) region of the Subantarctic zone is iron (Fe) and/or silicon (Si) limited and nanoeukaryotes dominate the phytoplankton community (Sedwick et al., 2002). South of the polar front in the High Nutrient Low Chlorophyll (HNLC) region, the concentrations of macronutrients are high but Fe is scarce; diatoms and nanoeukaryotes are the main primary producers (Blain et al., 2002; Geisen et al.,submitted). Finally, there are particular regions within the Southern Ocean such as around the Kerguelen plateau which is naturally fertilized in micronutrients such as Fe (Blain et al., 2008a) and where diatoms are the dominant phytoplankton.

The SO is known to be the vastest HNLC region of the world ocean due to the low input of new micronutrients, especially Fe (Martin, 1990; Moore et al., 2002). Thus, aerosols constitute an important source of new macro- and micronutrients to the open surface ocean (Cassar et al., 2007; Chester and Jickells, 2012) and the deposition of mineral dust is one of the main supply mechanisms of new Fe in the SO (Boyd and Ellwood, 2010). Moreover, past and present volcanism contributes temporally and locally to trace metal deposition (Gaiero et al., 2003).

Aerosols reach the sea surface through either gravitational settling of particles, also called dry deposition, or after a primary encounter of the aerosol particle with atmospheric water such as cloud or rain droplets, inducing a wet deposition. These two pathways are known to modify the physico-chemical parameters of the aerosol in different ways and thus alter its solubility (Jickells and Spokes, 2001). Several aerosol dissolution studies have been performed in the Mediterranean Sea (review Guieu and Ridame, 2020) and tropical Atlantic (*e.g.* Baker et al., 2007; Korte et al., 2018) and Pacific Oceans, but the aerosol dissolution remains less studied in the SO (Li et al., 2008).

Thus, we aim at studying the nutrient solubility from two contrasting natural aerosols that are desert dust and volcanic ash in the variable biogeochemical regions of the Southern Indian Ocean where macro- and micronutrient disposability has been shown to limit phytoplankton growth. By performing abiotic dissolution experiments in natural as well as in controlled artificial conditions, we address the parameters that influence abiotic release to seawater such as temperature, irradiation, and initial nutrient and ligand concentration.

2 Materials and methods

This study complements a parallel work which assessed the impact of desert and volcanic aerosols on phytoplankton during the same campaign. Both studies have been performed within the French project ITAliANO (ImpacT des Apports Atmosphériques de Nutriments sur les communautés phytoplanctoniques du transect OISO: des zones LNLC à HNLC) financed by the French Research Program LEFE (Les Enveloppes Fluides et l'Environnement). Thus more details on the experimental conditions can be found in Geisen et al. (submitted).

2.1 Characterization of dust and ash used in this study

The characterization of sample collection, size distribution, chemical and mineralogical composition of the dust and ash samples used in this study are fully described in Geisen et al. (submitted). Briefly, the aerosols were collected ground-based and are representative of a desert dust and a volcanic ash. A Patagonian arid surface soil from the south of Sierra Grande in Argentina was dry sieved below 20 µm to transform the soil into aerosols. The ash from the Eyjafjallajökull volcano in Iceland was collected the day of the explosive eruption (April 17th 2010 in Holtsa, 4-5 km south of the volcano) and sieved at 100 µm to remove large particles. The characterization of the aerosols, hereafter referred to as Pata and Eyja, is presented in Table VI-1. Manganese (Mn) content was determined with ICP after fusion and cobalt (Co) was measured with inductively coupled plasma mass spectrometry (ICP-MS 7500cx, Agilent) after acid digestion (according to Fu, 2018).

Table VI-1: Mineralogical and chemical properties (% and ppm, in weight) of the fine fraction of the Patagonian soil (< 20 µm) and the volcanic ash (< 100 µm) used in the abiotic dissolution experiment. n.d. stands for 'not detectable'. *: Data from Geisen et al. (in rev, L&O)

		Desert Dust (Pata)	Volcanic Ash (Eyja)
	Origin	Patagonia Argentina	Eyjafjallajökull Iceland
Mineralogy * (%)	Lime stones	calcite 2.9	n.d.
	Acidic rocks	albite 18.6; quartz 6.2	albite 23.4; analcime 1.0
	Clays	illite 20.6; smectite 2.8	smectite 10.9
	(Hydr)oxides	n.d.	hematite 0.1
	amorphous	48.3	63.7
Specific surface area ($m^2.g^{-1}$) *		62.1	7.3
	N (%) *	0.09 ± 0.01	0.03
	P (%) *	0.08 ± 0.01	0.18 ± 0.01
	Si (%) *	25.8	26.47
	Fe (%) *	4.55 ± 0.23	7.51 ± 0.28
	Mn (ppm)	886.7	1706.0
	Co (ppm)	12.3	13.7

2.2 Abiotic dissolution experiments

In all the experiments, materials were acid-washed (HCL Suprapur®) and manipulations took place under laminar flow hoods. Experiments were performed in polycarbonate bottles containing aerosols and seawater. After a gentle manual homogenization at successive times, samples for macro and micronutrient determination were filtered using 0.2 µm filters (PALL® Supor® 0.2 µm polyethersulfone) mounted on polyethylene syringes. Filters were acid-cleaned during the ship-based experiment.

2.2.1 Abiotic dissolution in artificial seawater

A series of dissolution experiments was performed in artificial seawater (ASW), prepared with SupraPur® quality chemical components in ultrapure water (Millipore®, resistivity of 18.2 $M\Omega.cm^{-1}$) at YBCII concentrations (Chen et al., 1996) but without nutrient or metal addition. Due to the small quantity of aerosol material available for this study, we decided to maximize the number of sampling times instead of the number of replicates, thus experiments were performed at a single run with particle concentration (PC) of 250 $mg.L^{-1}$ with 14 subsamples during the 48 h experiments (5', 10', 15', 30', 1 h, 1.5 h, 2 h, 2h30, 3.5 h, 4.5 h, 7 h, 24 h, 30 h, 48 h). Experiments were performed at room temperature (22 °C) on an agitation table at 100 rpm to limit particle settling.

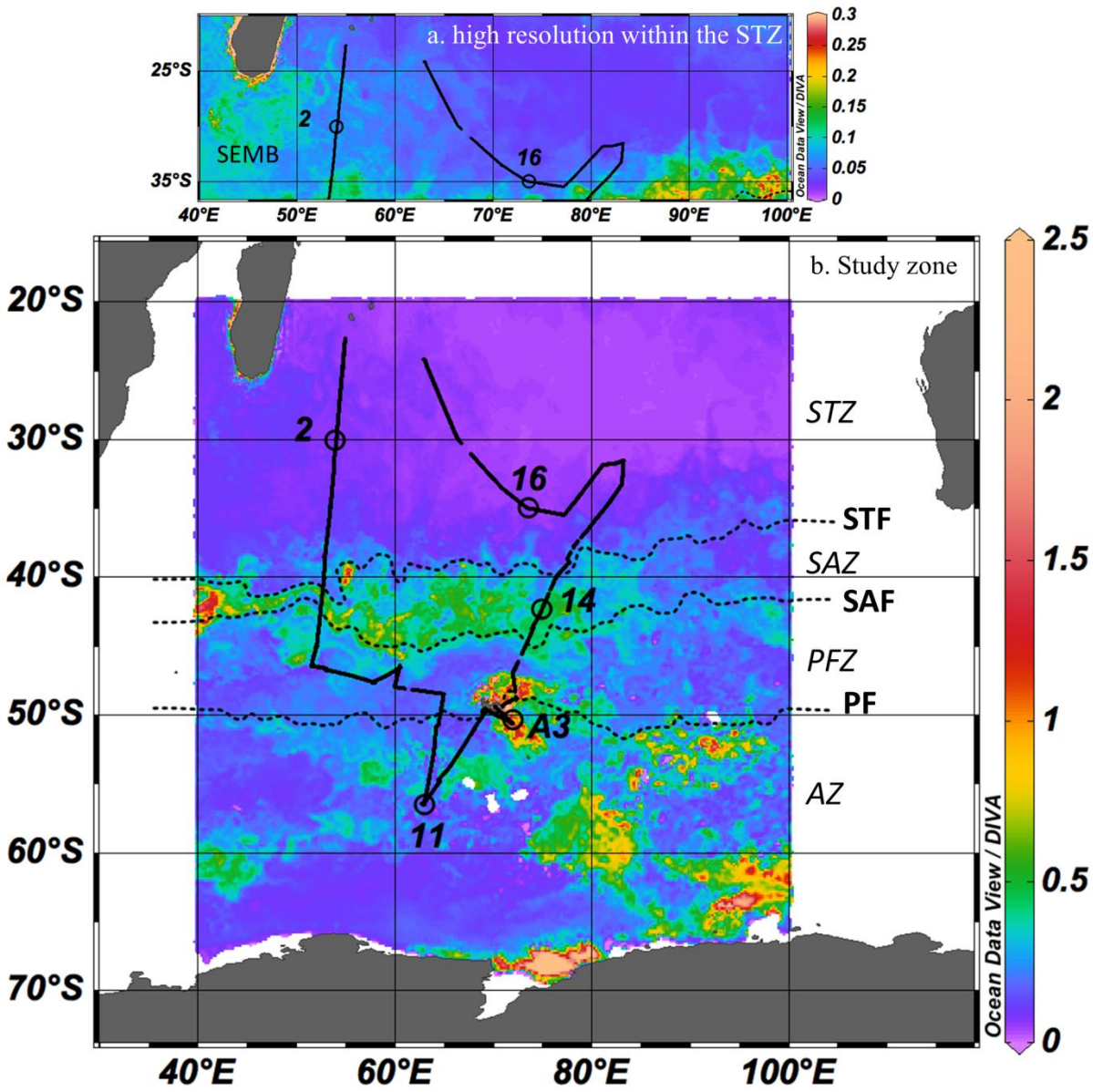

Figure VI-1: OISO-29 cruise transect with the locations of the five stations (LNLC-2, HNLC-11, Kerguelen-A3, HN-LSi-LC-14 and LNLC-16) where abiotic dissolution experiments were performed, and satellite-derived chlorophyll-a concentration (µg.L^{-1}) averaged over January 2019 (MODIS). The position of major fronts was determined from satellite-derived temperature data (January 2019, MODIS): STF: subtropical front (18 °C), SAF: subantarctic front (13 °C) and PF: polar front (5 °C). Fronts delimit the STZ: subtropical zone, SAZ: subantarctic zone, PFZ: polar front zone and AZ: antarctic zone. The map (a) shows the STZ with a higher resolution than the general map (b), thus enabling the detection of the southeast Madagascar bloom (SEMB). Figures were produced using Ocean Data View (Schlitzer, 2021). Figure from Geisen et al. (submitted).

2.2.2 Abiotic dissolution in natural seawater

A series of abiotic experiments was performed during the VT163/OISO-29 (MD217) cruise (Metzl and Lo Monaco, 2020) as part of the French OISO (Ocean Indien Service d'Observations) program on board the R/V *Marion Dufresne*. The cruise took place during

the austral summer, from the 5th of January to the 15th of February 2019. We performed abiotic dissolution experiments with natural seawater (NSW) collected at five stations (2, 11, A3, 14 and 16), located in contrasted biogeochemical regions (Figure VI-1, Table VI-2). Stations 2 and 16 are located in a LNLC region in the southwest Indian subtropical gyre. Station 14 is situated in a HN-LowSi-LC region in the SAZ, station 11 is found in the HNLC region in the AZ and station A3 is at the naturally Fe-fertilized Kerguelen plateau (Geisen et al., submitted).

Table VI-2: Initial physico-chemical and biological properties of the surface seawater used for the abiotic dissolution experiments. Mean nutrient concentration ± standard deviation of replicates. DL = detection limit. PP = primary production. Adapted from Geisen et al. (submitted)

Station	2	16	14	A3	11
Zone	STZ	STZ	SAZ	AZ	AZ
Region	LNLC	LNLC	HN-LSi-LC	Plateau	HNLC
Latitude, degrees S	29.97	35.00	42.49	50.64	56.50
Longitude, degrees E	54.11	73.47	74.90	72.05	62.99
Sampling date	12 Jan 2019	05 Feb 2019	30 Jan 2019	27 Jan 2019	23 Jan 2019
Temperature, °C	24.6	22.0	12.8	4.4	2.1
Salinity	35.47	35.48	34.49	33.83	33.83
NOx, µM	< DL	< DL	8.11±0.41	20.60±0.77	25.25±0.01
DIP, µM	0.03±0.00	0.09±0.01	0.65±0.02	1.04±0.05	1.58±0.16
dSi, µM	1.79±0.05	1.61±0.05	0.99±0.00	1.59±0.06	16.67±0.15
dFe, nM	0.54±0.12	0.37	0.39	0.35±0.13	0.27±0.02
dMn, nM	1.17±0.05	0.72±0.02	0.30±0.01	0.14±0.03	0.24±0.02
dCo, pM	4.6±0.7	7.9±1.3	8.9±1.2	20.0±1.2	14.3±1.9
PP, mg $C.m^{-3}.d^{-1}$	2.78	3.67	26.7	54.42	7.24
bSi, $\mu mol.L^{-1}$	< DL	< DL	0.11±0.02	2.31±0.79	0.96±0.48
Tchla, $\mu g.L^{-1}$	0.085	0.049	0.603	1.40	0.157

Surface water (~10 m depth) was collected with GoFlo sample bottles and Kevlar wire to avoid metal contamination and filtered on-line through acid-cleaned 0.2 µm capsule filters (Sartorius® Sartobran®-P-capsule 0.45/0.2 µm). At the five stations, representative PC of 2 $mg.L^{-1}$ Pata dust or 25 $mg.L^{-1}$ Eyja ash were directly added to 250 mL filtered NSW in triplicates mimicking a dry deposition event.

At the HNLC station 11, an additional set of experiments was performed mimicking a wet deposition event. The dissolution in artificial rainwater (ARW) occurred during 60 minutes with a PC of 100 $mg.L^{-1}$ dust and 1250 $mg.L^{-1}$ ash; then 2 % of unfiltered ARW was added into the bottles containing filtered NSW in order to obtain the same PC as in the dry deposition experiments. The bottles were then placed in on-deck incubators (mimicking local temperature and luminosity conditions of 10 m depth). The experiments ran for 48 h with

subsampling for macro- and micronutrients after 12 h, 24 h, 36 h and 48 h of contact time. Initial conditions were assessed in triplicates before aerosol addition. The chosen PC of 2 and 25 mg.L^{-1} corresponds to an estimated high dust deposition of 9 g.m^{-2} and a realistic 0.2 mm ash layer (see Geisen et al. (submitted) for further PC justification and Annex VII§2 for calculations).

2.3 Chemical analysis

2.3.1 Macronutrients

Samples were stored at +5 °C (dSi) or -20 °C (DIP and NOx) prior to on shore analysis. dSi and DIP were measured with a spectrophotometer (Thermo Scientific™ Evolution™ 220) according to the manual colorimetric methods of Grasshoff et al. (1999) and Murphy and Riley (1962), respectively. NOx was measured with the SEAL AutoAnalyzer 3HR, according to Aminot and Kérouel (2007). Detection limits (DL) are shown in Table VI-3.

Table VI-3. Detection limits (mean blanks + 3x SD of blanks) for macro and micronutrients in natural and artificial seawater

	Si (µM)	P (µM)	N (µM)	Fe (pM)	Mn (pM)	Co (pM)
ASW	0.04	0.05	0.09	4.6	9.2	0.1
NSW	0.03	0.03	0.08	5.0	16.5	0.2

2.3.2 Micronutrients

After filtration, samples for micronutrient determination were acidified before storage in HDPE vials at 5 °C prior to analysis. Natural and artificial SW samples were acidified with 0.2 % HCl UltraPur® and analyzed by ICP-MS coupled with an automated sample pre-concentration system (SeaFAST) according to Wuttig et al. (2019). Micronutrient DL are shown in Table VI-3. Pata and Eyja did not release significant amounts of nickel (Ni) and copper (Cu) to neither ASW nor NSW in this study and are thus not shown in the scope of this study which will focus on Fe, Mn and Co.

2.4 Solubility calculations

Dissolution of an element X will be expressed as a fractional solubility percentage (**%X_{sol}**), calculated according to:

$$\%X_{sol} = \frac{dX - dX_0}{X_{tot}} \times 100 \qquad \text{Equation VI-1}$$

where dX_0 (nmol.L^{-1}) is the initial background value (before aerosol addition) and X_{tot} (nmol.L^{-1}) is the total concentration of the element X in the aerosol, assuming that 100% of the element would dissolve. For literature comparison in the discussion section, we also normalized the dissolution by the experimental PC according to:

$$dX_{norm} = \frac{dX - dX_0}{PC}$$ Equation VI-2

2.5 Statistical analysis

Statistical analysis was performed solely on the NSW dataset (with n = 3) but not in ASW (n = 1). When the mean concentration of triplicates after 48 h of contact was significantly different from the initial concentration (one-way ANOVA followed by a Fisher LSD means comparison test), means of nutrient solubility at t48 h was compared between stations (one-way ANOVA) and between aerosol types (bilateral Student's t-test for independent samples). When assumptions for ANOVA were not respected, the tests were performed on the log-transformed data or means were compared using a Kruskal–Wallis test and a post hoc Dunn test). Statistical tests were performed using the XLSTAT software.

3 Results

3.1 Nutrient solubility from aerosols in artificial seawater

These results are part of Chapters II and III (for macro- and micronutrients, respectively) and for this reason are only briefly described here.

3.1.1 Macronutrients

The solubility kinetics differed according to the macronutrient: Si solubility for both Eyja and Pata increased steadily with time (respectively 0.12 % and 0.70 % at t48 h, Figure VI-2a,b) without reaching steady state, whereas NOx dissolution occurred within the first minutes after the aerosol addition in ASW (19.4 % and 10.2 % at t48 h, Figure VI-2e). Finally, Eyja released only low amounts of dissolved inorganic P (DIP; 0.13 % at t48 h, Figure VI-2c,d) whereas the main DIP release of Pata occurred within seven hours (1.6 % at t48 h, Figure VI-2d). Thus, Si and DIP solubility from Pata were higher compared to Eyja, whereas NOx solubility was lower.

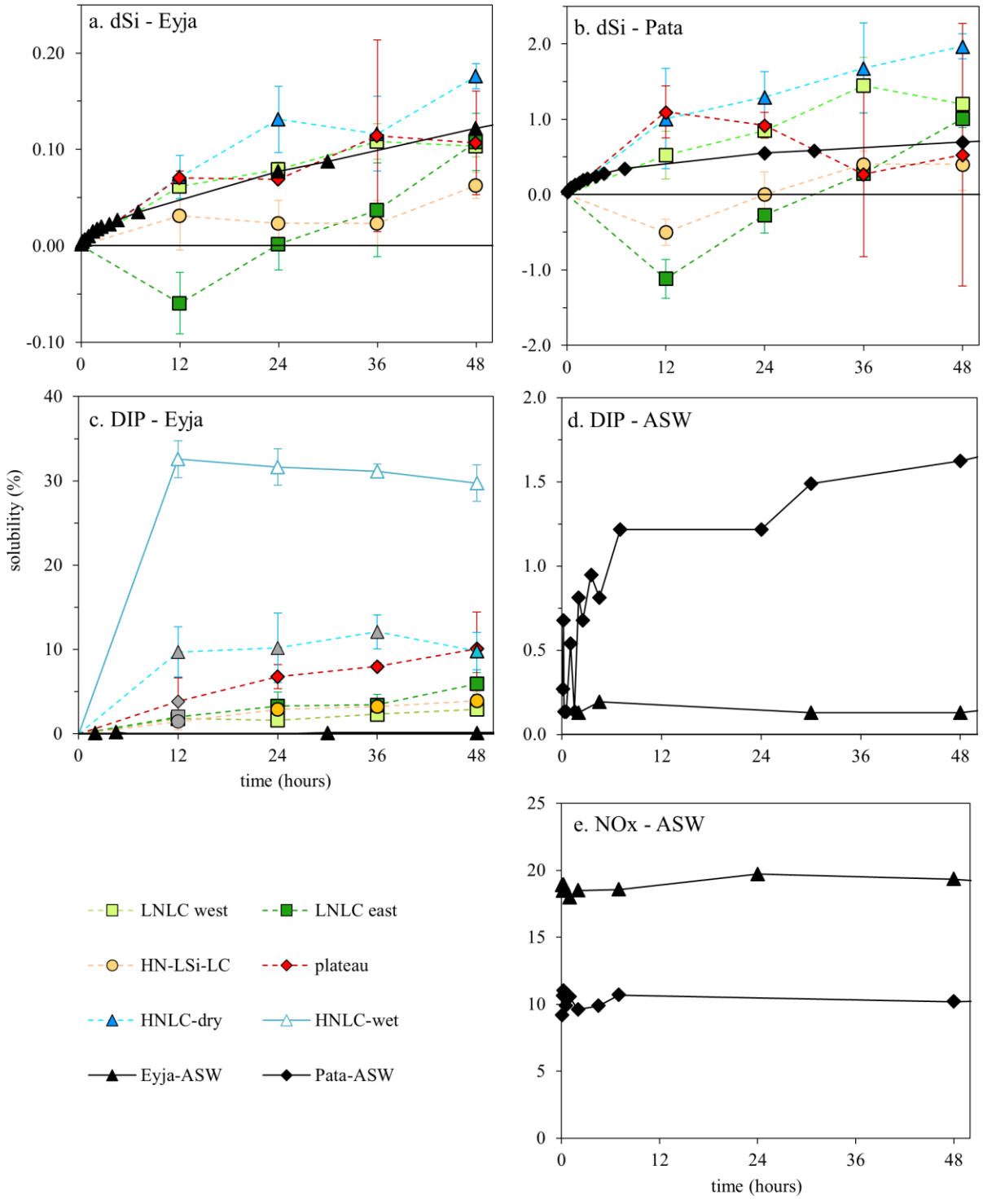

Figure VI-2: Solubility of macronutrients from Eyja and Pata in artificial and natural seawater from various regions of the Southern Indian Ocean, with (a) dSi from Eyja (b) dSi from Pata and (c) DIP from Eyja. No significant amount of DIP was released by Pata and no NOx was released by both aerosols to NSW over the experiment, thus panels (d) and (e) display only the release in ASW. **Note:** Silicon solubility after a wet deposition could not be calculated due to net dSi concentration decrease for both aerosols (a,b).

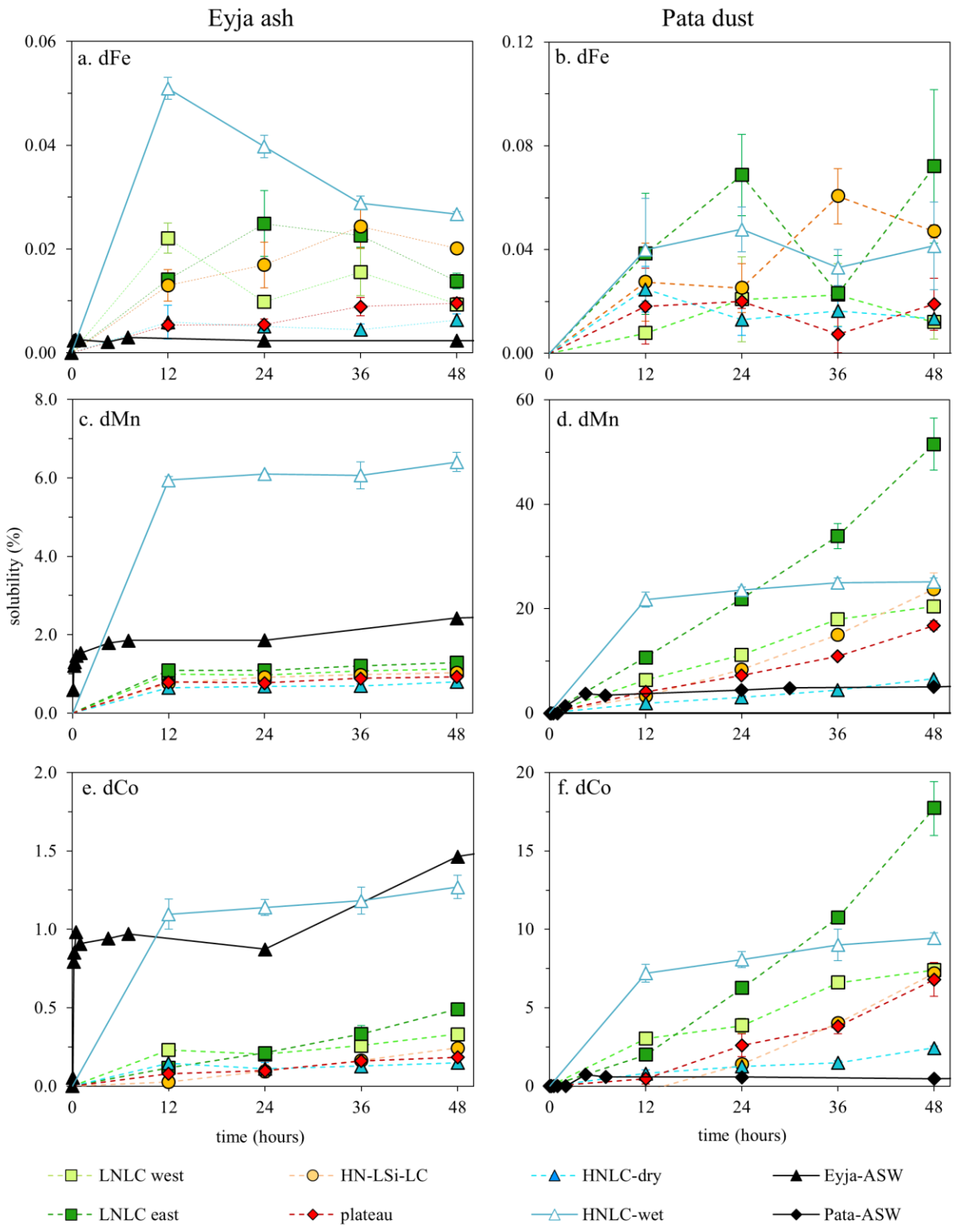

Figure VI-3: Solubility of micronutrients from Eyja (a,c,e) and Pata (b,d,f) in artificial and natural seawater from various regions from the Southern Indian Ocean, with iron (a,b), manganese (c,d) and cobalt (e,f). Iron solubility from Pata in ASW remained <DL.

3.1.2 Micronutrients

The release of the micronutrients Fe, Mn and Co tended towards a plateau representative of steady state (Figure VI-3). Eyja released the majority of soluble micronutrients within the first hours of contact, whereas Pata displayed an initial lag phase (1 h and 4.5 h for Mn and Co, respectively), and surprisingly no detectable amounts of dFe were released from Pata in ASW at t48 h of contact time. Iron solubility in ASW was 0.0023 % at t48 h (Figure VI-3a). After the initial lag phase, the Mn solubility from Pata was twice higher than Eyja (5.0 % and 2.4 % at t48 h, Figure VI-3c,d), whereas Pata Co solubility was three times lower (0.5 % and 1.5 %, Figure VI-3e,f).

3.2 Nutrient solubility in natural seawater

3.2.1 Macronutrients

3.2.1.1 Silicon

Silicon solubility in NSW depended on the water origin (*i.e.* station) and type of aerosol, reaching final solubilities at t48 h between 0.06-0.18 % for Eyja and 0.4-2.0 % for Pata, with a minimal solubility for both aerosols at HN-LSi-LC-14, significantly lower than the maximal solubility at HNLC-11 (Figure VI-2a,b and Figure VI-4a). Surprisingly, an initial dSi decrease was observed 12 h after the addition of both aerosols at the eastern LNLC-16, as well as after Pata addition at HN-LSi-LC-14. After this initial decrease, the solubility increased and reached positive net values. Moreover, the high variability in solubility for Pata at Kerguelen-A3 could not be connected to analytical issues.

3.2.1.2 Phosphorous and Nitrogen

Pata did not release significant amounts of DIP during the 48 h of contact to any of the tested natural SW at the low PC of 2 $mg.L^{-1}$, whereas DIP release from Eyja was measurable due to the higher PC of 25 $mg.L^{-1}$ (Figure VI-2c). A higher $\%P_{sol}$ was observed at HNLC-11 and Kerguelen-A3 (final solubility of ~10 %) compared to the stations north of the SAF (western LNLC-2 and HN-LSi-LC-14 with final solubility of 2.9 % and 3.9 %). Finally, the tested aerosols did not release significant amounts of NOx at the tested PC of 2 and 25 $mg.L^{-1}$.

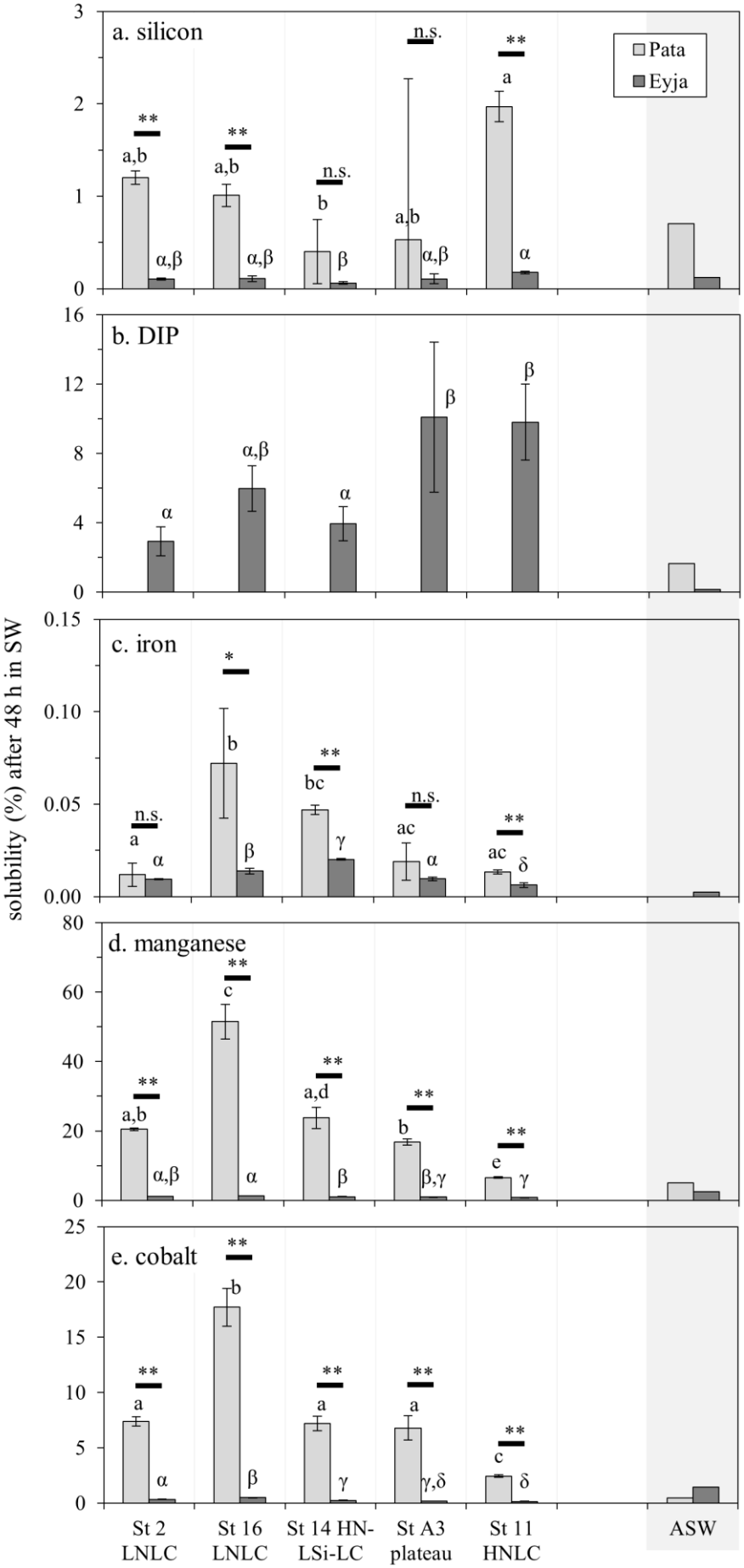

Figure VI-4: Fractional solubility of Pata (gray) and Eyja (dark gray) at t48 h in natural seawater at five stations within the Southern Indian Ocean compared to artificial seawater (shaded). (a) silicon, (b) DIP, (c) iron, (d) manganese, (e) cobalt. Error bars indicate standard deviation of triplicates.
Means that are not significantly different ($p > 0.05$) are labeled with the same letter for each element for Pata (Latin letters) and Eyja (Greek letters).
Within a station, a difference in solubility for Pata and Eyja is symbolized as follows *: p-value < 0.05; **: p-value < 0.01; n.s.: not significant.
Note: Pata did not release significant amounts of DIP (b) and neither aerosol was significant source of NOx, not shown in this figure.

3.2.2 Micronutrients

Significant amounts of the dissolved Fe, Mn and Co were released to NSW, whereas Co and Ni remained below DL. Several general trends can be observed, such as (i) the overall greater micronutrient solubility of Pata compared to Eyja; (ii) the increased solubilities at the eastern LNLC-16 compared to the other stations, with generally the lowest solubility at HNLC-11; and finally (iii) the maximal solubility for both aerosols of Mn, followed by Co, whereas Fe was the least soluble (Figure VI-3 and Figure VI-4b,c,d).

Moreover, after a dry deposition of Pata in NSW, the solubilities of Mn and Co did not reach steady state and the increase remained linear until the end of the incubation (Figure VI-3d,f). On the other hand, Eyja released micronutrients mainly within the first 12 h of contact. Finally, the low Fe solubility may explain the observed temporal variability (Figure VI-3a,b).

3.3 Nutrient solubility depending on the deposition mode

A direct comparison of wet and dry deposition modes was performed at HNLC-11. The simulated wet deposition of Eyja induced an increased solubility for the three micronutrients as well as DIP relative to the dry deposition (Figure VI-5). The same trend occurred for Pata, but the difference was significant only for Mn and Co (Figure VI-5c,d), but not for Fe (p-value < 0.1). Pata did not release significant amounts of DIP in neither dry nor wet deposition modes. Surprisingly, the wet deposition of both aerosols induced a significant decrease in dSi and NOx concentrations in the HNLC SW matrix (~1.7 µmol.L^{-1} dSi and ~0.4 µmol.L^{-1} NOx; data not shown).

Overall, the micronutrient release was faster in the wet compared to the dry deposition mode, and for most of the elements, we recorded steady state solubility during the 48 h of contact, indicating that the main dissolution occurred either within the first hour of contact in the ARW matrix or within the first 12 h in the NSW matrix. Noteworthy, the Fe solubility of Eyja ash in wet deposition mode decreased with time after a maximum of 0.051 % after 12 h in the SW matrix, until the final 0.027 % after 48 h (Figure VI-3a).

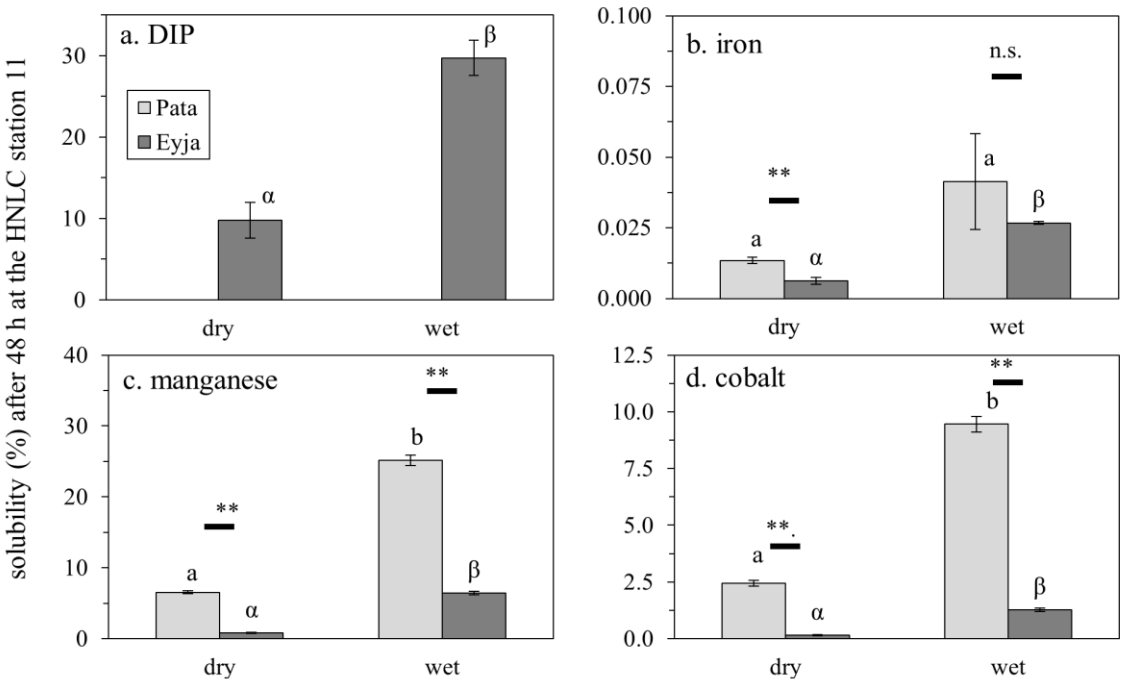

Figure VI-5: Fractional solubility at t48 h in natural seawater the HNLC station 11 in dry and wet deposition modes, with (a) DIP, (b) iron, (c) manganese and (d) cobalt. Error bars indicate standard deviation of triplicates. Means that are not significantly different ($p > 0.05$) are labeled with the same letter for each element for Pata (Latin letters) and Eyja (Greek letters). Difference in solubility for Pata and Eyja is symbolized as follows: **: p-value < 0.01, n.s.: not significant. **Note**: Pata did not release significant amounts of DIP (b) and a wet deposition of both aerosols was not a significant source of dSi and NOx, not shown in this figure.

4 Discussion

In the scope of this study, we tested the influence of the type of aerosol, as well as the SW origin and the deposition mode on abiotic macro- and micronutrient release. There was no clear trend stating that one aerosol, one SW type or one deposition mode induced a higher global solubility of every tested nutrient. Indeed, the Si and Mn solubilities from Pata were higher compared to Eyja in both natural and artificial SW (Figure VI-4a,d), whereas the opposite trend with a greater solubility of Eyja over Pata was observed for NOx, Fe and Co in ASW (shaded part of Figure VI-4c,e).

4.1 Dissolution kinetics

The majority of the elements tested in this study followed a rapid dissolution (P and N of both aerosols in ASW, as well as Mn and Co from Eyja in both ASW and NSW), defined by an immediate release of nearly all the soluble metals (Mahowald et al., 2018). However, the characteristic plateau of steady state was not observed for Si, indicating an intermediate behavior between rapid and gradual dissolution, progressively increasing over time, as observed in this study for instance for the Mn and Co solubilities of Pata at the eastern LNLC-16 (Figure VI-3d,f). Finally, the wet Fe solubility from Eyja displayed a particle reactive dissolution (initial increase followed by a secondary decrease of the dissolved concentration, Figure VI-3a) that can be linked to an adsorption of the element onto particles or the wall from experimental incubation bottles (Mahowald et al., 2018).

The high initial release from Eyja (Mn and Co for instance, Figure VI-3c,e) originated most probably from fast soluble surface metal salts (Ayris and Delmelle, 2012; Jones and Gislason, 2008) compared to Pata with gradual dissolution more characteristic of particles core dissolution. This difference cannot be explained by the extent of the exchange surface between the particle and the matrix, as the Pata sample had a 8.5 times greater specific surface area than the Eyja sample, caused by a twice higher clay content (Table VI-1) combined with a finer sieving step (< 20 compared to < 100 µm). Thus the soluble Mn and Co salt coating find most probably its origin during the volcanic eruption event (Delmelle et al., 2007). The role of mineralogy on Fe release has been demonstrated (Journet et al., 2008), and further discussion of the studied aerosols in natural SIO and SO water can be found in Geisen et al. (submitted).

4.2 Variability of nutrient solubility according to the seawater characteristics

Several physicochemical parameters differentiate between the dissolution experiments in artificial compared to the different natural SW. The presence of dissolved organic matter, variable temperature and light conditions and ambient nutrient concentrations, as well as the PC of the experiment are amongst the parameters that have been proven to influence nutrient solubility.

4.2.1 Comparison of artificial and natural seawater

In this study, the solubility varied according to three main behavior types depending on the element and aerosol:

1) A higher solubility in NSW compared to ASW (Fe from both aerosols, Figure VI-3a,b; DIP from Eyja, Figure VI-2c; as well as Mn and Co from Pata, Figure VI-3d,f);
2) A higher solubility in ASW compared to NSW (Mn and Co from Eyja, Figure VI-3c,e);
3) Similar solubility in NSW and ASW (Si from both aerosols in ASW was intermediate compared to the different NSW, Figure VI-2a,b).

Impact of PC - The experiments in ASW had a 125 and 10 times higher PC for respectively Pata and Eyja compared to the NSW experiments. Yet, it has been shown that a higher PC may reduce the solubility of Fe (Baker and Jickells, 2006; Guieu and Thomas, 1996; Sholkovitz et al., 2012) and P for desert dust (Ridame and Guieu, 2002). This conclusion seems to be confirmed with the data from this study, as Fe and DIP are more soluble in NSW with lower PC (solubility behavior type 1). Yet, a better sensitivity in the chemical analysis of the macronutrients DIP and NOx in NSW could have enabled further conclusions, since the dissolution of DIP by Pata and NOx by both aerosols remained below the DL, probably due to the low PC in NSW.

4.2.2 Influence of the seawater origin

Impact of the seawater temperature – The water temperature varied over 12.5 °C between the coldest HNLC-11 and the warmer LNLC-2 (2.1 and 24.6 °C respectively, Table VI-2). Significant correlations can be found between the NSW temperature and Mn and Co solubilities from both aerosols at t48 h but not for Fe and the macronutrients: thus, minimal Mn and Co solubilities were recorded at the coldest station (HNLC-11) and maximal solubilities at LNLC-16 (see linear regressions in Annex VII, Figure VII-4).

A similar link between the dissolution temperature and nutrient solubility has been demonstrated by the literature: for instance, mineral dust displayed a 4-24 fold increased Fe solubility in warmer SW at 29 °C compared to 17 °C in the Gulf of California (Félix-Bermúdez et al., 2020), and Si from pure minerals is also known to have greater solubility at higher temperature (Huertas et al., 1999 and references therein).

However, as the temperature is not the only varying parameter within the current experimental set up in the natural physicochemical conditions, it is not possible to draw definitive conclusions.

Impact of irradiation – Similar to temperature, the light availability in the surface waters is lower in the SO compared to the subtropical SIO; and the influence of photochemical reactions have been observed for Fe dissolution from aerosols at low pH with increased solubility under high light conditions (Hettiarachchi et al., 2019). Thus, the differences in nutrient solubility observed between the study areas (Figure VI-4) may be influenced by ambient temperature and light conditions that were simulated during the 48 h experiments in the on-board incubators.

Impact of ambient nutrient concentrations – The ambient dissolved nutrients follow North-South gradients, with overall depleted surface waters of the oligotrophic subtropical gyre and increasing nutrient concentrations towards the South (and thus with decreasing temperature), except for dMn displaying the opposite trend decreasing towards the South (Table VI-2; Annex VII, Figure VII-4). It can be assumed that a greater ambient concentration of an element lowers its solubility, as the environment is less undersaturated. In this study, only the Co solubility decreases with increasing ambient dCo concentration, whereas the solubilities of other elements (such as Si from both aerosols and Mn and P from Eyja) increase with increasing ambient concentrations, thus indicating that this parameter does not seem to control nutrient solubility.

Impact of dissolved organic matter – Despite a comparatively high ambient temperature (room temperature, ~20 °C) accompanied by the high luminosity of the clean laboratory compared to the on-deck incubators, the trace metal solubility was low in the ASW compared to the NSW experiment (Figure VI-4, with equivalent temperature and light conditions to LNLC stations). Another varying factor between the natural and artificial SW is the presence of dissolved organic matter (DOM) including organic ligands (Wagener et al., 2008). Indeed, 99.9 % of the dFe found in NSW is thought to be associated with organic complexing ligands (van den Berg, 1995). Their presence has been proven to control overall nutrient and especially Fe solubility (Liu and Millero, 2002). For instance, the presence of siderophores secreted by prokaryotic phytoplankton as well as saccharides produced and released by

eukaryotes such as diatoms may increase the Fe solubility and thus its bioavailability for phytoplankton (Hassler et al., 2011). Conversely, Bressac and Guieu (2013) performed artificial dust seeding experiments in the Mediterranean Sea in abiotic minicosms during spring/summer and winter with high and low DOM concentrations, respectively. The authors found an important Fe aggregation with increasing DOM concentration, resulting in a lower Fe solubility during summer due to the great DOM abundance and conclude on the unpredictable and contrasted response to different DOM types (Bressac and Guieu, 2013). Therefore, not solely the DOM quantity but also their quality is an important variable controlling Fe solubility.

Unfortunately, the presence of DOM has not been assessed during this study, but the highest amounts of different proxies for algal biomass (total chlorophyll, primary production and biogenic Si) have been measured at the plateau station A3 (Geisen et al. (submitted) and Annex VII, Figure VII-5). However, Gerringa et al. (2008) measured organic ligands in excess compared to dFe concentrations at both the reference Kerguelen plateau station A3 as well as at an equivalent HNLC station of the SO during the KEOPS-I cruise (Jan-Feb 2005, *i.e.* equally during the Austral summer). Thus, despite varying organic matter concentrations between the two SO stations, the equivalent ligand excess could explain the similar Fe solubility.

A significant difference in micronutrient solubility can also be observed between the western and the eastern LNLC stations (St 2 and 16). Indeed, the eastern and most oligotrophic station presents the highest Fe, Mn and Co solubilities of all tested stations in dry deposition mode (only behind the HN-LSi-LC-14 for Eyja Fe solubility, Figure VI-3). The main difference between the eastern and western LNLC stations is the proximity to the South East Madagascar bloom (SEMB), as shown by the increased satellite-derived chlorophyll-a concentration on Figure VI-1a. Thus, the station with lowest ambient algal biomass and most probably the lowest DOM pool presented surprisingly the highest solubilities, which may confirm the metal adsorption on DOM aggregations (Bressac and Guieu, 2013). Another particularity of the eastern LNLC station is the initial net decrease of dSi at t12 h after a deposition of both aerosols which could not be explained.

4.2.3 Role of the deposition mode

At the southernmost HNLC station, the simulated dry and wet deposition of desert dust and volcanic ash enabled to assess the influence of pH on the initial dissolution of nutrients. The aerosols endured a first dissolution at low pH before being added to the filtered SW. Except

for Pata Fe which was not significantly different, the micronutrient solubility in NSW, as well as DIP from Eyja, was higher after a preliminary one hour contact to artificial rainwater with pH 4.7 compared to a dry deposition simply to the NSW matrix at pH 8.1 (Figure VI-5). This result is consistent with literature data for desert dust (Desboeufs et al., 1999; Korte et al., 2018; Ridame and Guieu, 2002) as well as for volcanic ash (Duggen et al., 2010; Gislason and Oelkers, 2003), thought to dissolve more with decreasing pH at acidic concentrations.

In their dry and wet dissolution experiments of Saharan dust to unfiltered tropical Atlantic SW, Korte et al. (2018) found no NO_3^- release for both deposition modes and a net increase of H_4SiO_4 after a wet but not a dry deposition, *i.e.* the opposite as in our study. H_4SiO_4 adsorption onto (hydr)oxides such as ferrihydrite has been proven by the literature (Swedlund and Webster, 1999) and could play a role in dSi decrease following a wet deposition. However, the significant net NOx decrease after both Pata ane Eyja could not be explained by the literature and seems highly unlikely.

5 Conclusion

Our experiments displayed abiotic dissolution of several macro- and micronutrients in different natural seawater matrices from the Southern Indian Ocean as well as in ASW. We demonstrated the role of the aerosol origin on nutrient release, most certainly influenced by individual mineralogy of the aerosols, as previously demonstrated for Fe (Journet et al., 2008). Moreover, the nutrient release could be influenced by the origin and environmental conditions of the seawater (*e.g.*, temperature, light, ambient nutrient and ligand concentrations), as the micronutrients Fe, Mn and Co were overall more soluble at the eastern oligotrophic LNLC and HN-LSi-LC stations, whereas the macronutrient Si (and DIP for Eyja) dissolve more in the HNLC and Kerguelen plateau stations South of the polar front. This difference can be linked to variable physical, chemical and biological parameters. Indeed, the phytoplankton communities originated from individual zones of the Southern Indian Ocean produce variable quantities and qualities of dissolved organic matter including ligands that might locally influence the solubility of aerosols and thus nutrient release to the surface waters (Bressac and Guieu, 2013; de Leeuw et al., 2014).

It is difficult to draw definite conclusions, as these complex parameters may be synergistic or antagonistic and have a different weight on the solubility. To further understand the precise processes impacting nutrient solubility, it would have been interesting to measure the type and

abundance of DOM, including the concentrations of organic ligands, and to artificially modify the temperature and/or irradiance conditions to estimate their specific role in the release variability amongst SW.

Acknowledgements

The study has been financed by the French Research Program LEFE (Les Enveloppes Fluides et l'Environnement) through BISOU and ITALIANO projects and by the DADDY project supported by Labex IPSL. We thank INSU and the French oceanographic fleet ('Flotte océanographique française") for financial and logistic support to the OISO program and the VT163/OISO-29 oceanographic campaign (https://doi.org/10.17600/18000972). We thank the PACHIDERM analytical platform (LEMAR) for NOx and trace metal analysis; I. Djouraev (LOCEAN) for ICP-MS analysis at the Alysés platform, IRD; M. Benrahmoune and F. Kaczmar (LOCEAN) for managing clean labs and help in sample processing; F. Fu (LISA) for acid attack of aerosols; M. Mandeng-Yogo (LOCEAN) for IR-MS and CN analysis at the Alysés platform, IRD; S. Nowak (LISA) for XRS analysis at Paris Diderot University; L. Sicard (ITODYS) and M. Jean Pierre (LISA) for nitrogen BET analysis and C. Vaulot (IS2M) for SSA for krypton BET analysis.

VII. Annex PART B

1 Possible iron contamination

The nutrient solution from the +Si treatment (assessed by ICP-AES analysis) was contaminated with 0.23 nmol.L-1 Fe. As no significant difference in PP response between +Fe and +Si was observed at any station, we discuss the risk that the biological response to the +Si treatment was due to Fe contamination instead of actual Si addition.

When comparing flow cytometry data, we observe that in opposition to the +Fe and +FeSi treatments, the addition of Si alone did not enhance picoeukaryote cell abundance at the LNLC station 2, indicating that the Fe contamination of the Si treatment was negligible for this phytoplankton group at this station. Moreover, at the Kerguelen plateau station A3, Fe addition increased both pico- and nanoeukaryote abundances (+120 % and +50 % respectively, Fig. 3i,j), while the potential Fe contamination of the Si treatment was insufficient to trigger a response. Finally, the unexpected Synechococcus development after Si or FeSi additions (~+70 %) were not observed after Fe addition, demonstrating that the Synechococcus response was not induced by Fe contamination, but in fact by Si addition.

Thus, we cannot definitely exclude the influence of 0.23 nM Fe contamination within the Si treatment on PP at the western LNLC-2 as well as HN-LSi-LC-14 and Kerguelen-A3. However, since the cell abundance response differs between nutrient treatments at several stations for several phytoplankton groups, we support the statement that this potential Fe contamination was negligible and should not impact the general conclusions of this study.

2 Calculation of sinking velocities after representative aerosol deposition

In order to calculate the sinking velocity of aerosols in seawater, we applied the Stokes' law, assuming that the dust and ash particles were spherical. This is a simplification of the reality, but it gives an estimate of the depth reached by aerosols after the experimental 48h of incubation. The sinking velocity was calculated as follows:

$$S_v = \frac{2}{9} \times g \times r^2 \times \frac{\rho_{particle} - \rho_{SW}}{\eta_{SW}} \qquad \text{Equation VII-1}$$

where S_v is the sinking velocity, g is the Earth's gravitational acceleration (9.81 $m.s^{-2}$), r is the radius of the particle and $\rho_{particle}$ is the density of dust or ash particles. Seawater density and viscosity of respectively ρ_{SW} = 1027 $kg.m^{-3}$ and η_{SW} = 0.00141 $kg.m^{-1}.s^{-1}$ were calculated at 10°C, according to the Engineering Tool Box (2005). The particle radius was calculated as half of the median diameter (6.4 and 22.1 µm for Pata and Eyja, respectively). Further, we used a mean estimated dust density of 2650 $kg.m^{-3}$ (*e.g.*, Langmann, 2013) and an Eyja density of 1400 $kg.m^{-3}$ (Gudmundsson et al., 2012).

Applying Stokes' law, we obtain the following sinking velocities for both aerosols:

S_v-Pata = 2.2 $m.day^{-1}$

S_v-Eyja = 6.1 $m.day^{-1}$

After 48h of settling in seawater, the dust and ash particles would theoretically reach respectively 4.4 and 12.2 m depth. The mixed layer depth (MLD) ranks from 13 m to 50 m respectively in the LNLC and HNLC zones of the study area during austral summer (Hörstmann et al., 2021). Thus, the majority of dust/ash particles should theoretically not reach the MLD during the experimental time lapse. In this study, we used a PC of 2 and 25 $mg.L^{-1}$ respectively in the dust and ash treatments, which corresponds to an estimated deposition of 9 and 300 $g.m^{-2}$, assuming a mixing of aerosols within the 4.4 and 12.2 m upper layer. With a density of 1400 $kg.m^{-3}$ (Gudmundsson et al., 2012), the Eyja deposition of 300 $g.m^{-2}$ corresponds to an ash layer of 0.2 mm over the sea surface.

3 Contribution of phytoplankton size classes to the total biomass

The biomass fractions of micro-, nano- and picophytoplankton (Figure VII-1) were calculated according to Uitz et al. (2006) depending on their individual pigment signature:

$$f_{micro} = (1.41\ Fuco + 1.41\ Peri)/wDP \quad \text{Equation VII-2a}$$

$$f_{nano} = (1.27\ 19'HF + 0.60\ Allo + 0.35\ 19'BF)/wDP \quad \text{Equation VII-2b}$$

$$f_{pico} = (0.86\ Zea + 1.01\ Tchlb)/wDP \quad \text{Equation VII-2c}$$

where *wDP* is the weighted sum of the concentrations of the seven diagnostic pigments:

$$wDP = 1.41\ Fuco + 1.41\ Peri + 1.27\ 19'HF + 0.60\ Allo + 0.35\ 19'BF + 0.86\ Zea + 1.01\ Tchlb \quad \text{Equation VII-3}$$

The concentration of total chlorophyll-a (Tchla) associated with each size class was calculated as follows, with *x* standing either for *micro*, *nano* or *pico*:

$$Tchla_x = f_x \times Tchla \quad \text{Equation VII-4}$$

The diatom and dinoflagellate biomass were estimated using:

$$Chla_{diatom} = (1.41\ Fuco * Tchla)/wDP \quad \text{Equation VII-5a}$$

$$Chla_{dinoflagellate} = (1.41\ Peri * Tchla)/wDP \quad \text{Equation VII-5b}$$

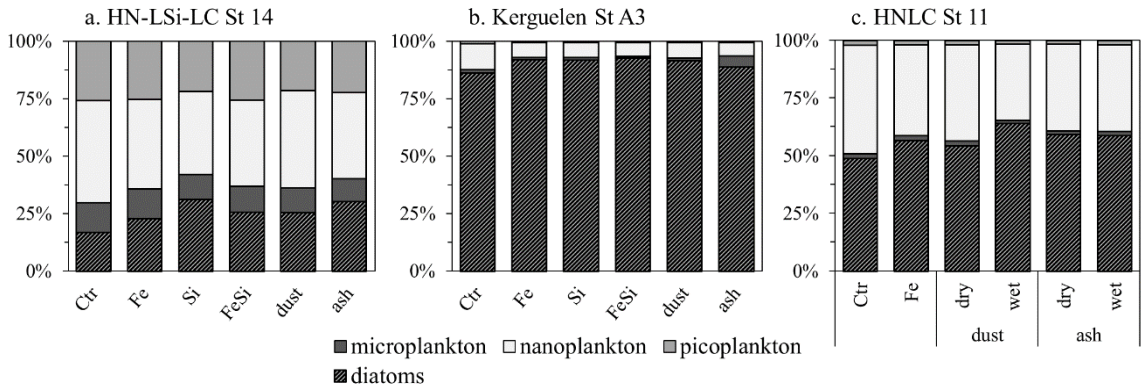

Figure VII-1: Phytoplankton community composition (%) with relative abundances of micro- (dark), nano- (light) and pico-phytoplankton (median grey) calculated from pigment analysis, according to Equation VII-4 and Equation VII-5. Diatom contribution within the micro-plankton size fraction is dashed.

4 Response of heterotrophic bacteria and haptophytes

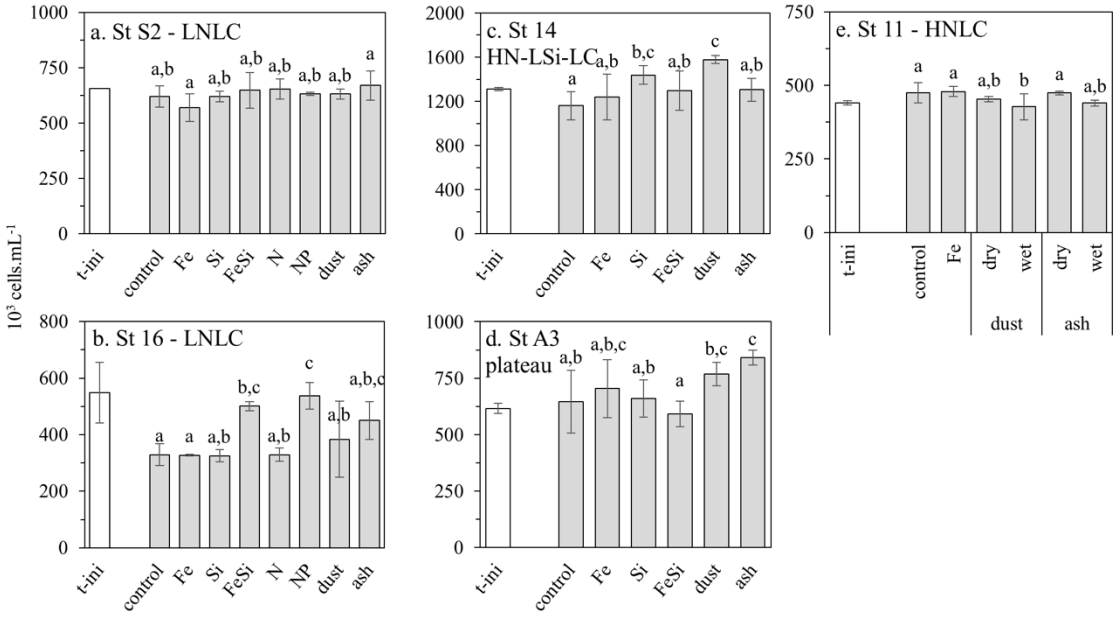

Figure VII-2: Cell abundance (cells.mL^{-1}) of heterotrophic bacteria at the beginning of the experiment (t-ini, white bar) and after 48 h of incubation for each treatment at the stations at LNLC St2 (a) and 16 (b), HN-LSi-LC St 14 (c), plateau St A3 (d) and HNLC St 11 (e). Error bars indicate standard deviation of triplicates. Means that are not significantly different are labeled with the same letter ($p > 0.05$) within a station.

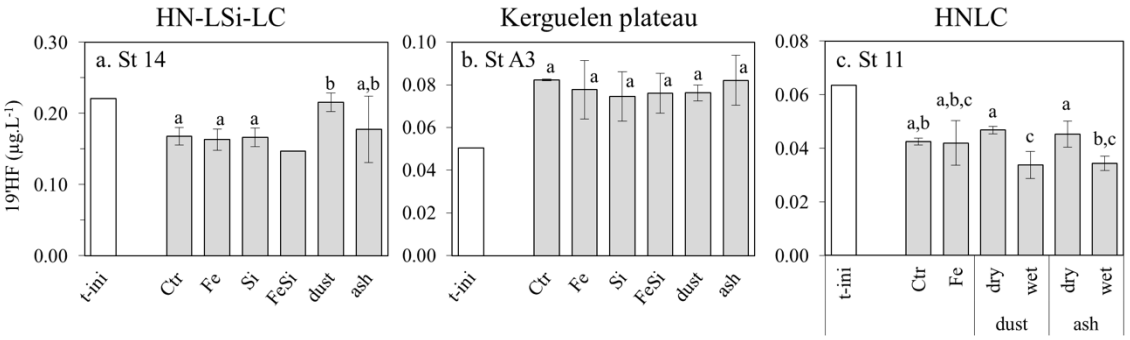

Figure VII-3: 19'Hexanoyloxyfucoxanthin concentration (19'HF, µg.L^{-1}) at the beginning of the experiment (t-ini, white bar) and after 48 h of incubation for each treatment at HN-LSi-LC St 14 (a), plateau St A3 (b) and HNLC St 11 (c). Error bars indicate standard deviation of triplicates. FeSi treatment at St 14 is not included in statistics, due to n = 1. Means that are not significantly different are labeled with the same letter ($p > 0.05$) within a station.

5 Linear regressions of nutrient solubility with temperature

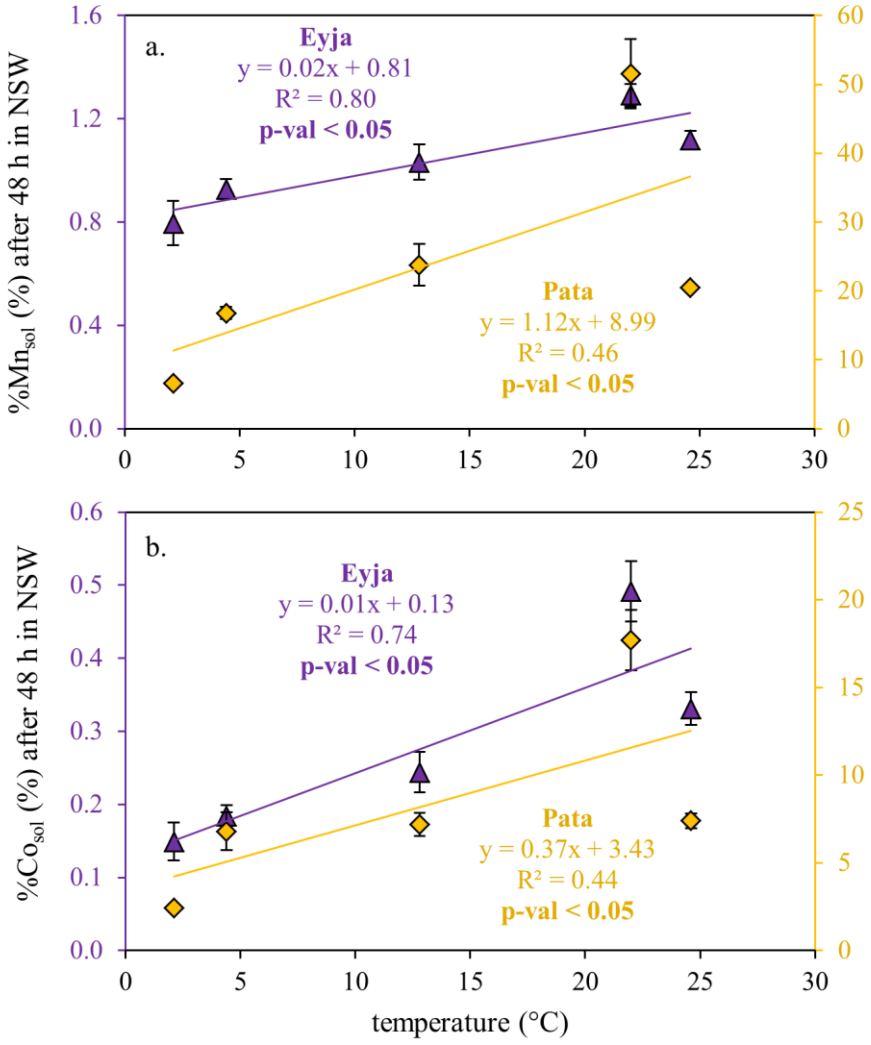

Figure VII-4: Linear regression of (a) manganese and (b) cobalt solubilities and the ambient sea surface temperature.

6 Ambient seawater characteristics of the Southern Indian Ocean

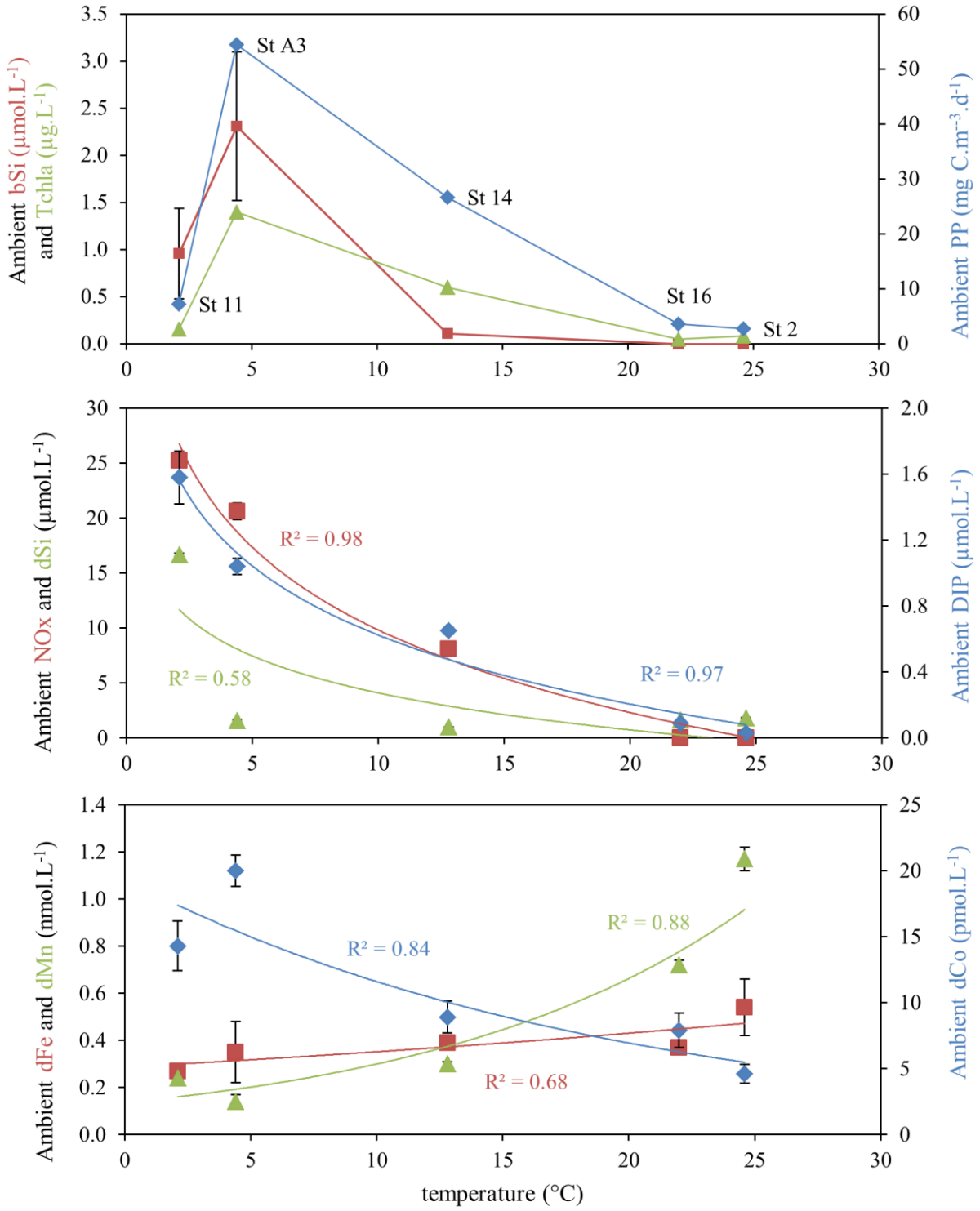

Figure VII-5: Correlations of (a) biomass proxies, (b) macro- and (c) micronutrients with the ambient sea surface temperature.

VIII. Conclusions générales et perspectives

1. Synthèse des principaux résultats

L'apport de nutriments nouveaux à l'océan fait partie intégrante des cycles biogéochimiques des nutriments et s'inscrit donc dans le cadre global du budget du carbone (Le Quéré et al., 2016) avec des implications potentielles pour le climat. Ces nutriments peuvent notamment être d'origine atmosphérique (Mahowald et al., 2018; Tagliabue et al., 2009). L'estimation la plus courante de leur biodisponibilité est la mesure de leur solubilité, même s'il a été montré que d'autres facteurs comme la spéciation redox du fer (Schroth et al., 2009) et la présence de ligands dans l'océan de surface (Gledhill, 2012) modifient la biodisponibilité des micronutriments et ainsi leur impact sur le phytoplancton. Une composante de cette thèse a été de quantifier l'apport nutritif atmosphérique d'origine naturelle dans son ensemble et s'est consacrée à une large gamme de macro- et micronutriments.

La variabilité des sources d'aérosols naturels et anthropiques cause une grande variabilité sur la solubilité, ce qui induit de grandes incertitudes dans les apports de nutriments atmosphériques dans les grands modèles biogéochimiques et climatiques (*e.g.* 100 % d'incertitude sur l'apport atmosphérique de Si soluble dans Tréguer et al., 2021). De plus, l'apport de nutriments par les cendres volcaniques reste souvent négligé ou comporte d'importantes incertitudes dans ces modèles (*e.g.* Mahowald et al. (2008) estiment une solubilité de P volcanique comprise entre 50-100 %). Ainsi, le premier objectif de cette thèse a été de **mieux définir la solubilité des macro- et micronutriments qui arrivent à l'océan par voie atmosphérique et proposer une gamme de variabilité en fonction des types d'aérosols (poussières désertiques et cendres volcaniques) selon le mode de dépôt (sec et humide).**

La dissolution de **huit aérosols** (quatre poussières désertiques, trois cendres volcaniques et un verre volcanique synthétique) en conditions contrôlées ultra-propres a permis de déterminer la solubilité de différents **macro- et micronutriments** (Chapitres II et III, respectivement). Nous avons utilisé un dispositif identique dans deux matrices distinctes : l'eau de mer artificielle pour estimer la solubilité du dépôt sec, l'eau de pluie artificielle pour celle du dépôt humide. L'homogénéité du protocole expérimental nous a permis de comparer l'effet de la matrice (impact du pH et charge ionique) sur la solubilité. L'utilisation de diverses sources

d'aérosols a permis quant à elle de quantifier une **gamme de variabilité naturelle de la solubilité de macro- et micronutriments** de différents types d'aérosols (Tableau VIII-1) qui pourra affiner les grandeurs de solubilités utilisées dans les modèles biogéochimiques.

Tableau VIII-1: Solubilités moyennes (±écart-types) en eau de pluie et eau de mer artificielles (temps de contact après ~1 h).

	Eau de pluie artificielle		**Eau de mer artificielle**	
	Désertique	Volcanique	Désertique	Volcanique
Si	0.12±0.10	0.024±0.025	0.07±0.05	0.009±0.004
P	12.7±10.2	4.0±5.8	1.2±1.0	0.6±0.6
N	5.8±7.3	4.4 [!]	4.3±4.4	18.0 [!]
Fe	0.011±0.004	0.044±0.050	0.006±0.006 [§]	0.008±0.006
Mn	3.3±5.4	0.88±0.91	5.9±5.5	0.85±0.69 [§]
Co	0.33±0.36 [§]	0.27±0.06 [@]	0.78±0.80 [§]	0.56±0.49 [@]
Cu	8.8±8.3	12.8±19.9	1.6±2.0 [@]	1.8±2.0
Ni	1.2±0.8	6.8±12.8	36.0 [!]	43.4±57.7 [@]

Note : Sauf mention contraire, les moyennes sont calculées avec n=4. Sinon : [§] n=3, [@] n=2 et [!] n=1.

Ainsi, la solubilité des macronutriments (Si, P, N) issus des poussières désertiques est globalement plus grande comparée aux cendres volcaniques, mis à part la cendre islandaise Eyja qui a un comportement plus proche des poussières désertiques, alors que la poussière sahélienne Bani agit plus comme une cendre. On peut souligner la composition particulière d'Eyja, caractérisée notamment par la présence d'argile induisant une surface spécifique élevée et de calcite induisant une augmentation du pH de l'eau de pluie ; de plus, cet aérosol est enrichi en N, P, Fe et Cd. La présence d'argiles peut être expliquée par les interactions magma-glace durant l'éruption (Paque et al., 2016) et permet d'expliquer que cette cendre se comporte de manière similaire à une poussière. D'un autre côté, Bani est majoritairement composée de quartz et présente une surface spécifique relativement faible. Ces particularités individuelles minéralogiques et élémentaires de nos aérosols expliquent la grande variabilité de la solubilité des macro- et micronutriments (jusqu'à un facteur 80 selon la source de l'aérosol, *e.g.* la solubilité en eau de pluie artificielle du Mn des poussières et Cu des cendres ; Tableau VIII-1).

Concernant les micronutriments, il n'y a pas de solubilité préférentielle séparant catégoriquement les poussières désertiques des cendres volcaniques au sein d'un même milieu de dissolution. On observe un effet de **matrice très marqué sur la solubilité des métaux** (Fe

et Cu) et de P, vraisemblablement induit par la différence de pH des milieux ; la solubilité étant plus importante dans l'eau de pluie que dans l'eau de mer artificielle. L'effet de la matrice sur la solubilité des autres métaux (et Si et N) dépend de l'aérosol : par exemple la poussière Douz relargue plus de Co, Ni et Mn dans l'eau de mer que dans l'eau de pluie, alors que l'inverse survient pour la cendre Chaitén. Les autres aérosols présentent également des solubilités préférentielles dans l'une ou l'autre des matrices, soulignant de nouveau **la variabilité plus importante entre les sources individuelles qu'entre les catégories d'aérosols.**

Des expériences de dissolution abiotique ont ensuite été menées en **conditions naturelles lors d'une campagne océanographique** (OISO 29) sur la cendre et la poussière ayant présenté les plus fortes dissolutions de Si en conditions artificielles. Nous avons appliqué un même protocole expérimental de simulation d'un dépôt atmosphérique dans des régions biogéochimiques contrastées de l'Océan Indien Sud et Austral, caractérisées par un gradient marqué de la température de l'eau de surface et de l'intensité lumineuse, ainsi que des concentrations différentes en macro- et micronutriments ; ces paramètres influençant la production primaire et la composition naturelle des communautés phytoplanctoniques.

Tableau VIII-2: Solubilités moyennes (±écart-types) en eau de mer naturelle (avec cinq stations dans l'Océan Indien et Austral) et artificielle (quatre poussières et quatre cendres) après un temps de contact après ~48 h ; et rapport des solubilités pour la poussière Pata et la cendre Eyja.

	Eau de mer naturelle NSW		**Eau de mer artificielle ASW**		**Rapport NSW/ASW**	
	Pata	Eyja	Désertique	Volcanique	Pata	Eyja
Si	1.02±0.89	0.11±0.05	0.41±0.28	0.11±0.07	1.5±1.3	0.9±0.4
P	<DL	6.8±3.4	2.4±1.7	0.9±0.7	$<DL_{NSW}$	52±27
Fe	0.033±0.028	0.11±0.05	0.010±0.008 §	0.011±0.018	$<DL_{ASW}$	4.9±2.0
Mn	23.8±15.7	1.0±0.2	11.7±5.7	1.0±1.1	4.4±2.9	0.4±0.1
Co	8.3±5.3	0.3±0.1	1.78±1.96	0.65±0.74 §	17±11	0.2±0.1

Note : Sauf mention contraire, les moyennes sont calculées avec n=4 en ASW (sinon : § n=3) et avec n=15 en NSW (triplicats de cinq stations) ; DL : limite de détection.

Nous observons ainsi une variation de la solubilité qui varie jusqu'à un facteur 8 selon la nature de l'eau de mer (*e.g.* pour le Mn issu de Pata, Tableau VIII-2). Certains micronutriments comme le Fe, Mn et Co sont généralement plus solubles dans les eaux chaudes et oligotrophes de l'Océan Indien Sud comparé aux eaux froides de la zone antarctique, soulignant ainsi un **effet potentiel de la température et/ou de l'intensité**

lumineuse sur la solubilité de ces métaux issus des deux aérosols. Cependant, ces paramètres ne sont pas les seuls facteurs qui modifient la solubilité des nutriments : en effet, les macronutriments Si et P sont plus solubles aux stations se trouvant au sud du front polaire, laissant supposer un effet de l'**origine de l'eau de mer pour la solubilité des nutriments**, incluant la concentration ambiante en nutriments. Ainsi, en plus de la forte variabilité des solubilités selon la source de l'aérosol (Tableau VIII-1) se rajoutent les caractéristiques de l'eau de mer (Tableau VIII-2).

Des différences de solubilité ont été mises en évidence selon la matrice eau de mer naturelle versus artificielle (NSW et ASW): ainsi Pata relargue globalement de plus grandes quantités en NSW (mis à part le DIP indétectable), alors que la solubilité de Eyja dépend de l'élément (50 fois plus de P en NSW versus 5 fois plus de Co en ASW et Si équivalent, Tableau VIII-2). Cette différence de solubilité entre stations et entre eau de mer naturelle et artificielle pourrait être due à la quantité et/ou qualité de la matière organique dissoute présente, les ligands naturellement présents dans l'eau de mer induisant une augmentation de la solubilité des métaux.

Finalement, au cours de cette même campagne océanographique, nous avons **quantifié la réponse des communautés phytoplanctoniques naturelles à un apport de poussières désertiques et cendres volcaniques**, au sein du gyre subtropical de l'océan Indien Sud (zone LNLC), dans les zones HN-LSi-LC et HNLC de l'océan Austral, et du plateau de Kerguelen (Chapitre V). L'apport de nutriments atmosphériques a majoritairement profité aux diatomées des différentes zones d'étude, modulant ainsi la composition de la communauté phytoplanctonique. De plus, la réponse la plus marquée a eu lieu au niveau de la station la plus productive du plateau naturellement fertilisé de Kerguelen avec un doublement de production primaire. Cela peut être expliqué par le fait que la communauté phytoplanctonique locale est acclimatée à des apports réguliers de nutriments.

De plus, malgré un plus grand relargage de métaux trace (Fe, Mn et Co) durant le dépôt humide des aérosols comparé au dépôt sec en zone HNLC (Chapitre VI), nous n'observons pas de différence majeure dans la réponse biologique.

De manière surprenante, et ce malgré des relargages significativement différents de macro- et micronutriments suite à (i) un dépôt de poussières comparé aux cendres et (ii) un dépôt sec comparé à un dépôt humide, nous enregistrons peu ou pas de différences de la réponse biologique (ni dans l'amplitude de la réponse, ni du type de phytoplancton qui profite).

2. Flux révisés de nutriments atmosphériques à l'océan de surface

De nombreuses études de modélisation existent sur l'estimation des flux de nutriments vers l'océan, mais des données de dissolution font à ce jour défaut pour boucler les cycles de certains nutriments. Ainsi, la contribution atmosphérique au cycle du silicium synthétisé par Tréguer et al. (2021) n'a pas été actualisée depuis ses versions précédentes (Tréguer et al., 1995; Tréguer and De La Rocha, 2013), faute de nouvelles données de dépôt et de solubilité. L'exemple du Si démontre que les données d'une gamme de solubilité de nutriments issus d'aérosols naturels manquent à ce jour, et nous proposons donc de réévaluer ces flux en nous basant sur l'approche expérimentale décrite dans ce manuscrit.

En utilisant les flux de matière proposés dans la littérature (voir Introduction générale de ce manuscrit, Tableau **I-2**), nous avons pu réestimer les flux de nutriments dissous donc potentiellement biodisponibles *via* la voie atmosphérique vers l'océan de surface. Nous basons notre calcul sur l'estimation d'un **dépôt annuel de 450 Tg.an^{-1}** de poussières désertiques sur l'océan global (Jickells et al., 2005).

Le dépôt annuel global de cendres volcaniques vers l'océan mondial n'a à ce jour pas été estimé. Olgun et al. (2011) proposent un flux de 128-221 Tg.an^{-1} vers l'Océan Pacifique. Sachant que la majorité du volcanisme actuel se situe au niveau de la ceinture de feu du Pacifique (Olgun et al., 2011 et auteurs cités), nous utilisons la valeur haute de cette estimation de **221 Tg.an^{-1} comme approximation du dépôt moyen de cendres volcaniques à l'océan global** (Tableau VIII-3).

Finalement, nous tenons compte dans notre calcul des **temps de contact** entre l'aérosol et le milieu de dissolution qui diffère en fonction du mode de dépôt (Tableau VIII-3): ainsi nous utilisons les données de solubilité obtenues après 1 h de contact en matrice eau de pluie et après 48 h de contact en matrice eau de mer :

Tableau VIII-3: Ordres de grandeur utilisés pour le calcul des flux de nutriments vers l'océan

	Désertique	Volcanique	Solubilité associée
Dépôt, Tg.an^{-1}	450 [a]	221 [b]	
Humide, %	80 [c]	30 [d]	1 h en eau de pluie artificielle [e]
Sec, %	20 [c]	70 [d]	48 h en eau de mer artificielle [f]

[a] Jickells et al. (2005) ; [b] Olgun et al. (2011) ; [c] Fan et al. (2006) ; [d] Jickells and Spokes (2001); [e] voir gamme Tableau VIII-1; [f] voir gamme Tableau VIII-2.

Grâce à ces estimations, nous pouvons effectuer des calculs de flux de nutriments pour chacun des aérosols, en utilisant les grandeurs physico-chimiques déterminées dans le cadre de cette thèse, qui sont (i) la **composition élémentaire** des aérosols et (ii) la **solubilité des nutriments** en fonction du mode de dépôt :

$$tX = dépôt\ total\ \times \%X_{aérosol} \quad \text{Équation VIII-1}$$

$$dX_{humide} = tX \times \%humide \times \%X_{sol(1h.ARW)} \quad \text{Équation VIII-2a}$$

$$dX_{sec} = tX \times \%sec \times \%X_{sol(48h.ASW)} \quad \text{Équation VIII-2b}$$

$$dX_{total} = dX_{humide} + dX_{sec} \quad \text{Équation VIII-3}$$

avec tX la teneur totale de l'élément X, $\%X_{aérosol}$ la teneur dans l'élément X dans l'aérosol, dX_{sec} et dX_{humide} la quantité de l'élément X dissoute après un dépôt sec et humide, respectivement. Finalement, dX_{total} correspond à la quantité totale de dX qui arrive à l'océan de surface. Nous appliquons le calcul de dépôt pour chacun de nos échantillons d'aérosols.

Tableau VIII-4: Estimation des dépôts atmosphériques ($Gg.an^{-1}$) de macro- et micronutriments dissous à l'océan de surface. Les moyennes ± écarts-types (et gamme min-max) sont calculés selon Équation VIII-3 et comparé à la littérature.

	Désertique	**Volcanique**	**Total aérosols naturels**		**Littérature**
Si	166±125	49±33	216±129	(54-424)	14000±14000 [a]
P	37.9±26.0	5.4±7.1	43.3±27.0	(7.3-85.3)	96.5 [b]
N	28.8±28.8	10.7 [!]	39.5±28.8	(13.6-79.2)	
Fe	1.8±0.4	1.1±0.7	2.9±0.7	(1.7-4.0)	700 (80-1830) [c]
Mn	13.6±12.3	2.9±4.2	16.5±13.0	(4.9-40.8)	300 [c]
Co	0.06±0.04	0.02±0.02	0.075±0.045	(0.027-0.138)	
Cu	0.69±0.57	0.27±0.30	0.96±0.65	(0.21-2.17)	3.2 [d]
Ni	0.30±0.27	0.77±1.16	1.07±1.21	0.12-3.16	

Note : Quand la solubilité d'un élément était <DL pour un aérosol en ASW (ou ARW), 100 % de dépôt humide (ou sec) ont été assumés pour l'aérosol en question, avant de calculer la moyenne présentée ici. [(!)]: n=1 pour l'estimation du dépôt de NOx *via* les cendres. [a]: Tréguer et al. (2021) ; [b] Mahowald et al. (2008) ; [c] Mahowald et al. (2018) ; [d] Jeandel and Oelkers (2015).

Ainsi, le dépôt atmosphérique de dSi vers l'océan de surface issu d'aérosols naturels (c'est-à-dire désertique + volcanique) se situe entre 54 et 424 $Gg.an^{-1}$ (Tableau VIII-4). Dans l'estimation de Tréguer et al. (2021), ce flux atmosphérique a été estimé à 0.5±0.5 Tmol $dSi.an^{-1}$ soit 14.0±14.0 Tg $dSi.an^{-1}$ qui est environ 30 fois supérieur à l'estimation haute calculée ici. Quant au P et au Cu, les estimations de la littérature se rapprochent de la limite supérieure de notre étude (Tableau VIII-4). D'un autre côté, Tagliabue et al. (2009) utilisent un dépôt de dFe dans leur étude de modélisation du Fe dans l'Océan Austral qui est plus élevé que celui trouvé dans nos calculs. Ils obtiennent un flux de dFe issu de poussières de 23.6-29.4 $Gg.an^{-1}$ seulement dans la région Sud de 35° S, en se basant sur une solubilité du Fe désertique de 0.5 %. Cette solubilité, utilisée fréquemment dans les études de modélisation (*e.g.* Mahowald et al., 2005; Tagliabue et al., 2008), est 7-42 fois plus grande que la gamme obtenue au bout de 48 h dans l'eau de mer naturelle de l'Océan Indien Sud et Austral (Tableau VIII-2). Ainsi, nous supposons que les études de la littérature surestiment largement la solubilité du Fe issu des aérosols, alors que notre étude minimise potentiellement sa solubilité en se basant sur des analogues de poussières (sols arides tamisés à 20 µm) et pas des aérosols à proprement dire (*i.e.* qui ont voyagé dans l'atmosphère et ont subi des altérations physico-chimiques).

3. Perspectives

Grâce au calcul des flux de nutriments vu dans le paragraphe précédent, nous montrons que les résultats obtenus au cours de cette thèse contribuent aux efforts d'améliorer la précision des cycles biogéochimiques en incluant la variabilité naturelle qui existe entre aérosols naturels.

Pourtant, plusieurs interrogations scientifiques persistent pour mieux définir cette variabilité naturelle de relargage de macro- et micronutriments à l'océan de surface. Ainsi au cours de cette thèse, nous avons identifié quelques limites dans la caractérisation des aérosols qui auraient permis de poursuivre davantage l'identification des sources de nutriments.

- Principalement, la **caractérisation de la partie amorphe** des aérosols aurait permis d'élargir la compréhension de l'origine des nutriments relargués. En effet, cette partie peut être biogénique, lithogénique ou pédogénique et ainsi contenir des phytolithes, de l'allophane, de la ferrihydrite ou encore du verre basaltique et contribuer de manière significative à la libération de nutriments comme le Si (Loucaides et al., 2008; Morin et al., 2015) et le Fe (Shi et al., 2009). Malheureusement, son analyse n'a pas pu être effectuée dans le cadre de mes travaux de recherche. Ainsi dans ce manuscrit, toute la partie non détectée par la méthode de DRX quantitative a été considérée comme amorphe (32.3-57.6 % pour les poussières et 63.7-100 % pour les cendres), ce qui peut donc surestimer sa proportion.
- La **matière organique** particulaire et dissoute (POM et DOM) dans l'eau de mer peut également jouer un rôle considérable dans la solubilité des nutriments (Bressac and Guieu, 2013), notamment les ligands qui jouent un rôle dans la biodisponibilité du Fe (Paris and Desboeufs, 2013; Wagener et al., 2008). La mesure de la DOM dans des expériences futures de dissolution abiotique en matrice naturelle permettrait de conclure sur la variabilité de solubilité détectée entre l'Océan Indien Sud et l'Océan Austral.
- Finalement, il aurait également été intéressant d'aborder la solubilité d'aérosols anthropiques en appliquant le même protocole mis en place dans les Chapitres II et III afin d'obtenir une base de données homogène de gammes de solubilités rencontrées pour différents types d'aérosols rencontrés dans l'atmosphère (Fishwick et al., 2018; Mahowald et al., 2008; Sedwick et al., 2007).

Un autre paramètre intéressant à prendre en considération est l'effet du **changement climatique** sur la dissolution de nutriments, puisqu'il a été démontré que les variations de pH et de température impactent la solubilité de plusieurs nutriments tels que le Fe (Trimborn et al., 2017). Un réchauffement et une acidification de l'eau de mer de surface et de l'eau de pluie auraient donc potentiellement un effet positif sur la solubilité, mais il reste à déterminer si ces nutriments seraient également biodisponibles (Fishwick et al., 2018). De plus, les changements futurs tendent vers une augmentation de la stratification et donc un amincissement de la couche de mélange dans lequel se dissolvent les aérosols (Deppeler and Davidson, 2017), augmentant ainsi pour un même dépôt la charge particulaire dans l'océan de surface. Et finalement, les modifications de l'utilisation des sols par l'Homme tendent à transformer les paysages (dont l'étendue des zones arides) ce qui cause des modifications de la masse totale d'aérosols émise dans l'atmosphère ainsi que des modifications des proportions du type de dépôt (sec ou humide) (Allen et al., 2016).

D'autres expériences au laboratoire non finalisées ou non réalisées dans le cadre de cette thèse, mais qui permettraient d'élargir la portée de ces travaux de recherche incluent :

- L'impact d'un dépôt d'aérosols sur les processus de biosilicification et de dissolution des diatomées en se servant de l'approche isotopique de marquage du silicium (^{30}Si) (Fripiat et al., 2009; Ragueneau et al., 2005).
- La quantification de la réponse des diatomées à l'échelle cellulaire (avec l'analyse de la structure des thèques jusqu'à l'expression des gènes).

On pourrait ainsi combiner des études du transcriptome à des analyses de morphologie des frustules, de croissance cellulaire et de métabolisme du silicium pour obtenir une compréhension plus précise de l'effet d'un apport atmosphérique de nutriments sur le développement de ce phytoplancton.

Bibliography

Achterberg, E. P., Moore, C. M., Henson, S. A., Steigenberger, S., Stohl, A., Eckhardt, S., Avendano, L. C., Cassidy, M., Hembury, D., Klar, J. K., Lucas, M. I., Macey, A. I., Marsay, C. M. and Ryan-Keogh, T. J.: Natural iron fertilization by the Eyjafjallajökull volcanic eruption, Geophys. Res. Lett., 40(5), 921–926, doi:10.1002/grl.50221, 2013.

Allen, R. J., Landuyt, W. and Rumbold, S. T.: An increase in aerosol burden and radiative effects in a warmer world, Nat. Clim. Chang., 6(3), 269–274, doi:10.1038/nclimate2827, 2016.

Aminot, A. and Kérouel, R.: Dosage automatique des nutriments dans les eaux marines : méthodes en flux continu., edited by Ifremer-Quae., 2007.

Anderson, L. D., Faul, K. L. and Paytan, A.: Phosphorus associations in aerosols: What can they tell us about P bioavailability?, Mar. Chem., 120(1–4), 44–56, doi:10.1016/j.marchem.2009.04.008, 2010.

Ardyna, M., Lacour, L., Sergi, S., d'Ovidio, F., Sallée, J. B., Rembauville, M., Blain, S., Tagliabue, A., Schlitzer, R., Jeandel, C., Arrigo, K. R. and Claustre, H.: Hydrothermal vents trigger massive phytoplankton blooms in the Southern Ocean, Nat. Commun., 10(1), doi:10.1038/s41467-019-09973-6, 2019.

Ayris, P. and Delmelle, P.: Volcanic and atmospheric controls on ash iron solubility: A review, Phys. Chem. Earth, 45–46, 103–112, doi:10.1016/j.pce.2011.04.013, 2012.

Baines, S., Twining, B. S., Brzezinski, M. A., Krause, J., Vogt, S., Assael, D. and McDaniel, H.: Significant silicon accumulation by marine picocyanobacteria, Nat. Geosci., 5(12), 886–891, doi:10.1038/ngeo1641, 2012.

Baker, A. R. and Croot, P. L.: Atmospheric and marine controls on aerosol iron solubility in seawater, Mar. Chem., 120(1–4), 4–13, doi:10.1016/J.MARCHEM.2008.09.003, 2010.

Baker, A. R. and Jickells, T. D.: Mineral particle size as a control on aerosol iron solubility, Geophys. Res. Lett., 33(17), L17608, doi:10.1029/2006GL026557, 2006.

Baker, A. R. and Jickells, T. D.: Atmospheric deposition of soluble trace elements along the Atlantic Meridional Transect (AMT), Prog. Oceanogr., 158, 41–51, doi:10.1016/j.pocean.2016.10.002, 2017.

Baker, A. R., Jickells, T. D., Witt, M. and Linge, K. L.: Trends in the solubility of iron, aluminium, manganese and phosphorus in aerosol collected over the Atlantic Ocean, Mar. Chem., 98(1), 43–58, doi:10.1016/j.marchem.2005.06.004, 2006.

Baker, A. R., Weston, K., Kelly, S. D., Voss, M., Streu, P. and Cape, J. N.: Dry and wet deposition of nutrients from the tropical Atlantic atmosphere: Links to primary productivity and nitrogen fixation, Deep. Res. Part I Oceanogr. Res. Pap., 54(10), 1704–1720, doi:10.1016/j.dsr.2007.07.001, 2007.

Baker, A. R., Lesworth, T., Adams, C., Jickells, T. D. and Ganzeveld, L.: Estimation of atmospheric nutrient inputs to the Atlantic ocean from 50°N to 50°S based on large-scale field sampling: Fixed nitrogen and dry deposition of phosphorus, Global Biogeochem. Cycles, 24(7), 1–16, doi:10.1029/2009GB003634, 2010.

van den Berg, C. M. G.: Evidence for organic complexation of iron in seawater, Mar. Chem., 50(1–4), 139–157, doi:10.1016/0304-4203(95)00032-M, 1995.

Bergametti, G. and Forêt, G.: Dust Deposition, in Mineral Dust, pp. 179–200, Springer Netherlands, Dordrecht., 2014.

Bishop, J. K. B., Davis, R. E. and Sherman, J. T.: Robotic observations of dust storm enhancement of carbon biomass in the North Pacific, Science (80-.)., 298(5594), 817–

821, doi:10.1126/science.1074961, 2002.
Blain, S., Sedwick, P. N., Griffiths, F. B., Quéguiner, B., Bucciarelli, E., Fiala, M., Pondaven, P. and Tréguer, P. J.: Quantification of algal iron requirements in the Subantarctic Southern Ocean (Indian sector), Deep. Res. Part II Top. Stud. Oceanogr., 49(16), 3255–3273, doi:10.1016/S0967-0645(02)00082-6, 2002.
Blain, S., Guieu, C., Claustre, H., Leblanc, K., Moutin, T., Quéguiner, B., Ras, J. and Sarthou, G.: Availability of iron and major nutrients for phytoplankton in the northeast Atlantic Ocean, Limnol. Oceanogr., 49(6), 2095–2104, doi:10.4319/lo.2004.49.6.2095, 2004.
Blain, S., Quéguiner, B., Armand, L. K., Belviso, S., Bombled, B., Bopp, L., Bowie, A. R., Brunet, C., Brussaard, C. P. D., Carlotti, F., Christaki, U., Corbière, A., Durand, I., Ebersbach, F., Fuda, J. L., Garcia, N., Gerringa, L., Griffiths, B., Guigue, C., Guillerm, C., Jacquet, S., Jeandel, C., Laan, P., Lefèvre, D., Lo Monaco, C., Malits, A., Mosseri, J., Obernosterer, I., Park, Y. H., Picheral, M., Pondaven, P., Remenyi, T., Sandroni, V., Sarthou, G., Savoye, N., Scouarnec, L., Souhaut, M., Thuiller, D., Timmermans, K. R., Trull, T. W., Uitz, J., Van Beek, P., Veldhuis, M., Vincent, D., Viollier, E., Vong, L. and Wagener, T.: Effect of natural iron fertilization on carbon sequestration in the Southern Ocean, Nature, 446(7139), 1070–1074, doi:10.1038/nature05700, 2007.
Blain, S., Sarthou, G. and Laan, P.: Distribution of dissolved iron during the natural iron-fertilization experiment KEOPS (Kerguelen Plateau, Southern Ocean), Deep Sea Res. Part II Top. Stud. Oceanogr., 55(5–7), 594–605, doi:10.1016/j.dsr2.2007.12.028, 2008a.
Blain, S., Quéguiner, B. and Trull, T. W.: The natural iron fertilization experiment KEOPS (KErguelen Ocean and Plateau compared Study): An overview, Deep Sea Res. II, 55, 559–565, doi:10.1016/j.dsr2.2008.01.002, 2008b.
Bonnet, S. and Guieu, C.: Dissolution of atmospheric iron in seawater, Geophys. Res. Lett., 31(3), 3–6, doi:10.1029/2003GL018423, 2004.
Bonnet, S., Guieu, C., Chiaverini, J., Ras, J. and Stock, A.: Effect of atmospheric nutrients on the autotrophic communities in a low nutrient, low chlorophyll system, Limnol. Oceanogr., 50(6), 1810–1819, doi:10.4319/lo.2005.50.6.1810, 2005.
Bostick, B. C.: Iron Speciation Influences Solubility in Dust Sources of HNLC Waters, , (December 2008), 2018.
Bowie, A. R., Van Der Merwe, P., Quéroué, F., Trull, T. W., Fourquez, M., Planchon, F., Sarthou, G., Chever, F., Townsend, A. T., Obernosterer, I., Sallée, J. B. and Blain, S.: Iron budgets for three distinct biogeochemical sites around the Kerguelen Archipelago (Southern Ocean) during the natural fertilisation study, KEOPS-2, Biogeosciences, 12(14), 4421–4445, doi:10.5194/bg-12-4421-2015, 2015.
Boyd, P. W. and Ellwood, M. J.: The biogeochemical cycle of iron in the ocean, Nat. Geosci., 3(10), 675–682, doi:10.1038/ngeo964, 2010.
Boyd, P. W., Watson, A. J., Law, C. S., Abraham, E. R., Trull, T. W., Murdoch, R., Bakker, D. C. E., Bowie, A. R., Buesseler, K. O., Chang, H., Charette, M., Croot, P., Downing, K., Frew, R., Gall, M., Hadfield, M., Hall, J., Harvey, M., Jameson, G., LaRoche, J., Liddicoat, M., Ling, R., Maldonado, M. T., McKay, R. M., Nodder, S., Pickmere, S., Pridmore, R., Rintoul, S., Safi, K., Sutton, P., Strzepek, R. F., Tanneberger, K., Turner, S., Waite, A. and Zeldis, J.: A mesoscale phytoplankton bloom in the polar Southern Ocean stimulated by iron fertilization, Nature, 407(6805), 695–702, doi:10.1038/35037500, 2000.
Boyd, P. W., Jickells, T. D., Law, C. S., Blain, S., Boyle, E. A., Buesseler, K. O., Coale, K. H., Cullen, J. J., De Baar, H. J. W., Follows, M., Harvey, M., Lancelot, C., Levasseur, M., Owens, N. P. J., Pollard, R., Rivkin, R. B., Sarmiento, J. L., Schoemann, V., Smetacek, V., Takeda, S., Tsuda, A., Turner, S. and Watson, A. J.: Mesoscale iron enrichment experiments 1993-2005: Synthesis and future directions, Science (80-.).,

315(5812), 612–617, doi:10.1126/science.1131669, 2007.
Boyd, P. W., Mackie, D. S. and Hunter, K. A.: Aerosol iron deposition to the surface ocean - Modes of iron supply and biological responses, Mar. Chem., 120(1–4), 128–143, doi:10.1016/j.marchem.2009.01.008, 2010.
Boyer, T. P., Garcia, H. E., Locarnini, R. A., Zweng, M. M., Mishonov, A. V., Reagan, J. R., Weathers, K. A., Baranova, O. K., Seidov, D. and Smolyar, I. V.: World Ocean Atlas 2018, NOAA Natl. Centers Environ. Inf. [online] Available from: https://www.ncei.noaa.gov/products/world-ocean-atlas, 2018.
Bressac, M. and Guieu, C.: Post-depositional processes: What really happens to new atmospheric iron in the ocean's surface?, Global Biogeochem. Cycles, 27(3), 859–870, doi:10.1002/gbc.20076, 2013.
Browning, T. J., Bouman, H. A., Henderson, G. M., Mather, T. A., Pyle, D. M., Schlosser, C., Woodward, E. M. S. and Moore, C. M.: Strong responses of Southern Ocean phytoplankton communities to volcanic ash, Geophys. Res. Lett., 41(8), 2851–2857, doi:10.1002/2014GL059364, 2014.
Bruggenwert, M. G. M., Keizer, P. and Koorevaar, P.: Adsorption of aluminium ions by montmorillonite: influence on aluminium speciation., Netherlands J. Agric. Sci., 35(3), 259–269, doi:10.18174/njas.v35i3.16723, 1987.
Bruland, K. W., Franks, R. P., Knauer, G. A. and Martin, J. H.: Sampling and analytical methods for the determination of copper, cadmium, zinc, and nickel at the nanogram per liter level in sea water, Anal. Chim. Acta, 105, 233–245, doi:10.1016/S0003-2670(01)83754-5, 1979.
Brzezinski, M. A.: The Si:C:N ratio of marine diatoms: interspecific variability and the effect of some environmental variables, J. Phycol., 21(3), 347–357, doi:10.1111/j.0022-3646.1985.00347.x, 1985.
Cassar, N., Bender, M. L., Barnett, B. A., Fan, S.-M., Moxim, W. J., Levy, H. and Tilbrook, B.: The Soutern Ocean biological response to aeolian iron deposition, Science (80-.)., 317, 1067–1070, doi:10.1038/050458a0, 2007.
Castillo, S., Moreno, T., Querol, X., Alastuey, A., Cuevas, E., Herrmann, L., Mounkaila, M. and Gibbons, W.: Trace element variation in size-fractionated African desert dusts, J. Arid Environ., doi:10.1016/j.jaridenv.2007.12.007, 2008.
Chapman, C. C., Lea, M. A., Meyer, A., Sallée, J. B. and Hindell, M.: Defining Southern Ocean fronts and their influence on biological and physical processes in a changing climate, Nat. Clim. Chang., 10(3), 209–219, doi:10.1038/s41558-020-0705-4, 2020.
Chen, W., Zhang, C., Song, L., Sommerfeld, M. and Hu, Q.: A high throughput Nile red method for quantitative measurement of neutral lipids in microalgae, J. Microbiol. Methods, 77(1), 41–47, doi:10.1016/j.mimet.2009.01.001, 2009.
Chen, Y. and Brantley, S. L.: Temperature- and pH-dependence of albite dissolution rate at acid pH, Chem. Geol., 135(3–4), 275–290, doi:10.1016/S0009-2541(96)00126-X, 1997.
Chen, Y. and Siefert, R. L.: Determination of various types of labile atmospheric iron over remote oceans, J. Geophys. Res. Atmos., 108(24), 1–8, doi:10.1029/2003jd003515, 2003.
Chen, Y., Street, J. and Paytan, A.: Comparison between pure-water- and seawater-soluble nutrient concentrations of aerosols from the Gulf of Aqaba, Mar. Chem., 101(1–2), 141–152, doi:10.1016/j.marchem.2006.02.002, 2006.
Chen, Y. B., Zehr, J. P. and Mellon, M.: Growth and nitrogen fixation of the diazotrophic filamentous nonheterocystous cyanobacterium Trichodesmium sp. IMS 101 in defined media: Evidence for a circadian rhythm, J. Phycol., 32(6), 916–923, doi:10.1111/j.0022-3646.1996.00916.x, 1996.
Chester, R. and Jickells, T. D.: The Transport of Material to the Oceans: The Atmospheric Pathway, in Marine Geochemistry, pp. 52–82, John Wiley & Sons, Ltd, Chichester, UK.,

2012.
Chever, F., Bucciarelli, E., Sarthou, G., Speich, S., Arhan, M., Penven, P. and Tagliabue, A.: Physical speciation of iron in the Atlantic sector of the Southern Ocean along a transect from the subtropical domain to the Weddell Sea Gyre, J. Geophys. Res. Ocean., 115(10), 1–15, doi:10.1029/2009JC005880, 2010.
Chou, L. and Wollast, R.: Steady-state kinetics and dissolution mechanisms of albite., Am. J. Sci., 285(10), 963–993, doi:10.2475/ajs.285.10.963, 1985.
Chou, L., Garrels, R. M. and Wollast, R.: Comparative study of the kinetics and mechanisms of dissolution of carbonate minerals, Chem. Geol., 78(3–4), 269–282, doi:10.1016/0009-2541(89)90063-6, 1989.
Cimino, G. and Toscano, G.: Dissolution of trace metals from lava ash: Influence on the composition of rainwater in the Mount Etna volcanic area, Environ. Pollut., 99(3), 389–393, doi:10.1016/S0269-7491(98)00004-9, 1998.
Closset, I., Lasbleiz, M., Leblanc, K., Quéguiner, B., Cavagna, A. J., Elskens, M., Navez, J. and Cardinal, D.: Seasonal evolution of net and regenerated silica production around a natural Fe-fertilized area in the Southern Ocean estimated with Si isotopic approaches, Biogeosciences, 11(20), 5827–5846, doi:10.5194/bg-11-5827-2014, 2014.
Conway, T. M., Wolff, E. W., Rothlisberger, R., Mulvaney, R. and Elderfield, H. E.: Constraints on soluble aerosol iron flux to the Southern Ocean at the Last Glacial Maximum, Nat. Commun., 6, doi:10.1038/ncomms8850, 2015.
Cornelis, J. T., Delvaux, B., Georg, R. B., Lucas, Y., Ranger, J. and Opfergelt, S.: Tracing the origin of dissolved silicon transferred from various soil-plant systems towards rivers: A review, Biogeosciences, 8(1), 89–112, doi:10.5194/bg-8-89-2011, 2011.
Cosentino, N. J., Ruiz-Etcheverry, L. A., Bia, G. L., Simonella, L. E., Coppo, R., Torre, G., Saraceno, M., Tur, V. M. and Gaiero, D. M.: Does Satellite Chlorophyll-a Respond to Southernmost Patagonian Dust? A Multi-year, Event-Based Approach, J. Geophys. Res. Biogeosciences, 125(12), 1–19, doi:10.1029/2020JG006073, 2020.
Coverly, S., Aminot, A. and Kérouel, R.: Nutrients in Seawater Using Segmented Flow Analysis, in Practical Guidelines for the Analysis of Seawater, CRC Press., 2009.
Crundwell, F. K.: On the Mechanism of the Dissolution of Quartz and Silica in Aqueous Solutions, ACS Omega, 2(3), 1116–1127, doi:10.1021/acsomega.7b00019, 2017.
Cutter, G., Casciotti, K., Croot, P., Geibert, W., Heimbürger, L.-E., Lohan, M., Planquette, H. and van de Flierdt, T.: Sampling and Sample-handling Protocols for GEOTRACES Cruises. Version 3, August 2017., , (August), 139pp. & Appendices [online] Available from: http://www.geotraces.org/images/stories/documents/intercalibration/Cookbook.pdf, 2017.
D'Ortenzio, F., Iudicone, D., de Boyer Montegut, C., Testor, P., Antoine, D., Marullo, S., Santoleri, R. and Madec, G.: Seasonal variability of the mixed layer depth in the Mediterranean Sea as derived from in situ profiles, Geophys. Res. Lett., 32(12), 1–4, doi:10.1029/2005GL022463, 2005.
Deer, W. A., Howie, R. A. and Zussman, J.: An introduction to the rock-forming minerals. Second edition, An Introd. to rock-forming Miner. Second Ed., 1992.
Delmelle, P., Villiéras, F. and Pelletier, M.: Surface area, porosity and water adsorption properties of fine volcanic ash particles, Bull. Volcanol., 67(2), 160–169, doi:10.1007/s00445-004-0370-x, 2005.
Delmelle, P., Lambert, M., Dufrêne, Y., Gerin, P. and Óskarsson, N.: Gas/aerosol–ash interaction in volcanic plumes: New insights from surface analyses of fine ash particles, Earth Planet. Sci. Lett., 259(1–2), 159–170, doi:10.1016/j.epsl.2007.04.052, 2007.
Delmelle, P., Maters, E. C., Calkins, J. A., Gaspard, F., Opfergelt, S. and Jenkins, S. F.: Eruptive style controls the formation of silicon hexafluoride salts on volcanic ash: The

case of the 2010 eruption of Eyjafjallajökull volcano, Iceland, Chem. Geol., 579(February), doi:10.1016/j.chemgeo.2021.120327, 2021.

Deppeler, S. L. and Davidson, A. T.: Southern Ocean phytoplankton in a changing climate, Front. Mar. Sci., 4(FEB), doi:10.3389/fmars.2017.00040, 2017.

Desboeufs, K. V.: Processus de dissolution des aérosols atmosphériques au sein des gouttes d'eau nuageuses. [online] Available from: https://tel.archives-ouvertes.fr/tel-00005175, 2005.

Desboeufs, K. V., Losno, R. R., Cholbi, S., Vimeux, F. and Cholbi, S.: The pH-dependent dissolution of wind-transported Saharan dust, J. Geophys. Res. Atmos., 104(D17), 21287–21299, doi:10.1029/1999JD900236, 1999.

Desboeufs, K. V., Losno, R. and Colin, J.-L.: Factors influencing aerosol solubility during cloud processes, Atmos. Environ., 35(20), 3529–3537, doi:10.1016/S1352-2310(00)00472-6, 2001.

Desboeufs, K. V., Sofikitis, A., Losno, R., Colin, J. L. and Ausset, P.: Dissolution and solubility of trace metals from natural and anthropogenic aerosol particulate matter, Chemosphere, 58(2), 195–203, doi:10.1016/j.chemosphere.2004.02.025, 2005.

Desboeufs, K. V., Leblond, N., Wagener, T., Bon Nguyen, E. and Guieu, C.: Chemical fate and settling of mineral dust in surface seawater after atmospheric deposition observed from dust seeding experiments in large mesocosms, Biogeosciences, 11(19), 5581–5594, doi:10.5194/bg-11-5581-2014, 2014.

Dove, P. M. and Elston, S. F.: Dissolution kinetics of quartz in sodium chloride solutions: Analysis of existing data and a rate model for 25°C, Geochim. Cosmochim. Acta, 56, 4147–4156, 1992.

Duce, R. A., LaRoche, J., Altieri, K., Arrigo, K. R., Baker, A. R., Capone, D. G., Cornell, S., Dentener, F. J., Galloway, J. N., Ganeshram, R. S., Geider, Ri. J., Jickells, T. D., Kuypers, M. M., Langlois, R., Liss, P. S., Liu, S. M., Middelburg, J., Moore, C. M., Nickovic, S., Oschlies, A., Pedersen, T., Prospero, J. M., Schlitzer, R., Seitzinger, S., Sorensen, L. L., Uematsu, M., Ulloa, O., Voss, M., Ward, B. and Zamora, L.: Impacts of atmospheric anthropogenic nitrogen on the open ocean, Science (80-.)., 320(5878), 893–897, doi:10.1126/science.1150369, 2008.

Dugdale, R. C., Wilkerson, F. P. and Minas, H. J.: The role of a silicate pump in driving new production, Deep Sea Res. Part I Oceanogr. Res. Pap., 42(5), 697–719, doi:10.1016/0967-0637(95)00015-X, 1995.

Duggen, S., Croot, P. L., Schacht, U. and Hoffmann, L. J.: Subduction zone volcanic ash can fertilize the surface ocean and stimulate phytoplankton growth: Evidence from biogeochemical experiments and satellite data, Geophys. Res. Lett., doi:10.1029/2006GL027522, 2007.

Duggen, S., Olgun, N., Croot, P., Hoffmann, L. J., Dietze, H., Delmelle, P. and Teschner, C.: The role of airborne volcanic ash for the surface ocean biogeochemical iron-cycle: a review, Biogeosciences, 7(3), 827–844, doi:10.5194/bg-7-827-2010, 2010.

Durant, A. J., Bonadonna, C. and Horwell, C. J.: Atmospheric and environmental impacts of volcanic particulates, Elements, 6, 235–240, doi:10.2113/gselements.6.4.235, 2010.

Durant, A. J., Villarosa, G., Rose, W. I., Delmelle, P., Prata, A. J. and Viramonte, J. G.: Long-range volcanic ash transport and fallout during the 2008 eruption of Chaitén volcano, Chile, Phys. Chem. Earth, 45–46, 50–64, doi:10.1016/j.pce.2011.09.004, 2012.

Erickson, D. J., Hernandez, J. L., Ginoux, P., Gregg, W. W., McClain, C. and Christian, J.: Atmospheric iron delivery and surface ocean biological activity in the southern ocean and Patagonian region, Geophys. Res. Lett., 30(12), doi:10.1029/2003GL017241, 2003.

Estrada, M., Delgado, M., Blasco, D., Latasa, M., Cabello, A. M., Benítez-Barrios, V., Fraile-Nuez, E., Mozetič, P. and Vidal, M.: Phytoplankton across tropical and subtropical

regions of the Atlantic, Indian and Pacific oceans, PLoS One, 11(3), 1–29, doi:10.1371/journal.pone.0151699, 2016.
Fan, S.-M., Moxim, W. J. and Levy, H.: Aeolian input of bioavailable iron to the ocean, Geophys. Res. Lett., 33(7), L07602, doi:10.1029/2005GL024852, 2006.
Félix-Bermúdez, A., Delgadillo-Hinojosa, F., Torres-Delgado, E. V. and Muñoz-Barbosa, A.: Does Sea Surface Temperature Affect Solubility of Iron in Mineral Dust? The Gulf of California as a Case Study, J. Geophys. Res. Ocean., 125(9), 1–18, doi:10.1029/2019JC015999, 2020.
Fishwick, M. P., Sedwick, P. N., Lohan, M. C., Worsfold, P. J., Buck, K. N., Church, T. M. and Ussher, S. J.: The impact of changing surface ocean conditions on the dissolution of aerosol iron, Global Biogeochem. Cycles, 28(11), 1235–1250, doi:10.1002/2014GB004921, 2014.
Fishwick, M. P., Ussher, S. J., Sedwick, P. N., Lohan, M. C., Worsfold, P. J., Buck, K. N. and Church, T. M.: Impact of surface ocean conditions and aerosol provenance on the dissolution of aerosol manganese, cobalt, nickel and lead in seawater, Mar. Chem., 198(October 2017), 28–43, doi:10.1016/j.marchem.2017.11.003, 2018.
Folger, D. W., Burckle, L. H. and Heezen, B. C.: Opal phytoliths in a North Atlantic dust fall, Science (80-.)., doi:10.1126/science.155.3767.1243, 1967.
Fraysse, F., Pokrovsky, O. S., Schott, J. and Meunier, J.-D.: Surface properties, solubility and dissolution kinetics of bamboo phytoliths, Geochim. Cosmochim. Acta, 70(8), 1939–1951, doi:10.1016/j.gca.2005.12.025, 2006.
Fraysse, F., Pokrovsky, O. S., Schott, J. and Meunier, J.-D.: Surface chemistry and reactivity of plant phytoliths in aqueous solutions, Chem. Geol., 258(3–4), 197–206, doi:10.1016/j.chemgeo.2008.10.003, 2009.
Fripiat, F., Corvaisier, R., Navez, J., Elskens, M., Schoemann, V., Leblanc, K., André, L. and Cardinal, D.: Measuring production – dissolution rates of marine biogenic silica by 30 Si-isotope dilution using a high-resolution sector field inductively coupled plasma mass spectrometer, Limnol. Ocean. Methods, 7, 470–478, doi:10.4319/lom.2009.7.470, 2009.
Fripiat, F., Cavagna, A. J., Savoye, N., Dehairs, F., André, L. and Cardinal, D.: Isotopic constraints on the Si-biogeochemical cycle of the Antarctic Zone in the Kerguelen area (KEOPS), Mar. Chem., 123(1–4), 11–22, doi:10.1016/j.marchem.2010.08.005, 2011.
Frogner, P., Reynir Gíslason, S. and Óskarsson, N.: Fertilizing potential of volcanic ash in ocean surface water, Geology, 29(6), 487, doi:10.1130/0091-7613(2001)029<0487:FPOVAI>2.0.CO;2, 2001.
Fu, F.: Etude des apports des métaux traces par le dépôt atmosphérique en Méditerranée occidentale, Université Paris Diderot - Paris VII., 2018.
Gaiero, D. M., Probst, J. L., Depetris, P. J., Bidart, S. M. and Leleyter, L.: Iron and other transition metals in Patagonian riverborne and windborne materials: Geochemical control and transport to the southern South Atlantic Ocean, Geochim. Cosmochim. Acta, 67(19), 3603–3623, doi:10.1016/S0016-7037(03)00211-4, 2003.
Galloway, J. N., Dentener, F. J., Capone, D. G., Boyer, E. W., Howarth, R. W., Seitzinger, S. P., Asner, G. P., Cleveland, C. C., Green, P. A., Holland, E. A., Karl, D. M., Michaels, A. F., Porter, J. H., Townsend, A. R. and Vörösmarty, C. J.: Nitrogen cycles: Past, present, and future., 2004.
Gassó, S. and Torres, O.: Temporal Characterization of Dust Activity in the Central Patagonia Desert (Years 1964–2017), J. Geophys. Res. Atmos., 124(6), 3417–3434, doi:10.1029/2018JD030209, 2019.
Geisen, C.: Macro- and micronutrient dissolution from desert and volcanic aerosols in rain and seawater: Impact on phytoplankton in the Southern Indian Ocean, Sorbonne Université., 2021.

Geisen, C., Ridame, C., Journet, E., Delmelle, P., Marie, D., Lo Monaco, C., Metzl, N., Ammar, R., Kombo, J. and Cardinal, D.: Phytoplanktonic Response to simulated Volcanic and Desert Dust Deposition Events in the South Indian and Southern Oceans, Submitt. to Limnol. Ocean., doi:doi.org/10.1002/essoar.10507198.2, 2021.

Gerringa, L., Blain, S., Laan, P., Sarthou, G., Veldhuis, M. J. W., Brussaard, C. P. D., Viollier, E. and Timmermans, K. R.: Fe-binding dissolved organic ligands near the Kerguelen Archipelago in the Southern Ocean (Indian sector), Deep. Res. Part II Top. Stud. Oceanogr., 55(5–7), 606–621, doi:10.1016/j.dsr2.2007.12.007, 2008.

Gili, S., Gaiero, D. M., Goldstein, S. L., Chemale, F., Koester, E., Jweda, J., Vallelonga, P. and Kaplan, M. R.: Provenance of dust to Antarctica: A lead isotopic perspective, Geophys. Res. Lett., 43(5), 2291–2298, doi:10.1002/2016GL068244, 2016.

Gislason, S. R. and Oelkers, E. H.: Mechanism, rates, and consequences of basaltic glass dissolution: II. An experimental study of the dissolution rates of basaltic glass as a function of pH and temperature, Geochim. Cosmochim. Acta, 67(20), 3817–3832, doi:10.1016/S0016-7037(00)00176-5, 2003.

Gledhill, M.: The organic complexation of iron in the marine environment: a review, Front. Microbiol., 3(FEB), doi:10.3389/fmicb.2012.00069, 2012.

Grand, M. M., Measures, C. I., Hatta, M., Hiscock, W. T., Landing, W. M., Morton, P. L., Buck, C. S., Barrett, P. M. and Resing, J. A.: Dissolved Fe and Al in the upper 1000 m of the eastern Indian Ocean: A high-resolution transect along 95°E from the Antarctic margin to the Bay of Bengal, Global Biogeochem. Cycles, 29(3), 375–396, doi:10.1002/2014GB004920, 2015a.

Grand, M. M., Measures, C. I., Hatta, M., Morton, P. L., Barrett, P., Milne, A., Resing, J. A. and Landing, W. M.: The impact of circulation and dust deposition in controlling the distributions of dissolved Fe and Al in the south Indian subtropical gyre, Mar. Chem., 176, 110–125, doi:10.1016/j.marchem.2015.08.002, 2015b.

Grasshoff, K., Kremling, K. and Ehrhardt, M.: Methods of Seawater Analysis, edited by K. Grasshoff, K. Kremling, and M. Ehrhardt, Wiley., 1999.

Gudmundsson, M. T., Thordarson, T., Hoskuldsson, A., Larsen, G., Bjornsson, H., Prata, F. J., Oddsson, B., Magnusson, E., Hognadottir, T., Petersen, G. N., Hayward, C. L., Stevenson, J. A. and Jonsdottir, I.: Ash generation and distribution from the April-May 2010 eruption of Eyjafjallajökull, Iceland, Sci. Rep., 2, 1–12, doi:10.1038/srep00572, 2012.

Guerzoni, S., Molinaroli, E. and Chester, R.: Saharan dust inputs to the western Mediterranean Sea: Depositional patterns, geochemistry and sedimentological implications, Deep. Res. Part II Top. Stud. Oceanogr., 44(3–4), 631–654, doi:10.1016/S0967-0645(96)00096-3, 1997.

Guieu, C. and Ridame, C.: Impact of atmospheric deposition on marine chemistry and biogeochemistry, in Atmospheric Chemistry in the Mediterranean Region: Comprehensive Diagnosis and Impacts, edited by F. Dulac, S. Sauvage, and E. Hamonou, Springer., 2020.

Guieu, C. and Thomas, A. J.: Saharan Aerosols: from the soil to the ocean, in The Impact of Desert Dust Across the Mediterranean, pp. 207–216., 1996.

Guieu, C., Loÿe-Pilot, M. D., Ridame, C. and Thomas, C.: Chemical characterization of the Saharan dust end-member: Some biogeochemical implications for the western Mediterranean Sea, J. Geophys. Res. Atmos., 107(15), doi:10.1029/2001JD000582, 2002.

Guieu, C., Dulac, F., Desboeufs, K. V., Wagener, T., Pulido-Villena, E., Grisoni, J. M., Louis, F., Ridame, C., Blain, S., Brunet, C., Bon Nguyen, E., Tran, S., Labiadh, M. and Dominici, J. M.: Large clean mesocosms and simulated dust deposition: A new methodology to investigate responses of marine oligotrophic ecosystems to atmospheric

inputs, Biogeosciences, 7(9), 2765–2784, doi:10.5194/bg-7-2765-2010, 2010.
Guieu, C., Aumont, O., Paytan, A., Bopp, L., Law, C. S., Mahowald, N. M., Achterberg, E. P., Marañón, E., Salihoglu, B., Crise, A., Wagener, T., Herut, B., Desboeufs, K. V., Kanakidou, M., Olgun, N., Peters, F. and Völker, C.: Global Biogeochemical Cycles deposition to Low Nutrient Low Chlorophyll regions, Global Biogeochem. Cycles, 28, 1–20, doi:10.1002/2014GB004852.Received, 2014a.
Guieu, C., Ridame, C., Pulido-Villena, E., Bressac, M., Desboeufs, K. V. and Dulac, F.: Impact of dust deposition on carbon budget: A tentative assessment from a mesocosm approach, Biogeosciences, 11(19), 5621–5635, doi:10.5194/bg-11-5621-2014, 2014b.
Guieu, C., Dulac, F., Ridame, C. and Pondaven, P.: Introduction to project DUNE, a DUst experiment in a low Nutrient, low chlorophyll Ecosystem, Biogeosciences, 11(2), 425–442, doi:10.5194/bg-11-425-2014, 2014c.
Gunnarsson, I. and Arnórsson, S.: Amorphous silica solubility and the thermodynamic properties of H4SiO4° in the range of 0°to 350°C at P(sat), Geochim. Cosmochim. Acta, 64(13), 2295–2307, doi:10.1016/S0016-7037(99)00426-3, 2000.
Guy, C. and Schott, J.: Multisite surface reaction versus transport control during the hydrolysis of a complex oxide, Chem. Geol., 78(3–4), 181–204, doi:10.1016/0009-2541(89)90057-0, 1989.
Haldar, S. K. and Tišljar, J.: Introduction to Mineralogy and Petrology., 2013.
Hamme, R. C., Webley, P. W., Crawford, W. R., Whitney, F. A., Degrandpre, M. D., Emerson, S. R., Eriksen, C. C., Giesbrecht, K. E., Gower, J. F. R., Kavanaugh, M. T., Pea, M. A., Sabine, C. L., Batten, S. D., Coogan, L. A., Grundle, D. S. and Lockwood, D.: Volcanic ash fuels anomalous plankton bloom in subarctic northeast Pacific, Geophys. Res. Lett., 37(19), doi:10.1029/2010GL044629, 2010.
Hans Wedepohl, K.: The composition of the continental crust, Geochim. Cosmochim. Acta, 59(7), 1217–1232, doi:10.1016/0016-7037(95)00038-2, 1995.
Hassler, C. S., Schoemann, V., Nichols, C. M., Butler, E. C. V. and Boyd, P. W.: Saccharides enhance iron bioavailability to Southern Ocean phytoplankton, Proc. Natl. Acad. Sci., 108(3), 1076–1081, doi:10.1073/pnas.1010963108, 2011.
Hernández-Ruiz, M., Barber-Lluch, E., Prieto, A., Logares, R. and Teira, E.: Response of pico-nano-eukaryotes to inorganic and organic nutrient additions, Estuar. Coast. Shelf Sci., 235(May 2019), doi:10.1016/j.ecss.2019.106565, 2020.
Hettiarachchi, E., Reynolds, R. L., Goldstein, H. L., Moskowitz, B. and Rubasinghege, G.: Bioavailable iron production in airborne mineral dust: Controls by chemical composition and solar flux, Atmos. Environ., 205(November 2018), 90–102, doi:10.1016/j.atmosenv.2019.02.037, 2019.
Ho, T. Y., Quigg, A., Finkel, Z. V., Milligan, A. J., Wyman, K., Falkowski, P. G. and Morel, F. M. M.: The elemental composition of some marine phytoplankton, J. Phycol., 39(6), 1145–1159, doi:10.1111/j.0022-3646.2003.03-090.x, 2003.
Hoffmann, L. J., Peeken, I. and Lochte, K.: Iron, silicate, and light co-limitation of three Southern Ocean diatom species, Polar Biol., 31(9), 1067–1080, doi:10.1007/s00300-008-0448-6, 2008.
Hoffmann, L. J., Breitbarth, E., Ardelan, M. V., Duggen, S., Olgun, N., Hassellöv, M. and Wängberg, S. Å.: Influence of trace metal release from volcanic ash on growth of Thalassiosira pseudonana and Emiliania huxleyi, Mar. Chem., 132–133(March 2012), 28–33, doi:10.1016/j.marchem.2012.02.003, 2012.
Hooper, J., Mayewski, P., Marx, S., Henson, S. A., Potocki, M., Sneed, S., Handley, M., Gassó, S., Fischer, M. and Saunders, K. M.: Examining links between dust deposition and phytoplankton response using ice cores, Aeolian Res., 36, 45–60, doi:10.1016/j.aeolia.2018.11.001, 2019.

Hörstmann, C., Raes, E. J., Buttigieg, P. L., Lo Monaco, C., John, U. and Waite, A. M.: Hydrographic fronts shape productivity, nitrogen fixation, and microbial community composition in the southern Indian Ocean and the Southern Ocean, Biogeosciences, 18(12), 3733–3749, doi:10.5194/bg-18-3733-2021, 2021.

Huertas, F. J., Chou, L. and Wollast, R.: Mechanism of kaolinite dissolution at room temperature and pressure Part II : Kinetic study, Geochim. Cosmochim. Acta, 63(19/20), 3261–3275, 1999.

Huertas, F. J., Caballero, E., Jiménez de Cisneros, C. and Linares, J.: Kinetics of montmorillonite dissolution in granitic solutions, Appl. Geochemistry, 16, 1–11 [online] Available from: papers2://publication/uuid/FE40FC5E-3887-4BAD-ACB7-C6E6F1828619, 2001.

Hutchins, D. A., Sedwick, P. N., DiTullio, G. R., Boyd, P. W., Quéguiner, B., Griffiths, F. B. and Crossley, C.: Control of phytoplankton growth by iron and silicic acid availability in the subantarctic Southern Ocean: Experimental results from the SAZ Project, J. Geophys. Res. Ocean., 106(C12), 31559–31572, doi:10.1029/2000JC000333, 2001.

Icenhower, J. P. and Dove, P. M.: The dissolution kinetics of amorphous silica into sodium chloride solutions: Effects of temperature and ionic strength, Geochim. Cosmochim. Acta, 64(24), 4193–4203, doi:10.1016/S0016-7037(00)00487-7, 2000.

Ingall, E. D., Feng, Y., Longo, A. F., Lai, B., Shelley, R. U., Landing, W. M., Morton, P. L., Nenes, A., Mihalopoulos, N., Violaki, K., Gao, Y., Sahai, S. and Castorina, E.: Enhanced iron solubility at low pH in global aerosols, Atmosphere (Basel)., 9(5), 1–17, doi:10.3390/ATMOS9050201, 2018.

Ito, A. and Wagai, R.: Data Descriptor: Global distribution of clay-size minerals on land surface for biogeochemical and climatological studies, Sci. Data, 4, 1–11, doi:10.1038/sdata.2017.1031, 2017.

Jacq, V.: Influence de la biodiversité des nutriments sur la fixation de N2 et réponse de Crocosphaera watsonii face à la limitation en fer, Université Pierre et Marie Curie - Paris VI. [online] Available from: https://tel.archives-ouvertes.fr/tel-01127359, 2014.

Jeandel, C. and Oelkers, E. H.: The influence of terrigenous particulate material dissolution on ocean chemistry and global element cycles, Chem. Geol., doi:10.1016/j.chemgeo.2014.12.001, 2015.

Jenny, H.: Factors of Soil Formation, Soil Sci., doi:10.1097/00010694-194111000-00009, 1941.

Jickells, T. D. and Moore, C. M.: The Importance of Atmospheric Deposition for Ocean Productivity, Annu. Rev. Ecol. Evol. Syst., 46(1), 481–501, doi:10.1146/annurev-ecolsys-112414-054118, 2015.

Jickells, T. D. and Spokes, L. J.: Atmospheric iron inputs to the oceans, in The Biogeochemistry of Iron in Seawater., 2001.

Jickells, T. D., An, Z. S., Andersen, K. K., Baker, A. R., Bergametti, G., Brooks, N., Cao, J. J., Boyd, P. W., Duce, R. A., Hunter, K. A., Kawahata, H., Kubilay, N., LaRoche, J., Liss, P. S., Mahowald, N. M., Prospero, J. M., Ridgwell, A. J., Tegen, I. and Torres, R.: Global Iron Connections Between Desert Dust, Ocean Biogeochemistry, and Climate, Science (80-.)., 308(5718), 67–71, doi:10.1126/science.1105959, 2005.

Jickells, T. D., Baker, A. R. and Chance, R.: Atmospheric transport of trace elements and nutrients to the oceans, Philos. Trans. R. Soc. A Math. Phys. Eng. Sci., 374(2081), doi:10.1098/rsta.2015.0286, 2016.

Johnson, M. S. and Meskhidze, N.: Atmospheric dissolved iron deposition to the global oceans: effects of oxalate-promoted Fe dissolution, photochemical redox cycling, and dust mineralogy, Geosci. Model Dev. Discuss., 6(1), 1901–1947, doi:10.5194/gmdd-6-1901-2013, 2013.

Johnson, M. S., Meskhidze, N., Kiliyanpilakkil, V. P. and Gassó, S.: Understanding the transport of Patagonian dust and its influence on marine biological activity in the South Atlantic Ocean, Atmos. Chem. Phys., 11(6), 2487–2502, doi:10.5194/acp-11-2487-2011, 2011.

Jones, M. T. and Gislason, S. R.: Rapid releases of metal salts and nutrients following the deposition of volcanic ash into aqueous environments, Geochim. Cosmochim. Acta, 72(15), 3661–3680, doi:10.1016/j.gca.2008.05.030, 2008.

Jongmans, A. G., Groenesteijn, K., Buurman, P. and Mulder, J.: Soil Surface Coatings at Costa Rican Recently Active Volcanoes, Soil Sci. Soc. Am. J., 60(6), 1871–1880, doi:10.2136/sssaj1996.03615995006000060036x, 1996.

Journet, E.: Etude du facteur minéralogique sur la solubilité et la spéciation redox du fer dissous dans le contexte biogeochimique du dépôt atmosphérique des aérosols désertiques sahélo-sahariens, 2008.

Journet, E., Desboeufs, K. V., Caquineau, S. and Colin, J.-L.: Mineralogy as a critical factor of dust iron solubility, Geophys. Res. Lett., 35(7), n/a-n/a, doi:10.1029/2007GL031589, 2008.

Kanakidou, M., Myriokefalitakis, S. and Tsigaridis, K.: Aerosols in atmospheric chemistry and biogeochemical cycles of nutrients, Environ. Res. Lett., 13(6), doi:10.1088/1748-9326/aabcdb, 2018.

Köhler, S. J., Dufaud, F. and Oelkers, E. H.: An experimental study of illite dissolution kinetics as a function of ph from 1.4 to 12.4 and temperature from 5 to 50°C, Geochim. Cosmochim. Acta, 67(19), 3583–3594, doi:10.1016/S0016-7037(03)00163-7, 2003.

Köhler, S. J., Bosbach, D. and Oelkers, E. H.: Do clay mineral dissolution rates reach steady state?, Geochim. Cosmochim. Acta, 69(8), 1997–2006, doi:10.1016/j.gca.2004.10.015, 2005.

Kooistra, W. H. C. F.: The Evolution of the Diatoms, in Handbook of Biomineralization: Biological Aspects and Structure Formation., 2008.

Korte, L., Pausch, F., Trimborn, S., Brussaard, C., Brummer, G.-J., van der Does, M., Guerreiro, C., Schreuder, L., Munday, C. and Stuut, J.-B.: Effects of dry and wet Saharan dust deposition in the tropical North Atlantic Ocean, Biogeosciences Discuss., (December), 1–20, doi:10.5194/bg-2018-484, 2018.

Krause, J. W., Brzezinski, M. A., Baines, S. B., Collier, J. L., Twining, B. S. and Ohnemus, D. C.: Picoplankton contribution to biogenic silica stocks and production rates in the Sargasso Sea, Global Biogeochem. Cycles, 31(5), 762–774, doi:10.1002/2017GB005619, 2017.

Krishnamurthy, A., Moore, J. K., Zender, C. S. and Luo, C.: Effects of atmospheric inorganic nitrogen deposition on ocean biogeochemistry, J. Geophys. Res., 112(G2), G02019, doi:10.1029/2006JG000334, 2007.

Krishnamurthy, A., Moore, J. K., Mahowald, N. M., Luo, C. and Zender, C. S.: Impacts of atmospheric nutrient inputs on marine biogeochemistry, J. Geophys. Res., 115(G1), doi:10.1029/2009jg001115, 2010.

Krueger, B. J., Grassian, V. H., Cowin, J. P. and Laskin, A.: Heterogeneous chemistry of individual mineral dust particles from different dust source regions: the importance of particle mineralogy, Atmos. Environ., 38(36), 6253–6261, doi:10.1016/j.atmosenv.2004.07.010, 2004.

Kubilay, N., Nickovic, S., Moulin, C. and Dulac, F.: An illustration of the transport and deposition of mineral dust onto the eastern Mediterranean, Atmos. Environ., 34(8), 1293–1303, doi:10.1016/S1352-2310(99)00179-X, 2000.

Kustka, A., Saudo-Wilhelmy, S., Carpenter, E. J., Capone, D. G. and Raven, J. A.: a revised estimate of the iron use efficiency of nitrogen fixation, with special reference to the

marine cyanobacterium Trichodesmium spp. (cyanophyta), J. Phycol., 39(1), 12–25, doi:10.1046/j.1529-8817.2003.01156.x, 2003.

Kutterolf, S., Freundt, A. and Peréz, W.: Pacific offshore record of plinian arc volcanism in Central America: 2. Tephra volumes and erupted masses, Geochemistry, Geophys. Geosystems, 9(2), n/a-n/a, doi:10.1029/2007GC001791, 2008.

Lafon, S., Rajot, J.-L., Alfaro, S. C. and Gaudichet, A.: Quantification of iron oxides in desert aerosol, Atmos. Environ., 38(8), 1211–1218, doi:10.1016/j.atmosenv.2003.11.006, 2004.

Lagerström, M. E., Field, M. P., Séguret, M., Fischer, L., Hann, S. and Sherrell, R. M.: Automated on-line flow-injection ICP-MS determination of trace metals (Mn, Fe, Co, Ni, Cu and Zn) in open ocean seawater: Application to the GEOTRACES program, Mar. Chem., 155, 71–80, doi:10.1016/j.marchem.2013.06.001, 2013.

Langmann, B., Zakšek, K. and Hort, M.: Atmospheric distribution and removal of volcanic ash after the eruption of Kasatochi volcano: A regional model study, J. Geophys. Res., 115(March), D00L06, doi:10.1029/2009JD013298, 2010a.

Langmann, B., Zakšek, K., Hort, M. and Duggen, S.: Volcanic ash as fertiliser for the surface ocean, Atmos. Chem. Phys., 10(8), 3891–3899, doi:10.5194/acp-10-3891-2010, 2010b.

Lawrence, C. R. and Neff, J. C.: The contemporary physical and chemical flux of aeolian dust: A synthesis of direct measurements of dust deposition, Chem. Geol., 267(1–2), 46–63, doi:10.1016/j.chemgeo.2009.02.005, 2009.

de Leeuw, G., Guieu, C., Arneth, A., Bellouin, N., Bopp, L., Boyd, P. W., Denier van der Gon, H. A. C., Desboeufs, K. V., Dulac, F., Facchini, M. C., Gantt, B., Langmann, B., Mahowald, N. M., Marañón, E., O'Dowd, C., Olgun, N., Pulido-Villena, E., Rinaldi, M., Stephanou, E. G. and Wagener, T.: Ocean-Atmosphere Interactions of Gases and Particles, edited by P. S. Liss and M. T. Johnson, Springer Berlin Heidelberg, Berlin, Heidelberg., 2014.

Li, F., Ginoux, P. and Ramaswamy, V.: Distribution, transport, and deposition of mineral dust in the Southern Ocean and Antarctica: Contribution of major sources, J. Geophys. Res., 113(D10), D10207, doi:10.1029/2007JD009190, 2008.

Liu, X. and Millero, F. J.: The solubility of iron in seawater, Mar. Chem., 77(1), 43–54, doi:10.1016/S0304-4203(01)00074-3, 2002.

Longhurst, A.: Ecological Geography of the Sea., 2007.

Loucaides, S., Van Cappellen, P. and Behrends, T.: Dissolution of biogenic silica from land to ocean: Role of salinity and pH, Limnol. Oceanogr., 53(4), 1614–1621, doi:10.4319/lo.2008.53.4.1614, 2008.

Louis, J., Bressac, M., Pedrotti, M. L. and Guieu, C.: Dissolved inorganic nitrogen and phosphorus dynamics in seawater following an artificial Saharan dust deposition event, Front. Mar. Sci., 2(MAY), 1–11, doi:10.3389/fmars.2015.00027, 2015.

Luo, C., Mahowald, N. M., Bond, T. C., Chuang, P. Y., Artaxo, P., Siefert, R. L., Chen, Y. and Schauer, J.: Combustion iron distribution and deposition, Global Biogeochem. Cycles, 22(1), doi:10.1029/2007GB002964, 2008.

Lützenkirchen, J., Abdelmonem, A., Weerasooriya, R., Heberling, F., Metz, V. and Marsac, R.: Adsorption of dissolved aluminum on sapphire-c and kaolinite: Implications for points of zero charge of clay minerals, Geochem. Trans., 15(1), 1–14, doi:10.1186/1467-4866-15-9, 2014.

Mackey, K. R. M., Buck, K. N., Casey, J. R., Cid, A., Lomas, M. W., Sohrin, Y. and Paytan, A.: Phytoplankton responses to atmospheric metal deposition in the coastal and open-ocean Sargasso Sea, Front. Microbiol., 3(OCT), 1–15, doi:10.3389/fmicb.2012.00359, 2012.

Mackey, K. R. M., Chien, C. Te, Post, A. F., Saito, M. A. and Paytan, A.: Rapid and gradual modes of aerosol trace metal dissolution in seawater, Front. Microbiol., 6(JAN), 1–11,

doi:10.3389/fmicb.2014.00794, 2015.
Mackey, K. R. M., Kavanaugh, M. T., Wang, F., Chen, Y., Liu, F., Glover, D. M., Chien, C. Te and Paytan, A.: Atmospheric and fluvial nutrients fuel algal blooms in the East China Sea, Front. Mar. Sci., 4(JAN), 1–13, doi:10.3389/fmars.2017.00002, 2017.
Mahowald, N. M., Kohfeld, K., Hansson, M., Balkanski, Y., Harrison, S. P., Prentice, I. C., Schulz, M. and Rodhe, H.: Dust sources and deposition during the last glacial maximum and current climate: A comparison of model results with paleodata from ice cores and marine sediments, J. Geophys. Res. Atmos., 104(D13), 15895–15916, doi:10.1029/1999JD900084, 1999.
Mahowald, N. M., Baker, A. R., Bergametti, G., Brooks, N., Duce, R. A., Jickells, T. D., Kubilay, N., Prospero, J. M. and Tegen, I.: Atmospheric global dust cycle and iron inputs to the ocean, Global Biogeochem. Cycles, 19(4), n/a-n/a, doi:10.1029/2004GB002402, 2005.
Mahowald, N. M., Jickells, T. D., Baker, A. R., Artaxo, P., Benitez-Nelson, C. R., Bergametti, G., Bond, T. C., Chen, Y., Cohen, D. D., Herut, B., Kubilay, N., Losno, R. R., Luo, C., Maenhaut, W., McGee, K. A., Okin, G. S., Siefert, R. L. and Tsukuda, S.: Global distribution of atmospheric phosphorus sources, concentrations and deposition rates, and anthropogenic impacts, Global Biogeochem. Cycles, 22(4), n/a-n/a, doi:10.1029/2008GB003240, 2008.
Mahowald, N. M., Engelstaedter, S., Luo, C., Sealy, A., Artaxo, P., Benitez-Nelson, C., Bonnet, S., Chen, Y., Chuang, P. Y., Cohen, D. D., Dulac, F., Herut, B., Johansen, A. M., Kubilay, N., Losno, R., Maenhaut, W., Paytan, A., Prospero, J. M., Shank, L. M. and Siefert, R. L.: Atmospheric Iron Deposition: Global Distribution, Variability, and Human Perturbations, Ann. Rev. Mar. Sci., 1(1), 245–278, doi:10.1146/annurev.marine.010908.163727, 2009.
Mahowald, N. M., Albani, S., Kok, J. F., Engelstaeder, S., Scanza, R. A., Ward, D. S. and Flanner, M. G.: The size distribution of desert dust aerosols and its impact on the Earth system, Aeolian Res., 15, 53–71, doi:10.1016/j.aeolia.2013.09.002, 2014.
Mahowald, N. M., Hamilton, D. S., Mackey, K. R. M., Moore, J. K., Baker, A. R., Scanza, R. A. and Zhang, Y.: Aerosol trace metal leaching and impacts on marine microorganisms, Nat. Commun., 9(1), doi:10.1038/s41467-018-04970-7, 2018.
Le Maitre, R. W., Streckeisen, A., Zanettin, B., Bas, M. J. Le, Bonin, B., Bateman, P., Bellieni, G., Dudel, A., Efremova, S., Keller, A. J., Lameyre, J., Sabine, P. A., Schmid, R., Sørensen, H. and Woolley, A. R.: Igneous Rocks: a classification and glossary of terms, recommendations of the International Union of Geological Sciences Subcommission on the Systematics of Igneous Rocks. [online] Available from: https://www.cambridge.org/core/product/identifier/S0026461X00042997/type/journal_article, 2002.
Malden, P. J. and Meads, R. E.: Substitution by Iron in Kaolinite, Nature, 215(5103), 844–846, doi:10.1038/215844a0, 1967.
Marañón, E., Fernández, A., Mouriño-Carballido, B., MartÍnez-GarcÍa, S., Teira, E., Cermeño, P., Chouciño, P., Huete-Ortega, M., Fernández, E., Calvo-Díaz, A., Morán, X. A. G., Bode, A., Moreno-Ostos, E., Varela, M. M., Patey, M. D. and Achterberg, E. P.: Degree of oligotrophy controls the response of microbial plankton to Saharan dust, Limnol. Oceanogr., 55(6), 2339–2352, doi:10.4319/lo.2010.55.6.2339, 2010.
Marcotte, A. R., Anbar, A. D., Majestic, B. J. and Herckes, P.: Mineral Dust and Iron Solubility: Effects of Composition, Particle Size, and Surface Area, Atmosphere (Basel)., 11(5), 533, doi:10.3390/atmos11050533, 2020.
Marie, D., Partensky, F., Vaulot, D. and Brussaard, C.: Enumeration of Phytoplankton, Bacteria, and Viruses in Marine Samples, Curr. Protoc. Cytom., 10(1),

doi:10.1002/0471142956.cy1111s10, 1999.
Maring, H.: Mineral dust aerosol size distribution change during atmospheric transport, J. Geophys. Res., 108(D19), 8592, doi:10.1029/2002JD002536, 2003.
Maring, H. B. and Duce, R. A.: The impact of atmospheric aerosols on trace metal chemistry in open ocean surface seawater, 1. Aluminum, Earth Planet. Sci. Lett., 84(4), 381–392, doi:10.1016/0012-821X(87)90003-3, 1987.
Marshall, W. L. and Warakomski, J. M.: Amorphous silica solubilities-II. Effect of aqueous salt solutions at 25°C, Geochim. Cosmochim. Acta, 44(7), doi:10.1016/0016-7037(80)90281-1, 1980.
Martin, J. H.: Glacial-interglacial CO 2 change: The Iron Hypothesis, Paleoceanography, 5(1), 1–13, doi:10.1029/PA005i001p00001, 1990.
Maters, E. C., Delmelle, P. and Bonneville, S.: Atmospheric Processing of Volcanic Glass: Effects on Iron Solubility and Redox Speciation, Environ. Sci. Technol., 50(10), 5033–5040, doi:10.1021/acs.est.5b06281, 2016.
McClain, C. R., Signorini, S. R. and Christian, J. R.: Subtropical gyre variability observed by ocean-color satellites, Deep. Res. Part II Top. Stud. Oceanogr., 51(1–3), 281–301, doi:10.1016/j.dsr2.2003.08.002, 2004.
McConnell, J. R., Aristarain, A. J., Banta, J. R., Edwards, P. R. and Simões, J. C.: 20th-Century doubling in dust archived in an Antarctic Peninsula ice core parallels climate change and desertification in South America, Proc. Natl. Acad. Sci. U. S. A., 104(14), 5743–5748, doi:10.1073/pnas.0607657104, 2007.
Mélançon, J., Levasseur, M., Lizotte, M., Delmelle, P., Cullen, J., Hamme, R. C., Peña, A., Simpson, K. G., Scarratt, M., Tremblay, J.-É., Zhou, J., Johnson, K., Sutherland, N., Arychuk, M., Nemcek, N. and Robert, M.: Early response of the northeast subarctic Pacific plankton assemblage to volcanic ash fertilization, Limnol. Oceanogr., 59(1), 55–67, doi:10.4319/lo.2014.59.1.0055, 2014.
Mélançon, J., Levasseur, M., Lizotte, M., Scarratt, M., Tremblay, J.-É., Tortell, P., Yang, G. P., Shi, G. Y., Gao, H., Semeniuk, D., Robert, M., Arychuk, M., Johnson, K., Sutherland, N., Davelaar, M., Nemcek, N., Peña, A. and Richardson, W.: Impact of ocean acidification on phytoplankton assemblage, growth, and DMS production following Fe-dust additions in the NE Pacific high-nutrient, low-chlorophyll waters, Biogeosciences, 13(5), 1677–1692, doi:10.5194/bg-13-1677-2016, 2016.
Menut, L., Siour, G., Bessagnet, B., Couvidat, F., Journet, E., Balkanski, Y. and Desboeufs, K. V.: Modelling the mineralogical composition and solubility of mineral dust in the Mediterranean area with CHIMERE 2017r4, Geosci. Model Dev., 13(4), 2051–2071, doi:10.5194/gmd-13-2051-2020, 2020.
Mermut, A. R. and Cano, A. F.: Baseline Studies of The Clay Minerals Society Source Clays: Chemical Analyses of Major Elements, Clays Clay Miner., 49(5), 410 LP – 432, doi:10.1346/CCMN.2001.0490510, 2001.
Meskhidze, N., Nenes, A., Chameides, W. L., Luo, C. and Mahowald, N. M.: Atlantic Southern Ocean productivity: Fertilization from above or below?, Global Biogeochem. Cycles, 21(2), 1–9, doi:10.1029/2006GB002711, 2007.
Meskhidze, N., Hurley, D., Royalty, T. M. and Johnson, M. S.: Potential effect of atmospheric dissolved organic carbon on the iron solubility in seawater, Mar. Chem., 194(June), 124–132, doi:10.1016/j.marchem.2017.05.011, 2017.
Metzl, N. and Lo Monaco, C.: Surface underway measurements of partial pressure of carbon dioxide (pCO2), salinity, temperature and other associated parameters during the R/V Marion Dufresne OISO-29 cruise (EXPOCODE 35MV20190109) in Indian Ocean from 2019-01-09 to 2019-02-08, NOAA Natl. Centers Environ. Information. Dataset [online] Available from: https://www.ncei.noaa.gov/access/metadata/landing-

page/bin/iso?id=gov.noaa.nodc:0208441 (Accessed 24 March 2021), 2020.
Millero, F. J., Huang, F., Zhu, X., Liu, X. and Zhang, J. Z.: Adsorption and desorption of phosphate on calcite and aragonite in seawater, Aquat. Geochemistry, 7(1), 33–56, doi:10.1023/A:1011344117092, 2001.
Millero, F. J., Woosey, R., Ditrolio, B. and Waters, J.: effect of Ocean acidification on the Speciation of Metals in Seawater, Oceanography, 22(4), 72–85 [online] Available from: http://tos.org/oceanography/assets/docs/22-4_millero.pdf, 2009.
Mills, M. M., Ridame, C., Davey, M., La Roche, J. and Geider, R. J.: Iron and phosphorus co-limit nitrogen fixation in the eastern tropical North Atlantic, Nature, 429(6989), 292–294, doi:10.1038/nature02550, 2004.
Lo Monaco, C. and Metzl, N.: VT 163 / OISO-29 cruise, RV Marion Dufresne, , doi:10.17600/18000972, 2019.
Moore, C. M., Hickman, A. E., Poulton, A. J., Seeyave, S. and Lucas, M. I.: Iron-light interactions during the CROZet natural iron bloom and EXport experiment (CROZEX): II-Taxonomic responses and elemental stoichiometry, Deep. Res. Part II Top. Stud. Oceanogr., 54(18–20), 2066–2084, doi:10.1016/j.dsr2.2007.06.015, 2007a.
Moore, C. M., Seeyave, S., Hickman, A. E., Allen, J. T., Lucas, M. I., Planquette, H., Pollard, R. T. and Poulton, A. J.: Iron-light interactions during the CROZet natural iron bloom and EXport experiment (CROZEX) I: Phytoplankton growth and photophysiology, Deep. Res. Part II Top. Stud. Oceanogr., 54(18–20), 2045–2065, doi:10.1016/j.dsr2.2007.06.011, 2007b.
Moore, J. K., Doney, S. C., Glover, D. M. and Fung, I. Y.: Iron cycling and nutrient-limitation patterns in surface waters of the world ocean, Deep. Res. Part II Top. Stud. Oceanogr., 49(1–3), 463–507, doi:10.1016/S0967-0645(01)00109-6, 2002.
Morel, A., Claustre, H. and Gentili, B.: The most oligotrophic subtropical zones of the global ocean: Similarities and differences in terms of chlorophyll and yellow substance, Biogeosciences, 7(10), 3139–3151, doi:10.5194/bg-7-3139-2010, 2010.
Moreno, T., Querol, X., Castillo, S., Alastuey, A., Cuevas, E., Herrmann, L., Mounkaila, M., Elvira, J. and Gibbons, W.: Geochemical variations in aeolian mineral particles from the Sahara-Sahel Dust Corridor, Chemosphere, doi:10.1016/j.chemosphere.2006.02.052, 2006.
Morin, G. P., Vigier, N. and Verney-Carron, A.: Enhanced dissolution of basaltic glass in brackish waters: Impact on biogeochemical cycles, Earth Planet. Sci. Lett., 417, 1–8, doi:10.1016/j.epsl.2015.02.005, 2015.
Murphy, J. and Riley, J. P.: A modified single solution method for the determination of phosphate in natural waters, Anal. Chim. Acta, doi:10.1016/S0003-2670(00)88444-5, 1962.
Myriokefalitakis, S., Nenes, A., Baker, A. R., Mihalopoulos, N. and Kanakidou, M.: Bioavailable atmospheric phosphorous supply to the global ocean: a 3-D global modeling study, Biogeosciences, 13(24), 6519–6543, doi:10.5194/bg-13-6519-2016, 2016.
Mysen, B. O., Holtz, F., Pichavant, M., Beny, J. M. and Montel, J. M.: The effect of temperature and bulk composition on the solution mechanism of phosphorus in peraluminous haplogranitic magma, Am. Mineral., 84(9), 1336–1345, doi:10.2138/am-1999-0910, 1999.
Nelson, D. M., Brzezinski, M. A., Sigmon, D. and Franck, V.: A seasonal progression of Si limitation in the Pacific sector of the Southern Ocean, Deep Sea Res. Part II Top. Stud. Oceanogr., 48(19–20), 3973–3995, doi:10.1016/S0967-0645(01)00076-5, 2001.
Nowak, S., Lafon, S., Caquineau, S., Journet, E. and Laurent, B.: Quantitative study of the mineralogical composition of mineral dust aerosols by X-ray diffraction, Talanta, 186(March), 133–139, doi:10.1016/j.talanta.2018.03.059, 2018.

Nozaki, Y.: Elemental Distribution: Overview, in Marine Chemistry and Geochemistry, pp. 7–13., 2001.

Oelkers, E. H., Schott, J. and Devidal, J.-L.: The effect of aluminum, pH, and chemical affinity on the rates of aluminosilicate dissolution reactions, Geochim. Cosmochim. Acta, 58(9), 2011–2024, doi:10.1016/0016-7037(94)90281-X, 1994.

Okin, G. S., Baker, A. R., Tegen, I., Mahowald, N. M., Dentener, F. J., Duce, R. A., Galloway, J. N., Hunter, K., Kanakidou, M., Kubilay, N., Prospero, J. M., Sarin, M., Surapipith, V., Uematsu, M. and Zhu, T.: Impacts of atmospheric nutrient deposition on marine productivity: Roles of nitrogen, phosphorus, and iron, Global Biogeochem. Cycles, 25(2), n/a-n/a, doi:10.1029/2010GB003858, 2011.

Olgun, N., Duggen, S., Croot, P. L., Delmelle, P., Dietze, H., Schacht, U., Óskarsson, N., Siebe, C., Auer, A. and Garbe-Schönberg, D.: Surface ocean iron fertilization: The role of airborne volcanic ash from subduction zone and hot spot volcanoes and related iron fluxes into the Pacific Ocean, Global Biogeochem. Cycles, 25(4), n/a-n/a, doi:10.1029/2009GB003761, 2011.

Olgun, N., Duggen, S., Andronico, D., Kutterolf, S., Croot, P. L., Giammanco, S., Censi, P. and Randazzo, L.: Possible impacts of volcanic ash emissions of Mount Etna on the primary productivity in the oligotrophic Mediterranean Sea: Results from nutrient-release experiments in seawater, Mar. Chem., 152, 32–42, doi:10.1016/j.marchem.2013.04.004, 2013.

Orsi, A. H., Whitworth, T. and Nowlin, W. D.: On the meridional extent and fronts of the Antarctic Circumpolar Current, Deep Sea Res. Part I Oceanogr. Res. Pap., 42(5), 641–673, doi:10.1016/0967-0637(95)00021-W, 1995.

Oxburgh, R., Drever, J. I. and Sun, Y. T.: Mechanism of plagioclase dissolution in acid solution at 25°C, Geochim. Cosmochim. Acta, 58(2), 661–669, doi:10.1016/0016-7037(94)90496-0, 1994.

Pacyna, J. M. and Pacyna, E. G.: An assessment of global and regional emissions of trace metals to the atmosphere from anthropogenic sources worldwide, Environ. Rev., doi:10.1139/a01-012, 2001.

Paparazzo, F., Crespi-Abril, A., Gonçalves, R., Barbieri, E., Gracia Villalobos, L., Solís, M. and Soria, G.: Patagonian Dust as a Source of Macronutrients in the Southwest Atlantic Ocean, Oceanography, 31(4), 33–39, doi:10.5670/oceanog.2018.408, 2018.

Paque, M., Detienne, M., Maters, E. C. and Delmelle, P.: Smectites and zeolites in ash from the 2010 summit eruption of Eyjafjallajökull volcano, Iceland, Bull. Volcanol., 78(9), doi:10.1007/s00445-016-1056-x, 2016.

Paris, R. and Desboeufs, K. V.: Effect of atmospheric organic complexation on iron-bearing dust solubility, Atmos. Chem. Phys., 13(9), 4895–4905, doi:10.5194/acp-13-4895-2013, 2013.

Paris, R., Desboeufs, K. V. and Journet, E.: Variability of dust iron solubility in atmospheric waters: Investigation of the role of oxalate organic complexation, Atmos. Environ., 45(36), 6510–6517, doi:10.1016/j.atmosenv.2011.08.068, 2011.

Paytan, A., Mackey, K. R. M., Chen, Y., Lima, I. D., Doney, S. C., Mahowald, N. M., Labiosa, R. and Post, A. F.: Toxicity of atmospheric aerosols on marine phytoplankton, Proc. Natl. Acad. Sci., 106(12), 4601–4605, doi:10.1073/pnas.0811486106, 2009.

Peers, G. and Price, N. M.: Copper-containing plastocyanin used for electron transport by an oceanic diatom, Nature, 441(7091), 341–344, doi:10.1038/nature04630, 2006.

Perron, M. M. G., Strzelec, M., Gault-Ringold, M., Proemse, B. C., Boyd, P. W. and Bowie, A. R.: Assessment of leaching protocols to determine the solubility of trace metals in aerosols, Talanta, 208, doi:10.1016/j.talanta.2019.120377, 2020.

Pierson, T. C., Major, J. J., Amigo, Á. and Moreno, H.: Acute sedimentation response to

rainfall following the explosive phase of the 2008-2009 eruption of Chaitén volcano, Chile, Bull. Volcanol., 75(5), 1–17, doi:10.1007/s00445-013-0723-4, 2013.
Price, N. M. and Morel, F. M. M.: Cadmium and cobalt substitution for zinc in a marine diatom, Nature, doi:10.1038/344658a0, 1990.
Pulido-Villena, E., Rrolle, V. and Guieu, C.: Transient fertilizing effect of dust in P-deficient LNLC surface ocean, Geophys. Res. Lett., 37(1), doi:10.1029/2009GL041415, 2010.
Pye, H. O. T., Nenes, A., Alexander, B., Ault, A. P., Barth, M. C., Clegg, S. L., Collett Jr., J. L., Fahey, K. M., Hennigan, C. J., Herrmann, H., Kanakidou, M., Kelly, J. T., Ku, I.-T., McNeill, V. F., Riemer, N., Schaefer, T., Shi, G., Tilgner, A., Walker, J. T., Wang, T., Weber, R. J., Xing, J., Zaveri, R. A. and Zuend, A.: The acidity of atmospheric particles and clouds, Atmos. Chem. Phys., 20(8), 4809–4888, doi:10.5194/acp-20-4809-2020, 2020.
Pyle, D. M.: Sizes of Volcanic Eruptions, Second Edi., Elsevier Inc., 2015.
Le Quéré, C., Andrew, R. M., Canadell, J. G., Sitch, S., Ivar Korsbakken, J., Peters, G. P., Manning, A. C., Boden, T. A., Tans, P. P., Houghton, R. A., Keeling, R. F., Alin, S., Andrews, O. D., Anthoni, P., Barbero, L., Bopp, L., Chevallier, F., Chini, L. P., Ciais, P., Currie, K., Delire, C., Doney, S. C., Friedlingstein, P., Gkritzalis, T., Harris, I., Hauck, J., Haverd, V., Hoppema, M., Klein Goldewijk, K., Jain, A. K., Kato, E., Körtzinger, A., Landschützer, P., Lefèvre, N., Lenton, A., Lienert, S., Lombardozzi, D., Melton, J. R., Metzl, N., Millero, F. J., Monteiro, P. M. S., Munro, D. R., Nabel, J. E. M. S., Nakaoka, S. I., O'Brien, K., Olsen, A., Omar, A. M., Ono, T., Pierrot, D., Poulter, B., Rödenbeck, C., Salisbury, J., Schuster, U., Schwinger, J., Séférian, R., Skjelvan, I., Stocker, B. D., Sutton, A. J., Takahashi, T., Tian, H., Tilbrook, B., Van Der Laan-Luijkx, I. T., Van Der Werf, G. R., Viovy, N., Walker, A. P., Wiltshire, A. J. and Zaehle, S.: Global Carbon Budget 2016, Earth Syst. Sci. Data, 8(2), 605–649, doi:10.5194/essd-8-605-2016, 2016.
Ragueneau, O., Savoye, N., Del Amo, Y., Cotten, J., Tardiveau, B. and Leynaert, A.: A new method for the measurement of biogenic silica in suspended matter of coastal waters: Using Si:Al ratios to correct for the mineral interference, Cont. Shelf Res., 25(5–6), 697–710, doi:10.1016/j.csr.2004.09.017, 2005.
Ralston, S. J.: Dissolution Rates of Allophane , Fe-Allophane , and Hisingerite and Implications for Aqueous Alteration on Mars and in Potential Returned Martian Samples, 2018.
Ras, J., Claustre, H. and Uitz, J.: Spatial variability of phytoplankton pigment distributions in the Subtropical South Pacific Ocean: Comparison between in situ and predicted data, Biogeosciences, 5(2), 353–369, doi:10.5194/bg-5-353-2008, 2008.
Redfield, A. C.: On the proportions of organic derivatives in sea water and their relation to the composition of plankton, Univ. Press Liverpool, James John, 176–192, 1934.
Rhein, M., Rintoul, S. R., Aoki, S., Campos, E., Chambers, D., Feely, R. A., Gulev, S., Johnson, G. C., Josey, S. A., Kostianoy, A., Mauritzen, C., Roemmich, D., Talley, L. D. and Wang, F.: Observations: Ocean, in Climate Change 2013: The Physical Science Basis. Contribution of Working Group I to the Fifth Assessment Report of the Intergovernmental Panel on Climate Change, pp. 255–315., 2013.
Richon, C., Dutay, J. C., Dulac, F., Wang, R., Balkanski, Y., Nabat, P., Aumont, O., Desboeufs, K. V., Laurent, B., Guieu, C., Raimbault, P. and Beuvier, J.: Modeling the impacts of atmospheric deposition of nitrogen and desert dust-derived phosphorus on nutrients and biological budgets of the Mediterranean Sea, Prog. Oceanogr., 163, 21–39, doi:10.1016/j.pocean.2017.04.009, 2018.
Ridame, C.: Chapitre 1 Caractéristiques de l'apport atmosphérique d'origine satarienne en Méditerranée., 2001.
Ridame, C. and Guieu, C.: Saharan input of phosphate to the oligotrophic water of the open

western Mediterranean Sea, Limnol. Ocean., 47(3), 856–869, 2002.
Ridame, C., Moutin, T. and Guieu, C.: Does phosphate adsorption onto Saharan dust explain the unusual N/P ratio in the Mediterranean Sea?, Oceanol. Acta, 26(5–6), 629–634, doi:10.1016/S0399-1784(03)00061-6, 2003.
Ridame, C., Dekaezemacker, J., Guieu, C., Bonnet, S., L'Helguen, S. and Malien, F.: Contrasted Saharan dust events in LNLC environments: impact on nutrient dynamics and primary production, Biogeosciences, 11(17), 4783–4800, doi:10.5194/bg-11-4783-2014, 2014a.
Ridame, C., Dekaezemacker, J., Guieu, C., Bonnet, S., L'Helguen, S. and Malien, F.: Contrasted Saharan dust events in LNLC environments: Impact on nutrient dynamics and primary production, Biogeosciences, 11(17), 4783–4800, doi:10.5194/bg-11-4783-2014, 2014b.
Rogan, N., Achterberg, E. P., Le Moigne, F. A. C., Marsay, C. M., Tagliabue, A. and Williams, R. G.: Volcanic ash as an oceanic iron source and sink, Geophys. Res. Lett., 43(6), 2732–2740, doi:10.1002/2016GL067905, 2016.
Romero, O. E., Lange, C. B., Swap, R. and Wefer, G.: Eolian-transported freshwater diatoms and phytoliths across the equatorial Atlantic record: Temporal changes in Saharan dust transport patterns, J. Geophys. Res. Ocean., 104(C5), 3211–3222, doi:10.1029/1999JC900061, 1999.
Sarmiento, J. L., Gruber, N., Brzezinski, M. A. and Dunne, J. P.: High-latitude controls of thermocline nutrients and low latitude biological productivity, Nature, 427(6969), 56–60, doi:10.1038/nature02127, 2004.
Scanza, R. A., Hamilton, D. S., Perez Garcia-Pando, C., Buck, C. S., Baker, A. R. and Mahowald, N. M.: Atmospheric processing of iron in mineral and combustion aerosols: Development of an intermediate-complexity mechanism suitable for Earth system models, Atmos. Chem. Phys., 18(19), 14175–14196, doi:10.5194/acp-18-14175-2018, 2018.
Scasso, R. A., Corbella, H. and Tiberi, P.: Sedimentological analysis of the tephra from the 12–15 August 1991 eruption of Hudson volcano, Bull. Volcanol., 56(2), 121–132, doi:10.1007/BF00304107, 1994.
Scheuvens, D., Schütz, L., Kandler, K., Ebert, M. and Weinbruch, S.: Bulk composition of northern African dust and its source sediments - A compilation, Earth-Science Rev., 116(1), 170–194, doi:10.1016/j.earscirev.2012.08.005, 2013.
Schlitzer, R.: Ocean Data View, [online] Available from: https://odv.awi.de, 2021.
Schroth, A. W., Crusius, J., Sholkovitz, E. R. and Bostick, B. C.: Iron solubility driven by speciation in dust sources to the ocean, Nat. Geosci., doi:10.1038/ngeo501, 2009.
Sedwick, P. N., Blain, S., Quéguiner, B., Griffiths, F. B., Fiala, M., Bucciarelli, E. and Denis, M.: Resource limitation of phytoplankton growth in the Crozet Basin, Subantarctic Southern Ocean, Deep. Res. Part II Top. Stud. Oceanogr., 49(16), 3327–3349, doi:10.1016/S0967-0645(02)00086-3, 2002.
Sedwick, P. N., Sholkovitz, E. R. and Church, T. M.: Impact of anthropogenic combustion emissions on the fractional solubility of aerosol iron: Evidence from the Sargasso Sea, Geochemistry, Geophys. Geosystems, 8(10), doi:10.1029/2007GC001586, 2007.
Shi, Z., Krom, M. D., Bonneville, S., Baker, A. R., Jickells, T. D. and Benning, L. G.: Formation of iron nanoparticles and increase in iron reactivity in mineral dust during simulated cloud processing, Environ. Sci. Technol., 43(17), 6592–6596, doi:10.1021/es901294g, 2009.
Sholkovitz, E. R., Sedwick, P. N. and Church, T. M.: On the fractional solubility of copper in marine aerosols: Toxicity of aeolian copper revisited, Geophys. Res. Lett., 37(20), n/a-n/a, doi:10.1029/2010GL044817, 2010a.

Sholkovitz, E. R., Sedwick, P. N. and Church, T. M.: On the fractional solubility of copper in marine aerosols: Toxicity of aeolian copper revisited, Geophys. Res. Lett., 37(20), n/a-n/a, doi:10.1029/2010GL044817, 2010b.
Sholkovitz, E. R., Sedwick, P. N., Church, T. M., Baker, A. R. and Powell, C. F.: Fractional solubility of aerosol iron: Synthesis of a global-scale data set, Geochim. Cosmochim. Acta, 89, 173–189, doi:10.1016/j.gca.2012.04.022, 2012.
Sieffermann, G., Jehl, G. and Millot, G.: Allophanes et minéraux argileux des altérations des basaltes du Mont Cameroun, Bull. du Groupe français des argiles, doi:10.3406/argil.1968.1096, 1968.
Sigurdsson, H., Houghton, B., Rymer, H., Stix, J. and McNutt, S.: Encyclopedia of Volcanoes., 2000.
Simonella, L. E., Palomeque, M. E., Croot, P. L., Stein, A., Kupczewski, M., Rosales, A., Montes, M. L., Colombo, F., García, M. G., Villarosa, G. and Gaiero, D. M.: Soluble iron inputs to the Southern Ocean through recent andesitic to rhyolitic volcanic ash eruptions from the Patagonian Andes, Global Biogeochem. Cycles, 29(8), 1125–1144, doi:10.1002/2015GB005177, 2015.
Singh, S., Elumalai, S. P. and Pal, A. K.: Rain pH estimation based on the particulate matter pollutants and wet deposition study, Sci. Total Environ., 563–564, 293–301, doi:https://doi.org/10.1016/j.scitotenv.2016.04.066, 2016.
Smith, J., Vance, D., Kemp, R. A., Archer, C., Toms, P., King, M. and Zárate, M.: Isotopic constraints on the source of Argentinian loess – with implications for atmospheric circulation and the provenance of Antarctic dust during recent glacial maxima, Earth Planet. Sci. Lett., 212(1–2), 181–196, doi:10.1016/S0012-821X(03)00260-7, 2003.
Sofikitis, A.: Source et évolution des formes redox du fer en phase aqueuse atmosphérique., 2004.
Solmon, F., Chuang, P. Y., Meskhidze, N. and Chen, Y.: Acidic processing of mineral dust iron by anthropogenic compounds over the north Pacific Ocean, J. Geophys. Res. Atmos., 114(2), 1–20, doi:10.1029/2008JD010417, 2009.
Stillings, L. L., Drever, J. I., Brantley, S. L., Sun, Y. and Oxburgh, R.: rates of feldspar dissolution at pH 3–7 with 0–8 m M oxalic acid, Chem. Geol., 132(1–4), 79–89, doi:10.1016/S0009-2541(96)00043-5, 1996.
Straub, S. M. and Schmincke, H. U.: Evaluating the tephra input into Pacific Ocean sediments: distribution in space and time, Geol. Rundschau, 87(3), 461–476, doi:10.1007/s005310050222, 1998.
Sunda, W. G.: Feedback Interactions between Trace Metal Nutrients and Phytoplankton in the Ocean, Front. Microbiol., 3, doi:10.3389/fmicb.2012.00204, 2012.
Swedlund, P. J. and Webster, J. G.: Adsorption and polymerisation of silicic acid on ferrihydrite, and its effect on arsenic adsorption, Water Res., 33(16), 3413–3422, doi:10.1166/jbt.2014.1268, 1999.
Tagliabue, A., Bopp, L. and Aumont, O.: Ocean biogeochemistry exhibits contrasting responses to a large scale reduction in dust deposition, Biogeosciences, 5(1), 11–24, doi:10.5194/bg-5-11-2008, 2008.
Tagliabue, A., Bopp, L. and Aumont, O.: Evaluating the importance of atmospheric and sedimentary iron sources to Southern Ocean biogeochemistry, Geophys. Res. Lett., 36(13), L13601, doi:10.1029/2009GL038914, 2009.
Tegen, I. and Kohfeld, K. E.: Atmospheric Transport of Silicon, silicon cycle Hum. perturbations impacts Aquat. Syst., 81–92, 2006.
Ternon, E., Guieu, C., Loÿe-Pilot, M.-D., Leblond, N., Bosc, E., Gasser, B., Miquel, J.-C. and Martín, J.: The impact of Saharan dust on the particulate export in the water column of the North Western Mediterranean Sea, Biogeosciences, 7(3), 809–826, doi:10.5194/bg-7-

809-2010, 2010.

Timmermans, K. R., Veldhuis, M. J. W., Laan, P. and Brussaard, C. P. D.: Probing natural iron fertilization near the Kerguelen (Southern Ocean) using natural phytoplankton assemblages and diatom cultures, Deep. Res. Part II Top. Stud. Oceanogr., 55(5–7), 693–705, doi:10.1016/j.dsr2.2007.12.008, 2008.

Tonnard, M., Planquette, H., Bowie, A. R., van der Merwe, P., Gallinari, M., Desprez de Gésincourt, F., Germain, Y., Gourain, A., Benetti, M., Reverdin, G., Tréguer, P. J., Boutorh, J., Cheize, M., Menzel Barraqueta, J.-L., Pereira-Contreira, L., Shelley, R. U., Lherminier, P. and Sarthou, G.: Dissolved iron in the North Atlantic Ocean and Labrador Sea along the GEOVIDE section (GEOTRACES section GA01), Biogeosciences, 1–53, doi:10.5194/bg-2018-147, 2020.

Tréguer, P. J. and De La Rocha, C. L.: The World Ocean Silica Cycle, Ann. Rev. Mar. Sci., (January 2013), doi:10.1146/annurev-marine-121211-172346, 2013.

Tréguer, P. J. and Pondaven, P.: Silica control of carbon dioxide, Nature, 406(6794), 358–359, doi:10.1038/35019236, 2000.

Tréguer, P. J., Nelson, D. M., Van Bennekom, A. J., DeMaster, D. J., Leynaert, A. and Queguiner, B.: The Silica Balance in the World Ocean: A Reestimate, Science (80-.)., 268(5209), 375–379, doi:10.1126/science.268.5209.375, 1995.

Tréguer, P. J., Sutton, J. N., Brzezinski, M., Charette, M. A., Devries, T., Dutkiewicz, S., Ehlert, C., Hawkings, J., Leynaert, A., Liu, S. M., Llopis Monferrer, N., López-Acosta, M., Maldonado, M., Rahman, S., Ran, L. and Rouxel, O.: Reviews and syntheses: The biogeochemical cycle of silicon in the modern ocean, Biogeosciences, 18(4), 1269–1289, doi:10.5194/bg-18-1269-2021, 2021.

Trimborn, S., Brenneis, T., Hoppe, C., Laglera, L., Norman, L., Santos-Echeandía, J., Völkner, C., Wolf-Gladrow, D. and Hassler, C. S.: Iron sources alter the response of Southern Ocean phytoplankton to ocean acidification, Mar. Ecol. Prog. Ser., 578, 35–50, doi:10.3354/meps12250, 2017.

Tuchowska, M., Muir, B., Kowalik, M., Socha, R. P. and Bajda, T.: Sorption of molybdates and tungstates on functionalized montmorillonites: Structural and textural features, Materials (Basel)., doi:10.3390/ma12142253, 2019.

Twining, B. S. and Baines, S. B.: The Trace Metal Composition of Marine Phytoplankton, Ann. Rev. Mar. Sci., 5(1), 191–215, doi:10.1146/annurev-marine-121211-172322, 2013.

Twining, B. S., Rauschenberg, S., Baer, S. E., Lomas, M. W., Martiny, A. C. and Antipova, O.: A nutrient limitation mosaic in the eastern tropical Indian Ocean, Deep. Res. Part II Top. Stud. Oceanogr., 166(May), 125–140, doi:10.1016/j.dsr2.2019.05.001, 2019.

Uitz, J., Claustre, H., Morel, A. and Hooker, S. B.: Vertical distribution of phytoplankton communities in open ocean: An assessment based on surface chlorophyll, J. Geophys. Res., 111(C8), C08005, doi:10.1029/2005JC003207, 2006.

Uitz, J., Claustre, H., Griffiths, F. B., Ras, J., Garcia, N. and Sandroni, V.: A phytoplankton class-specific primary production model applied to the Kerguelen Islands region (Southern Ocean), Deep Sea Res. Part I Oceanogr. Res. Pap., 56(4), 541–560, doi:10.1016/j.dsr.2008.11.006, 2009.

Vincent, J., Laurent, B., Losno, R., Bon Nguyen, E., Roullet, P., Sauvage, S., Chevaillier, S., Coddeville, P., Ouboulmane, N., di Sarra, A. G., Tovar-Sánchez, A., Sferlazzo, D., Massanet, A., Triquet, S., Morales Baquero, R., Fornier, M., Coursier, C., Desboeufs, K. V., Dulac, F. and Bergametti, G.: Variability of mineral dust deposition in the western Mediterranean basin and south-east of France, Atmos. Chem. Phys., 16(14), 8749–8766, doi:10.5194/acp-16-8749-2016, 2016.

Wagener, T., Pulido-Villena, E. and Guieu, C.: Dust iron dissolution in seawater: Results from a one-year time-series in the Mediterranean Sea, Geophys. Res. Lett., 35(16), 1–6,

doi:10.1029/2008GL034581, 2008.
Wang, R., Balkanski, Y., Boucher, O., Ciais, P., Peñuelas, J. and Tao, S.: Significant contribution of combustion-related emissions to the atmospheric phosphorus budget, Nat. Geosci., 8(1), 48–54, doi:10.1038/ngeo2324, 2015a.
Wang, R., Balkanski, Y., Boucher, O., Bopp, L., Chappell, A., Ciais, P., Hauglustaine, D., Peñuelas, J. and Tao, S.: Sources, transport and deposition of iron in the global atmosphere, Atmos. Chem. Phys., 15(11), 6247–6270, doi:10.5194/acp-15-6247-2015, 2015b.
Watson, A. J., Bakker, D. C. E., Ridgwell, A. J., Boyd, P. W. and Law, C. S.: Effect of iron supply on Southern Ocean CO2 uptake and implications for glacial atmospheric CO2, Nature, 407(6805), 730–733, doi:10.1038/35037561, 2000.
Wedepohl, K. H.: Chapter 5 The Composition of the Continental Crust, in International Geophysics, vol. 34, pp. 213–241., 1986.
Wedepohl, K. H.: The composition of the continental crust, Geochim. Cosmochim. Acta, 59(7), 1217–1232, doi:10.1016/0016-7037(95)00038-2, 1995.
Wei, Y., Sun, J., Chen, Z., Zhang, Z., Zhang, G. and Liu, X.: Significant contribution of picoplankton size fraction to biogenic silica standing stocks in the Western Pacific Ocean, Prog. Oceanogr., 192, 102516, doi:10.1016/j.pocean.2021.102516, 2021.
Weinbauer, M. G., Guinot, B., Migon, C., Malfatti, F. and Mari, X.: Skyfall - neglected roles of volcano ash and black carbon rich aerosols for microbial plankton in the ocean, J. Plankton Res., 39(2), 187–198, doi:10.1093/plankt/fbw100, 2017.
Westberry, T. K., Shi, Y. R., Yu, H., Behrenfeld, M. J. and Remer, L. A.: Satellite-detected Ocean Ecosystem Response to Volcanic Eruptions in the Subarctic Northeast Pacific Ocean, Geophys. Res. Lett., doi:10.1029/2019gl083977, 2019.
Whitney, F. A., Crawford, D. W. and Yoshimura, T.: The uptake and export of silicon and nitrogen in HNLC waters of the NE Pacific Ocean, Deep. Res. Part II Top. Stud. Oceanogr., doi:10.1016/j.dsr2.2005.02.006, 2005.
Winton, V. H. L., Bowie, A. R., Edwards, R. L., Keywood, M., Townsend, A. T., van der Merwe, P. and Bollhöfer, A.: Fractional iron solubility of atmospheric iron inputs to the Southern Ocean, Mar. Chem., 177, 20–32, doi:10.1016/j.marchem.2015.06.006, 2015.
Witham, C. S., Oppenheimer, C. and Horwell, C. J.: Volcanic ash-leachates: a review and recommendations for sampling methods, J. Volcanol. Geotherm. Res., 141(3–4), 299–326, doi:10.1016/j.jvolgeores.2004.11.010, 2005.
Wolff-Boenisch, D., Gislason, S. R. and Oelkers, E. H.: The effect of crystallinity on dissolution rates and CO2 consumption capacity of silicates, Geochim. Cosmochim. Acta, 70(4), 858–870, doi:10.1016/j.gca.2005.10.016, 2006.
Wollast, R. and Chou, L.: Rate Control of Weathering of Silicate Minerals at Room Temperature and Pressure, in Physical and Chemical Weathering in Geochemical Cycles, pp. 11–32, Springer Netherlands, Dordrecht., 1988.
Wong, C. S. and Matear, R. J.: Sporadic silicate limitation of phytoplankton productivity in the subarctic NE Pacific, Deep. Res. Part II Top. Stud. Oceanogr., doi:10.1016/S0967-0645(99)00075-2, 1999.
Wuttig, K., Townsend, A. T., van der Merwe, P., Gault-Ringold, M., Holmes, T., Schallenberg, C., Latour, P., Tonnard, M., Rijkenberg, M. J. A., Lannuzel, D. and Bowie, A. R.: Critical evaluation of a seaFAST system for the analysis of trace metals in marine samples, Talanta, 197(January), 653–668, doi:10.1016/j.talanta.2019.01.047, 2019.
Yoon, J. E., Yoo, K. C., MacDonald, A. M., Yoon, H. Il, Park, K. T., Yang, E. J., Kim, H. C., Lee, J. Il, Lee, M. K., Jung, J., Park, J., Lee, J., Kim, S., Kim, S. S., Kim, K. and Kim, I. N.: Reviews and syntheses: Ocean iron fertilization experiments - Past, present, and future looking to a future Korean Iron Fertilization Experiment in the Southern Ocean

(KIFES) project, Biogeosciences, 15(19), 5847–5889, doi:10.5194/bg-15-5847-2018, 2018.

Zender, C. S., Bian, H. and Newman, D.: Mineral Dust Entrainment and Deposition (DEAD) model: Description and 1990s dust climatology, J. Geophys. Res. D Atmos., 108(14), doi:10.1029/2002jd002775, 2003.

Zhang, J., Zhang, G. S. and Liu, S. M.: Dissolved silicate in coastal marine rainwaters: Comparison between the Yellow Sea and the East China Sea on the impact and potential link with primary production, J. Geophys. Res. D Atmos., 110(16), 1–10, doi:10.1029/2004JD005411, 2005.

Zhang, Y., Mahowald, N. M., Scanza, R. A., Journet, E., Desboeufs, K. V., Albani, S., Kok, J. F., Zhuang, G., Chen, Y., Cohen, D. D., Paytan, A., Patey, M. D., Achterberg, E. P., Engelbrecht, J. P. and Fomba, K. W.: Modeling the global emission, transport and deposition of trace elements associated with mineral dust, Biogeosciences, 12(19), 5771–5792, doi:10.5194/bg-12-5771-2015, 2015.

Zhuang, G. and Duce, R. A.: The adsorption of dissolved iron on marine aerosol particles in surface waters of the open ocean, Deep Sea Res. I, 40(7), 1413–1429, 1993.

Zysset, M. and Schindler, P. W.: The proton promoted dissolution kinetics of K-montmorillonite, Geochim. Cosmochim. Acta, 60(6), 921–931, doi:10.1016/0016-7037(95)00451-3, 1996.

Table des figures

Table des tableaux

Abbreviations

chemical elements		**dissolved form**
aX	*amorphous element X*	
bX	*biogenic element X*	
dX	*dissolved element X*	
dX0	*initial value of dX (in ARW or ASW)*	
LX	*Lithogenic element X*	
Al	Aluminum	dAl
Ca	Calcium	dCa
Cd	Cadmium	dCd
Co	Cobalt	dCo
Cu	Copper	dCu
Fe	Iron	dFe
K	Potassium	dK
Mg	Magnesium	dMg
Mn	Manganese	dMn
Mo	Molybdenum	dMo
N	Nitrogen	NOx
Na	Sodium	dNa
Ni	Nickel	dNi
O	Oxygen	
P	Phosphorous	DIP
Si	Silicon	dSi
Ti	Titanium	dT
V	Vanadium	dV
Zn	Zinc	dZ

measuring units	
L	liter
g	gram
m	meter
mol	mole
h	hour
min	minute
Δ	delta = variation
ρ	rho = rate
°C	degree Celsius
ppm	part per million
power of 10	
T	tera = 10^12
G	giga = 10^9
M	mega = 10^6
k	kilo = 10^3
m	milli = 10^-3
µ	micro = 10^-6
n	nano = 10^-9
p	pico = 10^-12

ARW	artificial rainwater
ASW	artificial seawater
AZ	Antarctic Zone
CBD	citrate, bicarbonate, dithionite extraction method
CC	Creative Commons license
Chl	Chlorophyll
DL	detection limit
DLe	experimental detection limit
DMS	diméthylsulfure
DOM	dissolved organic matter
EC	Evapocondensé
HDPE	high density polyethylene
HNLC	High Nutrients-Low Chlorophyll

HN-LSi-LC	High Nitrate-Low Silicate-Low Chlorophyll
HSVA	hot spot volcanic ash
ICP-AES	inductively coupled plasma atomic emission spectroscopy
ICP-MS	inductively coupled plasma mass spectrometry
IR-MS	isotope ratio mass spectrometer
LDPE	low density polyethylene
LNLC	Low Nutrients-Low Chlorophyll
MLD	mixed layer depth
nEC	Non évapocondensé
NSW	natural seawater
OISO	Océan Indien Service d'Observations
OM	organic matter
PC	particle concentration
PCA	principal component analysis
PE	polyethylene
PF	Polar Front
PFZ	Polar Front Zone
pH	potential of hydrogen
POC	Carbone organique particulaire
PP	primary production
RC	reduction coefficient
SAF	Subantarctic Front
SAZ	Subantarctic Zone
SD	standard deviation
SEMB	South East Madagascar Bloom
SF-ICP-MS	sector field inductively coupled plasma mass spectrometer
SIO	South Indian Ocean
SML	surface mixed layer
SO	Southern Ocean
SSA	specific surface area
St	station
STF	South Tropical Front
STZ	South Tropical Zone
SW	sea water
SZVA	subduction zone volcanic ash
Tchla	total chlorophyll a
TM	trace metal
XRD	X-ray diffraction

Dissolution de macro- et micronutriments issus d'aérosols désertiques et volcaniques dans l'eau de pluie et eau de mer: Influence sur le phytoplancton de l'Océan Indien Austral

Résumé

Les aérosols constituent une source importante de macro- et micronutriments pour l'océan hauturier. Cependant, uniquement les nutriments dissous sont considérés comme biodisponibles, c'est-à-dire assimilables par le phytoplancton. Ainsi, la quantification de leur solubilité se révèle primordiale pour (i) estimer l'influence d'un dépôt d'aérosols sur le phytoplancton, et (ii) boucler les cycles biogéochimiques de ces éléments. Dans le cadre de cette thèse, nous avons établi des gammes de solubilité de deux types d'aérosols (désertique ou volcanique) selon le mode de dépôt (sec et humide), en intégrant la variabilité en fonction de l'origine des aérosols. Ainsi, le macronutriment silicium issu des poussières désertiques est plus soluble comparé aux cendres volcaniques (jusqu'à 0.7 % contre 0.2 %), notamment *via* la dissolution du quartz. Le micronutriment fer se dissout majoritairement dans l'eau de pluie lors d'un dépôt humide des aérosols à l'océan *via* la dissolution d'aluminosilicates, avec une solubilité généralement inférieure à 0.14 % et 0.02 %, dans l'eau de pluie et eau de mer respectivement, et ce indépendamment du type d'aérosol. L'ensemble de ces résultats permet ainsi une révision des flux de nutriments atmosphériques à l'océan de surface qui pourra être *in fine* intégrée dans les estimations globales de modélisation biogéochimique. La réponse biologique suite à un apport de nutriments par voie atmosphérique a été déterminée dans l'Océan Indien Austral et les nutriments ont majoritairement profité à la communauté de diatomées, notamment au niveau du plateau de Kerguelen.

Mots clés: macro- et micronutriments, silicium, fer, aérosols naturels, poussières désertiques, cendres volcaniques, solubilité, dissolution, Océan Indien Austral, phytoplancton.

Macro- and micronutrient dissolution from desert and volcanic aerosols in rain and seawater: Impact on phytoplankton in the Southern Indian Ocean

Abstract

Aerosols are an important source of macro- and micronutrients for the open ocean. However, only dissolved nutrients are considered bioavailable, *i.e.*, assimilable by phytoplankton. Thus, the quantification of their solubility is essential to (i) estimate the influence of aerosol deposition on phytoplankton, and (ii) closing the biogeochemical cycles of these elements. We thus established the solubility ranges of two types of aerosols (desert or volcanic) according to the deposition mode (dry and wet), by integrating the variability depending on the aerosol origin. Thus, the macronutrient silicon found in desert dust is more soluble compared to volcanic ash (up to 0.7 % against 0.2 %), in particular *via* the dissolution of quartz. The micronutrient iron dissolves mainly in rainwater during wet deposition of aerosols in the ocean *via* the dissolution of aluminosilicates, with solubilities generally below 0.14% and 0.02%, in rainwater and seawater respectively, regardless of the type of aerosol. Thus, these results allow a re-estimation of atmospheric nutrients fluxes to the surface ocean which could ultimately be integrated into global biogeochemical models. Finally; the biological response to an atmospheric nutrient input has been determined in the Southern Indian Ocean and the nutrients have mainly benefited the diatom community, especially at the Kerguelen plateau.

Keywords: macro- and micronutrients, silicon, iron, natural aerosols, desert dust, volcanic ash, solubility, dissolution, Southern Indian Ocean, phytoplankton.